Link Acquisition for the Optical Formation Metrology Testbed

Experimental simulation of a spacecraft-to-spacecraft laser ranging scenario

AE5822

Samuele Malta

Delft University of Technology

TUDelft

AIRBUS

Link Acquisition for the Optical Formation Metrology Testbed

Experimental simulation of a spacecraft-to-spacecraft laser ranging scenario

by

Samuele Malta

to obtain the degree of Master of Science

at the Delft University of Technology,

to be defended publicly on Monday November 11, 2024.

TUDelft

Acknowledgements

Summary

This thesis describes the implementation of an innovative experimental set-up to perform simulations of laser link acquisitions between two spacecraft, in the context of laser ranging interferometry missions, which are increasingly relevant in the fields of gravimetry and gravitational waves detection. The objective of the project is to reproduce realistic laser beam characteristics, demonstrate the ability of the Optical Formation Metrology Testbed (OFMT) to perform autonomous link acquisition procedures and define requirements for the OFMT architecture based on the experimental results.

To achieve the goals set, the OFMT set-up has been assembled and aligned, the relevant beam properties have been measured, the supporting experimental infrastructure to conduct the acquisition tests has been integrated, the necessary calibration procedures have been carried out and finally the acquisition tests have been defined and performed, followed by a comprehensive analysis of the results.

From the evaluation of the test runs and the measurements of the beam characteristics, it can be concluded that the OFMT set-up represents a new way of successfully recreating laser beams between spacecraft that are placed far apart from each other, following a design path that had not previously been covered by other experimental architectures of this kind. Additionally, the work outlined in this thesis demonstrates the ability of the set-up to carry out autonomous link acquisition procedures, paving the way for further developments of the instruments.

Contents

List of Figures

List of Tables

Nomenclature

Abbreviations

Abbreviation	Definition
ADC	Analog to Digital Converter
AEI	Albert Einstein Institute
AOM	Acousto Optic Modulator
BBO	Big Bang Observer
BS	Beam Splitter
CAD	Computer Aided Design
CCD	Charge Coupled Device
CCR	Corner Cube Retroreflector
CMOS	Complementary Metal Oxide Semiconductor
CTE	Coefficient of Thermal Expansion
DAC	Digital to Analog Converter
DC	Direct Current
DLR	Deutsche Zentrum für Luft- und Raumfahrt
DOF	Degree Of Freedom
DPA	Dynamic Power Attenuator
DPS	Differential Power Sensing
DWS	Differential Wavefront Sensing
ESA	European Space Agency
F-C	Fiber Coupled
F-S	Free Space
FOV	Field Of View
FPGA	Field Programmable Gate Array
FSM	Fast Steering Mirror
FSM-IFO	Fast Steering Mirror next to the IFO
FSM-OMT	Fast Steering Mirror in the OMT
GFZ	GeoForschungsZentrum
GOCE	Gravity Field and Steady-State Ocean Circulation Explorer
GPS	Global Positioning System
GRACE	Gravity Recovery and Climate Experiment
GRACE-FO	GRACE Follow On
GRAIL	Gravity Recovery and Interior Laboratory
HXP	Hexapod
I-P	In Plane
IFO	Interferometer
IFP	In Field Pointing
LAGEOS	LAser GEOdynamic Satellite
LEO	Low Earth Orbit
LET	Laboratory for Enabling Technologies
LIGO	Laser Interferometer Gravitational-Wave Observatory
LISA	Laser Interferometer Space Antenna
LLS	Laser Link Simulator
LOS	Line Of Sight
LRI	Laser Ranging Interferometer

Abbreviation	Definition
NGGM	Next Generation Gravity Mission
O-P	Out of Plane
OA	Optical Axis
OFMT	Optical Formation Metrology Testbed
OGSE	Optical Ground Support Equipment
OMT	Optical Metrology Terminal
PAAM	Point Ahead Angle Mechanism
PBS	Polarizing Beam Splitter
PM	Polarization Maintaining
PTA	Pulsar Timing Array
QPD	Quadrant Photodetector
RF	Radio Frequency
RMS	Root Mean Square
S/C	Spacecraft
SCPI	Standard Commands for Programmable Instruments
SHWS	Shack Hartmann Wavefront Sensor
SM	Steering Mirror
STR	Star Tracker
TX	Transmitted
VOA	Variable Optical Attenuators
WFE	Wavefront Error

Symbols

Symbol	Definition	Unit
A	Amplitude	[m]
C	Capacitance	[F]
f	Frequency	[Hz]
I	Intensity	[W/m^2]
k	Spiral pitch	[-]
L	Length	[m]
m_{flat}	Flatness parameter	[-]
n_{scan}	Scan amplitude parameter	[-]
P	Power	[W]
R	Resistance	[Ω]
r	Radius	[m]
T	Time	[s]
α	Half angle	[rad]
Δ, δ	Difference	[-]
ϵ	Aperture radius	[m]
η_{het}	Heterodyne efficiency	[-]
θ	Spiral angle	[rad]
λ	Wavelength	[m]
ρ	Distance from the centre	[m]
τ	Transmittance	[-]
ϕ	Phase	[rad]
ω	Beam waist	[m]

1

Introduction

The exploration and observation of planet Earth have been central to human curiosity and scientific inquiry since antiquity. From the ancient Greeks' early attempts to measure the Earth's circumference to the modern era of satellite-based observations, humanity's quest to understand our planet's inner workings has been fuelled by an insatiable thirst for knowledge and a deep-seated fascination with the world around us.

Throughout history, the study of Earth has been motivated by various objectives, ranging from practical navigation and resource management to philosophical inquiries into our place in the cosmos. Eratosthenes' groundbreaking calculation of the Earth's circumference in 240 B.C. [60] marked a pivotal moment in this journey, demonstrating humanity's capacity for scientific reasoning and empirical observation on scales that went beyond single nations and individuals. Since then, successive generations of scientists, explorers, and scholars have continued to build upon this foundation, employing increasingly sophisticated tools and techniques to unlock the secrets of our planet's past, present, and future.

1.1. Space-based gravimetry and gravitational waves detection

In recent decades, the urgency of studying Earth's dynamics has intensified, driven by the growing awareness of anthropogenic climate change and its profound impacts on our environment and society. The need to monitor and understand the Earth's changing climate has become increasingly apparent, prompting concerted efforts to collect and analyse data on a global scale. Central to this endeavour is the acquisition of precise information regarding the distribution of mass within and around the Earth, including variations in land ice, ocean currents, and atmospheric circulation patterns. The importance of these data cannot be overstated. They serve as critical inputs for climate models, enabling scientists to simulate and predict future climate scenarios with greater accuracy. By understanding the mechanisms driving Earth's climate system, researchers can identify potential tipping points, assess the risks posed by extreme weather events, and inform policymakers about the urgent need for mitigation and adaptation measures.

Moreover, the study of Earth's gravitational field offers unique insights into the planet's interior structure and dynamic processes. Changes in mass distribution, such as melting glaciers or shifts in groundwater storage, manifest as detectable variations in the Earth's gravitational field. By analysing these gravitational anomalies, scientists can infer valuable information about subsurface geology, tectonic activity, and hydrological cycles. Traditionally, such measurements have been conducted using ground-based instruments, such as gravimeters and GPS receivers. While valuable and still used to this day to monitor local gravity field variations in circumscribed areas [6], these methods are limited in their spatial coverage and in their sensitivity by environment noise [51], making it challenging to precisely monitor large-scale changes in Earth's gravity field comprehensively. In recent years, however, the advent of satellite-based gravity missions has revolutionized our ability to study Earth's gravitational dynamics from space. Satellite missions such as the Gravity Recovery and Climate Experiment (GRACE) and its successor, GRACE Follow-On (GRACE-FO), have provided unprecedented insights into the Earth's

gravitational field, offering global coverage and high-resolution measurements of mass redistribution over time [58][59][28]. By precisely measuring changes in the distance between twin satellites orbiting in tandem, these missions have enabled scientists to track variations in Earth's gravity field with unparalleled precision, revolutionizing our understanding of processes such as ice sheet dynamics, groundwater depletion, and sea level rise. An example of the results coming from data retrieved in these type of missions is the famous "Potsdam potato", in Figure 1.1, that depicts (not to scale) gravity field anomalies at the surface of the Earth. The field of space-based gravimetry is in rapid expansion and further missions that build on the knowledge gained from GRACE and GRACE Follow-On are already planned: GRACE Continuity has been accepted and currently has a planned launch for 2028 [31] while the development of a Next Generation Gravity Mission (NGGM) under the supervision of the European Space Agency (ESA) is underway [38]. Furthermore, the study of Earth's gravity field has
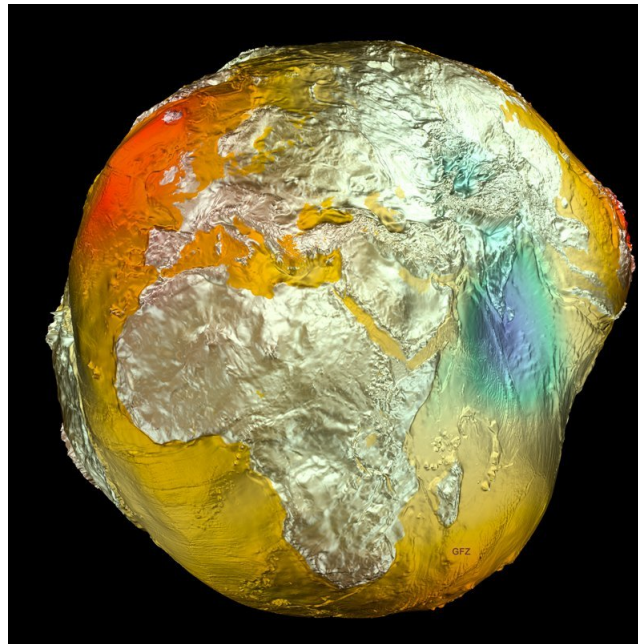
Figure 1.1: The famous "Potsdam potato", obtained from the elaboration, at the GFZ Helmholtz-Zentrum in Potsdam, of data retrieved by GOCE, GRACE and LAGEOS [27].

implications beyond our planet's boundaries. The insights gained from satellite-based gravity missions can inform our understanding of planetary dynamics across the solar system and even shed light on fundamental questions in cosmology and astrophysics. Projects such as the Gravity Recovery and Interior Laboratory (GRAIL) [67], which studied the Moon's gravitational field, and proposed missions to explore the gravitational dynamics of Mars [63] underscore the broader significance of gravitational research in planetary science.

In parallel, advancements in gravitational wave astronomy have opened new windows onto the universe's gravitational landscape, providing direct evidence of cataclysmic events such as black hole mergers and neutron star collisions. The success of ground-based detectors like the Laser Interferometer Gravitational-Wave Observatory (LIGO) and Virgo has paved the way for ambitious space-based missions such as the Laser Interferometer Space Antenna (LISA), which aims to detect gravitational waves from sources in space with unprecedented sensitivity [2], Taiji and TianQin, two planned Chinese missions for gravitational waves detection [32][35]. Even more ambitious missions have been proposed in this field, such as the Big Bang Observer (BBO) [15], but they have not been adopted yet and remain in a speculative phase. The intersection of gravitational research with other fields of astrophysics and fundamental physics promises to unlock new frontiers of knowledge, revealing insights into the nature of space-time, the origins of cosmic structures, and the fundamental forces shaping the universe. Figure 1.2 depicts an artistic representation of the gravitational waves generated by two merging black holes, the event detected by LIGO in 2015, which marked the first direct experimental detection of gravitational waves.
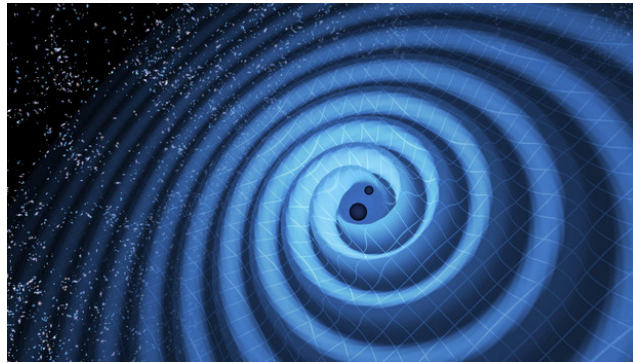
Figure 1.2: Artistic representation of gravitational waves generated by the merger of two black holes [7].

The link between these two fields, Earth gravimetry from space and space-based gravitational wave detectors, is that they are both enabled by similar technological advancements in optical metrology, specifically laser ranging interferometry. Achieving ever so sensitive displacement measurement instruments has made this type of missions, once thought out of reach, one of the most exciting and rapidly developing fields of science. In the next sections the basic principles underlying optical metrology techniques applied to gravimetry and gravitational waves detection are analysed in detail.

1.2. Displacement measurement for space-based gravimetry and gravitational waves detection

In the preceding section, the importance and relevance of space-based gravimetry and gravitational wave detection missions have been outlined, alongside the introduction of the working principle of the instruments used in these missions, employing optical metrology techniques for displacement measurement. Subsequently, the following paragraphs address the measurement principle characterizing these missions, underscoring the significance of highly precise, long-range displacement measurement achievable solely through the adoption of optical metrology solutions. This objective is exemplified by considering two mission architectures representing distinct scientific objectives. Specifically, GRACE Follow-On, representing the pioneering use of a laser ranging interferometer in space as a technology demonstrator, and LISA, the Large Interferometer Space Antenna—an ESA mission for gravitational wave detection slated for launch in the 2030s and nearing the design and implementation phase.

1.2.1. GRACE Follow-On

The GRACE Follow-On mission, like its predecessor GRACE, aims at measuring gravity field anomalies on the Earth, using two satellites flying on a polar orbit in a tandem configuration, separated by around 220 km. The distance between the two satellites changes when they are affected by different forces, like residual atmospheric drag in Low Earth Orbit (LEO), micro-meteorite and space debris impact and different gravity pull. The last force is what is of interest for the science of the mission. The way in which the gravitational field anomaly can be extrapolated by the change in distance between the two spacecraft is exemplified in Figure 1.3. When the first satellite encounters a location on Earth with a higher local concentration of mass, the additional gravitational pull with a component in the direction of flight causes it to speed-up and increase the distance between the two spacecraft. As can be seen by the scenario 2 in Figure 1.3, when the spacecraft 1 is over the mass anomaly, the distance between the two satellites is larger than the starting, or nominal, scenario 1. From scenario 3 in Figure 1.3 it can be seen that when the first spacecraft moves away from the mass anomaly, it is pulled back by the component of the gravitational acceleration that is now in the opposite direction of the flight path, causing spacecraft 1 to move closer to spacecraft 2. At the same time, spacecraft 2 is now moving closer to spacecraft 1 because it is close to the mass anomaly and is subjected to the same forces that characterized the first satellite in scenario 1. Once both spacecraft will have passed the mass anomaly the situation will be the same as the nominal one, until they fly over another mass anomaly.

Monitoring the variations in the distance between the two spacecraft allows for retrieving information regarding the forces that cause the displacement. The gravitational force anomalies to be measured are
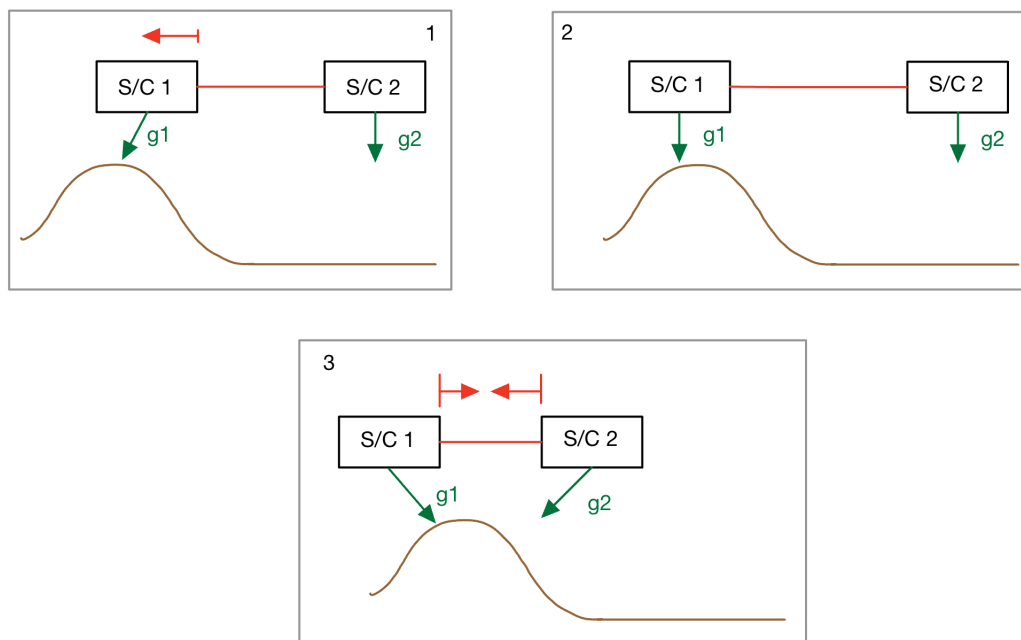
Figure 1.3: GRACE (and GRACE Follow-On) measurement principle visualized.

extremely minute, and therefore cause extremely small distance variations between the two satellites (GRACE Follow-On can detect displacements in the order of hundreds of nanometer due to gravitational anomalies) which poses challenging requirements to the instruments onboard the spacecraft.

1.2.2. LISA

The Large Interferometer Space Antenna is the third large-class mission adopted by the European Space Agency as part of its Cosmic Vision program. Its objective is to measure gravitational waves, allowing scientists to gain unprecedented insights into the most extremes events in the cosmos.

Gravitational waves are ripples in the fabric of spacetime, a consequence of Einstein's theory of general relativity. These waves are produced by the acceleration of massive objects, such as black holes, neutron stars, or other dense astrophysical bodies. When these objects orbit each other or collide, they emit gravitational waves that propagate through the universe, carrying information about their origins and dynamics. Gravitational waves are extraordinarily weak, making their detection a formidable challenge, since they effectively are minuscule expansions and contractions of the fabric of spacetime itself. The key to LISA's success lies in its ability to detect gravitational waves at lower frequencies than ground-based detectors like LIGO and Virgo, which at low frequencies are limited by seismic noise (earthquakes, waves, human activities etc.) and gravity gradient noise. While ground-based detectors excel at capturing high-frequency gravitational waves produced by stellar-mass objects, LISA's space-based configuration allows it to detect lower frequency waves emitted by supermassive black hole mergers, binary systems in our galaxy, and other sources. By observing gravitational waves across a broad spectrum of frequencies, LISA complements the capabilities of ground-based detectors, providing a more comprehensive view of the universe's gravitational landscape.

The mission consists of three spacecraft positioned in a triangular configuration, each separated by millions of kilometres, orbiting around the Sun at a fixed distance from the Earth. An artistic representation of the mission configuration is depicted in Figure 1.4.
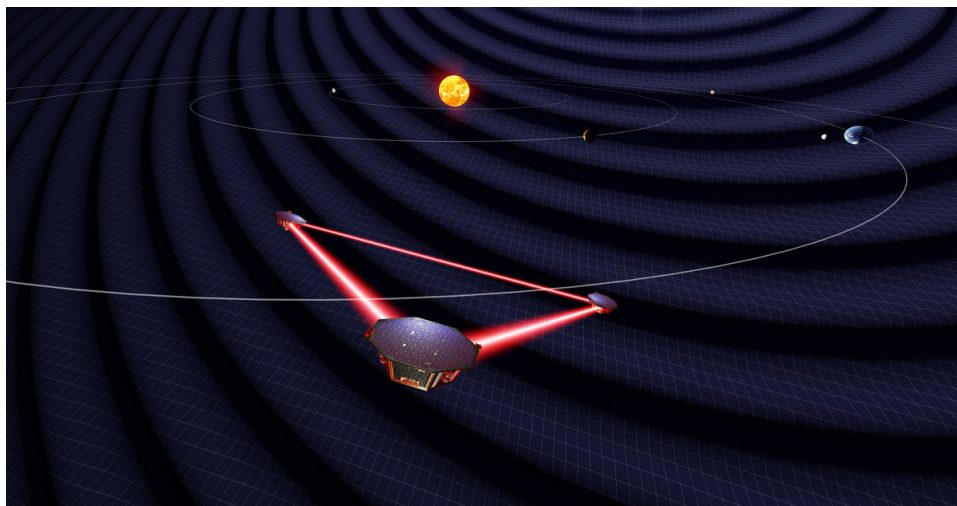
Figure 1.4: Artistic representation of LISA's mission configuration [20].

As gravitational waves pass through the spacecraft array, stretching spacetime, they cause minute fluctuations in the distances between the spacecraft. By measuring the variation in the distance between the satellites, the characteristics of the gravitational waves can be retrieved, but the challenges involved in performing this measurement are even greater than those related to the GRACE and GRACE Follow-On missions, as the displacement to be measured are orders of magnitude smaller than those of the gravimetry missions and the distance between the spacecraft of the configuration is considerably larger: each arm of the LISA constellation measures 2.5 million kilometres, while the nominal distance between the GRACE Follow-On satellites is approximately 220 kilometres.

The previous sections introduced the scientific need for gravimetry and gravitational waves detection missions and how the most effective method to achieve the science objectives of these missions is to fly satellites in formation, precisely monitoring the variations in the distance between them. The unprecedented sensitivities to be achieved in the displacement measurements performed by LISA and NGGMs spacecraft can be achieved effectively only through the use of optical metrology techniques, that take advantage of highly stable laser sources in combination with phenomena originating from wave properties of electromagnetic radiation. The concept and working principle of laser ranging interferometry is presented in Section 2.2, providing the theoretical basis to understand the displacement measurement principle utilised in GRACE Follow-On, LISA and all the other proposed gravimetry and gravitational waves detection missions mentioned in Section 1.1.

1.3. Research Questions and thesis objectives

The increased interest in gravimetry and gravitational waves detection missions led to the necessity for further development of instrumental hardware that could help in gaining more insights into the behaviours and interactions of laser ranging setups with the space environment; the Optical Metrology Terminal (OMT) and the Optical Formation Metrology Testbed (OFMT) projects have therefore been established. The former is an innovative design concept aiming to move beyond the GRACE-FO architecture and challenges, while the latter is a laboratory testbed conceived to demonstrate the capabilities of the new instrument architecture under realistic conditions. When the spacecraft are launched and inserted in their orbits, the level of uncertainty they have on their relative attitudes does not allow them to immediately establish a laser link, but they need to perform a delicate link acquisition procedure. Link acquisition strategies and procedures are therefore one of the most critical aspects of laser ranging missions and the extensive literature study performed in Chapter 3 outlines the need for further studies in this field, especially when applied to innovative setups like the OMT (and OFMT).

The following Research Question and sub-questions have therefore been developed:

R.Q. : How can link acquisition strategies be recreated in the OFMT setup under realistic laboratory conditions?

- ***R.Q. 1: How can conditions in the lab be recreated realistically (especially with regards to the received beam), and how does the setup compare with previous link acquisition setups in this aspect?***
- ***R.Q. 2: How well can the OFMT setup perform autonomous link acquisition strategies and procedures?***
- ***R.Q. 3: What requirements does the OFMT link acquisition procedure put on the instrument's hardware?***

In order to answer the research questions presented, a set of goals have been laid down for the thesis project. For the first research question the following goals have been identified:

- Build and align the OFMT setup.
- Measure the beam parameters to assess both the quality of the alignment and the recreation of the beam characteristics.
- Assess the alignment accuracy from the results of acquisition tests.
- Compare the results with the parameters of the other setups found in literature.

For the second research question the set of goals are focused on the acquisition tests:

- Build and assemble the supporting infrastructure to provide an interface with the components of the OFMT setup and perform the tests.
- Develop and implement an autonomous acquisition procedure to run the acquisition tests.
- Calibrate the OFMT components.
- Define and perform link acquisition tests, with a focus on functionality other than performance.

Finally, for the last research question the goals that have been set focus on the analysis of the results and the lessons learned while building and aligning the components of the setup:

- Identify which components are necessary in the OFMT setup for the acquisition.
- Identify possible supporting or alternative methods for the assembly and alignment if deemed not accurate enough.
- Identify design requirements for the OFMT architecture based on the acquisition results.

In the following chapters the work performed to accomplish the goals set in the previous paragraphs is presented, as well as the results achieved which allow to answer the research questions previously defined.

2

Theoretical Background

2.1. Lasers and Optics

Following the introduction given in Section 1, in this chapter the main theoretical topics regarding lasers, optics and interferometry, which are necessary for the correct understanding of the work described in the next chapters, are provided. A general background knowledge in optics is assumed, and the reader can find additional information in the sources.

2.1.1. Introduction to the laser

The Laser (Light Amplification by Stimulated Emission of Radiation) is a self-excited oscillator. It has three main components: an active medium, a resonator and a pump system [49]. The active medium amplifies the electromagnetic radiation and is located inside the resonator; the pump system "pumps" energy into the active medium and the resonator makes the interaction between the electromagnetic field and the active medium possible. One of the mirrors of the resonator is a partial reflector and lets out a portion of the electromagnetic radiation accumulated inside, which represents the output of the laser system. In Figure 2.1 a simple drawing shows the components of a laser and their interaction.
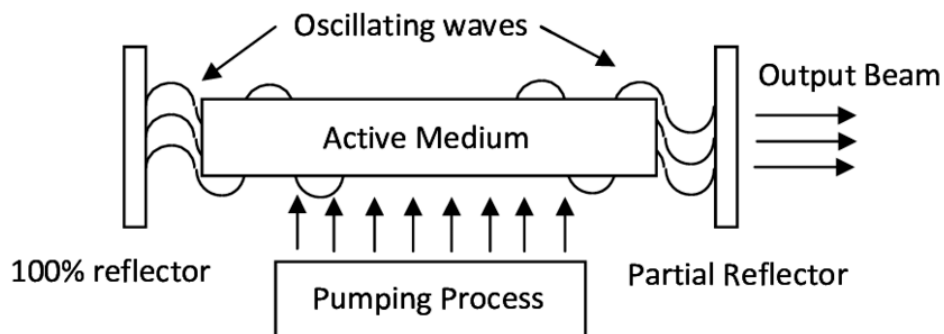
Figure 2.1: Laser system with components and their interaction [36].

The exact physics behind the working principle of the lasers is not needed for a full understanding of the thesis work, as it is sufficient to say that the main characteristics that differentiate a laser source from most other light sources are the spatial and temporal coherence. In optics, coherence is strongly related to the ability of light to exhibit interference effects. Spatial coherence means a strong correlation between the electric fields at different locations across the beam profile, while temporal coherence means a strong correlation between the electric fields at one location but at different times [45].

2.1.2. Laser beam properties

When dealing with light emitted from a laser source, most of the time it is in the form of a well directed light beam, called a laser beam. Light propagates mostly in one direction, with most of the optical power

concentrated in a small area [46]. The usual type of beam emitted by laser sources is the Gaussian beam.

In a Gaussian beam, the intensity profile can be described using a Gaussian function, and the phase profile is approximated by a polynomial of at most second order [47]. The intensity of a Gaussian beam as a function of the radius r and the longitudinal position z is here presented as an example:

$$I(r, z) \;=\; \frac{P}{\pi \omega(z)^2/2} exp \left(\frac{r^2}{\omega(z)^2} \right) \,, \tag{2.1}$$

where P is the optical power and $\omega(z)$ is the beam radius. The beam radius is the distance from the beam axis where the intensity drops to $1/e^2$ of the maximum value [47].

The position at which the beam is focused corresponds to the beam waist, where the beam radius is at its minimum and the phase profile is flat [47]. The beam profile before the beam waist is converging, while after the beam waist it diverges. The Electric field distribution of a Gaussian beam around its beam waist is represented in Figure 2.2.
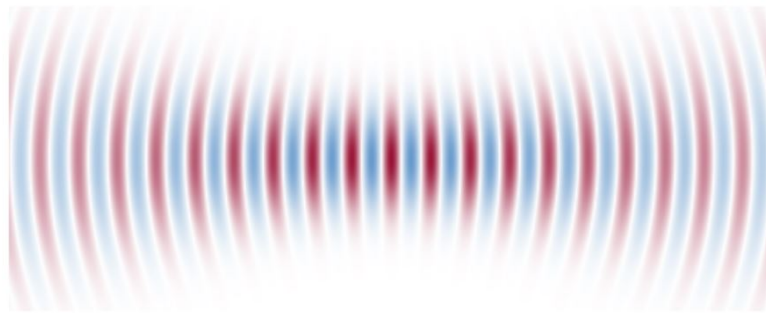
Figure 2.2: Electric field distribution of a Gaussian beam around its beam waist [47].

Wavefront
An important feature of laser beams and electromagnetic waves in general is the notion of wavefront. Wavefronts are surfaces connecting points with the same phase of a monochromatic wave [48]. As an example, in Figure 2.3 the wavefront of a Gaussian beam for a particular moment in time is shown.
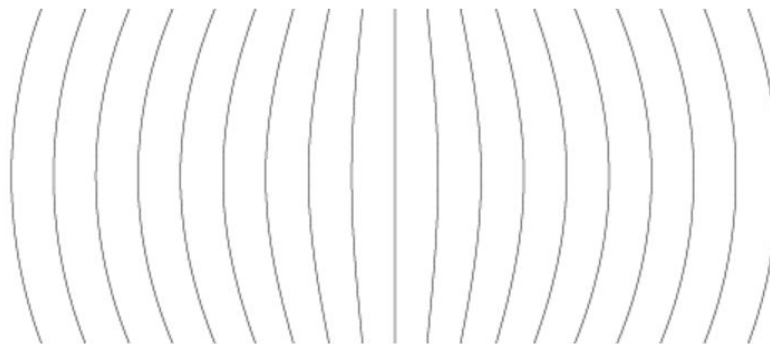
Figure 2.3: Wavefronts of a Gaussian beam for a given moment in time [48].

For Gaussian beams with a perfect beam quality, the wavefronts are flat at the beam waist. From Figure 2.3 it is also noticeable that for perfect Gaussian beams the concavity of the wavefront changes on the two sides of beam waist along the direction of propagation.

Beam quality
The beam quality is an important indicator for laser beams, it can be defined in different ways, but it is usually understood as how tightly can a laser beam be focused under certain conditions [44]. For

a Guassian beam, a high beam quality means that the beam has smooth wavefronts, which become flat at the beam waist. The beam quality is extremely important for laser interferometry applications as it affects the spatial coherence of the laser beam, which needs to be very high in high precision laser metrology environments.

2.1.3. Polarization

Electromagnetism can be described as a wave phenomenon and for the applications involved in this thesis work, this is the most suitable description of light. Light waves are transverse waves, meaning that the oscillations occur in the plane perpendicular to the direction of motion; this type of waves are characterized by a polarization state, which is a property indicating the direction in which the oscillations take place. For light waves the direction of polarization is taken as the direction in which the electric field oscillates (the magnetic field always oscillates perpendicularly to the electric field and the direction of motion).

The simplest form of polarization is linear polarization, which means that the electric field fluctuates in a linear direction perpendicular to the beam axis [40]. An example of this tipe of polarization is shown in Figure 2.4.
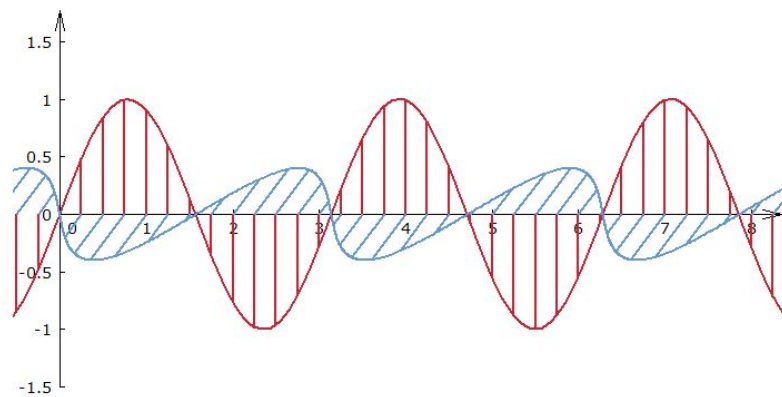
Figure 2.4: Representation of linear polarization of light [40].

Other types of polarization states include circular and elliptical polarization. In circular polarization the electric field vector rotates around the beam axis, once per optical cycle, and maintains a constant magnitude [40]. This happens when the vertical and horizontal components of the electric field vector oscillate with equal magnitude and a 90° relative phase change. When the horizontal and vertical oscillations don't have the same magnitude the resulting polarization state is called elliptical, where the electric field vector moves along an ellipse [40]. For circular and elliptical polarization it is possible to identify a direction of rotation: it can either be left or right circular (or elliptical) polarization, if the electric field vector rotates towards the left, or the right, when seen in the direction of propagation.

Oftentimes light (especially natural light) can also be unpolarized, when the polarization state is constantly changing randomly. Light can also be found in-between the two extremes of polarized and unpolarized light, and a degree of polarization can be defined, indicating how close or how far from a fully polarized state the light is.

2.1.4. Optical aberrations

Optical aberrations are imperfections that affect the performance of optical systems making it deviate from the ideal scenario obtained using the paraxial approximation in ray optics. Effects due to the wave behaviour of light, like diffraction, are not included in the aberrations. There are many kinds of optical aberrations, the main ones being defocus, chromatic aberrations, spherical aberrations, astigmatism, coma, field curvature, and image distortion [39]. The most relevant ones for the laser metrology application discussed in this thesis are further expanded in the following paragraphs.

The defocus occurs when the distances withing the imaging system are not matching with the position of the imaged objects, making the image blurry. This effect can be corrected by adjusting the location

of the elements of the setup. Spherical aberrations affect images going through the outer parts of a spherical lens, where the curvature of the surface is too strong and leads to a degradation of the image quality [39]. Spherical aberration effects can be reduced by using optical elements that are less affected by these phenomenon.

When the angle between the light ray and the optical axis (OA) is large, astigmatism effects can become more relevant and the result is that the point images become elliptical in shape. It cannot be compensated by one lens, but more lenses in a system can together decrease the overall astigmatism of the image [39]. Coma is a similar effect to astigmatism in the sense that it occurs when the angle between the light ray and the optical axis is large, and the ray goes through the outer parts of the lens as well. The image of a point affected by coma can somewhat resemble the shape of a comet [39]. Aperture stops can limit the effects of coma.

Zernike polynomials

A useful method for characterizing monochromatic optical aberrations is by using Zernike polynomials. The Zernike model is based on orthogonal functions that depend on polar coordinates ρ and φ. The radial part being described by polynomials while the other by the factor $cos\ m\varphi$ (or $sin\ m\varphi$) [39]. The wavefront errors $W(\rho, \varphi)$ can then be decomposed with respect to the position:

$$W(\rho, \varphi) = \sum_{n=0}^{\infty} \sum_{m=-n}^{n} a_n^m Z_n^m(\rho, \varphi) \,, \qquad (2.2)$$

where Z_n^m are called Zernike polynomials [39].

Different orders and degrees of these polynomials identify different optical effects and aberrations, which are summarized in Figure 2.5.
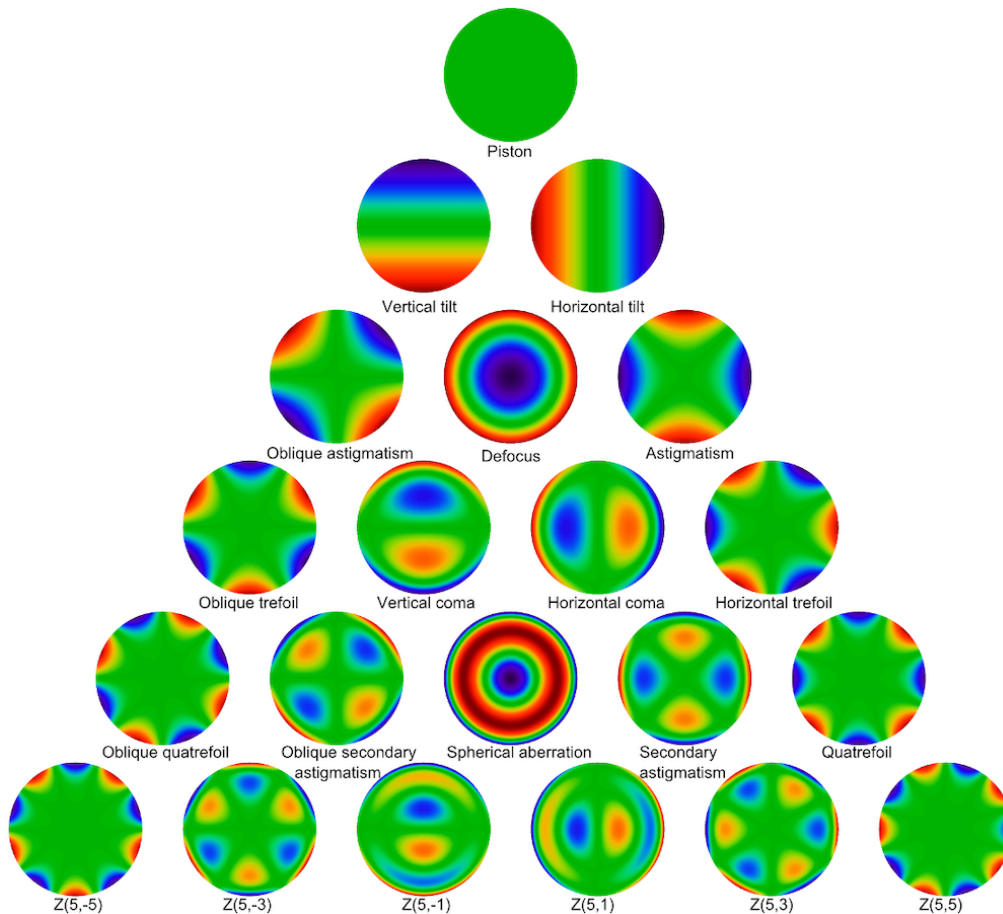
Figure 2.5: Zernike polynomials and associated wavefront errors [5].

2.2. Laser ranging interferometry for optical metrology

In Section 1 the science objectives to be achieved and the recent developments in the fields of gravimetry and gravitational waves detection have been outlined, along with the operating and planned space missions to explore a new way of gathering the relevant data for these new fields. The measurement principle identified in Section 1.2 links distance variations between satellites to gravity field anomalies and to the passage of gravitational waves, while at the end of Section 1.2.2 laser ranging interferometry has been identified as the best way to achieve the required precision in the displacement measurements.

In the first part of this section the working principle of laser ranging interferometry is explored, introducing homodyne and heterodyne interferometry, and how heterodyne interferometry is the best option to meet the requirements on the displacement measurement. The second part concentrates on measuring the beat note signal and showing how to link the phase measurements to displacement measurements.

2.2.1. Heterodyne interferometry for displacement measurement

The wave behaviour of light introduces a wealth of phenomena that manifest themselves under different conditions. Interference is the phenomenon of interest in the metrology application at hand, but it requires a number of conditions to be met. Since interference is an effect which occurs when two or more light beams are superimposed, the three requirements placed on the beams for this to happen are: spatial and temporal overlap of the light fields, phase coherence of the light fields and non-orthogonal polarization states [42].

Laser sources under certain conditions can meet the requirements for interference patterns to appear when superposed. In addition to this, the stability provided by lasers, locked to an optical cavity, and their capacity of achieving a high energy density in the beam make them ideal candidate for very precise long range optical metrology applications.

In this section two types of interferometry are explored, homodyne and heterodyne interferometry, involving two laser sources emitting electromagnetic waves at the same wavelength or at slightly different wavelengths respectively. It will be shown how heterodyne interferometry is the better option, for this specific application, to perform optical displacement metrology through the detection of a beat note.

Homodyne interferometry

Homodyne interferometry is the first light interferometry technique developed and is performed with the superimposition of two beams with the same frequency. When the two beams are in phase, the resulting wave has twice the amplitude of the originals, while when the two beams are out of phase by π the resulting wave has zero amplitude ("black screen"). This resulting behaviour is shown in Figure 2.6, but there is a whole spectrum of possibilities in between these two scenarios. One of the first demonstration
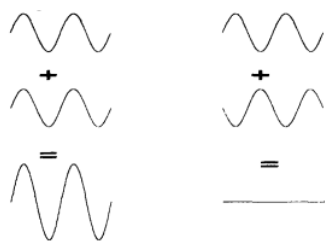
Figure 2.6: Behaviour of two waves superposition, in phase on the left and out of phase on the right [3].

of homodyne interferometry was the instrument developed by Michelson, which is particularly useful to monitor distance variations between different elements of the setup. The Michelson's interferometer components are represented in Figure 2.7. When the movable mirror changes its position it causes the interference pattern on the screen to change and by monitoring the change in the interference pattern the difference in the optical paths of the beams can be retrieved, extrapolating the information on the mirror displacement.

Homodyne interferometry presents a few aspects that make it less attractive for this space displacement metrology application, compared to the heterodyne counterpart [54].

The main complication for homodyne interferometry is that the signal is proportional to the phase change due to the displacement of the mirror (or the corresponding element in an interferometric setup) plus a phase component due to fluctuations in the optical path or in laser wavelength variations [3]. This characteristic (the fact that the information is carried on a DC signal) can cause the interferometer to present a very low sensitivity to the signal of interest due to the noise introduced by the dependency on oscillations of the optical path and the laser wavelength instability.

This problem can be solved by applying a small frequency difference between the two superimposing signals, effectively obtaining a heterodyne interferometer. Heterodyne interferometry does come with its own set of complications of course, mainly the need for two different highly stable laser sources and more complex detector electronics [54].
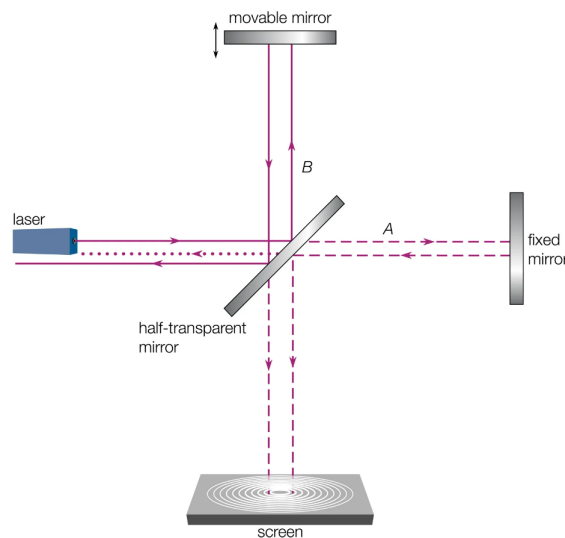
Figure 2.7: Michelson's interferometer setup [14].

Homodyne interferometry is still a widely employed technique for the most diverse applications, including metrology setups, and represents in many cases the best option to achieve the necessary scientific results. It is for example used to measure surface phenomena in microstructure, measuring surface deformations at the nanometer scale [29]. The choice between homodyne and heterodyne interferometry ultimately depends on the specific requirements of the application and the expected noise sources and their levels.

Heterodyne inteferometry

Optical heterodyne interferometry, or heterodyne detection, involves an optical signal and a local oscillator, which are linearly superimposed and detected by a photodetector. A beam splitter could for example be used to align the two beams and have them mode-matched. The photocurrent resulting on the photodetector has two different components: a constant component which is proportional to the sum of the local oscillator and the optical signal power, and an oscillating component with a frequency corresponding to the frequency difference between the signal and the local source, and amplitude proportional to the product of electric field amplitudes of the signal and local oscillator [43]. The oscillating part of the photocurrent is called beat note, and it is the part where the signal information is carried. The resulting intensity on the detector is mathematically described in the following section in Equation 2.3. A further advantage of heterodyne detection is that a strong local oscillator can work as a signal gain for a weak incoming optical signal, which would be hardly measurable with direct detection [43].

The problems previously highlighted for the homodyne interferometry technique can be resolved by using the heterodyne detection method, as a demodulation system can be locked to the beat signal, and in demodulation the variations caused by the dependencies on the setup instabilities can be filtered out [3].

The beat note signal, as introduced in the previous paragraphs, can be observed when two laser beams

with different optical frequencies are superimposed on a photodetector measuring the intensity of the resulting electromagnetic field. There are however some conditions that need to be met in order for the beat note signal to be measured. The spatial distribution of the two light fields must overlap and they must not be orthogonal, the polarization states must also not be orthogonal, the optical frequency difference must be within the bandwidth of the photodetector and the wavelengths must be in the sensitive range of the detector [41].

An example setup for heterodyne detection is shown in Figure 2.8.
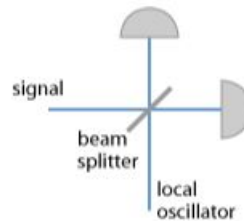
Figure 2.8: Setup schematics to perform heterodyne detection[43].

2.2.2. Displacement information from the beat note

In Section 1.2 the measurement principle of gravimetry and gravitational waves detection missions has been tackled, showing that it is based on performing displacement measurements between two (or more) spacecraft, monitoring the variation of the distance between them. Laser ranging interferometry has also been identified as the go-to technology for precise long range displacement measurement and in Section 2.2.1 heterodyne interferometry has been identified as the best methodology to achieve the desired laser interferometric performance. In the last part of this section the technique to extrapolate distance variation information from the beat note signal of a heterodyne detection system will be explained.

The advantage of using laser interferometry to monitor distance variations is that it allows the measurements of displacements far smaller than the laser wavelength, by tracking the phase difference between an incoming laser beam and a local laser source, as a shift in the phase difference between the two lasers corresponds to a variation in the distance between the two sources. Figure 2.9 shows the visualization of how the displacement information is encoded in the phase difference between two beams.
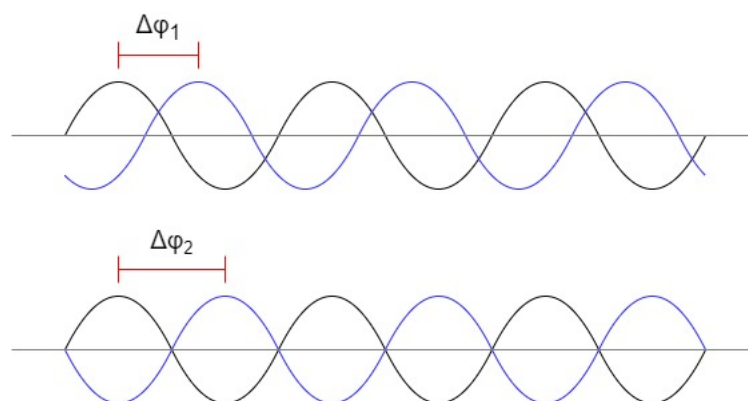
Figure 2.9: Phase difference variation between two separate laser sources.

Taking the black sine wave as the local laser and the blue sine wave as the incoming laser beam, it is possible to see that in the bottom diagram the phase difference $\Delta\varphi$ has increased compared to the phase difference in the top diagram, as the incoming laser's sine wave has shifted to the right

of the page. A shift in the sine wave could correspond to an increase, or decrease, of the distance between the two spacecraft. Measuring the change in the phase difference between the two beams would therefore allow to measure the change in the distance between the two satellites, which is the information needed for the science missions previously introduced.

In order to retrieve the phase difference information from the beat note signal generated during the heterodyne detection on the photodetector, the study of the heterodyne signal intensity needs to be performed. The intensity of the heterodyne signal is given by Equation 2.3 [52].

$$I = I_1 + I_2 + 2\sqrt{\eta_{het}I_1I_2}\, cos(2\pi(f_2 - f_1)t + (\phi_2 - \phi_1)) \tag{2.3}$$

In Equation 2.3 I_1 is the intensity of the local laser source, I_2 is the intensity of the incoming laser, η_{het} is the heterodyne efficiency, f_1 and f_2 are the optical frequencies of the local laser source and the incoming laser respectively, and ϕ_1 and ϕ_2 are the phases of the local and incoming lasers respectively. The beatnote signal allows the phase information to be down-converted into a radio frequency signal, given by the difference in the frequencies of the two lasers. The electric signal from the photodetector is then fed to a digital signal processing unit, where a phasemeter tracks the phase and the frequency of the beat signal, from which the displacement information can be retrieved [34], as shown in Equation 2.4

$$\delta z = \frac{\lambda}{4\pi}(\Delta\phi_{S/C1} - \Delta\phi_{S/C2}) \tag{2.4}$$

,

where δz is the displacement, while $\Delta\phi_{S/C1}$ and $\Delta\phi_{S/C2}$ are the phase differences ($\phi_2 - \phi_1$) measured from the beat notes on both spacecraft, but knowing that the value of $\Delta\phi_{S/C2}$ is predetermined as the laser in the slave spacecraft is offset phase-locked.

Heterodyne efficiency
The term introduced in Equation 2.3 named η_{het}, heterodyne efficiency, refers to the amount of "overlapping" between the two beams. The heterodyne efficiency term is introduced in the equation due to the single-mode nature of heterodyne detection, meaning that only light sources with the same mode can lead to an effective observation. If the incoming beam possesses other modes compared to the local oscillator, interference still occurs on the photodetector, but the local oscillations of intensity cancel out by integrating over the detector surface [43].

This characteristic of heterodyne detection can be useful if one of the objective is the suppression of unwanted light contributions, like straylight; on the other end though, it would greatly reduce the detection efficiency when the sources to measure are a superposition of many different modes. It could be possible to measure the signal corresponding to one mode at a time by having a local oscillator consisting of different spatial modes, but while the heterodyne signal would be proportional to the local oscillator power in the corresponding mode, the noise level would be determined by the total local oscillator power, showing that heterodyne detection is essentially a single mode technique [43].

<div align="right">

3

</div>

<div align="right">

State of the art

</div>

3.1. Long range displacement metrology in space

In Section 2.2 interferometric techniques have been introduced, heterodyne detection has been identified as the best methodology to achieve the accuracy required, and the extrapolation of displacement information from the phase of the beat note signal has been explained. In this section an overview of the state of the art of long range displacement metrology setups is given, with particular attention to the two missions introduced in Section 1.2, Grace Follow-On and LISA, and introducing a new setup developed at Airbus Defence & Space in Friedrichshafen, the Optical Metrology Terminal (OMT).

3.1.1. GRACE Follow-On

The great success of the GRACE mission, introduced in Section 1.1, has pushed the science team behind it to develop a successor as quickly as possible to guarantee a continuity in the gravimetry data, allowing for the acquisition of even more insights into the dynamic behaviour of the Earth. Given the strict time constraints for the development of the new mission and the necessity of ensuring a reliable continuation of the time series of data, the GRACE Follow-On spacecraft and mission configuration are basically identical to those of the GRACE mission, including the microwave ranging instrument. An artistic representation showing both spacecraft with laser and microwave links is shown in Figure 3.1.

GRACE-FO mission requirements

The GRACE Follow-On mission consists of two spacecraft flying in tandem configuration in a Low Earth Orbit, with an average altitude of around 490 km [23] and a separation between the spacecraft that is allowed to vary between 170 km and 270 km [26]. In Table 3.1 the requirements and parameters for the GRACE Follow-On mission Laser Ranging Interferometer (LRI) are summarized [13, 57, 37].
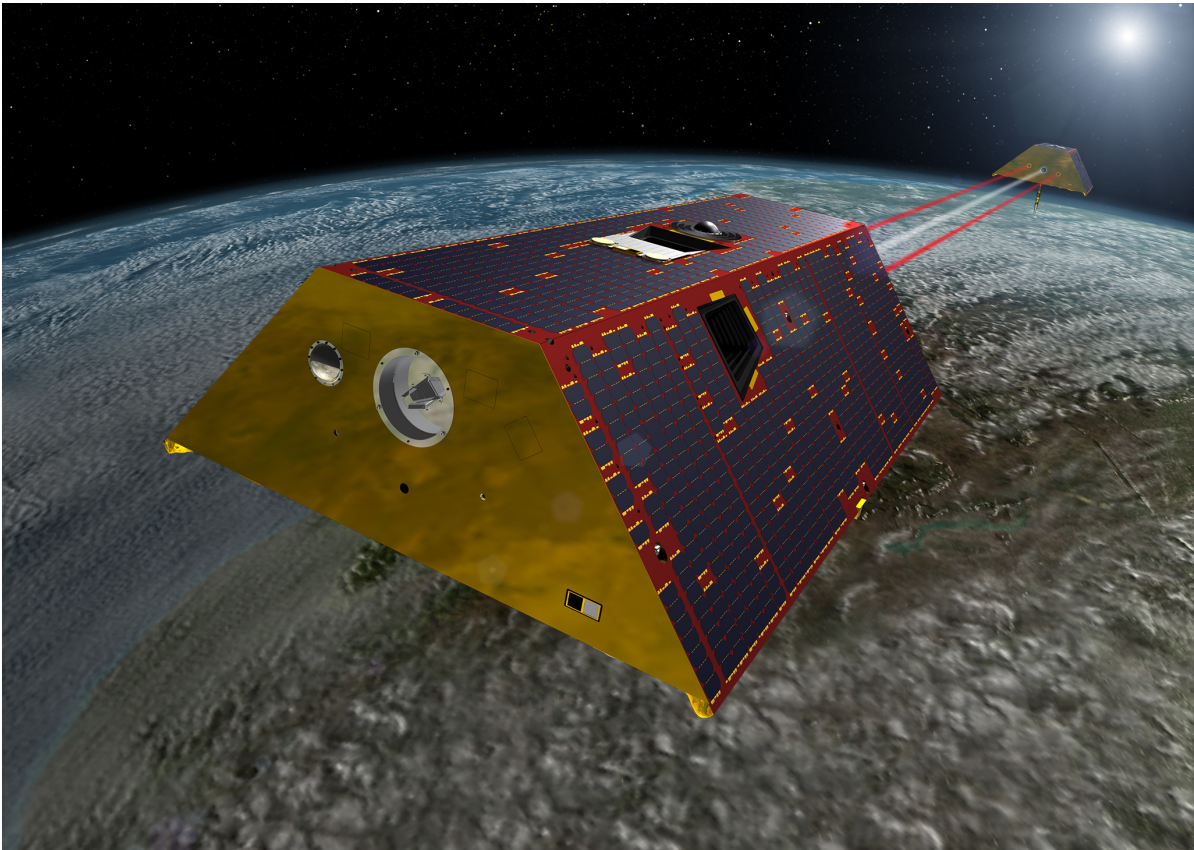
Figure 3.1: Artistic representation of the GRACE Follow-On spacecraft in orbit, with the microwave and laser links highlighted [22].

Parameter	Value	Unit
Spacecraft separation	220 ± 50	km
Ranging noise	80	$nm/\sqrt{Hz} \times \tilde{U}_{NSF}(f)$
Measurement Band	2-100	mHz
Laser power	25	mW
Wavelength	1064	nm
Laser frequency stability	30	$Hz/\sqrt{Hz} \times \tilde{U}_{NSF}(f)$
Transmit beam waist radius	2.5	mm
Field of regard	4.5	$mrad$
Receive aperture radius	4	mm
Effective received power	≈ 200	pW
Beam alignment error	50	μrad
Pointing stability	20	$\mu rad/1\ orbit$
Rotational coupling factor	200	$\mu m/rad$

Table 3.1: Parameters and requirements for the GRACE Follow-On Laser Ranging Instrument [13, 57, 37].

The main instrument, given what was previously said about trying to get a reliable continuation of the time series of measurements, was the microwave ranging instrument, the same as was used for GRACE. The Laser Ranging Interferometer was only included as a technology demonstrator. GRACE Follow-On represented the first implementation in space of long range laser interferometry between two spacecraft.

GRACE-FO LRI instrument architecture

The Laser Ranging Instrument in the GRACE Follow-On mission, which was solely intended as a technology demonstrator, had to be integrated in the existing spacecraft design and configuration, meaning that some adaptations had to be included. Since the microwave setup constitutes the main instrument for the mission, the microwave antenna was placed directly on the line-of-sight (LOS) between the two spacecraft. Behind the microwave antenna a propellant tank further limited the space available for the LRI, which meant that the LRI was implemented with a race-track configuration, introducing an offset between the incoming and the transmitted beams, going around the existing spacecraft architecture.

The components of the LRI for the two satellites is represented in Figure 3.2. There are three main
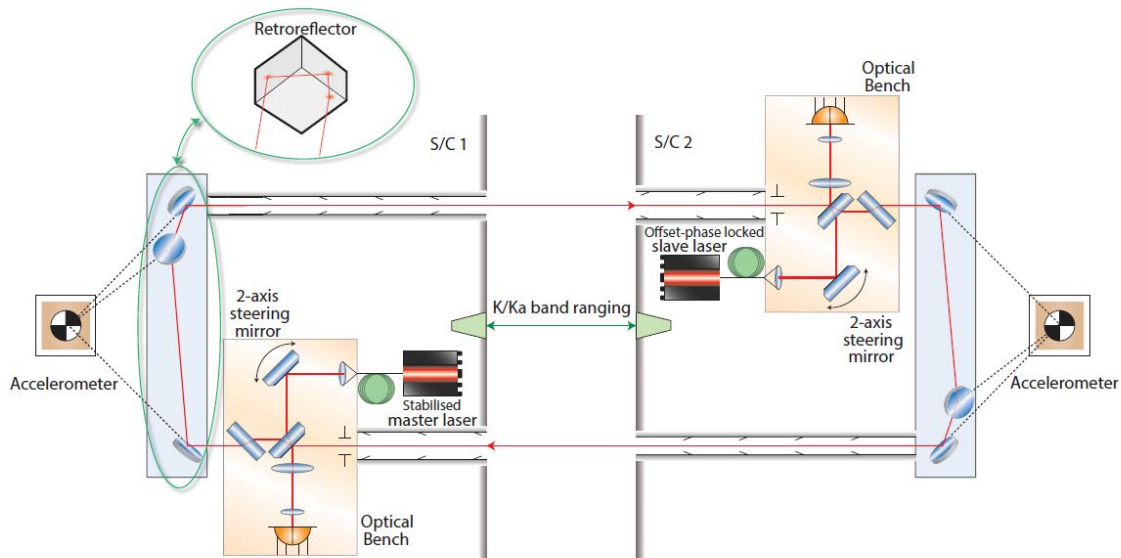
Figure 3.2: GRACE Follow-On Laser Ranging Instrument architecture [13].

elements that make up the instrument in each spacecraft: the retroreflector, the optical bench and the laser subsystem. The retroreflector is composed of three mutually perpendicular mirrors and its design allows for the pathlength across this component to be independent of the incident angle, and for the outgoing beam to be reflected exactly parallel to the incoming beam. In order to reduce the coupling to the spacecraft jitter in the measurements, the virtual vertexes of the retroreflectors are aligned to the spacecraft centre of mass, which is surrounded by accelerometers.

Given the large distance between the two spacecraft, it is not possible to just reflect back the laser coming from the other satellite, because due to the beam spreading only a small portion of the laser front is intercepted by the entrance aperture of the receiving platform (from Table 3.1 it can be seen that only a couple hundreds pW are received), meaning that the laser power received is not sufficient to enable a reflection that ensures a powerful enough beam back at the sending spacecraft. This means that the laser beam has to be regenerated by the receiver; the optical bench therefore includes an active transponder system, with a two-dimensional beam steering mechanism (the fast steering mirror) for alignment of the local laser with the weak incoming beam without affecting the measurement path. The beam substitution occurs at the beam splitter, which has a reflectivity of over 90%, meaning that most of the local laser continues the incoming beam path towards the retroreflector and eventually to the other spacecraft, while a small portion of the beam power is sent to the photodetector, along with the majority of the received beam.

The phase measurement on the photodetector is realized by a heterodyne detection scheme, introduced in Section 2.2.1, creating a beat note with an offset between the frequencies of the lasers on the two spacecraft. One of the two lasers, called the master laser, is frequency-stabilized to an optical cavity, to diminish the laser noise in the measurement signal, while the other laser, called the slave laser, is offset phase-locked to the received master laser. Due to orbital dynamics, the laser frequency

is affected by Doppler shifts that can range between ± 3 MHz [34]; the slave laser is therefore locked to the master laser with a frequency difference beyond the Doppler shift, to avoid sign changes in the measurement signal while maintaining the beat note frequency in the dynamic range of the photodetector. GRACE Follow-On employs beat note frequencies in the range from 4 MHz to 16 MHz.

From Equation 2.3 the phase difference between the laser beams is measured as $\Delta\phi = \phi_2 - \phi_1$ and the displacement signal δz is determined by the phase difference detected on both spacecraft using Equation 2.4, given that the value of $\Delta\phi_{S/C2}$ is predetermined by the offset phase-lock of the slave spacecraft.

Another important feature of the photodetectors is the measurement of the relative tilt between the incoming and the local beams, to feed the control loop of the fast steering mirror and ensure a proper beam regeneration that preserves the wavefront characteristics and direction. For this reason the photodetectors used are quadrant photodetectors, whose surface area is divided into four segments, each with a separate phasemeter measurement channel. A relative tilt between the two beams wavefronts is detected as a phase shift between different segments of the photodetector. This technique is known as differential wavefront sensing (DWS) and is further explored in Section 3.1.2.

3.1.2. Differential Wavefront Sensing

Differential Wavefront Sensing (DWS) is a technique employed in all of the laser ranging interferometry missions discussed in this thesis work, and allows a precise and autonomous alignment of the local beam with the incoming beam for an accurate beam regeneration procedure. The crucial component employed for this technique is the Quadrant Photodetector (QPD), which has an active area divided into four segments; a relative tilt of the beams leads to different phase shifts in the active areas. A misalignment in the beams leads to changes in the phase of the beat note measured in the four quadrants of the photodetector. Measuring the phase of the beat note in the different QPD sectors provides information on how to steer the local beam to achieve a perfect alignment. Figure 3.3 depicts a diagram of the DWS working principle, and further details on the exact calculations to be performed in order to retrieve the tilt of the beams are available in the work by Dr. Mandel [34].
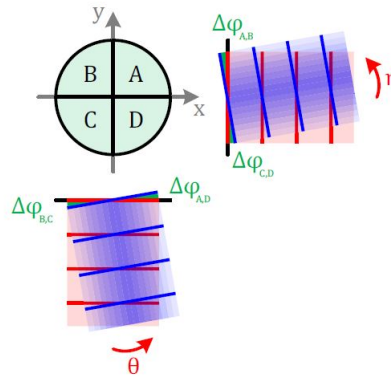
Figure 3.3: Diagram of the Differential Wavefront Sensing technique working principle [34].

3.1.3. LISA

The LISA mission and its scientific objectives have been introduced in Section 1.2.2, while in this section a more in-depth analysis of the mission configuration and the instrument design is given. To better understand the LISA architecture and layout an additional consideration on gravitational waves detector and their sensitivity to different parts of the gravitational waves spectrum is needed. Different detectors measure different parts of the spectrum: ground-based gravitational waves detectors using interferometry, like LIGO and VIRGO, detect high-frequency gravitational waves [4], while Pulsar Timing Array (PTA) techniques can be used to measure very low frequency gravitational waves [30]. Looking at the diagram in Figure 3.4 it can be seen how LISA is placed in-between the portions of the spectrum covered by PTA and ground-based interferometers. Ground based detectors will never be able to reach
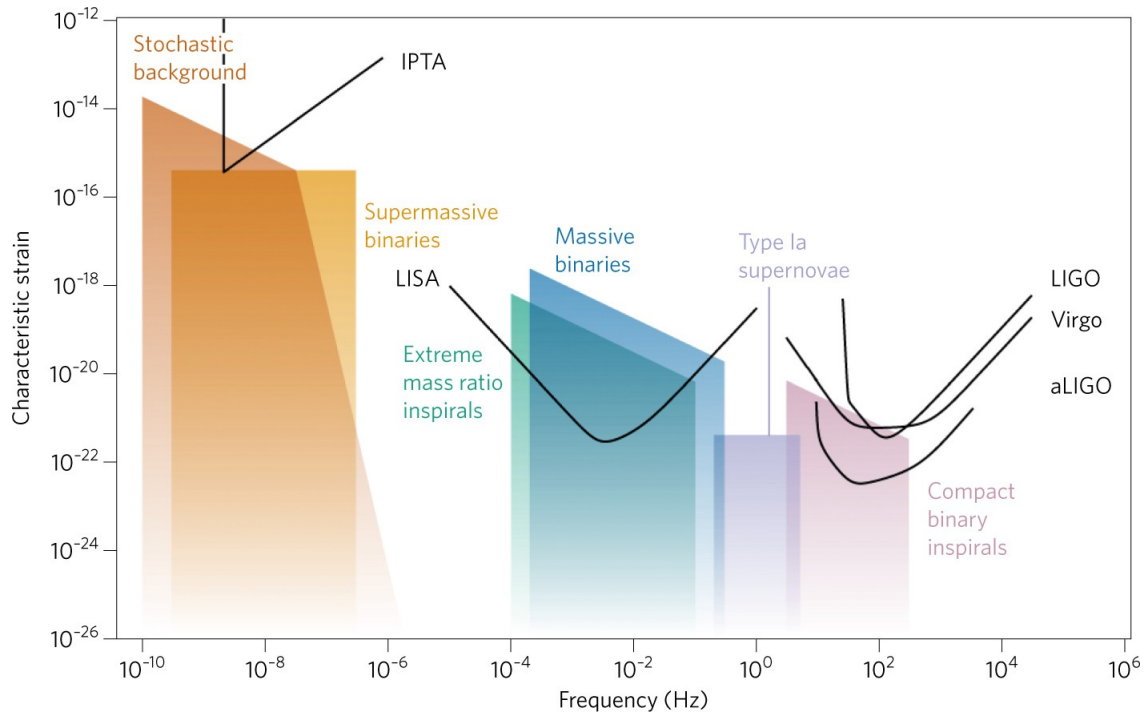
Figure 3.4: Gravitational waves spectrum and sensitivity of different gravitational waves detectors [30].

detections below 1 Hz due to the terrestrial gravity-gradient noise, while a space-based detector, free of such noise, can peak into the 10^{-4} to 1 Hz, where the most exciting gravitational wave sources radiate most of their power [12]. Since the frequency range in which LISA can make the observations is determined by the interferometer arm length, the requirement on the distance between the spacecraft is set, and as stated in Section 1.2.2 the different satellites of the constellation are separated by 2.5 million kilometres.

The centre of the formation is on the ecliptic plane, 1 AU from the Sun, either trailing or leading the Earth (it is still to be conclusively decided), with an inclination of $60°$ with respect to the ecliptic [12]. This heliocentric orbits allow for the triangular configuration to be maintained.

A technology demonstration mission was launched in 2015, LISA Pathfinder, which demonstrated critical technological capabilities needed for the success of the full scale mission. This said, the mission's technical requirements are still not entirely defined. The major technical challenge is the achievement of a $12 \, pm/\sqrt{Hz}$ accuracy (the current target for the mission), which requires a significant dampening of laser frequency noise (up to 5 orders of magnitude) and a highly stable measurement environment in the spacecraft.

LISA instrument architecture

The overall scope and layout of the mission, along with the most critical technological challenges have been laid out. In the following paragraphs the instrument architecture that characterizes LISA is investigated. The constellation is composed of three identical spacecraft, each with two identical optical assemblies, pointing towards identical assemblies on the other spacecraft to form the interferometer. Each optical assembly can be divided in three different elements: the telescope system and detection setup, the reference mass, and the local laser. A representation of a possible instrument assembly for LISA is represented in Figure 3.5, with all the elements discussed included.

Exactly like in the GRACE Follow-On mission, LISA needs a transponder system as well, due to the very low power in the laser received from the distant spacecraft. The beam is therefore regenerated with a local laser source, using a technique similar to the one introduced in Section 3.1.1 for the LRI instrument on GRACE Follow-On. Once the local laser beam is aligned with the incoming beam, a portion of it is focused on a photodetector for the heterodyne detection scheme; from here, the beat
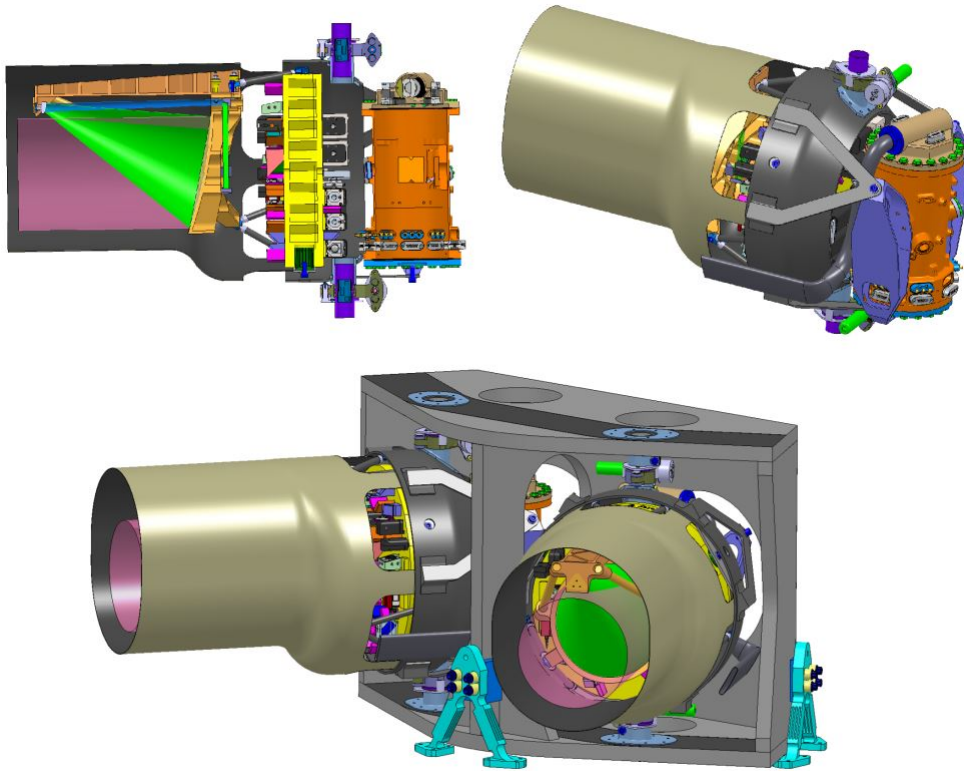
Figure 3.5: Three dimensional drawing of the LISA instrument assembly. Courtesy of Airbus D&S GmbH.

note signal is elaborated and the phase difference between the two beams is monitored to retrieve the displacement information, in similar fashion to what was explained in Sections 2.2.2 and 3.1.1. Compared to GRACE Follow-On, the signal processing and measurement strategies of LISA present a higher complexity, due to the need for the suppression of strong noise sources, laser frequency noise being the most prominent.

One of the main differences with the GRACE Follow-On mission is the inclusion of a Cassegrain type telescope in the assembly, which is used to focus the very weak beam from the distant spacecraft and ensure proper regeneration of the beam as well as the correct detection on the photodetector. The telescope is then employed for the pointing of the beam, as the setup in the LISA instrument does not include an In Field Pointing (IFP) mechanism, like a Fast Steering Mirror (FSM).

The third crucial element of the assembly is proof mass, which consists of a free-flying polished platinum-gold cube, serving as an optical reference for the light beams reflecting on it [12]. The spacecraft chassis mainly serve to shield the proof masses from solar radiation pressure, meaning that the space-craft position does not enter in the measurements directly, even though it is still necessary to keep the spacecraft relatively centred on their proof masses, through a drag-free control system consisting of accelerometers and electrical thrusters, using capacitive sensing to retrieve the displacements of the masses with respect to the spacecraft [12].

It is important to note that another difference with the GRACE Follow-On setup is that each interfer-ometer arm in LISA, is actually "divided" into three segments, on which interferometry measurements are performed. The three segments in which the overall arm is separated are: the portion between the reference mass of S/C_1 and its optical bench, the long portion between the optical benches of S/C_1 and S/C_2, and finally the last bit between the optical bench of S/C_2 and its reference mass.

3.1.4. Optical Metrology Terminal

The Optical Metrology Terminal (OMT) is a compact and flexible laser ranging interferometer that can be used to gain more in-depth understanding of different system architectures for missions beyond GRACE Follow-On. It was developed at the Laboratory for Enabling Technologies (LET) at Airbus Defence and Space in Friedrichshafen. One of the main objectives to be achieved with the OMT project is the study of tilt-to-length coupling, as it represents one of the main noise sources for both GRACE Follow-On and LISA. The design is based on the LRI instrument on GRACE Follow-On but incorporates different design choices, due to the fact that its development, unlike that of the LRI, is not limited by already existing spacecraft constraints. The OMT therefore combines the benefits of an on-axis layout with the robust approach of a retroreflector [34]. A picture of the breadboard model of the OMT developed by Dr. Mandel is presented in Figure 3.6.
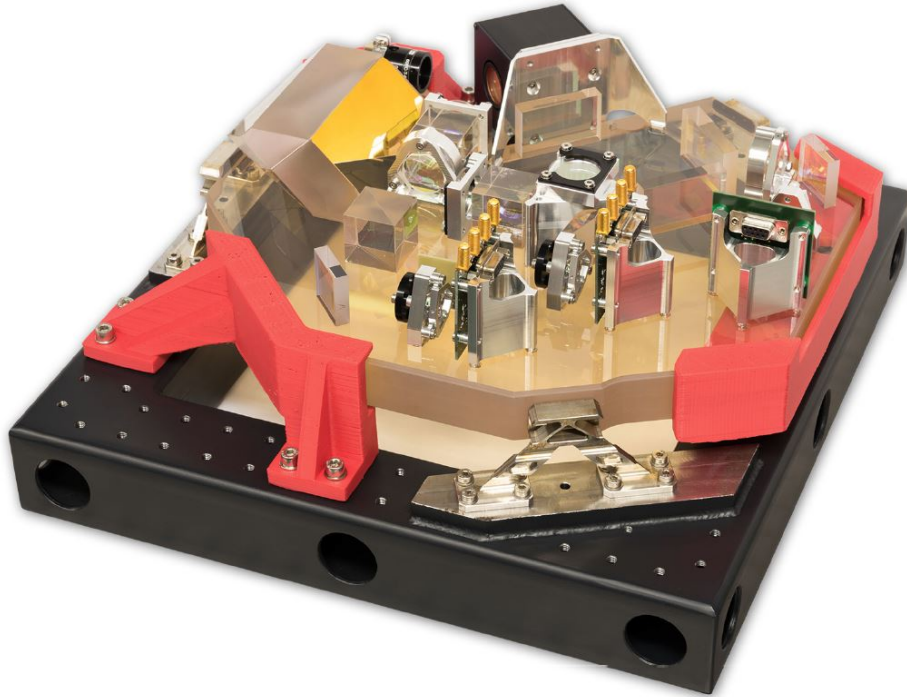
Figure 3.6: Breadboard model of the Optical Metrology Terminal [34].

The advantage of using a retroreflector is that it is by design insensitive to spacecraft jitter, and using an on-axis configuration also presents a number of advantages. The first point in favor of an on-axis configuration is that only one path is required from the instrument to the outside of the spacecraft, and at very short distances, including ground testing, it is easier to establish a laser link with an on-axis configuration compared to a bi-axial design. In the case of large spacecraft separation, an on-axis architecture allows to share a common telescope for both beams to increase the power at the receiving spacecraft and finally, the enclosed area between the laser beams is zero, limiting the Sagnac effect, particularly for use in Pendulum orbits [34].

OMT performance requirements

Considering that the OMT is not designed for a specific mission, a set of performance requirements has been derived from studies related to future gravity missions. A spacecraft separation between 50 km and 300 km is considered, allowing for versatile mission scenarios, with the design including a transponder system for proper laser power levels. The displacement accuracy is set at 50 nm/$\sqrt{\text{Hz}}$ with a measurement band of 1-200 mHz. The noise requirement on the elements of the OMT is derived considering the frequency stability requirement for GRACE Follow-On, corresponding to 30 Hz/$\sqrt{\text{Hz}}$, which leads to an error contribution of 32 nm/$\sqrt{\text{Hz}}$ [34]. The field of regard of the instrument is 5 mrad, allowing for small pointing deviations, with a jitter allocation a factor or two smaller than that

of GRACE Follow-On. Another element of error could be temperature stability. Based on data from previous missions, stabilities of 4 mK/$\sqrt{Hz}$ are possible. Finally, geometrical requirements applied to the design include a clearance around the reference point of at least ±15 cm and overall dimensions of the instrument within $40 \times 30 \times 15$ cm^3 [34]. The requirements just introduced are summarized in Table 3.2.

Parameter	Value	Unit
Spacecraft separation	50-300	km
Ranging accuracy	50	$nm/\sqrt{Hz}$
Measurement band	1-200	mHz
Laser wavelength	1064	nm
Frequency stability	30	$Hz/\sqrt{Hz}$
Field of regard	5	$mrad$
Spacecraft attitude jitter	100	$\mu rad/\sqrt{Hz}$
Beam deviation	50	μrad
Temperature range	10-30	$^\circ C$
Temperature stability	4	$mK/\sqrt{Hz}$
Reference point clearance	>15	cm
Maximum dimensions	$40 \times 30 \times 15$	cm^3

Table 3.2: Performance requirements for the Optical Metrology Terminal [34].

OMT instrument architecture

The instrument is characterized by a corner cube retroreflector, a fast steering mirror, polarization dependent beam separation (due to the on-axis design), magnifying pupil imaging systems, an acquisition sensor and a measurement assembly with QPDs where the beat note is detected [34]. In Figure 3.7 the measurement path of the instrument is visualized.
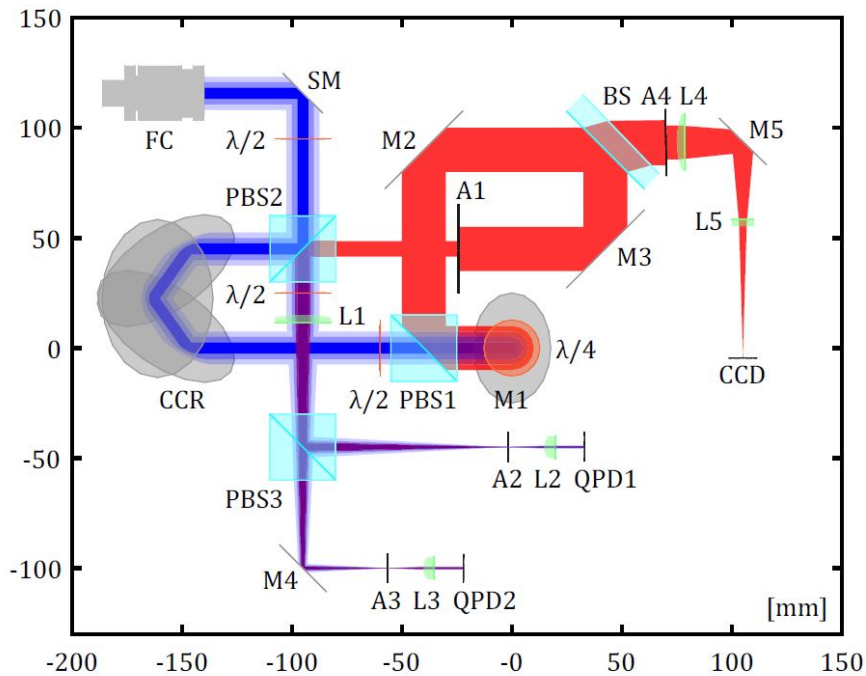
Figure 3.7: Critical measurement path of the Optical Metrology Terminal visualized [34]. The incoming beam is red, while the local beam is blue.

The line-of-sight is perpendicular to the paper plane, while the optical reference point is positioned on

the line-of-sight underneath the paper plane. The beams are characterized by a circular polarization state in the flight phase between the terminals (the two beams have a different direction of rotation for the polarization) which allows for the separation of the beams in the instrument regardless of the orientation of the spacecraft. A $\lambda/4$ waveplate is used at the entrance before the mirror M1 to convert the beams to and from linear polarization. A polarizing beam splitter (PBS1 in Figure 3.7) reflects the incoming beam (red) towards the acquisition detector, CCD in Figure 3.7, and most of it is re-directed towards a second polarizing beam splitter (PBS2 in Figure 3.7) where it encounters the local laser beam (blue) for beam regeneration. Part of the local beam continues towards a third polarizing beam splitter (PBS3 in Figure 3.7) together with the received beam, but they are not interfering yet as they still possess perpendicular polarization states. Before the third polarizing beam splitter a $\lambda/2$ waveplate rotates the polarization of the two beams by $45°$, positioning them in a "X" configuration with respect to the the parallel and perpendicular axes to the paper plane, and a lens (L1 in Figure 3.7) focuses the two beams towards the photodetectors. The beamsplitter PBS3 now divides the two beams in two different paths, with vertical and horizontal polarization, but due to the fact that they were positioned in a "X" configuration, they have the same polarization state in the two beams following PBS3, meaning that interference occurs. After an aperture and a lens, the resulting interfering beams are focused on the quadrant photodetectors (QPD1 and QPD2 in Figure 3.7) where the beat note is detected. The signal on the QPDs is used to perform Differential Wavefront Sensing (DWS), a technique already introduced for GRACE Follow-On in Section 3.1.1 and analysed in Section 3.1.2, which is then fed to the control loop of the steering mirror (SM in Figure 3.7) that aligns the local beam with the received beam for beam regeneration. At PBS2 the majority of the local beam continues on the measurement path towards the corner cube retroreflector (CCR in Figure 3.7) and is then transmitted towards M1 and then to the distant spacecraft, after being imprinted a circular polarization state. A 3D CAD representation of the breadboard and the beam paths is visible in Figure 3.8, which could be helpful in better understanding the layout of the instrument.
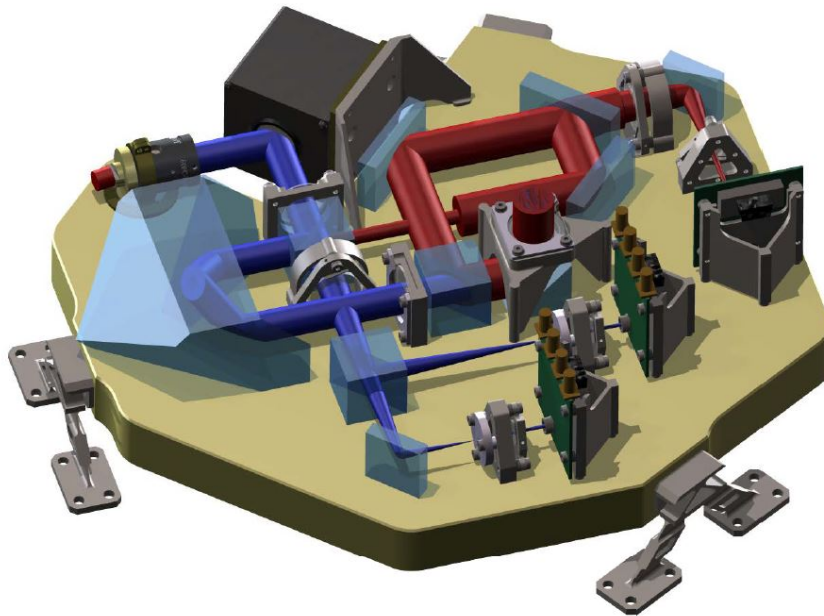
Figure 3.8: Three dimensional CAD design of the OMT [34].

3.2. Link acquisition strategies and procedures

In Section 3.1 different state of the art solutions for space-based long range laser interferometry have been explored. One aspect that all the missions introduced have in common and that has not been touched upon yet, is that they all share one necessity: a reliable, fast and efficient link acquisition procedure. When the spacecraft have been launched and inserted in the correct orbits, before sci-

ence operation can begin, the laser on each satellite needs to be pointed in pitch and yaw towards the opposite satellite, and the laser frequencies must differ by less than the photodetector bandwidth [65]. On ground alignment and tuning and spacecraft pointing through attitude sensors are not enough to achieve the laser link between the satellites, because the attitude sensors uncertainty cone is considerably larger than the field of view of the instruments, and on-ground alignment precision is hardly maintained through the launch procedures due to different sources of errors and misalignments. The principal causes of changes in the setup and laser tuning between the on-ground and operational conditions are the mechanical loads experienced during launch, the change of forces and conditions when shifting into a micro-gravity environment and the uncertainties introduced by thermal environment variations. It is also possible that the laser link could be lost during science mode due to external factors; link re-acquisition procedures are therefore a fundamental aspect to be investigated for laser ranging missions.

The following sections introduce different link acquisition procedures and scanning strategies, starting from the state of the art missions explored in Section 3.1 (GRACE Follow-On and LISA), and then discussing alternative solutions found in literature.

3.2.1. GRACE Follow-On link acquisition

In the next paragraphs the link acquisition and re-acquisition procedures as well as the spatial and frequency scanning strategies employed for the GRACE Follow-On LRI instrument are examined. In the first part of the analysis the components available on the spacecraft for the acquisition procedures and the technical limitations are introduced, as well as the starting uncertainty conditions, while in the second part the acquisition strategies and procedure are detailed.
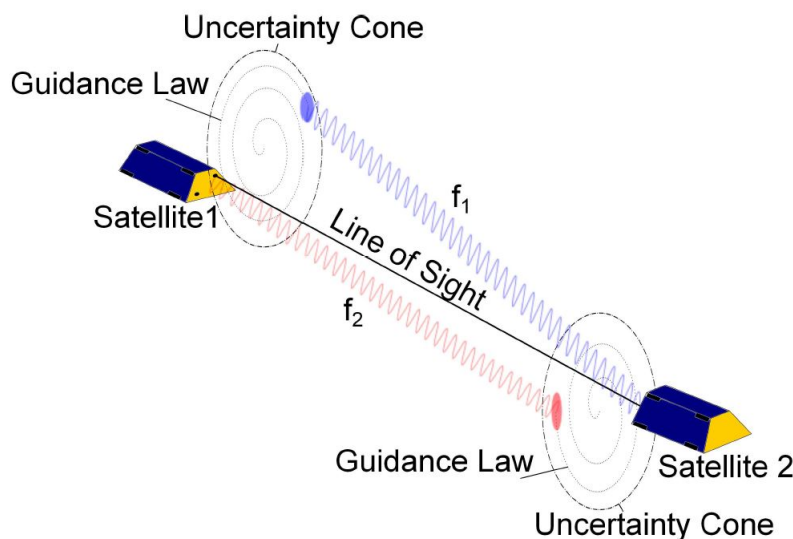
Figure 3.9: Initial conditions of line-of-sight and uncertainty cones for the link acquisition procedures in GRACE Follow-On [1].

GRACE Follow-On link acquisition components and initial conditions

In Section 3.1.1 one of the main limitations to the design of the LRI instrument onboard GRACE Follow-On was introduced, which was the need to fit the system in an already existing spacecraft architecture. This meant that some compromises had to be made, no dedicated acquisition sensor could be included in the design, due to reliability, space and budget limitations, and the acquisition procedure had to be performed using the FSM (fast steering mirror) and the detection occurred on the QPDs used for the science mode. The QPDs have a very limited field-of-view and for the detection to happen all of the degrees of freedom need to fall into their acceptable range. The degrees of freedom for the detection are 5: two spatial degrees of freedom for the pointing of each spacecraft and one degree of freedom for the frequency of the slave laser, which needs to fall in the frequency bandwidth of the detector when it interferes with the master laser (locked to a cavity). An additional aspect that influences the available

procedures for the link acquisition is the inability of the two satellites to communicate with each other, meaning that all the elaboration of information and the commands need to be performed on ground.

The initial conditions for the link acquisition procedure are dependent on the pointing accuracy of the two spacecraft, the uncertainty on the frequency of the lasers and the uncertainty on the relative alignment between the attitude sensors and the optical instruments. Figure 3.9 depicts the initial condition for the link acquisition of GRACE Follow-On. The line-of-sight between the satellites is represented, as well as the uncertainty cones deriving from the accuracy of the attitude sensors of the spacecraft. A graphical representation of the two lasers is also depicted, and it can be seen that while the two satellites fall in the uncertainty cones of each other, their laser's diameters are too small to acquire a signal from the start, therefore the uncertainty cones need to be scanned until the exact location for acquisition is found. The uncertainty cone dimension for GRACE Follow-On is 3 mrad, compared with a beam divergence angle of 135 µrad [25], while the uncertainty on the offset between the laser's frequency on each satellite is ± 1 GHz [65], demonstrating the need for a reliable and efficient scanning strategy.

GRACE Follow-On link acquisition strategy and procedure

The goal of the acquisition is to bring the frequency offset between the lasers to within $\approx$ 20 MHz, while aligning the two beams well enough so that the transition to DWS can be established [65]. The definition of the order and speed of the different scans, as well as the communication of the information exchange and different phases of the acquisition constitute the link acquisition procedure.

For GRACE Follow-On the link acquisition procedure is characterized by three nested scans, to go through every point of the uncertainty space identified by the 5 degrees of freedom. The slowest scan performed is the frequency scan on the slave spacecraft. The laser frequency is changed linearly through the uncertainty field, and while the frequency scan in being performed, the whole spatial uncertainty field is examined, maintaining the change in frequency within the detector frequency bandwidth. The intermediate speed scan is the spatial scan on the master spacecraft. The FSM on the master spacecraft performs a discrete point and stare scan, going through the whole uncertainty cone. During each step of the discrete scan, the slave spacecraft performs a fast spatial scan, scanning through all of its uncertainty cone. This strategy ensures that every possible point is investigated and a link signal is eventually acquired. The only parameters left to define are the spacings and the dimensions of each scanning step to ensure the robustness of the procedure against environmental noises and external changes (i.e. spacecraft jitter).

As was introduced previously, the two GRACE Follow-On spacecraft cannot communicate between each other, therefore once the full scan has been completed, the data from the spacecraft is sent down to Earth for analysis and new commands are uploaded, to perform a re-acquisition scan around the points that led the highest beat note amplitude in the initial scan [65]. The re-acquisition scan is considerably faster, due to the uncertainty space being significantly smaller, and it leads the two satellites directly into science mode. The reacquisition scan is then performed every time the two spacecraft lose the fine link and exit the science mode.

The frequency scan is performed with a rate of 11 kHz/s [25]. For the spatial scans two different strategies have been adopted for the Master and Slave spacecraft. The Master satellite performs a slow discrete hexagonal scan, shown on the right of Figure 3.10, while the Slave spacecraft carries out a fast Lissajous continuous scan for every step of the hexagonal scan. The Lissajous strategy is depicted on the left in Figure 3.10. The Lissajous pattern is defined by two synchronous sinusoidal motions in both FSM axes. The ratio between the frequencies of the scan in the two axes is 36, to achieve the required space between the steps, due to the beam diameter [25], while accounting for the errors in positioning due to the mirror response function, which creates greater deviations from the nominal path at greater speeds and accelerations [24]. The maximum speed of the fast spatial scan is therefore limited by the speed of the fast steering mirror and the best combination between scan speed and the arm separation, as a faster movement of the steering mirror causes greater deviations from the nominal track, therefore requiring a smaller arm separation reducing the benefits in terms of scan-time for a faster mirror movement.
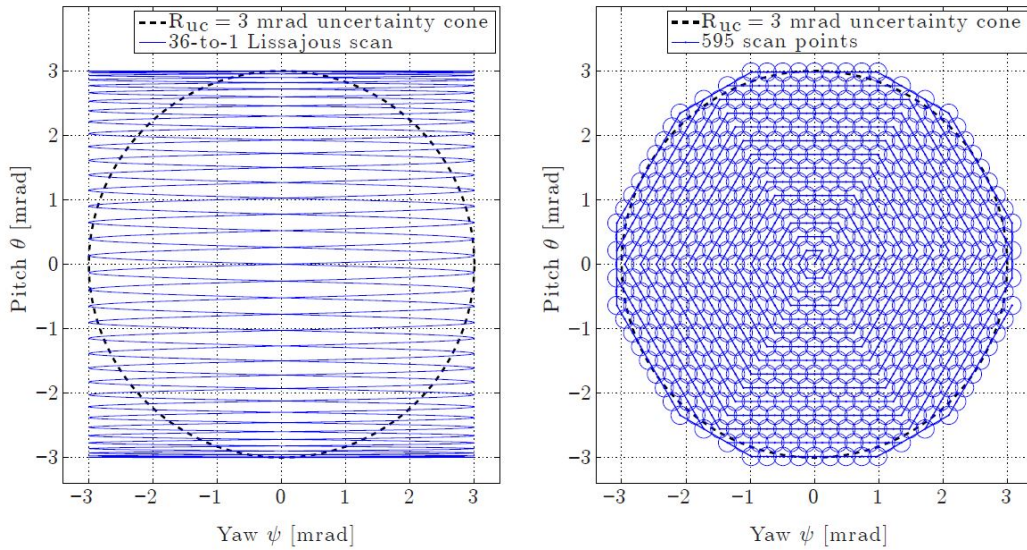
Figure 3.10: Spatial scans for the GRACE Follow-On LRI. Lissajous scan on the left for the Slave spacecraft and hexagonal scan on the right for the Master spacecraft [65].

3.2.2. LISA link acquisition

The architecture of the LISA mission is completely different compared to that of GRACE Follow-On, and the differences are apparent in the link acquisition process as well. The most intuitive variations are the number of spacecraft, two for GRACE Follow-On and three for LISA, and the distance between the spacecraft, ≈ 220 km for GRACE and ≈ 2.5 million km for LISA. Even though the different challenges and architectures present different problems and approaches to link acquisition, there still are some valid considerations that can be extended from GRACE Follow-On to LISA, as will be shown in the following paragraphs.

LISA link acquisition components and initial conditions

In Section 3.1.3 the instrumentation onboard each spacecraft of the constellation was explored, noting how a FSM was not included in the design, and the pointing of the laser is performed through telescope pointing. Another difference with the GRACE Follow-On spacecraft, other than the absence of the FSM, is the presence of a dedicated acquisition sensor, which eases the requirements on the link acquisition procedures as the laser link can be acquired in steps without having to switch directly to the beat note detection on the QPDs. The dedicated acquisition sensor allows the telescope pointing mechanism to perform an effective scan even without the performance of a FSM.

The initial conditions for the link acquisition depend on the accuracy of the attitude sensors, just like for GRACE Follow-On; the difference is that for LISA, the situation depicted in Figure 3.9 has to be expanded to include a third satellite. The initial half-cone angle of uncertainty is expected to be 15.2 μrad, while the received beam is expected to have a half-cone angle of 1.43 μrad [10]. The field of

	STR	CCD	QPD
Field-of-View	0.3 rad	155 μrad	1 μrad

Table 3.3: Field-of-View for different sensors on the LISA spacecraft [10].

view of the different sensors included in the LISA spacecraft are summarized in Table 3.3, showing how the uncertainty cone for the link acquisition can be reduced in steps by going from one sensor to the next, before reaching the level of pointing precision necessary for detection on the QPD [10].

LISA link acquisition strategy and procedure

The acquisition sequence for the LISA mission takes the name of "Constellation acquisition", due to the fact that three different double laser links need to be acquired. Another main difference with the

GRACE Follow-On mission is also that the procedure is performed autonomously by the spacecraft, there is no communication with the Earth to receive commands, but the satellites communicate with each other through laser satellite communication, once a link is established.

The process of single-link acquisition can be divided into four phases: calibration phase, signal acquisition on the acquisition sensor, signal fine acquisition on the acquisition sensor and finally signal acquisition on the quadrant photodetector [9]. The calibration phase is performed to reference the telescope line-of-sight to the star trackers, eliminating the off-set that causes a further deviation between the star tracker and the CCD line-of-sight [9]. The calibration is performed by detecting guide stars on both the star tracker and the CCD, and from the attitude calculated by both, the determination of the offset between the two can be performed.

The second step of the procedure is the acquisition on the acquisition sensor, the goal of which is the detection of the laser signal on the CCD of both spacecraft on one arm of the constellation. One spacecraft (for the sake of reasoning called S/C1) starts to scan the uncertainty cone where the other spacecraft (S/C2) is expected to be sited, and the laser of S/C1 is switched off between each scanning position. While S/C1 is scanning, S/C2 stares at the where it calculated the first spacecraft should be placed, until it receives a signal on the acquisition sensor. The offset between the on-ground calculated position of the S/C1 and the real one can be calculated by the position of the incoming laser on the detector, as shown in Figure 3.11; using the information from the acquisition sensor, S/C2 is able to perform an attitude correction to point towards S/C1, which in the meantime has continued the scanning procedure. This implies that, while it is correcting its attitude, S/C2 is no longer able to see the incoming beam on its sensor. S/C1 maintains into its field-of-view the scanning location that generated a signal on the detector of S/C2 for enough time to allow S/C2 to turn on the laser towards S/C1, which will be able to detect it, as its laser is turned off at every scanning step [9]. The laser needs to be turned off for the detection to happen because the straylight from the local laser blinds the sensor and does not allow for the identification of the far spacecraft's laser. This acquisition strategy could however be changed, because while switching off the laser ensures better detection performance by reducing the straylight, it creates an unstable thermal environment which could deteriorate the performance of the system. An optimal solution is still being studied.
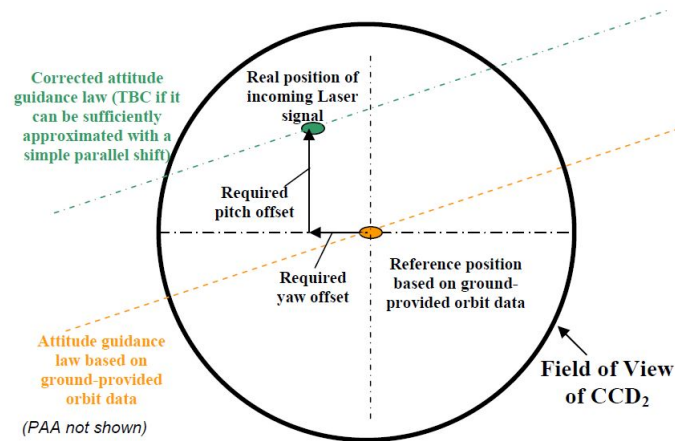
Figure 3.11: Calculation of the offset between pre-determined and real position of remote spacecraft [9].

Upon detection of the signal, S/C1 calculates the real position of S/C2 in the same fashion as previously explained and shown in Figure 3.11.

The third step in the acquisition is the fine acquisition on the acquisition sensor, to bring the incoming laser within the field of view of the QPD, to ensure that a frequency search can be performed. A laser on-off strategy is implemented to ensure that both spacecraft can detect the incoming beam and align themselves with the LOS between the satellites.

The final step is the acquisition on the QPD, for which S/C2 scans the frequency of its local laser until a

beat note is detected on the QPD. As soon as a signal is received, the QPD can be used as an attitude sensor [9], but the local laser has to still be turned on and off until S/C1 has detected a beat note as well. The detection on S/C1's QPD should happen shortly after the detection by S/C2, since the entity of the Doppler shift is fairly known based on ground-provided navigation data.

The procedure has to be repeated for the other arms of the constellation, while maintaining the links previously obtained.

The scanning strategy employed to cover the uncertainty cone of the various acquisition step is an Archimedian spiral from the centre, with constant tangential velocity [10]. The parametric equations for the motion are expressed in Equation 3.1

$$\begin{cases} \rho = \frac{k \cdot r}{\pi} \cdot \theta \\ \theta = \left(\frac{2 \cdot \pi \cdot a \cdot (t - t_0)}{k \cdot r} \right)^{1/2} \end{cases} \tag{3.1}$$

where ρ is the distance from the centre, k is a parameter from 0 to 1 representing the spiral pitch, θ is the angle spanned by the spiral, a is the constant tangential velocity, t_0 is the starting time of the scan, t is the current time and r is the radius of the laser beam cone. Additional conditions are imposed to ensure the covering of the uncertainty cone in N+1 rounds, these conditions are defined in Equations 3.2 and 3.3 [10]

$$N = \left(\frac{R}{k \cdot r} - 1 \right) \cdot \frac{1}{2} \tag{3.2}$$

$$a \cdot \Delta t_{id} = 2\pi \cdot k \cdot r \cdot (N + 1)^2 \tag{3.3}$$

where R is the radius of the uncertainty cone, N+1 are the rounds needed to cover the uncertainty cone and Δt_{id} is the ideal time required to cover the uncertainty cone. A diagram representing the Archimedian spiral which has just been introduced is visible in Figure 3.12, in which the ρ and θ parameters are also highlighted.
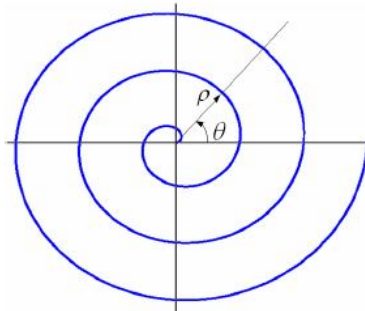
Figure 3.12: Archimedian spiral, the scan strategy planned for LISA [8].

3.2.3. Alternative solutions for link acquisition

In Sections 3.2.1 and 3.2.2 the link acquisition strategies and procedures for the GRACE Follow-On and LISA missions have been examined, and while GRACE Follow-On has been launched and the link acquisition procedures have proven successful, LISA is still in its development phase, some changes in strategy and procedure are highly probable. In the development of these missions, and other similar scenarios, different strategies and procedures have been proposed in literature. These additional options are explored in this section, as they might be useful in the development of link acquisition strategies for the OFMT and they could turn out to be more suitable for certain mission scenarios.

Alternative acquisition procedures

In the research carried out for their PhD dissertation [33], Mahrdt analysed different scan hierarchies and procedures that could be applied to missions similar to GRACE Follow-On, implementing different nesting configurations of the three different scans involved: the frequency scan, the slave spatial

scan and the master spatial scan. The first option they considered was the one implemented for the actual GRACE Follow-On mission, which consists in a slow frequency scan, an intermediate master spatial scan and a fast slave spatial scan; the details of the implementation of this strategy have been discussed in Section 3.2.1. The other three options considered are collected in Table 3.4. Mahrdt

	Slow scan	Intermediate scan	Fast scan
a	Frequency scan	Slave spatial scan	Master spatial scan
b	Slave spatial scan	Frequency scan	Master spatial scan
c	Slave spatial scan	Master spatial scan	Frequency scan

Table 3.4: Alternative link acquisition procedures considered by Mahrdt [33].

compares the different procedures in terms of total acquisition times. It is relevant to notice that the only variable which influences the total time is position of the frequency scan in the order of scans, as interchanging slave and master scans in any of the three configuration (a,b or c) would yield the same result. The frequency scan has been assumed to be a linear ramp with a constant scan rate, starting from a lower bound, and more details on the assumptions and methodology used is available in their work [33].

The result of the study is that in order to obtain with scan **(c)** the same total scan time that is needed in scan **(a)**, the frequency scan rate needs to be very high, leading to a strongly reduced SNR [33]. To achieve a similar results with scan **(b)** there are a great number of difficulties encountered, mainly the slave scan might take too long, leading to pointing noise potentially shifting the scan position and creating gaps in the cone coverage. The solution to the problem would be an increased overlap between the spatial captures, but it would lead to greatly increased scan times [33].

Other approaches have been investigated, that don't rely on sequential nested scans but rather perform dual scans, checking the spatial uncertainty cones simultaneously. One approach following this philosophy was proposed by Zhang et al. [66], which consists in modulating the power of the two lasers to different frequencies within the photodetector bandwidth to allow for the distinction between them after demodulation. The two lasers can then scan the uncertainty cones simultaneously and independently until one satellite detects enough power from the distant satellite, and through Differential Power Sensing (DPS) determines the attitude of the line-of-sight and starts scanning towards that direction, so that the other satellite can also get a signal and adjust its pointing further, until both satellites lock their beams to the line-of-sight. This method, further explained in more detail in their work [66], would allow to accomplish the spatial scan acquisition within an average time of 10 seconds for a 1-mrad uncertainty cone [66], according to the authors.

Another dual-scan approach was proposed by Hechenblaikner [21], in which a GRACE Follow-On scenario is studied, with the inclusion of dedicated acquisition sensors on each spacecraft, similar to the design introduced with the OMT architecture [34] in Section 3.1.4. The spatial scans are performed simultaneously by both spacecraft, similar to the scenario proposed by Zhang et al. [66], but in this approach the power of the lasers are not modulated. Once a satellite acquires a signal from the other distant laser on the detector, it re-orients itself along the line-of-sight and turns on its laser to allow the acquisition of the distant spacecraft as well. The spatial scan is therefore finished, proving to be twice as fast and much more robust against beam jitter compared to a single scan method (again involving an acquisition sensor) and it is significantly faster than the approach used in GRACE Follow-On, analysed in Section 3.2.1, which did not employ a dedicated acquisition sensor [21].

Alternative scanning strategies
Alternative spatial scanning strategies have been proposed for missions related to laser satellite communication, which also involve link acquisition processes, but often-times operate a dedicate link acquisition laser beacon or manipulate the beam to make the acquisition easier, both strategies not feasible for the scientific applications presented in this study. There are however some spatial scanning patterns that could be transferable, mainly the raster scan, the raster spiral scan and the rose scan [55, 56, 62]. Random spatial scans were instead the focus of the work by Ales et al. who studied normal random scans and uniform random scans [1].

Raster scanning is a strategy applicable to a rectangular uncertainty space, in which the scan starts at one corner and goes through the uncertainty space one (horizontal or vertical) line after the other, sequentially. It is uniform and easy to implement but takes more time and does not search from high to low probability regions [55]. Another disadvantage of this scanning technique is that it is not robust against spacecraft jitter, but on the other hand it can scan the whole area efficiently and it is easy to implement on hardware [56].

A variation of the raster scan is the raster spiral scan, which is implemented by creating a "rectangular" spiral, starting from the centre. Figure 3.13 shows the raster spiral scan. The advantages of a raster
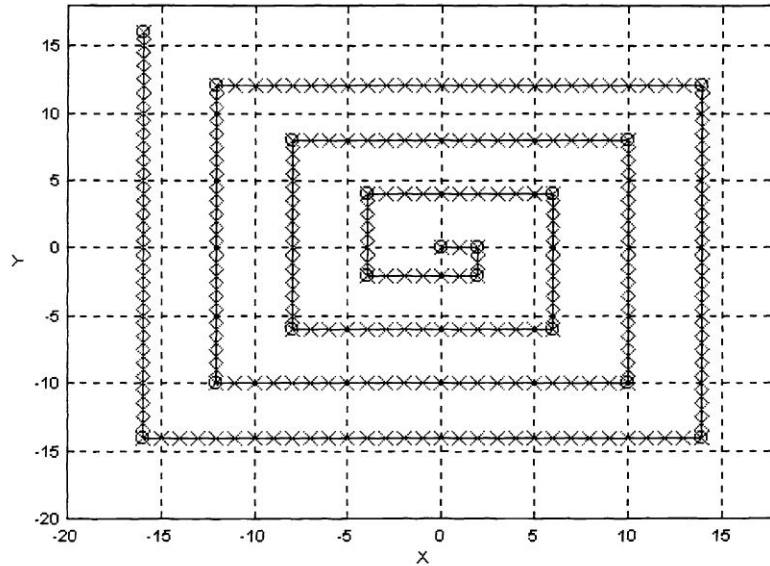
Figure 3.13: Raster spiral scanning strategy, starting from the centre of the uncertainty space [55].
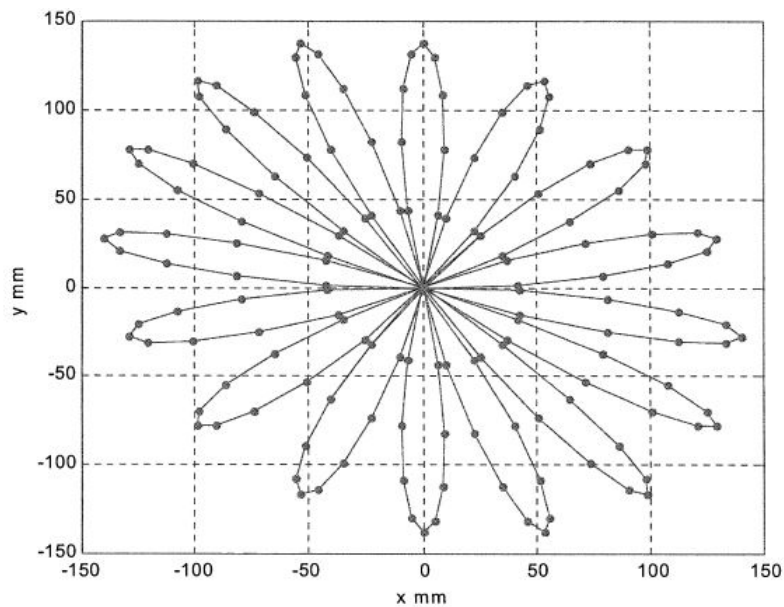
Figure 3.14: Rose scanning strategy [56].

spiral scan is that it covers the uncertainty field more uniformly compared to a circular spiral scan, it scans from regions of high probability to regions of low probability, unlike the nominal raster scan, and it is easy to define the amount of overlap [55, 56]. The main disadvantages are represented by the

fact that the function to generate it is not a sine wave and it is more difficult to implement, and it is still relatively slow compared to other methods [56].

The last scanning technique coming from laser satellite communication link acquisition strategies is the rose scan. The rose scan is generated using sine wave basic functions creating an amplitude modulated signal, it scans very uniformly over the uncertainty area and there can be areas of aliasing between the scanned beams to overcome vibrations [56]. The result of the scan is represented in Figure 3.14. The advantages of the rose scan is that it doesn't suffer excessively from vibrations, but some uncovered areas in the uncertainty space can occur and it is more complex to implement on hardware [56].

The random techniques introduced by Ales [1] were instead intended for laser ranging interferometry missions with scientific optical metrology objectives, meaning that they are intended for the same types of missions analysed in this study. With a random guidance, the uncertainty area is covered according to randomly generated pointing directions. If the initial pointing uncertainty is normally distributed, the pointing coordinates of the guidance law are generated according to a Gaussian distribution, while when the initial pointing offset has a uniform distribution within the uncertainty cone, a uniform distributed random pointing pattern is preferred [1]. With a uniform random pattern the area covered is a square rather than a circle. From the results in the work by Ales [1] it seems that for certain parameters and conditions the random scanning strategies might prove to be more efficient than their continuous counterparts.

3.3. Experimental setups for link acquisition testing

In Section 3.2 the need for effective and efficient link acquisition strategies has been outlined and the procedures implemented for Grace Follow-On and LISA have been introduced in Sections 3.2.1 and 3.2.2. Before these procedures can be implemented on a space mission they need thorough tests on ground, through experimental setups that aim at recreating conditions as close to the operational ones as possible, even though for such large long ranging missions this is nearly impossible. Experimental on ground testing is not just useful for validation of space mission procedures, but it is beneficial for validating new, alternative and innovative strategies that could be applied to future instrument architectures. In this section an overview of relevant experimental setups for laser ranging link acquisition is provided, but only the important details and considerations that could be useful for the implementation of the link acquisition setup for the OFMT are explored, a more in depth overview of the setups is available at the sources cited on the topics.

3.3.1. Fiber OGSE

The AEI (Albert Einstein Institute) and the DLR Institute for Space Systems in Bremen jointly developed an experimental setup to simulate the intersatellite laser link in the GRACE-FO mission. It makes use of optical fibers to guide the laser from one terminal to the other and it is part of the Grace Follow-On ground support equipment, leading to it being named Fiber Optical Ground Support Equipment (OGSE). One of the objectives of the Fiber OGSE, and the one relevant for this work, was the experimental demonstration of the link acquisition techniques for the LRI instrument on board Grace Follow-On [24].

The schematics of the Fiber OGSE is represented in Figure 3.15 with the two spacecraft mockups on each side. Most of the work done on the Fiber OGSE, its components description and reasoning behind design choices is provided in the cited references [19, 24, 53]. The setup allows to simulate spacecraft separation of 40 meters [24]. Spacecraft separation is one of the main parameters to consider if a representative scenario for the operational conditions is to be achieved, but since recreating the exact conditions of spacecraft separation is impossible with on ground testing (220 km for Grace Follow-On and 2.5 million km for LISA), a compromise between all the relevant variables is therefore desirable.

Another relevant aspect of the setup is the attenuation of the laser power to accurately simulate the conditions of the received beam. This is achieved in multiple steps with the Dynamic Power Attenuator. The first attenuation is provided by the fiber collimator on the transmitted beam (TX), and to keep this gain as linear as possible, a collimator with coupling efficiency insensitive to laser tilts was chosen. The second attenuation is given by the DPA, which measuring the TX angle attenuates its power applying an RF signal to one of the AOMs. Finally another static attenuation is introduced through a static

Figure 3.15: Schematic representation of the components in the Fiber OGSE used for link acquisition validation of Grace Follow-On [53].

attenuator, visible in Figure 3.15 as well, to achieve the picowatt level laser power [19].

The dynamic misalignment between the two spacecraft due to the uncertainty in the attitude determination by the star trackers and the small internal deviations in the positioning of the optical board with respect to the spacecraft (due to the microgravity environment and the launch loads) is introduced through a static offset of the received or transmitted beam collimator, which sits on a 4 DoF mount, as seen in Figure 3.15 [24]. On top of the initial static misalignment, the movable mountings of the collimators have also been used to simulate the spacecraft jitter during the acquisition procedures [19], which could introduce errors and deviations, which, if not accounted for, could lead to an unsuccessful link acquisition.

From Figure 3.15 two separate AOMs for each beam are visible, one of their uses is the transmitted beam attenuation, as previously explained, while the other one is to introduce a Doppler shift in the beam. The AOMs have +85 and -85 MHz nominal frequencies and can simulate a Doppler shift of about ± 10 MHz [53]. A final parameter that has to be considered for a proper realistic scenario implementation is the shape of the received beams, because the spreading of the beam due the great distance between the spacecraft leads to a basically flat wavefront (spherical wavefront with an extremely large radius of curvature) and intensity profile. The beam shape is recreated in the setup by spreading the beam through the collimator, achieving a Gaussian beam diameter of 16.5 mm [24].

3.3.2. Laser Link Simulator

The Laser Link Simulator (LLS) is an experimental test bed developed by Koch as part of their PhD work [24] which can be used to simulate intersatellite laser ranging interferometers like the LRI used on Grace Follow-On and novel instruments that will be developed for a NGGM and in some parts for LISA as well. The LLS is equipped with LRI-like optical breadboards and follows more or less a similar system design, including the fact that it is a fiber-coupled system. In Figure 3.16 is a schematic representation of the setup and its components.

As with the Fiber OGSE in Section 3.3.1, the details on the development of the system, the reasoning behind the many design choices and the overall description of the implementation are available in the associated literature, mainly the dissertation by Koch, the creator of the setup [24]. The idea behind the overall design in inspired by the Fiber OGSE, but there are some substantial differences, mainly the placement of the optical breadboards on top of Hexapods, visible in Figure 3.16, and the fact that the transmitted laser is dumped, and a new laser source is used instead; this was done because the absolute pathlength of the interferometric signal was determined to be not of interest for the tests carried out [24]. A close-up view of the optical breadboard is provided in Figure 3.17, where the dumped TX (transmitted) beam is clearly visible and the local laser source is split to provide both the local beam and the transmitted beam for the other terminal. A redundant beam has been introduced and dumped

Figure 3.16: LLS schematic architecture and components [24].

Figure 3.17: LLS optical breadboard setup [24].

as well.

For the received beam, the process of simulating the large distance between the spacecraft is similar to what was done in the Fiber OGSE in Section 3.15, the fiber collimator used is the same, and a large 2" lens collimates the output of the optical fiber to a beam 4 cm in diameter creating a flat-top beam if only the central part of the spread Gaussian front is considered. The misalignment of the terminals along the line-of-sight is implemented with the Hexapods and a control loop calculated the power drop to be applied to the received beam due to the misalignment. In Figure 3.18 represents the misalignment of the beam and the effect this has on the beam power, demonstrating how the control loop implements the calculation of the attenuation by measuring the beam and LOS angles.

The final aspects reproduced in the setup are the attenuation of the beam power and the Doppler shift caused by the relative velocity between the two spacecraft, achieved using AOMs, multipliers and optical attenuators, with the difference that while in the Fiber OGSE mechanical attenuators were used, in the LLS setup Variable Optical Attenuators (VOA) have been included [24].

The LLS, compared to the Fiber OGSE, was not developed specifically to be representative of one
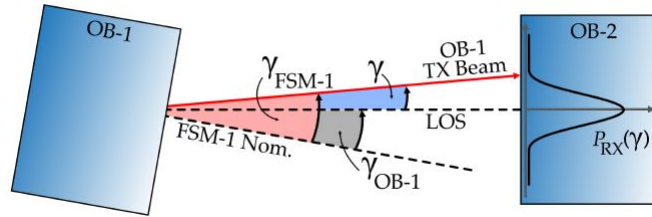
Figure 3.18: LLS transmitted beam misalignment and effect on the received power [24].

space mission, but represents a versatile testbed that can be adapted to provide insights for a wider range of mission scenarios. The LLS can therefore be slightly changed to simulate conditions similar to those found in the LISA mission scenario, mainly increasing the delay time used in the FSM control, because the flight time of the laser between the LISA spacecraft is longer, reducing the output power to pW level (using the VOAs) and fiber collimators need to be replaced with telescope simulators [24].

3.3.3. Free-space link acquisition demonstrator for Taiji

The setups introduced in Sections 3.15 and 3.3.2 are characterized by the fact that they are both fiber coupled designs and they are mainly intended for Grace Follow-On and NGGM-like missions. Gao et al. developed an experimental setup for simulation of link acquisition procedures for space based gravitational waves detection missions such as LISA and Taiji, employing a free-space laser connection between the two terminals [17]. An overview of the setup is provided in Figure 3.19, showing the 10 m separation between the terminals.
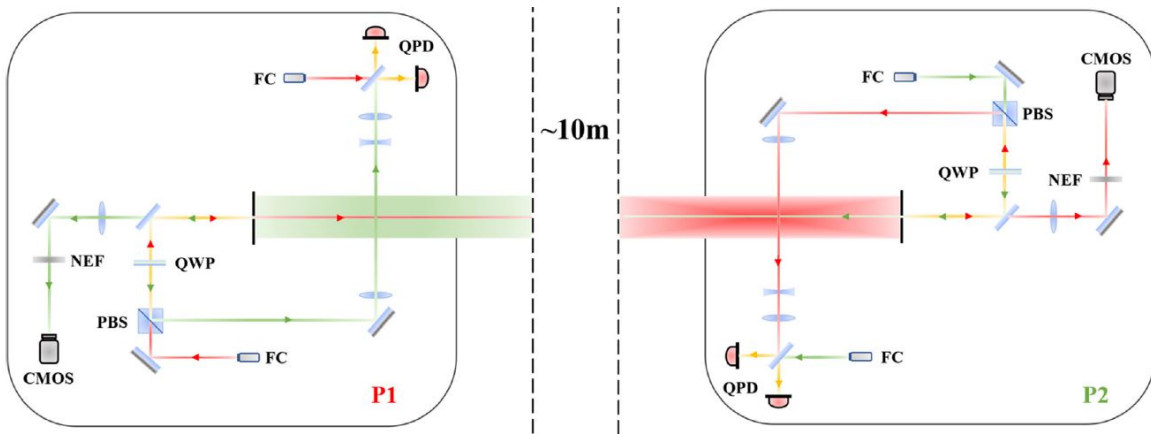
Figure 3.19: Laser link acquisition demonstrator for LISA and Taiji based on a free-space connection [17].

The optical benches represented in Figure 3.19 are placed on top of Hexapods to simulate the motion of the satellites, while the telescopes are replaced by small apertures, to simulate far field beam receiving characteristics. The PAAM (Point Ahead Angle Mechanism) is replaced by a mirror as no lateral motion is introduced in the system. The conditions of pointing precision and field of view of the various sensors are reproduced to be as close as the real ones as possible. A detailed description of the setup and the components used is available in Gao's work [17].

The most important characteristic to replicate is the flat top beam shape, for this purpose the authors introduced an approximate coefficient, m_{flat} to evaluate how the beam in the experiment compares to the Taiji mission's conditions. Equation 3.4 shows how can the m_{flat} parameter be calculated,

$$m_{flat} = \frac{\sqrt{\omega_0^2 + \frac{\lambda^2 L^2}{\pi^2 \omega_0^2}}}{\epsilon} \tag{3.4}$$

where ω_0 is the beam radius, L is the platform separation, ϵ is the aperture radius and λ is the wavelength [17]. The higher m_{flat}, the more the beam resembles a flat top beam; for the Taiji mission conditions the value of m_{flat} would be as large as 2.5×10^4. The only variables that can be manipulated on ground to simulate the flat top beam characteristics are the beam radius ω_0 and the aperture radius ϵ.

Another parameter was introduced to simulate the scanning process: the scanning range coefficient n_{scan} defined as

$$n_{scan} = \frac{\alpha}{\sqrt{\frac{\omega_0^2}{L^2} + \frac{\lambda^2}{\pi^2 \omega_0^2}}} \tag{3.5}$$

where α is the half angle of the scanning range and the other variables were already introduced for the other parameter m_{flat} in Equation 3.4 [17]. One final parameter introduced was the receiving laser power P_{rec}, defined as

$$P_{rec} = \frac{\pi^2 \epsilon^4}{\lambda^2 L^2} \tau P_{out} \tag{3.6}$$

where τ is the transmittance in space, P_{out} is the outgoing laser power at the transmitting telescope and the other variables were already introduced earlier in Equations 3.4 and 3.5.

The three parameters are coupled and should therefore be considered comprehensively. The value obtained in the experimental setup are far from those found for the Taiji mission real conditions, as can be seen from the comparison in Table 3.5. It is clear that there is a big discrepancy between the real conditions and what can be achieved in a laboratory setting. In order to make the experimental results more valuable and representative to gain insights into the in space link acquisition procedure, the authors implemented a number of counter measures.

Parameter	Taiji	Experiment
m_{flat}	2.5×10^4	13
n_{scan}	14.4	1.1
P_{rec}	$1.5\ nW$	$\approx 1\ \mu W$

Table 3.5: Comparison of the coefficients between Taiji and the experiment setup [17].

Regarding the small value of n_{scan}, the implication is that the link is easily acquired by the two terminals; to correct for this, a threshold is set for the receiving laser spot on the Complementary Metal Oxide Semiconductor (CMOS) image sensor [17]. The scanning continues until the maximum detected grey value of the CMOS image sensor exceeds the threshold. The flat top beam can be approximated with a value of m_{flat} of 13, as can be seen in Table 3.5, which is far less than that of the actual Taiji mission, the influence of in-flat top properties on the target precision has to be carefully considered. The authors evaluate the effect of the flat top properties of the beam on the detection using numerical methods, simulating the experiment, and comparing it with the ideal results that should be obtained, showing agreement between the two [17].

The experimental setup shares many similarities with the ones already introduced earlier, an accurate description of the optical breadboard is provided in the work by the authors [17]. The breadboards are then placed on Hexapods, 10 meters apart, and the beam is enclosed in a tube to limit the effects of the air movement and temperature changes on the beam quality. A picture of the laboratory setup is shown in Figure 3.20. The main difference with the GRACE Follow-On setups is instead the free-space configuration, which does not include a lens system resulting in a smaller beam diameter at the receiving platform, with a beam waist radius at the aperture of ω_z = 6.5 mm [17].
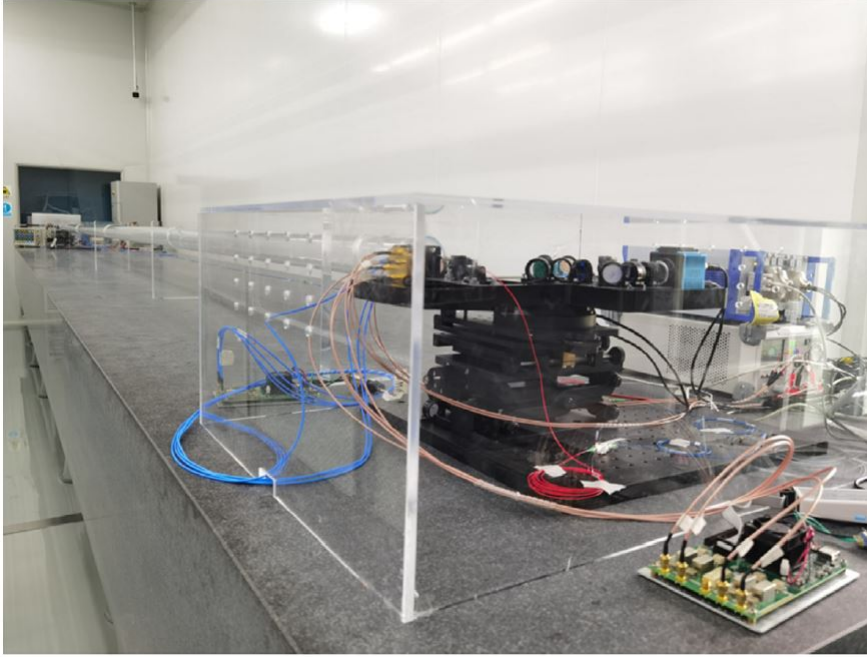
Figure 3.20: Experimental setup for Taiji link acquisition using a free space laser beam [17].

3.3.4. Small free space experimental setup for Taiji link acquisition

In addition to the setup introduced in Section 3.3.3, another smaller free space setup was constructed by Gao et al. with 1.5 meters of separation between the two terminals [16]. A detailed analysis of the construction of the setup and the analysis and tests carried out is available in the work by the authors [16] and it will not be summarized here due to the similarities with the systems previously introduced. Figure 3.21 presents the overall architecture and layout of the components, with the main concept being similar to that of Section 3.3.3, but using a simpler approach, with the CMOS image sensor measurement being carried out on one platform only.
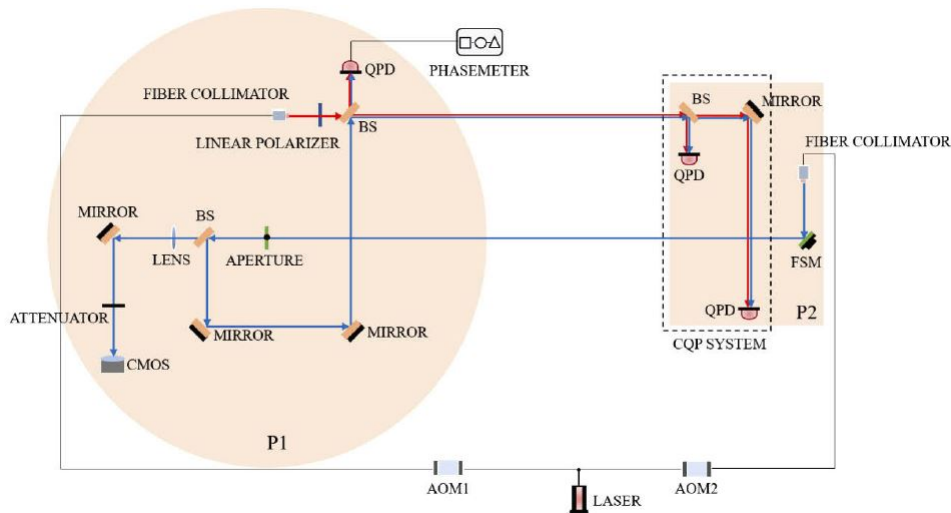
Figure 3.21: Experimental free space setup for Taiji, employing a smaller distance and a simpler platform design [16].

As with the experimental setup in Section 3.3.3, the shape of the incoming beam has been deemed the most important characteristic to recreate. For this purpose the same parameters already introduced in the previous section in Equations 3.4 and 3.5 are used for this experiment as well. The partial derivatives of the parameters with respect to the beam diameter are calculated, showing that m_{flat}

increases with the increase of z and the decrease of ϵ, while it firstly decreases and then increases with the increment of ω_0, taking a minimum value when $\omega_0 = \sqrt{\lambda z/\pi}$ is at its minimum. Since the z distance on ground is limited, an aperture with smaller diameter is used to replace the telescope in the experiment [16]. The partial derivative for the n_{scan} parameter is calculated as well, showing that n_{scan} increases with the increase of z and α while it first increases and then decreases with the increment of ω_0. For this reason the parameters need to be traded off, between flat beam top simulation and scanning range.

In Table 3.6 a comparison between the Taiji and the experimental parameters is shown. Due to the limitations of the on ground experiment, the values of n_{scan} and m_{flat} cannot be restored. The smaller n_{scan} will cause an easier beam detection on the CMOS image sensor, while the smaller m_{flat} will cause the increment of in-flat top properties, which might have an influence in the acquisition procedure and especially in the DWS read-out [16].

Parameter	Taiji	Experiment
Platform separation (z)	$3 \times 10^6\ km$	$1.5\ m$
Beam waist radius (ω_0)	$30\ cm$	$0.43\ mm$
Beam radius at receiving aperture ($\omega(z)$)	$5\ km$	$1.26\ mm$
Aperture radius (ϵ)	$30\ cm$	$0.4\ mm$
Scanning range (α)	$24\ \mu rad$	$2\ mrad$
Flat top beam approximate coefficient (m_{flat})	30667	3.2
Scanning range coefficient (n_{scan})	16.8	1.2
CMOS FOV (θ_{CMOS})	$200\ \mu rad$	$25.6\ mrad$
CMOS resolution	$640 \times 512\ pixel$	$640 \times 512\ pixel$

Table 3.6: Comparison of parameters between the Taiji mission and the experimental setup developed by Gao et al. [16].

Another aspect that can be grasped by looking at the values in Table 3.6 is that the setup developed in Section 3.3.3 presents a significant improvement compared to the one just analysed, mostly due to the increased distance between the platforms.

One final useful consideration that can be extracted from the work by Gao et al. [16] is the influence of in-flat top properties. As a result of the limited laser transmitted distance on ground, the far-field wavefront characteristics can hardly be restored. From Figure 3.22 the effect of this in-homogeneity can be appreciated, as the beam transmitting direction is consistent with the aperture size, while the intensity profile is not uniform. This characteristics could influence the acquisition precision and the DWS accuracy [16].
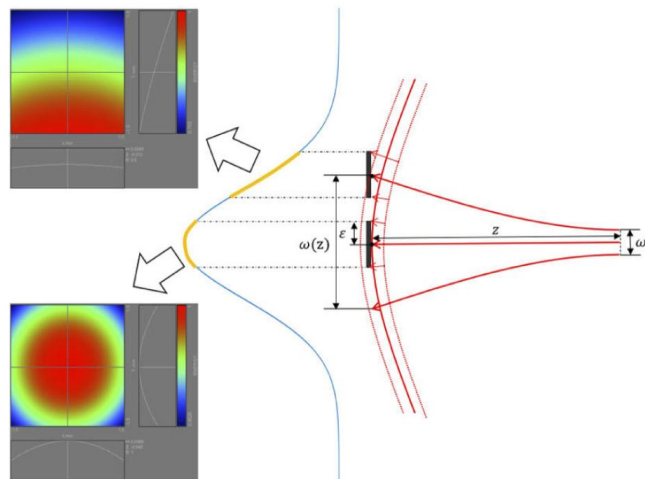
Figure 3.22: Diagram showing the intensity profile and wavefront at the receiving aperture for a non flat top beam [16].

3.3.5. Wuchenich setup

The last experimental setup analysed is from the PhD work carried out by Wuchenich [64], aimed at demonstrating an inter-satellite laser interferometry architecture to be used for Grace Follow-On and future similar missions. The focus is in particular on the experimental demonstration of the acquisition system. The sketch layout of the components is depicted in Figure 3.23, and more information on the design process and relevant design choices can be found in the source of the work [64].
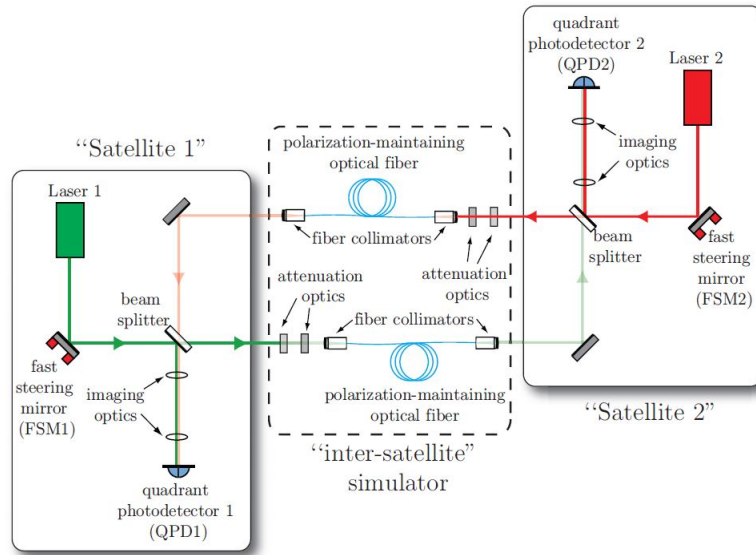
Figure 3.23: Simplified sketch of the experimental link acquisition setup created by Wuchenich [64].

The general idea behind the setup is similar to what has already been introduced in Sections 3.15 and 3.3.2, but no AOMs are used in this case. Two different laser sources are used and the link between the platforms is fiber coupled, in contrast to what has just been presented in Sections 3.3.3 and 3.3.4. Standard optical components for polarization and straylight are included in the setup but not discussed in the thesis. To mimic the beat note amplitude decrease on the local and distant spacecraft, due to reduced power on the distant spacecraft and reduced contrast in the local one, attenuation optics combined with fiber collimators and Polarization Maintaining (PM) optical fibers are used between the two platforms [64]. The effect on the power of the misalignment of the FSM is accounted for with the degraded coupling into the fiber.

A more detailed setup representation is available in Figure 3.24, in which every component of the experiment is depicted and described.
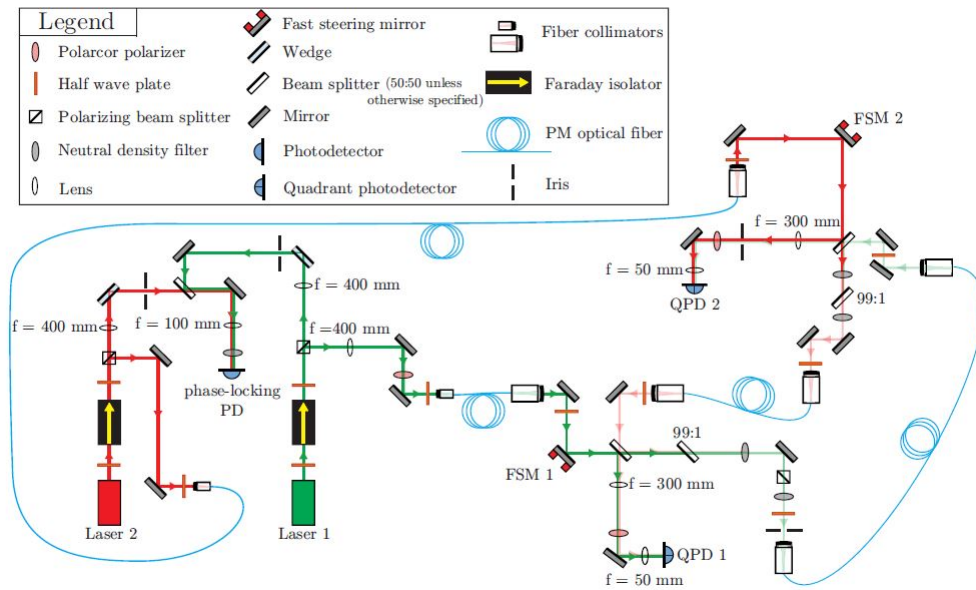
Figure 3.24: Complete diagram of the link acquisition setup developed by Wuchenich [64].

The beam waist for Grace Follow-On is 2.5 mm, while the components used in this experiment can reach up to 2 mm of beam radius [64], but the limited distance over which the beam can spread means that the conditions at the receiving aperture are far from realistic. The final aspect about the work by Wuchenich that is relevant for the Master's thesis at hand and not already treated in the previously described works, is the FSM calibration and the effect of the FSM on the beam quality, which will not be treated in this literature review, but is available in [64].

3.4. Optical Formation Metrology Testbed - OFMT

From the experience gained with the OMT project introduced in Section 3.1.4, a new development is underway at Airbus Defence & Space in Friedrichshafen, which aims at combining two OMTs to recreate a "constellation" setup, to study critical aspects that influence these types of optical metrology missions, with particular attention given to the tilt-to-length coupling occurring in the measurements. The name of this project is "Optical Formation Metrology Testbed", OFMT for short, and the first part of the endeavour is the study of different link acquisition strategies, building on the work performed by other teams around the world and introduced in the previous sections. The work carried out in this thesis is an integral part of the link acquisition definition for the setup and represents a contribution to the whole OFMT project. The design of the OFMT and the experimental lay-out are not part of the thesis work, but they are introduced here to provide the necessary background required to understand the activities and the results presented in the following chapters.

3.4.1. OFMT components

The final configuration of the OFMT set up will be made up of two OMTs facing each other, with one of them placed on a Hexapod to provide scanning motions, static offsets and spacecraft jitter simulations. For the initial part of the project, concerning the link acquisition, an ensamble of elements is used to recreate the behavior of the second terminal, since only one OMT is available at the moment: an interferometer (IFO for short), a fast steering mirror (FSM) and two mirrors placed on the Hexapod. The whole system is visualized in the CAD drawings of Figures 3.25 and 3.26, which show the set up from two view points.

The components can be divided into three groups: the interferometer-FSM-Hexapod assembly, the lens system and finally the OMT and box enclosure, which are here analysed to explain the design choices adopted.
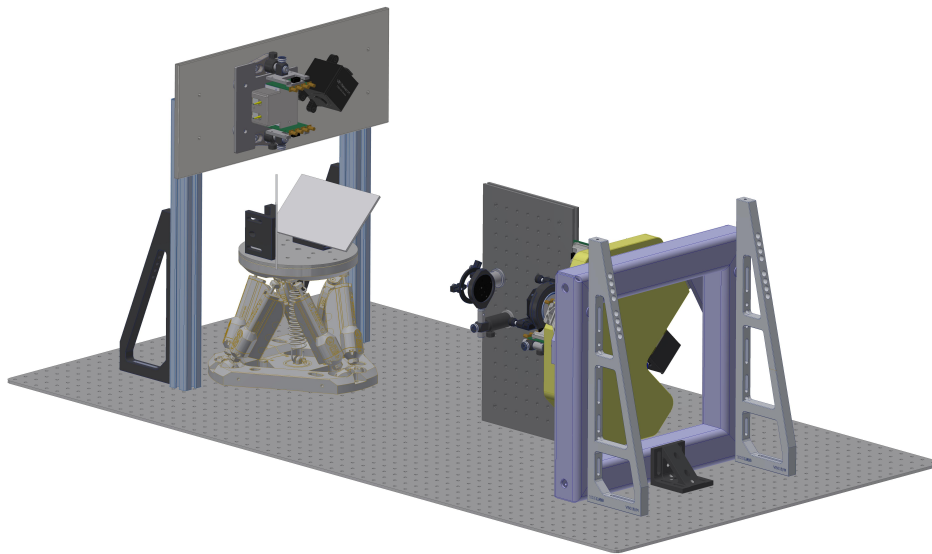
Figure 3.25: CAD model of the OFMT set up for link acquisition, focusing on the interferometer, FSM, mirrors and Hexapod assembly. Courtesy of Airbus D&S.
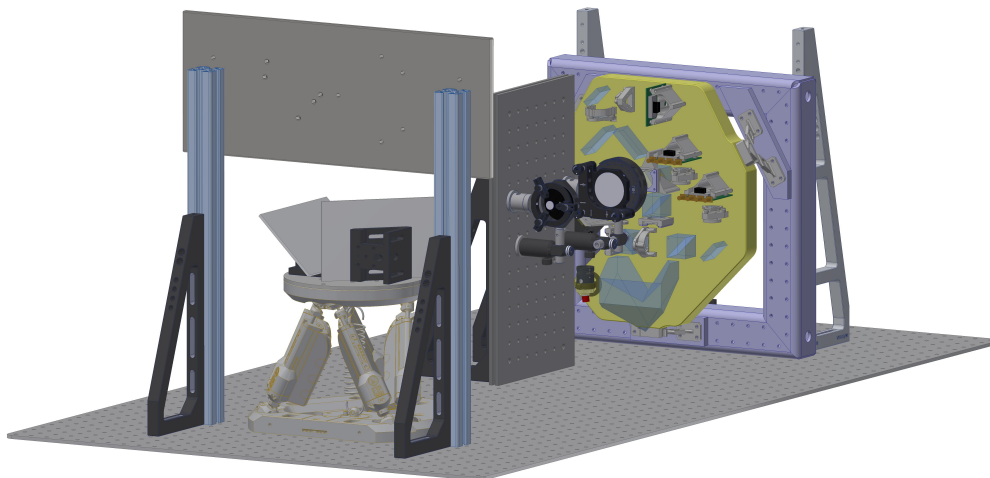
Figure 3.26: CAD model of the OFMT set up for link acquisition, focusing on the OMT. Courtesy of Airbus D&S.

Interferometer-FSM-Hexapod assembly

The Interferometer-FSM-Hexapod assembly acts as the second spacecraft in the constellation, in the absence of the other OMT, and will eventually be replaced by another OMT in the future stages of the OFMT project. The interferometer has been built by E. Germano in their Master's thesis and details regarding its design can be found in their work. The interferometer is mounted on a steel plate above the Hexapod, as can be seen in Figure 3.25, and next to it is the Fast Steering Mirror (FSM) which reflects the beam coming from the interferometer onto the Hexapod. The FSM has been included to

be able to simulate IFP architectures, necessary in the recreation of a GRACE-FO-like scenario. The third element in the assembly is the Hexapod, which allows for the implementation of telescope pointing strategies, i.e. the LISA link acquisition procedure, and can be used to generate static offsets in the line-of-sight between the two terminals. There is one additional piece of equipment that can be spotted on the Hexapod in Figures 3.25 and 3.26, which is the mirrors assembly, made up of two large mirrors that deflect the beam coming down vertically from the FSM, horizontally towards the OMT. The mirrors are included to achieve the full beam excursion required to recreate the scanning of the uncertainty cone.

Lens system

A crucial element of the OFMT setup is the lens system, which allows to simulate a spacecraft separation of around 100 meters, by imaging the origin of the scanning pattern 100 meters away from the OMT reference point, while also spreading the beam and maintaining it collimated at the OMT entrance aperture. This feature of the setup sets it apart from all the other link acquisition experiments presented in Section 3.3 and allows it to achieve greater simulated distances while maintaining a free-space configuration, essential for extracting pathlength information. The assembly is composed of four elements: a spherical lens, an aspheric lens, a field stop and a $\lambda/4$ waveplate, with the lenses mounted on a breadboard on the line-of-sight between the OMT and the Interferometer-FSM-Hexapod assembly. The ray-tracing simulation showing the two lenses is depicted in Figure 3.27, where the magnification effect is clearly visible, as a collimated beam enters the aspheric lens on the right side, gets enlarged and collimated again when coming out from the second, spherical, lens on the left side.
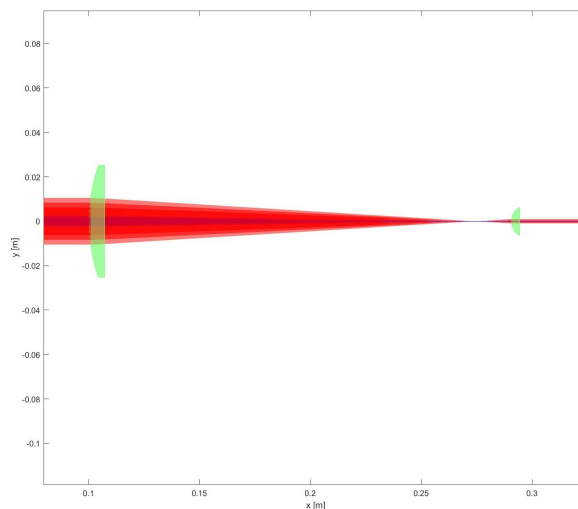
Figure 3.27: Ray tracing simulation of the lens system. Courtesy of Airbus D&S.

The choice of the lenses to be used is the result of a trade-off conducted between two factors: the magnification of the interferometer beam on the OMT entrance aperture, to simulate the largest possible distance, and the diameter of the OMT beam on the interferometer photodetector, as it cannot be too small in order to be correctly detected. The small lens was chosen to be an aspheric lens, to reduce spherical aberrations, especially considering that, during the acquisition, the beam will be hitting the lens close to the edges as well.

The final elements of the lens system are the field stop placed between the first and second lens, to make sure that no beam can reach the OMT by going through the second lens and not through the first one, and the $\lambda/4$ waveplate to change the polarization of the incoming and outgoing beams from linear to circular and vice-versa.

OMT and box enclosure

The final elements that complete the setup are the OMT, already introduced and analysed in Section 3.1.4, and the box that surrounds the whole experiment, to prevent any wandering beam from creating

an unsafe envinronment in the lab and to limit the amount of dust that falls onto the components. The OMT has to be aligned in order to have the aperture on the optical axis of the lens system, and regenerates the incoming beam sending back to the interferometer its local beam which is then detected again and super-imposed in the IFO.

The box around the setup is made of aluminium and the interior is covered by a black foil. Of the eight total panels that constitute the box, the four panels facing the edges of the table are easily removable to allow immediate access to the setup. Three holes strategically placed in the corner of the panels allow for the passage of the necessary cables that go in and out of the box. In Figure 3.28 the aluminium profiles that outline the structure of the box are visible, the aluminium panels are not included as they would not add any visual value.
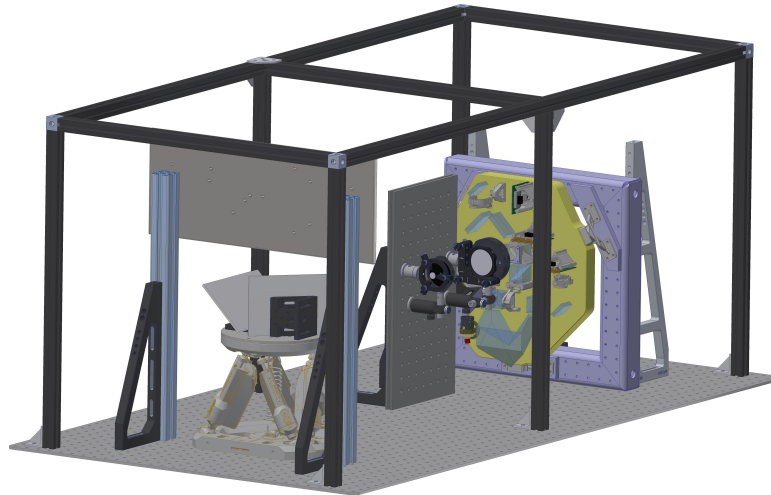
Figure 3.28: OFMT CAD drawing model including aluminium profiles that make up the box. Courtesy of Airbus D&S.

<div align="right">

4

</div>

Methodology

Following the extensive literature review presented in Chapter 3, the Research Questions introduced in Section 1.3 have been developed, identifying the need for further studies in instrumental hardware for space-based laser ranging interferometry missions, with special attention to the needs of link acquisition procedures. This chapter of the thesis contains the core information on the work performed in the project to achieve the goals set in Section 1.3. The chapter is structured in sections that define the activities carried out to answer the Research Questions and the goals, in the order in which they have been set-out, which corresponds closely with the chronological order in which the various tasks have been performed.

In order to answer the first question, regarding how can the link acquisition conditions found in space-based inter-satellite laser ranging interferometry be recreated in the laboratory, the OFMT setup needs to be assembled, aligned and the beam has to be characterized. The assembly of the experimental hardware is detailed in Section 4.1, while the beam characterization, together with the comparison between the OFMT setup and the other link acquisition laboratory reproductions analysed in Section 3.3, is shown in the Results chapter, in Section 5.1. The final goal to achieve in order to answer the first research question is the assessment of the relative alignment accuracy from acquisition tests and from the calibration procedures; the former is carried out in Section 5.2.4 in the Results, while the latter is tackled in Section 4.3.

The second research question focuses on the ability of the OFMT to perform link acquisition procedures, and to answer this question four goals have been defined in Sections 1.3. The activities related to the first goal, building and assembling the infrastructure to control the setup, send the commands and record the data, are described in Section 4.2 and 4.4. Once the infrastructure to perform the tests is completed, the software to run the acquisition tests autonomously needs to be created; the steps detailing the functionalities of the control software are included in the previously mentioned Section 4.4, while the autonomous procedure for the acquisition is shown in Section 4.5.3, with a flow chart in Figure 4.21. The last step needed to fully constrain the acquisition procedure is the definition of the acquisition commands and procedures, as well as the initial offsets; this activity is tackled in Section 4.5. In order to effectively run the acquisition tests defined, the calibration of the components has to be performed, to ensure the commands generated on the computer yield in reality the same results they achieve in simulation, and to obtain a calibration law between the position of the beam on the acquisition detector and the necessary FSM angles in the OMT to successfully engage DWS. The final objective of the acquisition tests defined is to achieve a laser link between the terminals and to be able to maintain it by engaging DWS.

The final research question concerns the requirements that the link acquisition procedure imposes on the OFMT architecture and control. This question is answered by monitoring the behaviour of the instrument during operations, and by examining the link acquisition tests results, paying attention to the weak points and identifying the necessary elements to achieve a successful, reliable and representative link acquisition setup. The discussion regarding the instrument requirements is detailed in the Results

chapter, in Section 5.3.

4.1. Assembly and alignment of experimental setup

As it was mentioned in the introduction to this Chapter, the first step to be performed in order to answer the research questions identified is to build the experimental setup. In this section the process of assembly and alignment of the experimental hardware is analysed and explained, as it represents a crucial step for the correct execution of the test runs and the assessment on the reliability of the results. The assembly and alignment process can be divided in three distinct parts, the ones in which the OFMT has already been divided in Section 3.4: the IFO-FSM-Hexapod assembly, the lens system and finally the OMT and the box.

4.1.1. Assembly and alignment of the Interferometer - FSM - Hexapod mirrors

The process of assembly started from the large mirrors to be placed on the Hexapod, which had to be glued onto the respective mounts. The gluing operation and the structure supporting the mirrors during the curing of the glue were tested beforehand as the curing time of the glue, which is the two component epoxy "UHU Plus Schnellfest", requires the whole process to be performed quickly.

Profiles and supporting brackets have been used to ensure the correct positioning of the mirrors on their mounting structures and rubber elements for padding were used to protect the mirrors. An additional small nylon thread has been added between the mirror surface and the mounting bracket, where the glue was then placed, to make sure that the thickness of the glue over the surface would be uniform. This was especially important because of the difference in the Coefficient of Thermal Expansion (CTE) between the two materials (glass and aluminium), which could lead to optical misalignments in the setup if not compensated for.

The second step of the assembly process was the assembly and alignment of the IFO and FSM on the mounting plate, visible in Figures 3.25 and 3.26.
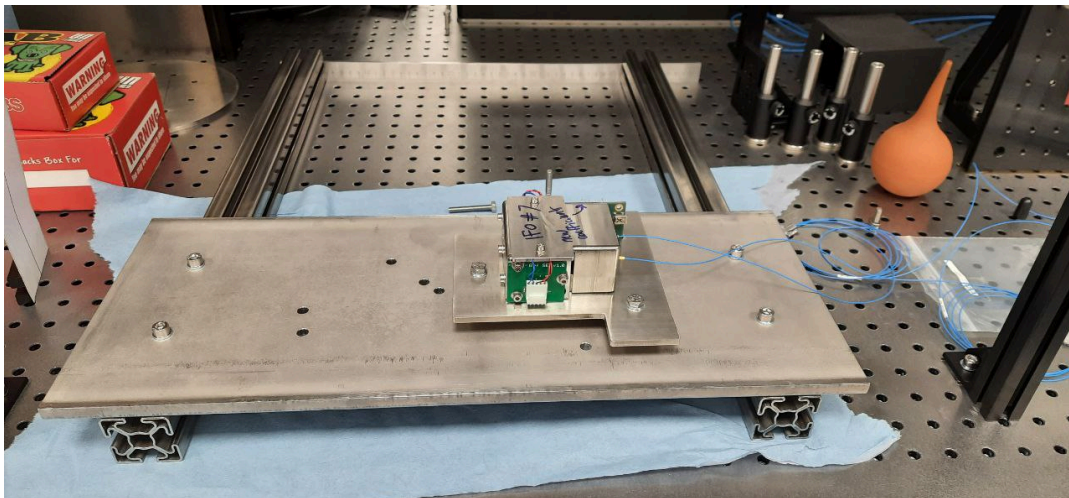
Figure 4.1: IFO positioned on the steel plate ready to be aligned.

The operation started with screwing of the steel plate onto its profiles, ensuring that the plate was perfectly horizontal with respect to the table using a bubble level. For the mounting and alignment of the interferometer to happen correctly, the bottom part of the profiles would have to be exactly parallel to the table, and while this could be achieved by already placing the whole setup in its final, vertical configuration, it would make the alignment process considerably harder. A thick ruler pushed against two aluminium posts screwed on the table was therefore used to ensure the correct orientation of the steel plate while laying horizontally on the surface of the optical table. The IFO was then placed on the steel plate, ready to be aligned with a line of holes on the table, in order for the beam to then be parallel to the surface of the table. The setup described is visible in Figure 4.1.

The alignment process itself was conducted in two steps: a preliminary coarse alignment and then a fine alignment, to reach the maximum accuracy achievable, considering the absence of precision translation stages in the connection of the interferometer to the plate. The coarse alignment was performed using viewing cards (as the laser is infrared) with a cardboard post to provide a vertical reference. The alignment was performed with two cardboard posts placed one close and one further away from the interferometer, to ensure a straight line alignment.

The fine alignment was carried out using two variable aperture pupils and a powermeter. The power meter was positioned behind the pupil and the IFO was then moved to maximize the power going through the aperture, as the power reading is maximum when the beam is exactly centered on the pupil. The process was repeated iteratively for the two pupils, again one close to the steel plate and one further away on the table, both exactly centered on the optical table holes to ensure a straight line alignment. The fist pupil of the system is visible in Figure 4.2, while it is being used for the fine alignment of the FSM.

Once the IFO was aligned and securely tightened on the steel plate, the following step involved the alignment of the Fast Steering Mirror, in a similar way to what has just been described for the interferometer. The first difference between the alignment of the FSM and the alignment of the IFO is that the whole steel plate mount needed to be turned by 90° in order to perform the FSM alignment, because in the experiment the mirror will be reflecting the beam downward perpendicularly to the table plane, when in the zero-position. The Fast Steering Mirror needs to be turned on with 0 Volts applied to both axes in order to place the mirror in the nominal rest position; performing the alignment with the mirror turned off would result in a unanticipated offset of the beam during operation. In Figure 4.2 the FSM is clearly visible (the black block) on the steel plate, with the input cable connected to provide the nominal zero-position. The alignment of the Fast Steering Mirror was carried out in the same way as the IFO, by performing a coarse alignment with the viewing card and a fine alignment with the aperture pupils, even though maintaining a precise positioning of the FSM was significantly harder, and the limitations imposed by the locations of the holes predisposed on the steel plate meant that the freedom of movement for the FSM was constrained, but it was still possible to achieve the necessary range of motion.
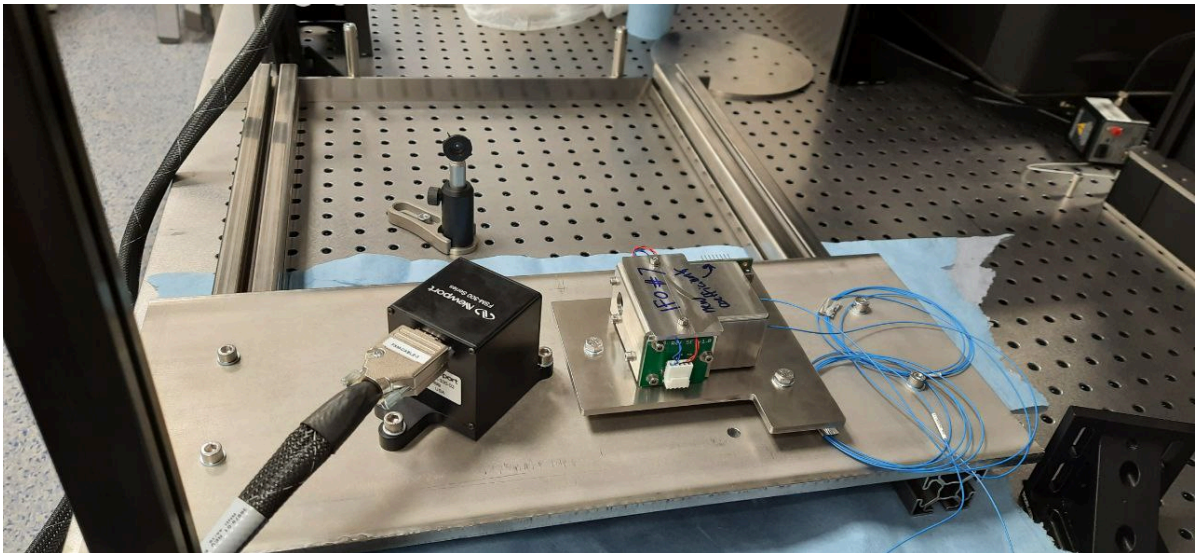
Figure 4.2: FSM positioned on the steel plate for the alignment.

The third and final step of this assembly and alignment procedure was the mounting and alignment of the two mirrors on the Hexapod plate, which are not positioned directly on the Hexapod head to avoid any damages to the surface, and because one of the two mirrors needs to be glued. A steel plate was used between the Hexapod and the mirrors, with holes in strategic places to allow for the mounting of the mirrors on the plate and the plate itself onto the Hexapod head. The whole assembly visible in Figure 4.2 is positioned vertically on the profile legs, with the steel plate for the mirrors mounted

underneath, so that the laser beam coming from the interferometer is reflected downwards by the Fast Steering Mirror perpendicularly to the table and onto the first of the two mirrors.

The first mirror, at a 45° angle with respect to the table plane, reflects the beam coming vertically from the Fast Steering Mirror, horizontally towards the second mirror. The first mirror is not glued on the plate but it is screwed onto it. The alignment process was not performed directly on the Hexapod but the plate was mounted on posts on the table to avoid damages or glue-spills on the Hexapod. This meant that the first mirror had to be realigned once the plate was positioned in its final location. For the alignment of the mirrors a camera was used, placed on a rail that quickly and with adequate repeatability allows for changes in distance between the measurement points, and through iterative steps the in-plane and out-of-plane angles of the beam can be adjusted. It unfortunately turned out that gluing the mirrors on their brackets resulted in slight misalignments which were corrected inserting aluminium tape of varying thicknesses beneath the brackets. A great deal of attention needs to be put on the screwing of the mirror in place, as it is extremely easy to accidentally change the alignment of the mirror in the process. In Figure 4.3b the two mirrors are placed on the steel plate, the first one has already been aligned and is used to perform the alignment of the second mirror. In Figure 4.3a the camera on the rail is clearly visible. This setup makes the alignment very fast and precise, which are two important aspects considering that manually aligning the mirrors requires many different tries. Once the mirrors were in place and aligned, the position of the second mirror was maintained through the use of some posts and a bracket, while the glue was applied to the mirror bracket and it was then placed back on the plate.

The final step of the whole process was placing the plate with the mirrors onto the Hexapod head, where the first mirror was screwed back into its position through a second, faster, alignment, while the procedure was completed with the testing of the alignment of the whole assembly.
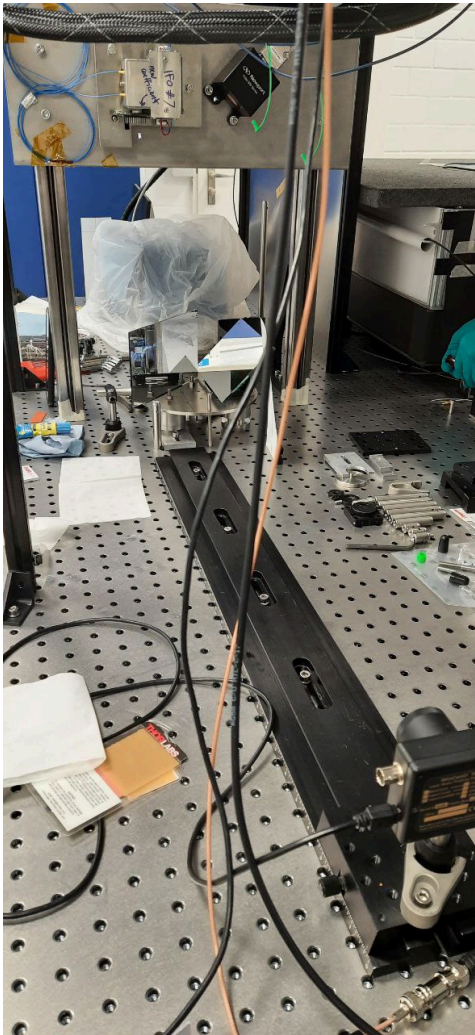
(a) Mirrors on steel plate and rail with camera.

(b) Mirrors on camera to be aligned and fixed.

Figure 4.3: Alignment of the mirrors on the steel plate, using a camera on a rail.

4.1.2. Assembly and alignment of the lens system

The elements that allow for the simulation of a 100 meters distance between the two terminals of the experiment, and the recreation of the beam characteristics mentioned in the first research question, are the lenses, which together with a field stop and the wave plate compose what is referred to here as the lens system. This assembly was already introduced in Section 3.4 when presenting the OFMT, in this section its alignment is tackled in detail.

For the alignment of the lenses two instruments have been used: the Shack-Hartmann Wavefront Sensor (SHWS) and the camera on the rail, already seen in Figure 4.3a. The two lenses were initially positioned at their approximate final location on the vertical breadboard based on measurements on the CAD, the height was adjusted so to be hit exactly in the centre by the beam coming from the mirrors on the Hexapod. For the fine alignment the SHWS was positioned after the second lens of the system and its internal laser was used to perform the fine adjustments, reflecting the laser back to the sensor using a mirror after the first, aspheric lens, on the Hexapod side. The setup is visible in Figure 4.4. The alignment was performed by adjusting the screws on the mounts to decrease the wavefront RMS error below a value of $\lambda/30$ (reasonable value achievable with commercial lenses), with special attention to the tilts and de-focus components of the errors. A dedicated process of alignment was employed [18], due to the large number of degrees of freedom (six in total, three for each lens) and of values to minimize (the several orders of Zernike polynomials). The process consisted in creating a linear system and assuming a linear behaviour of the misalignment errors with respect to the changes in the

degrees of freedom. Each degree of freedom was changed separately from the others by a certain amount and the resulting change in the errors was noted. By repeating this process for each degree of freedom a linear system was obtained using which the errors could be imposed to be zero, deriving the necessary changes in the lenses' degrees of freedom. The alignment was then completed manually to compensate for the intrinsic errors in the linearity assumptions of the method.
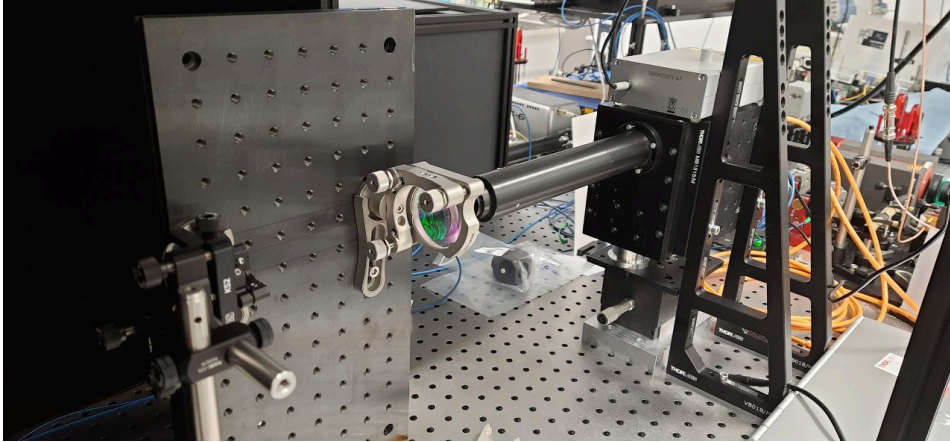
Figure 4.4: Alignment of the lens system using the Shack-Hartmann wavefront sensor.

Following the alignment with the internal laser of the SHWS, the same alignment check was performed using the laser beam coming from the IFO, and the results confirmed that the alignment was maintained and the wavefront error remained the same, indicating not only a good alignment of the lens system, but of the previous elements as well (the IFO, FSM and the two mirrors on the Hexapod).
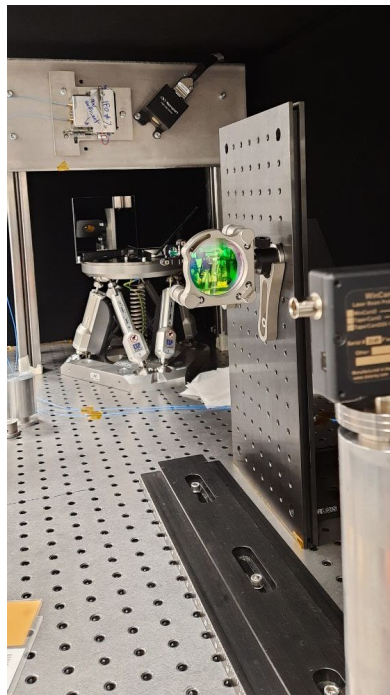
Figure 4.5: Assessment of beam collimation after lens system using the camera.

The final step in the alignment of the lenses was the collimation check, in which the collimation of the laser beam coming from the interferometer was checked after the lens system using the camera on the rail, as previously mentioned. The setup is visible in Figure 4.5, where by moving the camera back and forth on the rail the alignment and collimation of the beam can be evaluated, and they both

turned out be quite good, considering that the beam misalignment is reduced by a factor 10 through the lens system, making the initial small misalignment after the Hexapod mirrors even smaller at the OMT entrance aperture.

The remaining two components of the lens system, the field stop and the waveplate, have been aligned in two different ways. The field stop was placed in the focal point of the first lens with the beam going through the middle of the hole. This was achieved using a viewing card, and while the precision in the placement might not be ideal, it was deemed sufficient; should the field stop position significantly affect the performance, it is possible to intervene to reduce the effects. To ensure the absence of clipping issues in the beam path, some tests have been conducted by translating the Hexapod to reproduce the maximum allowable range; the outcome was positive, indicating that the position of the field stop should be adequate for its purpose.

The alignment of the waveplate was instead carried out using a polarimeter. As introduced in Section 3.4 when talking about the OFMT architecture, the polarization of the beams between the two terminals is circular, in opposite directions for each of the two beams. The waveplate was aligned making sure that the correct polarization state was achieved on each side of the setup. This check allowed for the estimation of the effects of the mirrors and the other components on the polarization of the beam coming from the interferometer. It was reassuring to conclude that the correct polarization state was maintained throughout the setup.

With these final elements included the only component missing to complete the OFMT architecture is the OMT itself.

4.1.3. Assembly and alignment of OMT and protective box

The final step in the completion of the setup was the positioning of the OMT and the alignment of the optical axis. The OMT, introduced in Section 3.1.4, was build by Dr. Mandel in their PhD work [34] and is the core measuring system of the OFMT acquisition setup. It was moved into its position on the opposite side of the IFO-FSM-Hexapod assembly and it was maintained in a fixed position with a system of brackets. The height of the OMT aperture and the inclination of the OMT plane have been adjusted to have the optical axis of the OMT local laser aligned with the interferometer laser using a viewing card, at least to a level where very fine alignments and adjustments could then be performed using the Hexapod and Fast Steering Mirrors.

Figure 4.6: Lens focusing the incoming beam on the detector with spacers for fine alingment.

The alignment of the internal components of the OMT and their interactions with the rest of the setup was checked as well, by monitoring the beam path inside the OMT, by measuring the output of the dedicated

acquisition sensor and by assessing the signal reaching the QPDs. On the acquisition sensor the dot of the incoming beam was clearly visible, even though it was not properly focused, which required some adjustments of the distance between the acquisition sensor and the lenses that focus the incoming beam onto it. The adjustments have been performed using spacers made up of thin, peelable shims 50 μm thick. The spacers were placed on the lens and the detector to change the distance between them until the detector was correctly placed in the focal point of the lens system. By doing so the dot on the sensor became smaller and better defined, which will make for a more precise detection. The lens with the spacers on the mounting bolts is shown in Figure 4.6.

The correct alignment of the whole OFMT setup was verified by the measurement of a beat note signal on the QPDs of the OMT and on the QPD of the interferometer, when the frequencies of the local lasers are set with a small difference between each other.

The final step described in this section is the construction of the protective box around the whole setup. The box performs two roles: it is firstly a protective layer against the laser beams wandering around in the setup, which have to be fully enclosed in order to comply with the safety regulations, and secondly it provides protection to the setup, both from dust and light, as it helps in keeping the optics clean and it greatly reduces the amount of straylight affecting the measurements, thanks to the black surface covering the interior walls.

A picture of the full setup assembled, missing the field stop and waveplate before the OMT, is visible in Figure 4.7. It can be useful to compare it to the CAD designs of Figures 3.25 and 3.26 to easily identify all the elements in the setup.
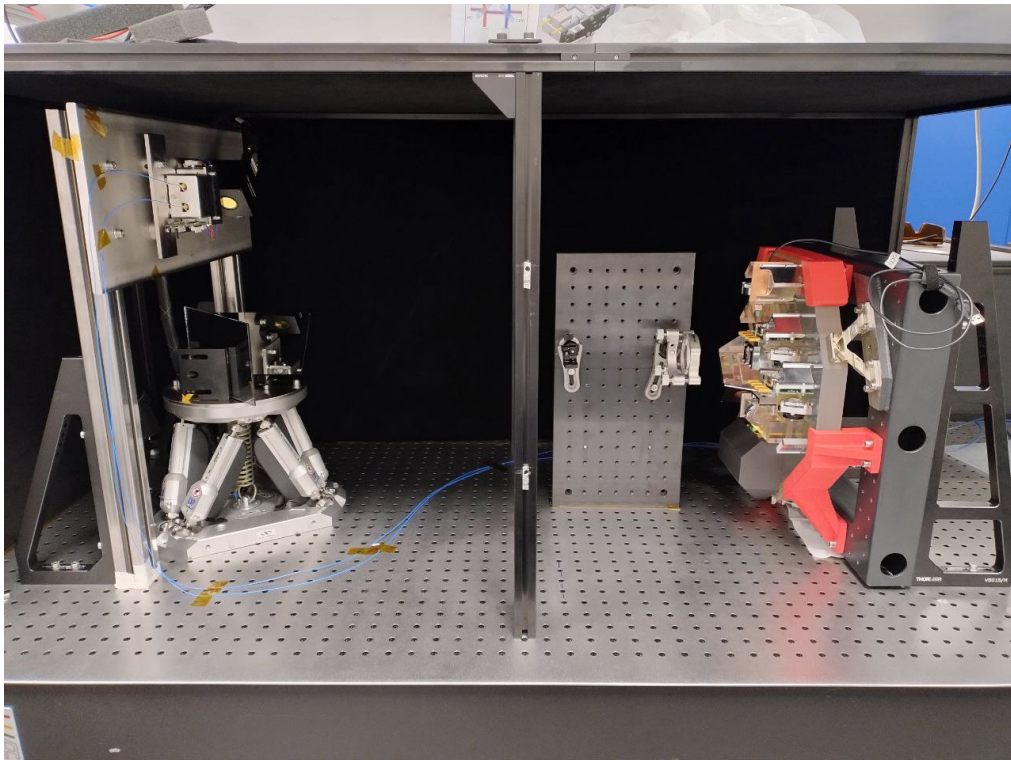
Figure 4.7: OFMT setup without field stop and waveplate from the side.

4.2. Experimental support infrastructure

Once the construction of the hardware for the experiment is completed, the following steps needed to achieve a successful autonomous link acquisition test and answer the second research question include the creation of the experimental support infrastructure, detailed in this section. The numerous elements of the setup need to be controlled and monitored precisely for the acquisition tests to be performed correctly. The core of the instrument is a workstation with FPGA boards that is used to manage all the components in the experiment and perform the required analysis (e.g. DWS, beat note detection). Most of it had already been implemented for the realization of the OMT, but new parts of code and new components have been added to support the inclusion of new elements in the OFMT setup. In particular the following aspects are covered: the control of the FSM over the Hexapod, the acquisition of the status from the two FSMs, the code to run acquisition tests autonomously and the temperature sensors to monitor the temperature variations in the setup.

4.2.1. Hexapod FSM control

The control of the FSM over the Hexapod became more important following unexpected developments in the control of the Hexapod movement. It was in fact discovered that the Hexapod is not capable of performing trajectories that involve simultaneous translations and rotations, while controlling the speed of the movement, which is a requirement to generate a representative spiral scan, for example. The limitation of the Hexapod made it necessary to perform the scan solely with the FSM, using the Hexapod only to provide static offsets to the beam. To drive the FSM movement, providing the necessary bandwidth to generate a fast spiral scan, a waveform generator is used. The waveform generator used is the Rigol DG4162, shown in Figure 4.8, which provides two channels and numerous built-in functions. It is also possible to control the waveform generator remotely and upload arbitrary waveforms to the two channels, which were used for each of the two FSM axes.
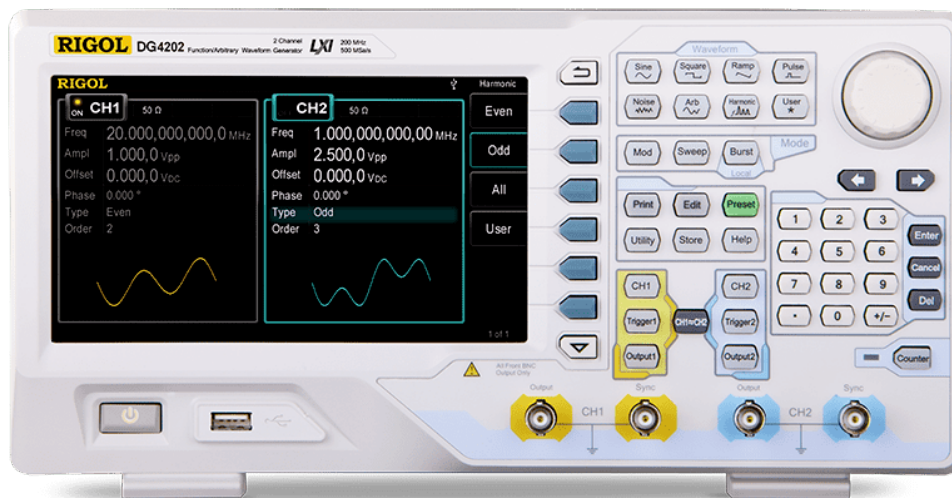
Figure 4.8: Rigol DG4000 series, the waveform generator used to control the FSM over the Hexapod [50].

The remote communication with the waveform generator is performed using the Standard Commands for Programmable Instruments (SCPI), which is a well known and widely used standard to communicate with laboratory equipment. The control of the instrument was therefore included in the overall infrastructure built in C++, using the NI-VISA libraries to write and read the SCPI commands from the waveform generator, connected to the work station via a USB interface.

The main functions to be implemented with the waveform generator were the possibility to output arbitrary waveforms, defined point by point, and the ability to set DC values on the outputs (when a detection happens). The implementation of this commands in a code form is presented in Appendix A.

The DG4162 presents two limitations which required a more complex approach to the control of the acquisition:

- It is not possible to define a different temporal spacing between the arbitrarily defined points, as the only parameter defined is the period of the arbitrary function; this results in a series of (temporally) equally spaced points, which repeats itself after each period.

- It is also not possible to stop the arbitrary waveform to a certain value, or even read a specific output point of the active waveform, as the instrument does not keep track of the values of the outputs during the generation of the waveform.

These two aspects made it necessary to find a way to monitor the FSM angles values during the acquisition to then set them to the point where the detection on the acquisition sensor occurred, by stopping the arbitrary output on the waveform generator and setting a DC value. The output reading of the FSMs is covered in the next paragraphs.

4.2.2. FSM voltages reading

In section 4.2.1 the requirement of using a waveform generator has been detailed, as well as the limitations it comes with, in particular its inability to stop at a specified location while generating an arbitrary waveform. This restriction means that when the acquisition sensor detects a beam, the current voltage outputs of the FSM over the Hexapod (also referred to as "FSM IFO") need to be read and then uploaded to the waveform generator as DC values. The reading cannot happen by sending a query to the waveform generator because it cannot handle simultaneous tasks (outputting an arbitrary waveform and retrieving the voltage values of the outputs), which means that the communication port of the FSM driver has to be used, by connecting it to one of the Analog to Digital Converter (ADC) inputs on the work station.

In the same way, reading the output of the FSM inside the OMT (also referred to as "FSM OMT") remotely requires to either re-program parts of the FPGA, as this functionality had not been implemented during the development of the OMT, or to connect the ADC outputs to the FSM driver, just like the other FSM. The second option is the faster and more convenient of the two.

The cables for the connection of the two FSMs have to be built, because they need to connect to a SMA port on the workstation side, and they need to include a voltage divider setup as well as a capacitor to suppress high frequency noise that has been shown to affect the readings, according to preliminary tests. The schematic of the simple circuit implemented is shown in the Figure 4.9, where the $\pm$ 10 V generator simply represents the range of values that the FSM driver could output (based on the available range of the FSM), R1 and C are the resistor and capacitor added to the cable respectively, R2 is the resistor internal to the FPGA's ADC and "FPGA Pin 1" and "FPGA Pin 2" are simply the FPGA ADC input and the FPGA ground respectively.

The values for the resistor differ between the cable for the FSM over the Hexapod and for the one in the OMT, because they have different ranges available: the FSM over the Hexapod is free to span the full $\pm$ 10 V range, while the FSM in the OMT is limited to $\pm$ 2.5 V. For both connections, the maximum input to the ADC can be $\pm$ 1 V (between the "FPGA Pin 1" and "FPGA Pin 2"), which requires a scaling factor of 10 for the input coming from the FSM over the Hexapod and a scaling factor of 4 for the input from the FSM OMT. Due to availability of components, the values presented in Table 4.1 have been used for the two cables, with the abbreviations according to Figure 4.9. In the table, the resulting voltage ratio and the cut-off frequency are shown. The voltage ratio defined as the initial voltage at the FSM driver output divided by the voltage at the ADC input, while the cut-off frequency is the frequency at which the signal is attenuated by 3 dB.

	R1 (Ω)	C (μF)	R2 (Ω)	V ratio	F_{cut} (Hz)
FSM IFO	1000	2.2	50	$\approx$20	$\approx$1500
FSM OMT	300	2.2	50	$\approx$ 7	$\approx$ 500

Table 4.1: Components used in the communication cables between the FSM drivers and the FPGA.

The voltage ratio for the two setups is higher than the one required, because of safety factors in the implementation, as well as the available resistors. The lower cut-off frequency of the FSM in the OMT should not represent an issue, since the signals of interest should be located in the tens of Hz range.
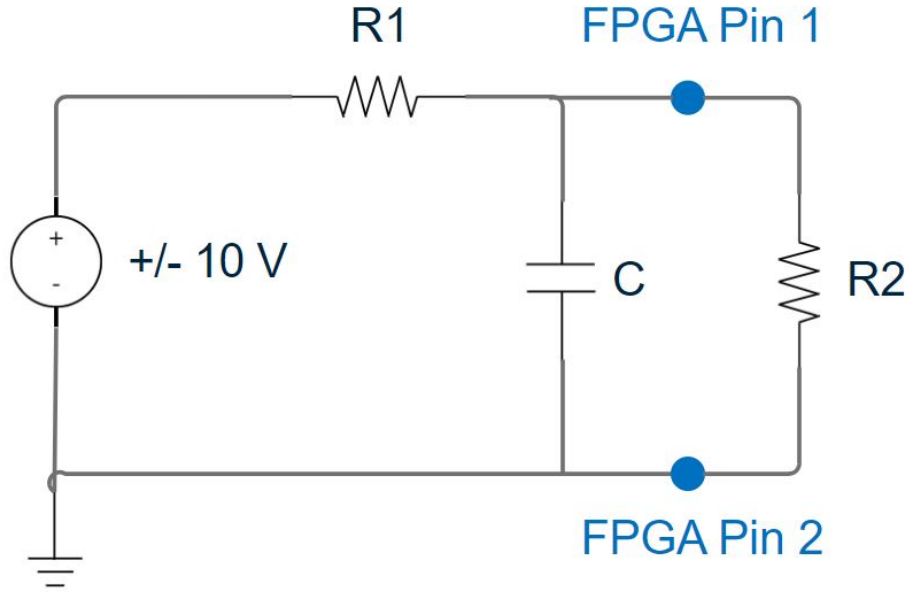
Figure 4.9: Drawing of the cable components used to read the voltage outputs of the FSMs.

Because of imperfections during soldering, the effective voltage ratio between the ADC input voltage and the initial voltage will differ from the values shown in Table 4.1, which means that a calibration is necessary. The calibration is performed by scanning the whole motion range of the FSMs while reading the voltage output on the workstation, using the communication cables built, a scaling factor between the theoretically calculated voltage of the FSM based on the ADC value and the actual FSM voltages is then calculated and applied to the measurements.

Even after the calibration, the voltage reading was still noisy, leading to an uncertainty on the results, which was quantified by measuring a known voltage for an extended period of time, to determine the precision of the measurements around the actual value. The precision range was then taken as RMS of the error with respect to the mean value measured. The same measurement has been performed at different voltage values in the relevant range for the tests performed, to make sure that the errors maintain approximately the same amplitude. The errors for the measurements on the different axes of the FSMs are summarized in Table 4.2, along with the respective effects on the optical angles of the beams.

FSM axis	Voltage uncertainty (mV)	Angular uncertainty (µrad)
FSM OMT X	$\pm$ 1.2	$\pm$ 4.4
FSM OMT Y	$\pm$ 1	$\pm$ 5.2
FSM IFO X	$\pm$ 1.5	$\pm$ 7.9
FSM IFO Y	$\pm$ 1.2	$\pm$ 4.4

Table 4.2: Uncertanties on FSMs angles measurements

It is to be noted that the measurements could still be affected by an error in accuracy, meaning that the voltage measured by the system might be off with respect to the actual voltage given as input, while maintaining the noisy range measured earlier. A proper determination of the accuracy of the measurement would require a thorough analysis, which was not performed due to the available time and the limited effects it would have on the objective of the thesis work (building the setup and demonstrating its ability to perform link acquisition procedures) and considering that other non-measurable uncertainties in the system (like the actual reference point position of the OMT) have a greater impact on the overall results accuracy; but from the tests conducted, measuring the error in accuracy by giving known voltage inputs covering the relevant range of the FSMs, it is usually found in the range of $\pm$ 0.01 V. This

source of error was therefore added to the ones shown in Table 4.2, but any conclusion drawn from the effects of these errors should be taken carefully.

4.2.3. Temperature monitoring

Temperature fluctuations in optical setups can have relevant effects on the performance of the systems, leading to inconsistencies and unexpected results. For this reason it was decided to place two temperature sensors inside the OFMT box: one on the table surface, measuring the ambient temperature inside the box, and the other one on the metal plate on which the acquisition sensor is mounted, to monitor the temperature of the camera (in the vicinity of the acquisition sensor). In Figure 4.10 is a picture of the temperature sensors used. The temperature sensors had been developed, calibrated and successfully
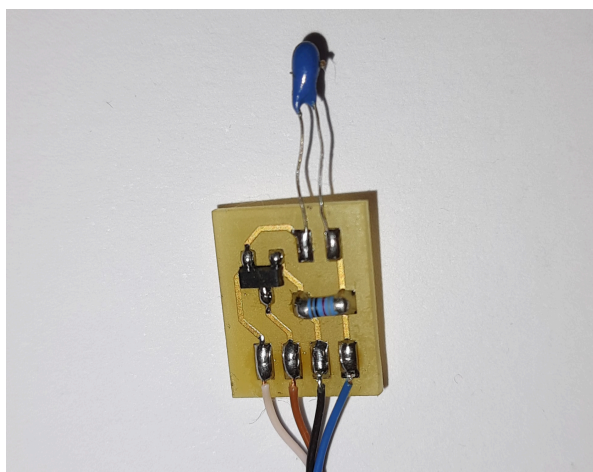
Figure 4.10: Temperature sensor developed for the OMT project and re-used in the OFMT setup to monitor the temperature inside the box and on the acquisition camera.

employed in the OMT setup, meaning that they only needed to be plugged in for the purposes of this work. A newly developed section of the acquisition procedure software is dedicated to logging the temperature data in order to evaluate whether there are any correlations between temperature changes and other variables of the setup.

In order to assess the possible effects of temperature on the acquisition, test runs to monitor the relevant acquisition parameters (position of the beam on the detector and FSMs voltages) while recording temperature data, have been performed in search of any correlation between the variables. The results of the temperature testing have been included in the setup alignment results in Section 5.1.

4.3. Calibration of the setup

The assembly of the experimental setup presented in Section 4.1 and the realization of the supporting infrastructure in Section 4.2, are followed by the calibration of the components in the assembly, a necessary step to be carried out before the acquisition tests can be performed, since the calibration step has been identified at the start of this Chapter as an important activity to answer both the first and the second research question.

In the context of this thesis work, the calibration procedures are not aimed at determining the absolute errors on the alignment of the individual components or the correct recreation of the desired offsets using the Hexapod and FSMs, but they are more focused on the creation of a relationship between the beam spot position on the acquisition sensor and the necessary FSM OMT angles required to successfully engage DWS. Another step is anyway included in the calibration procedures: the validation of the IFO-FSM-Hexapod assembly. This is carried out by performing a scanning pattern with the FSM IFO, measuring the resulting beam position on a camera placed in front of the lens system and comparing these results with simulation results replicating the procedure. This last verification determines whether the alignment of the components described in Section 4.1 introduced any unwanted shifts or discrepancies with respect to the ideal assembly created in the ray tracing tool, but it does not provide an absolute indication on the correct reproduction of the desired angles, meaning that the setup is partially un-calibrated from this point of view, relying solely on the internal calibration of the individual components. It is important to stress that the fine alignment of the elements and the exact reproduction of the commands is not essential for the achievement of the goals of this thesis work (considering that the setup is then controlled in closed-loop), as long as the errors do not interfere with the correct execution of the link acquisition procedure.

4.3.1. Validation of the FSM alignment over the Hexapod

The validation of the Fast Steering Mirror placed over the Hexapod is performed to ensure that the alignment of the components does not introduce unwanted shifts in the resulting beam, which could affect the scanning procedures. It is performed using a camera and comparing the barycenter of the spots seen on the camera with those seen in simulation, while performing a pre-determined scanning pattern with the FSM. The scanning range is between $\pm 2\ mrad$ on both axes of the steering mirror (the range is limited by the dimensions of the camera available). The comparison between the points detected with the camera and the simulation results is presented in Figure 4.11.
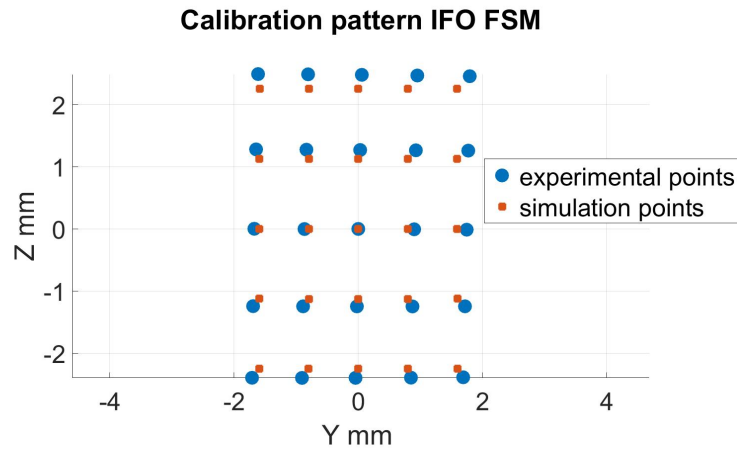
Figure 4.11: Comparison between the calibration pattern detected in the simulation and experimentally on the camera, positioned before the lens system.

It is clear from the comparison that the alignment of the components on the Hexapod side of the lens system does not introduce any noticeable deviations on the beam, as the experimental points closely match the simulated ones. The only appreciable differences are a small scaling (which depends on the effective position of the camera detector, that differs from the position of the sensor used in the simulation) and a slight tilt, due to the camera mount not being perfectly straight over the table.

4.3.2. Calibration of the acquisition sensor and FSM OMT

The objective of the acquisition sensor calibration is to link the position of the spot on the detector with the angles to assign to the FSM in the OMT in order to point the local beam in the anti-parallel direction with respect to the incoming beam, enabling DWS on the OMT and establishing a laser link. This operation therefore requires the scanning of the largest possible area by the laser beam from the IFO, using the Hexapod, and engaging DWS on the OMT for each scanning point to then obtain a calibration law. The beam on the IFO side of the lens system has to go through the reference point of the OMT with different combinations of in-plane and out-of-plane angles to cover in a grid-like manner the field of view reachable with the Hexapod.

Calibration pattern

The first step in the calibration is to determine the calibration pattern. Two variables are needed to define the pattern: the scanning range (the same value is used for in-plane and out-of-plane angles) and the number of scanning points. The scanning range needs to be the largest possible to ensure that every possible point reached during the acquisition tests lies in the calibrated range. Given the Hexapod's legs available range, the maximum angle that can be reproduced on the side of the IFO with respect to the lens system is $\pm15\ mrad$. On the OMT side of the lens system, the maximum angle achievable is $\pm1.5\ mrad$ due to the $\approx \times10$ enlargement of the beam caused by the lenses. The number of scanning points was decided to be 25, five points for the in-plane and 5 for the out-of-plane angle. This number allows for a thorough calibration, covering the whole scanning range without having an overlap between the points on the detector.

The scanning is performed using the Hexapod, which is commanded to make the beam coming from the IFO go through the reference point of the OMT on the Hexapod's side of the lens system with the in-plane and out-of-plane angles identified for the calibration procedure. The commands are generated with a dedicated Matlab code that takes into consideration the maximum and minimum legs extension when generating the translation and angle instructions for the Hexapod.

Detector spot and FSM calibration

When the beam from the IFO enters the OMT, a small part of it is directed towards the detector, where it is focused by two lenses. The position of the spot on the detector provides information about the angle with which the beam enters the OMT; the calibration is therefore necessary to link the spot on the detector with the voltages to assign to the FSM controller to send the local OMT beam towards the IFO with the same angle as the incoming beam. The calibration is performed by scanning the field of view with a pattern defined in the previous section. At each point of the scan, the position of the beam spot on the detector is recorded, as well as the voltages assigned to the FSM in the OMT when DWS is engaged.

For the DWS control to be engaged, the beams need to interfere to generate a beat note and the phase shifts on the quadrants of the QPD need to be small enough that the controller doesn't diverge; this means that the beams need to have a small difference in their frequencies and they need to be closely aligned, an operation that has to be performed by manually changing the FSMs voltages. In order to obtain a beat note on the QPD the AOMs are set to two different frequencies: 80 MHz and 80.01 MHz specifically.

An easier way to carry out the calibration is by engaging the DWS control when the incoming beam is in the neutral position and then proceeding with the setting of the calibration points with the Hexapod while maintaining DWS engaged so that when the scan point is reached, the FSM in the OMT is still directing the beam in the same direction as the incoming beam and the voltage values can be noted down. It is important when engaging DWS the first time to make sure that it is engaged in the right position, which is the position that yields the maximum beat note power. There are in fact multiple positions where DWS can lock successfully and that do not correspond to the correct beam orientation with respect to the incoming beam, but all of the incorrect locations are characterized by a significantly lower beat note signal power compared to the right steering mirror position's beat signal power. For example, Figure 4.12a shows the beat note signal power when DWS is engaged in the correct location and the local OMT beam is directed in the anti-parallel direction with respect to the incoming beam, with which it overlaps in the free-space section of the setup between the terminals. Figure 4.12b instead shows the beat note signal power that is measured when the DWS control is engaged in the wrong

location. If DWS is engaged in the wrong location, the local OMT beam does not overlap with the beam coming from the IFO, and this can be easily verified by using a viewing card and placing it in the beam path between the terminals. In addition to sending the beam in the wrong direction, an incorrect locking of DWS is less stable and more prone to disengaging during the calibration procedure, and when performing acquisition tests as well.

For reference, Table 4.3 shows the mechanical angle values given to the FSM in the OMT to engage DWS in the correct and incorrect positions when the incoming beam has no offsets from the FSM over the Hexapod or from the Hexapod itself. The correct position angles correspond to the beat note signal power shown in Figure 4.12a, while the incorrect position angles correspond to the signal power shown in Figure 4.12b.

DWS engaging position	FSM X (mrad)	FSM Y (mrad)
Correct	≈ 0.2096	≈ 0.7074
Incorrect	≈ 0.5371	≈ 0.7074

Table 4.3: Voltage values for the FSM in the OMT for the correct and incorrect DWS engagement
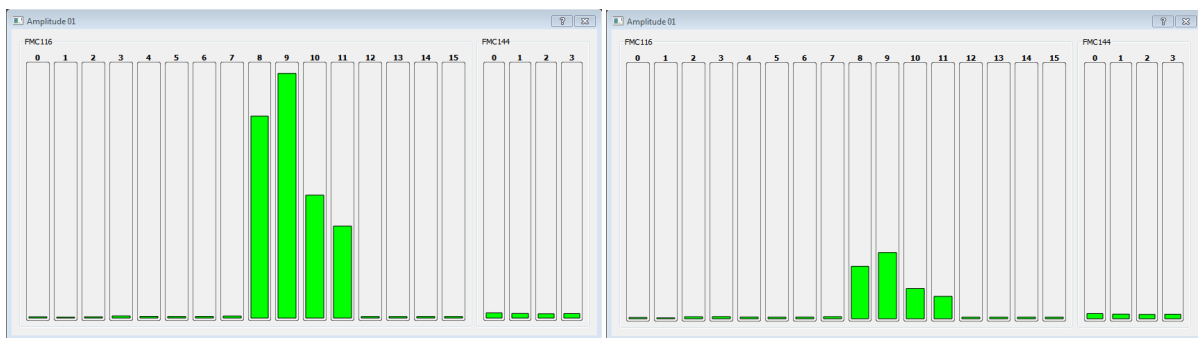
(a) Beat note power when DWS is engaged correctly.   **(b)** Beat note power when DWS is not engaged correctly.

Figure 4.12: Comparison between beat note signals power when DWS is engaged in the correct location and when it is engaged in the wrong point.

The position of the beam spot on the detector is determined as the barycenter of the beam spot, based on the pixels' intensities. During the calibration a threshold was set for the lowest intensities used to determine the spot position, to avoid fluctuations in the measurements. A ghost beam was also measured on the detector, caused by the back reflection of a PBS, which inserted a significant amount of noise in the measurements. An image processing algorithm to eliminate the ghost beam pixels from the barycenter calculation was needed to perform the calibration successfully.

Calibration results
The position of the beam spot on the acquisition sensor has been recorded for each scanning point and the results are presented in Figure 4.13a, where the two axes of the camera have been transformed from pixels to millimeters, knowing the camera resolution and detector's dimensions. The central point of the scan has been taken as the centre of the coordinate system and the position of the other points is expressed as an offset with respect to the centre.

An initial validation of the calibration procedure can be performed by observing the comparison between the experimental results and the simulation results, obtained by performing ray tracing simulations reproducing the calibration procedure and collecting the beam spots on the detector. The comparison is shown in Figure 4.13b, where it is possible to see that the pattern is similar, but there seems to be a scaling effect between the simulation and the experimental calibration, as the experimental points are slightly scaled down. Another thing that can be noticed is the behaviour of the experimental spots in the upper-left part of Figure 4.13a, where the points seem to be slightly out of place, due to the diffraction effects which affect the beam that reaches the detector in that area, even thought the resulting offset is not significant.
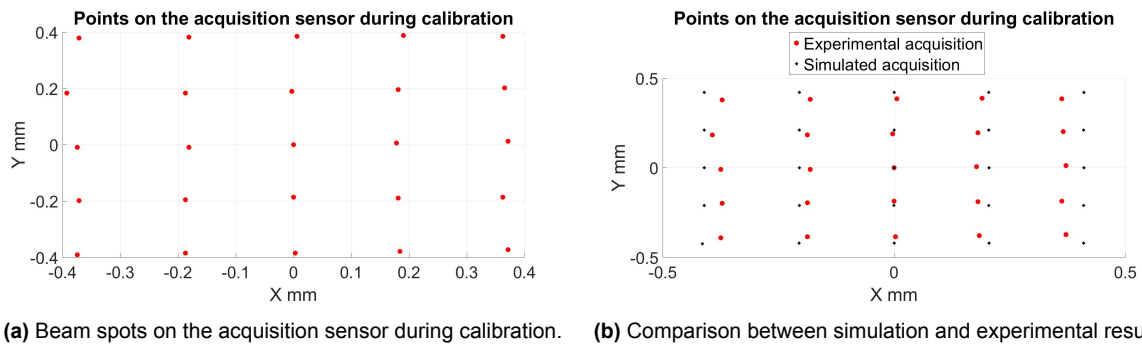
(a) Beam spots on the acquisition sensor during calibration.   **(b)** Comparison between simulation and experimental results.

Figure 4.13: Position of the beam spots on the acquisition sensor during the calibration and comparison with simulation results.

The scaling effect is probably due to the differences between the ray tracing setup and the laboratory setup, mostly regarding the position of the components. The two main sources of the scaling have been identified as the different position of the acquisition sensor, which had to be changed in order to correctly focus the beam on the detector; and the different location of the OMT reference point, due to the position of the lens system being slightly different to the one used in the simulation. Changing this two parameters causes the whole calibration pattern on the sensor to scale as a whole, becoming larger or smaller depending on the offsets applied to the components.

To verify the hypothesis regarding the scaling, two simulation runs have been performed changing the position of the lens system and the position of the acquisition sensor (CCD) separately. The results are shown in Figure 4.14, where the same points found in Figure 4.13b are depicted, along with the spots on the camera obtained from simulations to which adjustments have been implemented. The change in position of the detector by 3 mm causes a slight scaling down of the simulation pattern; the translation of the whole lens system by 3.5 mm towards the IFO makes the simulation resemble the experiment much closer. The simulations performed with the adjusted parameters validate the hypothesis introduced earlier, indicating that the calibration procedure has been performed successfully, at least with regards to the acquisition on the detector; and the differences between the experimental results and the simulation are due to a combination of the lens system and acquisition sensor positions being slightly off with respect to the simulation, shifting the effective OMT reference point and causing a scaling in the calibration pattern.
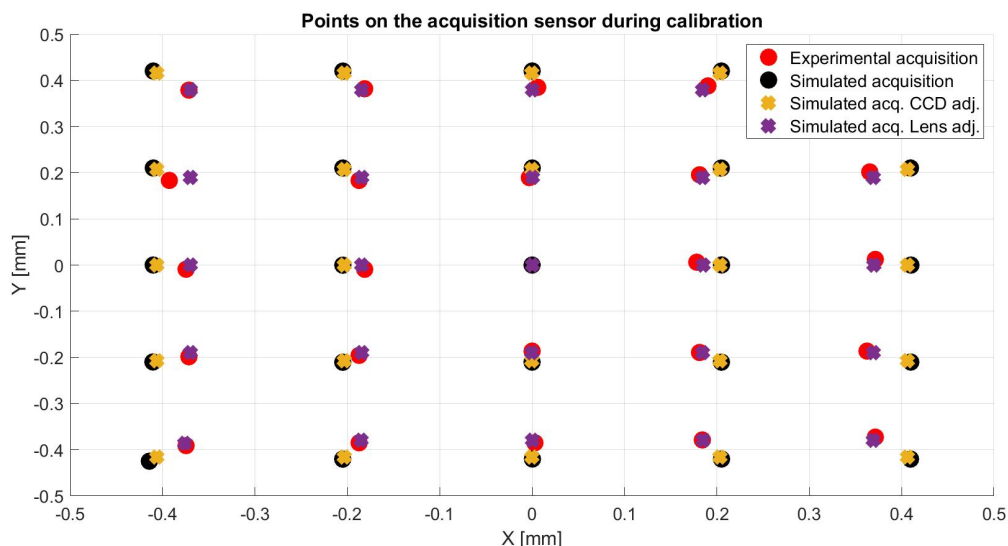

Figure 4.14: Comparison between calibration experimental results, simulation, and simulation with adjusted parameters

It is important to remember that a scaling difference between the simulated and experimental calibra-

tions is not critical, as the objective of the calibration is to find a function that links the position of the beam spot on the detector to the angle to be provided to the FSM OMT in order to engage DWS with the incoming beam. With this aspect in mind, for each calibration point the DAC value of the FSM in the OMT was noted down while DWS was engaged, to then retrieve a calibration law. The DAC values are shown in Figures 4.15a and 4.15b for the horizontal and vertical FSM axis respectively.
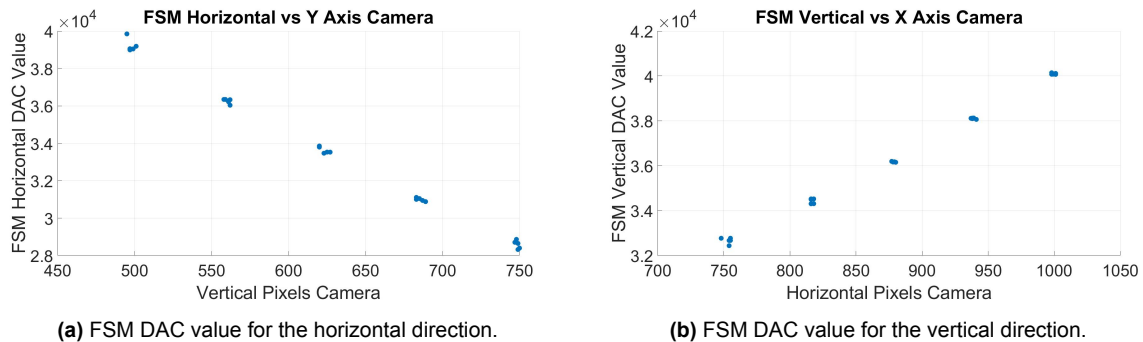

(a) FSM DAC value for the horizontal direction.

(b) FSM DAC value for the vertical direction.

Figure 4.15: DAC values for the FSM control during the calibration procedure for each calibration point with DWS engaged.

It is possible to notice a nice linear trend in the FSM voltage values with respect to the position of the spot on the detector. This means that a linear fit would be possible and it would make for a very easy and effective calibration law.

The last step of the calibration is to find a relation between the spot position on the detector and the associated FSM voltage value needed to engage DWS. The linear fit is shown in Figures 4.16a and 4.16b. With the result obtained it is now possible to link any beam spot position on the acquisition detector to the necessary angles that need to be set on the FSM in order to engage DWS with the incoming beam, provided that it does not change its angle of incidence with the OMT.

(a) FSM DAC value for the horizontal direction with linear fit.

(b) FSM DAC value for the vertical direction with linear fit.
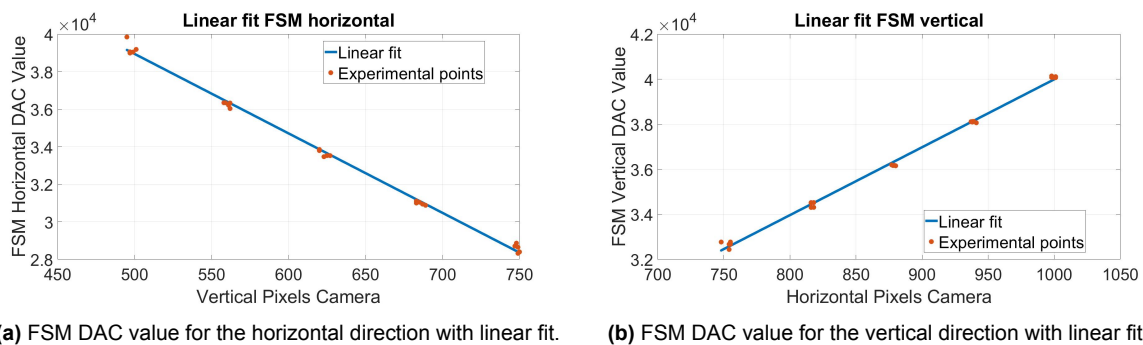
Figure 4.16: DAC values for the FSM control during the calibration procedure for each calibration point with linear fitting and without outlier points.

Calibration validation

The calibration process can be validated by assigning a validation pattern to the Hexapod, similar to the one used for the calibration pattern, but without using the same points. For each point of the validation pattern the spot position on the acquisition sensor is read and the corresponding FSM angles are set, according to the calibration law derived previously. If the incoming and outgoing beams are aligned to a level that allows DWS to be engaged, the calibration has been successful.

This test procedure has been carried out and DWS has been engaged for every point, demonstrating that the correlation between the position of the points on the detector and the FSM angles derived in the calibration is good enough to perform an autonomous acquisition.

4.4. Autonomous acquisition control

The last element of the experiment support infrastructure is the computer program to perform the steps of the acquisition tests autonomously. The code developed allows for two different operational modes: the user can either decide to perform a full scan with the FSM without interrupting it when a detection occurs, while saving the data to be stored in a file, which can be read aftwerwards to evaluate the results; or the user could opt for a "first detection scan", meaning that the scanning sequence is initiated and it is stopped as soon as a detection occurs, after which the FSMs are set to the correct position, according to the calibration and to the scan point at which the beam was detected, and finally DWS is engaged, establishing a laser link and terminating the acquisition procedure.

There are three main elements implemented in the control system that allow for the acquisition to be performed autonomously: the autonomous file loading and scanning, the autonomous detection and setting of the FSMs, and the autonomous DWS engagement and file saving. The detailed description of the steps which compose the acquisition procedure is provided when introducing the various acquisition test that have been run, but in this section a quick overview of the operations autonomously performed by the control software is given.

The user can choose the appropriate scan commands file generated in Matlab, containing the necessary information to command the waveform generator, which is then uploaded by the program to the waveform generator through the SCPI communication protocol. The scan starts when the user presses the dedicated button, which turns "ON" the outputs of the waveform generator, setting off the acquisition procedure. The program then switches between the different operation settings and actions by employing a state machine, guiding the acquisition process.

When performing a "first detection scan", once a beam spot is detected on the camera, the program saves the position where the detection happened, interrupts the scan on the FSM and sets the waveform generator to the value the FSM had when the beam was observed, reading the FSM driver output through the cables described in Section 4.9. After setting the steering mirror over the Hexapod, it proceeds to calculate the necessary voltage values for the second steering mirror to point the OMT local beam in the antiparallel direction with respect to the incoming beam, based on the spot position on the detector and the calibration laws obtained in Section 4.3.2, and sets the FSM OMT accordingly.

The last step performed is the engagement of DWS, preceded by the reset of the phasemeter readout. The values needed by the DWS, like the PID loop constants and settings, had already been determined during the calibration procedures of the OMT project. The engagement of DWS is the most delicate part of the autonomous acquisition. Depending on the values of the phases on each quadrant of the QPD, one reset of the phasemeter readout might not be enough and multiple phasemeter readouts might have to be called, because DWS can successfully engage only when the differences between the phases values are smaller than π, otherwise the DWS controller diverges. A check on the phase differences is put in place to ensure that DWS can be engaged correctly; when the differences between the phases are larger than π, the program enters into a loop where it resets the phasemeter at intervals of 2 seconds until the phases differ by less than π, or the maximum number of iterations for the loop is reached. The 2 seconds waiting time is needed for the phasemeter reset to be effective. Once DWS has been engaged, the user can save the file with the results and the acquisition procedure is terminated.

When performing a "full scan" instead, the scanning pattern is never interrupted, even when the beam is detected on the acquisition sensor, and DWS is never engaged, letting the waveform generator perform the whole scan. The FSMs voltages, the acquisition camera outputs and the other relevant data are logged throughout the scanning procedure and they can then be evaluated to identify the points in which a detection occurred.

Figure 4.17 shows the User Interface window for the newly developed program that commands the autonomous scan procedures and displays the relevant data from the test. The "FSM file name" section shows the name and location of the file containing the commands for the FSM over the Hexapod to generate the acquisition scan. The initial offsets of the Hexapod have to be provided externally in the appropriate window. In the "Scan options" section it is possible to select whether to perform a "Full scan" or not (the other option is a "First acquisition scan"). If the "Full scan" option is selected, DWS will not be engaged and the only outputs of the test will be the beam sposts detected on the camera and the
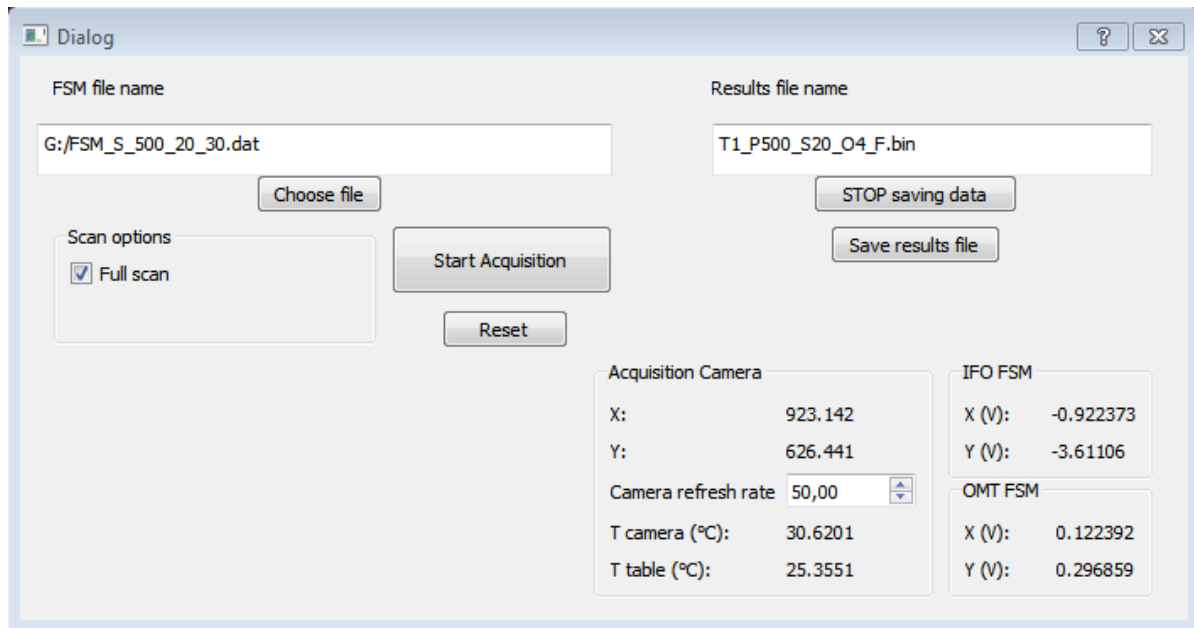
Figure 4.17: User interface for the autonomous link acquisition procedure.

scanning FSM voltages. Under "Results file name" the name for the file where the data from the tests can be saved has to be provided, with a binary format. The "STOP saving data" button allows the user to interrupt the logging of data, while the "Save results file" saves into the file provided in the "Results file name" window the data obtained from the test. The "Start Acquisition" button sets off the scanning from the FSM and initiates the acquisition, while the "Reset" button re-initializes all the variables needed for the scan and turns off the scanning on the FSM. Finally, in the bottom right corner the data regarding the FSMs voltages, as well as the beam position on the camera and the temperatures measured in the setup are displayed. The Camera refresh rate can be adjusted in the appropriate field.

4.5. Definition of the acquisition tests

In the previous sections the hardware and software required to perform the acquisition tests have been outlined, in this section the creation of the acquisition commands is tackled, completing the preparation work necessary to answer the second research question and achieve a successful autonomous link acquisition. In order to run acquisition tests on the setup, the commands for the different components need to be generated, mainly the scanning commands for the FSM and the Hexapod. An overview of the command generation for all the parts of the system is provided below, but depending on the type of acquisition performed, not all of the elements might be included in the test.

Following the description of the commands definition, the acquisition procedure performed is presented, along with the relevant parameters that characterize it.

4.5.1. FSM commands

The scanning procedure is performed by the FSM over the Hexapod, and the commands for this element are generated by running an optimization routine which includes executing ray tracing simulations in Matlab (within the ray tracing tool developed internally). There are three main steps to follow when generating the commands for the Fast Steering Mirror: defining the scan geometry, setting up the simulation parameters, and finally performing the ray tracing simulation which is used to obtain the commands for the steering mirror angles.

The first step, the geometry definition, consists in determining the position in space where the beam has to hit and the in-plane and out-of-plane angles it needs to have while doing so. The scan pattern is defined in the OMT reference plane, so that it can be correctly imaged onto the appropriate location in the instrument. This means that there are two spatial coordinates that fully constrain the position of the beam when it intercepts the OMT reference plane, and along with the in-plane and out-of-plane angles they ensure that the correct scan is performed. The outcome of the geometry definition step is therefore a quadruplet of values for each scan point to be commanded: the two positions in the reference plane and the two angles of the beam. The different scan geometries implemented are discussed later in this section.

The second step is the set up of the simulation parameters, which include the components in the ray tracing simulations as well as the definition of the optimization routine. The components included in the ray tracing are the bare minimum needed for the scan, to make the simulation faster; this means that for a scan performed by the FSM on top of the Hexapod, only the rectangular mirrors are necessary, along with a virtual sensor on the reference plane of the OMT. The objective function to minimize is then defined as the sum of two elements; the first one is the normalized difference between the beam position on the sensor and the ideal position obtained in the geometry definition, and the second one is the normalized difference between the in-plane and out-of-plane angles measured on the sensor and the ones identified in the geometry definition. In certain applications, like the generation of the spiral scan from the FSM over the Hexapod when the spiral origin is placed on the FSM surface, the objective function to minimize is composed only of the angular elements, the in-plane and out-of-plane angles, as the vertex of the scan cone is placed on the surface of the mirror and eliminates 2 degrees of freedom. The optimization routine employed is *fminsearch*, from Matlab, which finds the minimum of an unconstrained multi-variable function without using derivatives information. For each point of the scan the function changes the FSM angles to minimize the value of the objective function, so that by then using the angles obtained as the commands for the steering mirror, the scan designed in the geometry definition can be reproduced in the experiment.

The third and final step consists of actually running the the simulation by providing the information regarding the scan dimensions, the geometrical parameters, the origin of the scan and the values for the tolerances to be used in the optimization routine.

Geometry definition

In the previous paragraph the fist step of the FSM commands generation was described as the definition of the scan pattern's geometry, which is treated here in more detail. There are three main scan patterns which could be used in the acquisition tests: the spiral scan, the Lissajous scan and the hexagonal scan. They have already been introduced in Sections 3.2.1 and 3.2.2 and the definitions have been adapted for the purpose of the work carried out in this thesis.

The spiral scan, as defined in Equations 3.1, 3.2 and 3.3, is reproduced by defining the centre of the spiral scan, the radius of the uncertainty cone to be covered, the origin of the uncertainty cone (the position from where the spacecraft emits the beam), the beam diameter and the overlap between two adjacent arms of the spiral. The spiral is then discretized in a pre-defined number of equally distant points, which are all placed on the reference plane of the OMT, and the normalized vector that connects the points to the origin of the uncertainty cone defines the in-plane and out-of-plane angles the beam needs to have to perform the scan with the right inclination. The positions of the scan points on the reference plane and their in-plane and out-of-plane angles are the information that are then used in the optimization to recreate the scan with the FSM.

The hexagonal scan is similar to the spiral scan in the sense that the scan begins in the centre of the uncertainty cone, but then the area of interest is covered performing ever bigger hexagons, which maintain a constant distance between each hexagon. An additional difference is that the Hexagonal scan is usually defined as a discrete scan, employing a step and stare approach. The geometry of the hexagonal scan is shown in Figure 4.18.
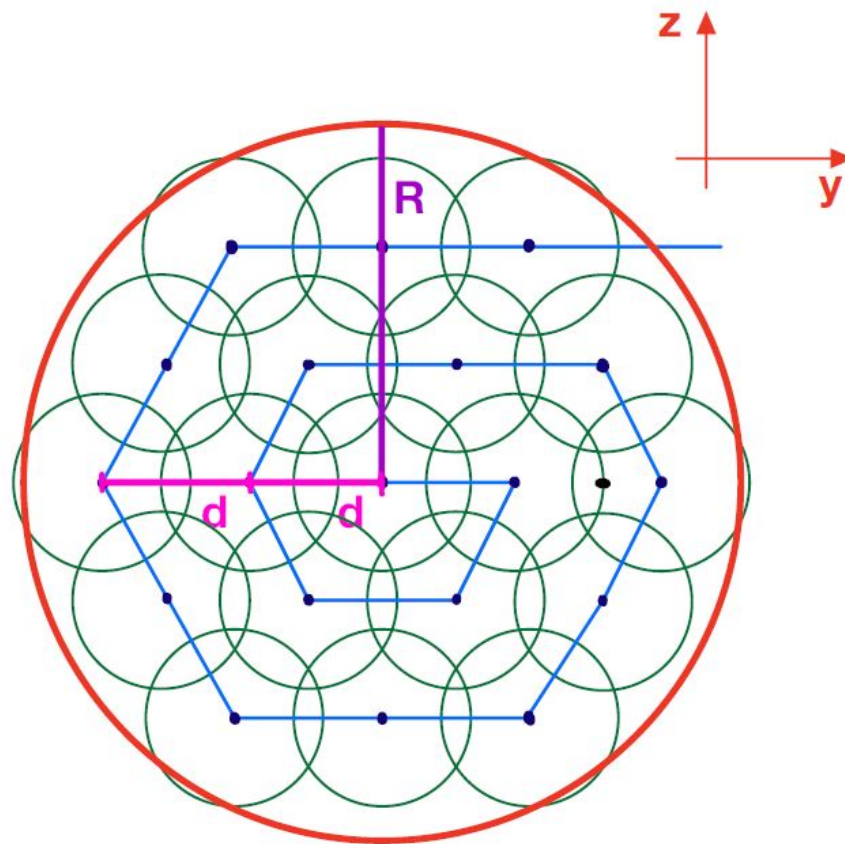

Figure 4.18: Geometry of the hexagonal scan

From the diagram it is possible to identify the uncertainty area, delineated by the red circumference, with radius R. The green circles represent the area covered by the beam in every stop-and-stare location. The black dots represent the discrete scan points, connected by the blue line, which outlines the overall movement during the scan, drawing an hexagon on the scanning plane. The distance between the scan points is chosen based on the beam radius (the radius of the green circles), to ensure an overlap between the areas covered in each step by the beam so that no point in the uncertainty area is missed by the scan.

The Lissajous scan covers a rectangular area, performing two sinusoidal scans in the two directions of the scanning plane. The points (x and y) of the Lissajous scan in the reference plane can be defined by two equations [61]:

$$x = A_x cos(\ 2\pi n_x f_0 t \ ) \ , \tag{4.1}$$

and

$$y = A_y cos \left(\ 2\pi n_y f_0 t + \frac{k\pi}{4n_x} \ \right) \ . \tag{4.2}$$

Where A_x and A_y are the amplitudes of the two scans (both coincide with the uncertainty cone radius), n_x and n_y are the frequency ratios between the two scans (e.g. for n_x = 10 and n_y = 1, for every 10 full periods on the x, one period on the y is completed), f_0 is the frequency with which the scans are performed, and k is a factor that defines the shape of the Lissajous, as shown in Figure 4.19. Just
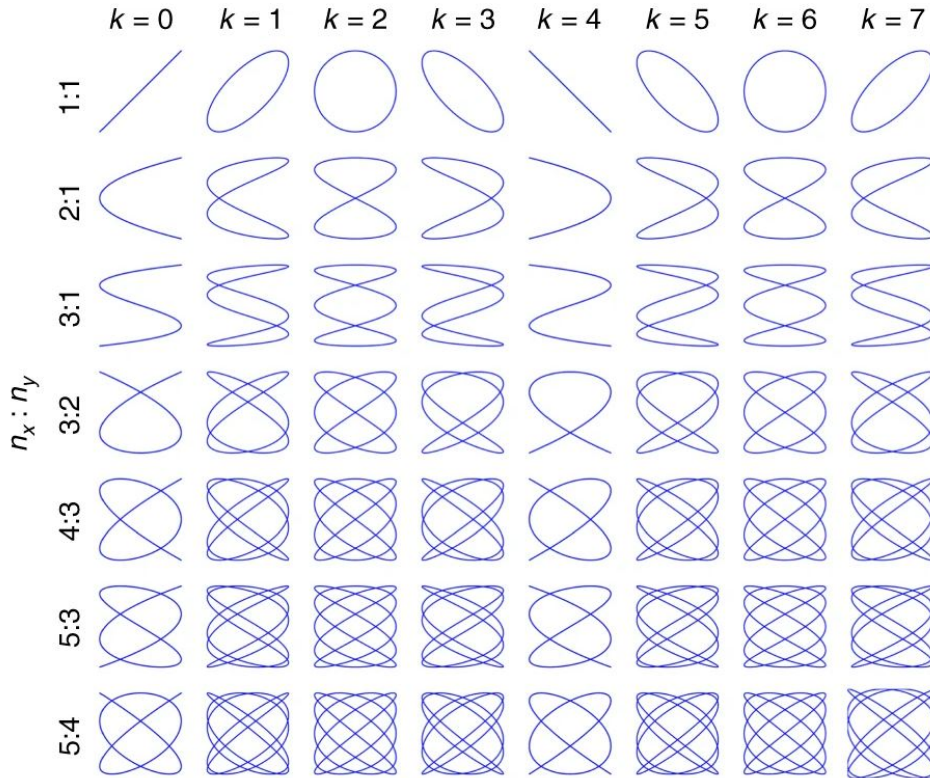

Figure 4.19: Different shapes of Lissajous figures depending on the n_x,n_y and k parameters [61].

like with the spiral scan, the vector connecting each point of the scan with the origin of the uncertainty cone defines the in-plane and out-of-plane angles that are used in the optimization routine. The points resulting from Equations 4.1 and 4.2 are the positions at which the beam intercepts the reference plane and along with the two in-plane and out-of-plane angles fully define the geometry of the scan.

4.5.2. Hexapod commands
The Hexapod was initially included in the setup to perform telescope-pointing scans while providing static misalignment offsets in the meantime. Due to the problems mentioned in Section 4.2.1, mainly the inability of the Hexapod to perform trajectory maneuvers involving translations and rotations at the same time and controlling the speed, the Hexapod has so far only been used to provide the offsets between the optical axes and the line-of-sight to simulate the initial conditions of the acquisition procedure between the two spacecraft in space.

The initial conditions for the acquisition procedure are represented in Figure 3.9, where the two optical axes of the spacecraft are not aligned with the line-of-sight, and the spatial scanning allows for the correction of these offsets. Figure 4.20 shows the angles between the optical axes of the two spacecraft and the line-of-sight in pink (since it is a 2D representation, only one angle per spacecraft is shown, in reality they are 2 angle per spacecraft and 4 in total).
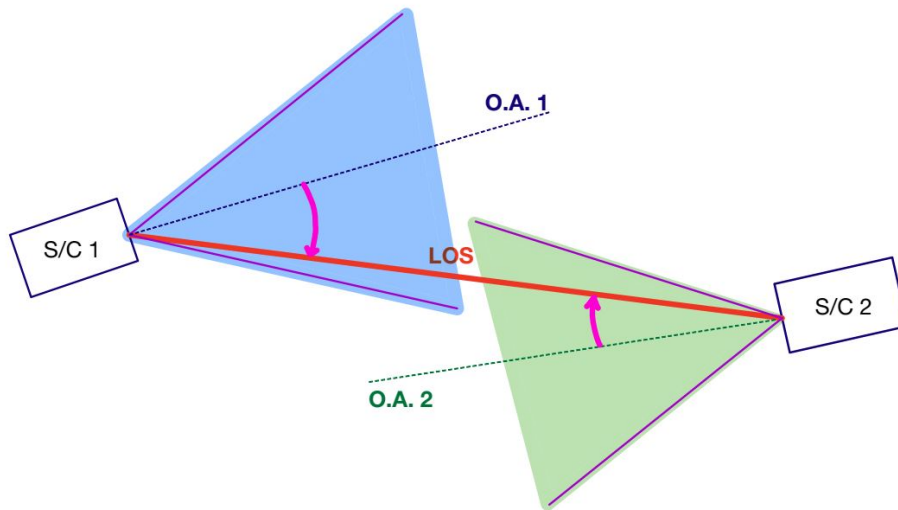
Figure 4.20: Initial misalignment of LOS and optical axes.

The deviation of the optical axes of the two terminals from the line-of-sight can be recreated in the OFMT by using the Hexapod. The offsets should then be compensated by the FSMs in the OMT and over the Hexapod when DWS is engaged. Checking that the FSMs angles correspond to those expected for the correction of the Hexapod offsets is a way to ensure the correct alignment of the setup and the successful outcome of the acquisition procedure.

In practice the commands for the Hexapod consist in translating the Hexapod head to recreate the offset between the terminals due to the misalignment of the OMT optical axis, and then rotating the head to provide the IFO setup angular misalignment. When calculating the magnitude of these commands, the scaling of the lens system simulating the 100 m distance between the spacecraft has to be taken into consideration.

4.5.3. Spiral scan acquisition test

The acquisition test performed to validate the ability of the OFMT to autonomously perform link acquisition tests is a spiral scan acquisition. In Section 4.5.1 the definition of the spiral scan, the Lissajous scan and the hexagonal scan have been covered, but due to time limitations only one scan could be performed to demonstrate the OFMT capabilities. The decision for the scan geometry landed on the spiral scan because it can very effectively cover the uncertainty space and it is easy to implement, compared to the Lissajous scan for example, in which the parameters included in Equations 4.1 and 4.2 need to be carefully chosen based on the acquisition needs to avoid missing out on certain spots of the scanning area. Furthermore, the spiral scan can cover the uncertainty space faster than the Hexagonal scan, which is designed to be used in a step and stare strategy, usually coupled with a Lissajous scan on the other terminal like in the GRACE-FO link acquisition procedure described in Section 3.2.1.

The acquisition strategy devised consists in performing the spatial scan with the FSM over the Hexapod, covering the uncertainty space, until the beam is detected on the acquisition sensor in the OMT, at which point the scanning FSM is stopped and set to the values it had at the detection moment and the local FSM in the OMT is set according to the calibration laws. The last step needed to acquire the laser link is engaging DWS, which is performed autonomously by the control program.

Eventually, when the IFO, FSM and large mirrors assembly over the Hexapod will be replaced by a second OMT, it will be possible to perform double scanning acquisitions with both terminals using a dedicated acquisition sensor, but for now a single scanning strategy has been used. Another option would have been to carry out a GRACE-FO-like acquisition with both FSM scanning the uncertainty space until a beat note is detected on the QPDs, but this would have required further preparation works on the IFO side and the simpler spiral scan performed by the FSM over the Hexapod was found to be the best option among the procedures available to test the OFMT link acquisition.

One element that is not included in the definition of the scanning procedure, but that is always part of laser link acquisitions in space is the frequency scanning, which could be performed by the AOMs in the OFMT setup. In the strategy chosen for the experiments, the frequency scanning would occur after the beam detection and the setting of the FSM in the OMT according to the calibration, in order to detect a beat note on the QPD and engage DWS. The frequency scanning was skipped in the tests carried out in this thesis work because it is not essential to the initial demonstration of the OFMT abilities. A fixed and known frequency shift was chosen for the beams of the two terminals, which lies in the bandwidth of the QPD to allow for an immediate beat note detection when the beams are spatially close enough.

Acquisition procedure

The procedure followed in the test is better showcased by the flowchart diagram in Figure 4.21.

The first step when performing the scan is deciding between a full scan or a first detection scan. In a full scan the scanning pattern is carried out completely and DWS is never engaged, but the detection points and the corresponding FSM IFO values are saved in a file to be later analyzed to identify the points in which the acquisition sensor detected the beam. On the other hand in a first detection scan as soon as the acquisition sensor detects the beam, the scan is interrupted, the scanning FSM is set to the value it had at the time of the detection and the FSM OMT is set according to the calibration laws; the last step consists in engaging DWS and establish a laser link.
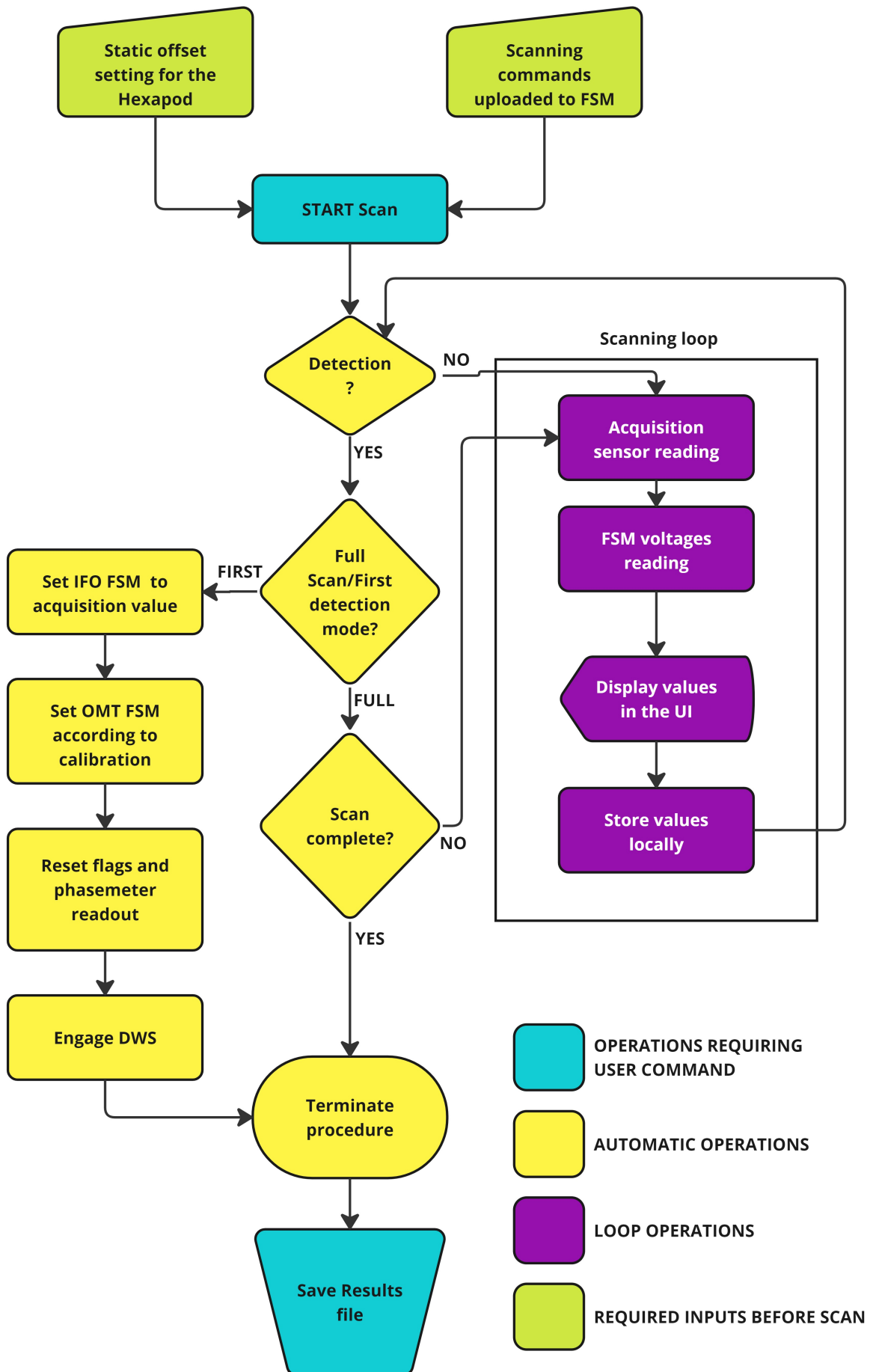
Figure 4.21: Acquisition procedure flow chart

For both scenarios, the second step before starting the procedure is setting the scanning commands to the FSM and providing the static offsets to the Hexapod to simulate the initial LOS and optical axes offsets. Once this is done the scan can be initiated. When a detection occurs, if the scanning mode is "Full scan", the FSM continues with the scanning pattern and the system simply saves locally the FSM values and the acquisition detector values, for the user to then save them in a file once the procedure is terminated. If the scanning mode is a "First detection" mode instead, when the acquisition detector identifies a beam spot, the scanning pattern is terminated and the FSM performing the scan is set to the value it had when the detection occurred, while the FSM OMT is set based on the spot position on the camera, according to the calibration. The last step is resetting the flags and the phasemeter readout to then engage DWS and establish the laser link. The file with the data and results can again be saved by the user.

Both types of acquisition tests are performed as they provide different results and insights into the setup and its performance.

Scanning strategy

The scanning pattern used for the FSM IFO is a constant tangential velocity spiral scan, like the one used for LISA, and described in Sections 3.2.2 and 4.5.1. The commands for the FSM are defined following the procedure described in Section 4.5.1, with a Matlab script. The parameters used in the definition of the scan pattern are summarized in Table 4.4 for the different types of scans that have been tested, where the beam overlap is defined as the distance between the two adjacent arms of the spiral as a fraction of the beam radius. The origin of the spiral cone is placed on the FSM over the Hexapod.

Scan number	Scan half-angle [mrad]	Scan duration [s]	Beam overlap	Scan points
1	30	100	1.3	1000
2	30	500	1.3	1000
3	30	500	2	1000

Table 4.4: Spiral scan parameters

The scan half-angle and the number of points used to generated the commands are kept constant in all the different types of scan tried. The scan duration is changed to evaluate the effect of different scanning speeds on the acquisition procedure and to check whether a fast scan poses any problems to the camera for the correct detection of the beam. The beam overlap is changed to investigate the effect that increasing the distance between the spiral arms might have on the results of the acquisition.

The resulting spiral defined using the parameters of the scans 1 and 2 in Table 4.4 is shown in Figure 4.22.

The related commanded spiral is over-imposed on the spiral definition in Figure 4.23 and it can be seen that the command generation routine, which includes an optimization step, created a perfect replica of the spiral in terms of the position of the beam on the reference plane of the OMT. The in-plane and out-of-plane angles are also recreated perfectly as can be seen by the optimization function values in Figure 4.24, which are always around the value of 10^{-11} (it is adimensional because of its definition). The objective function value, as explained in Section 4.5.1, is the normalized difference between the ideal in-plane and out-of-plane angles defined as a vector, and the actual ones generated with the FSM commands. The commands on the FSM to generate the spiral shown in Figure 4.23 are displayed in Figures 4.25 and 4.26, and as expected they are two sinusoidal waves on the x and y axes, which increase in amplitude along the scan.
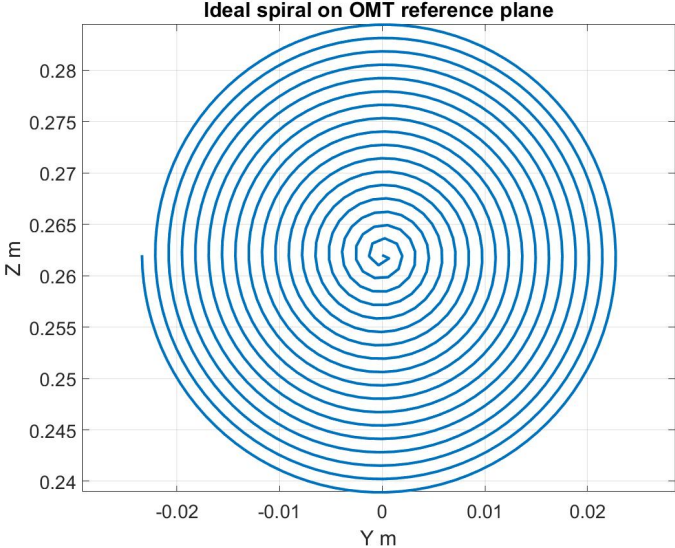
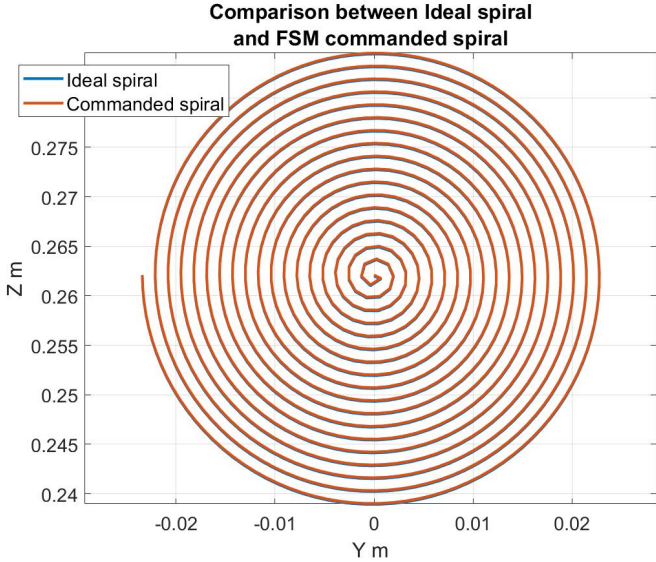**Figure 4.22:** Ideal spiral on OMT reference plane.

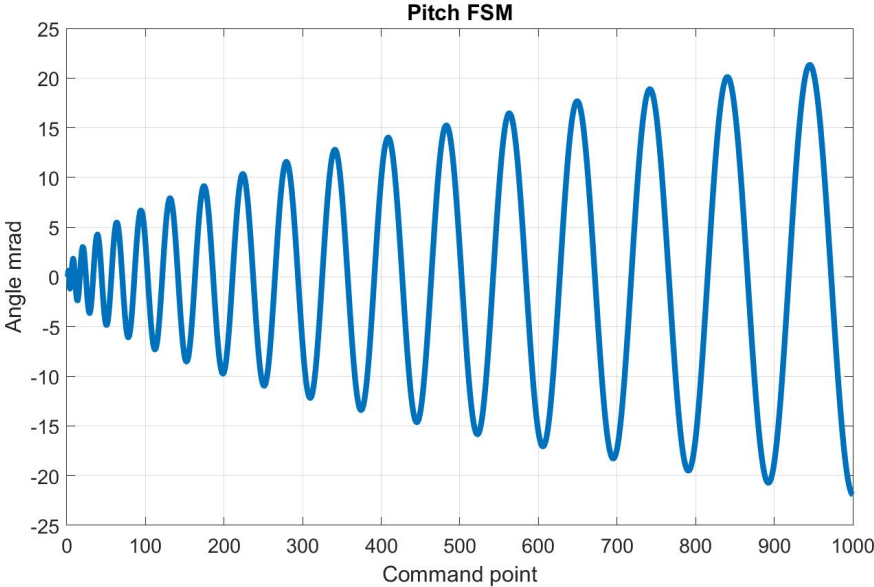**Figure 4.23:** Ideal and commanded spirals on OMT reference plane.

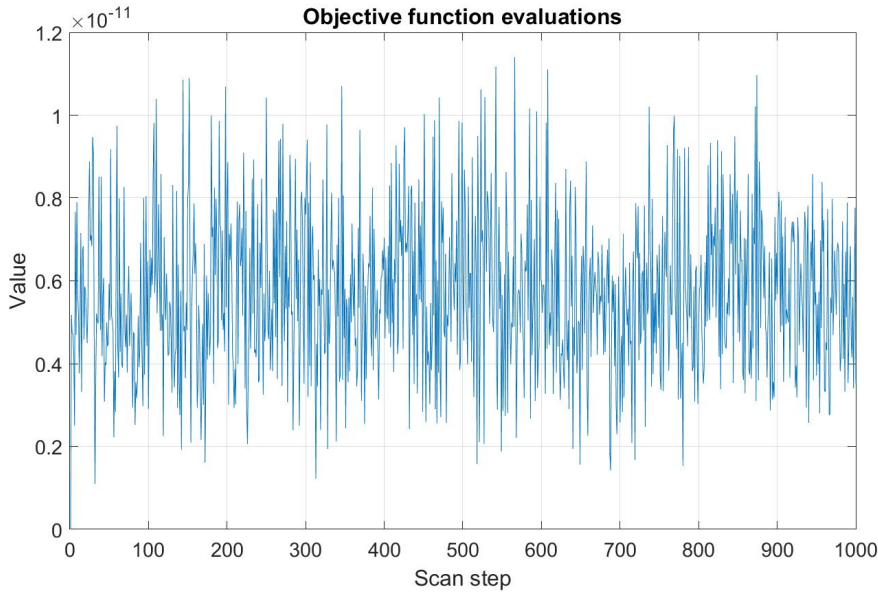**Figure 4.25:** FSM pitch commands to generate the spiral scan.

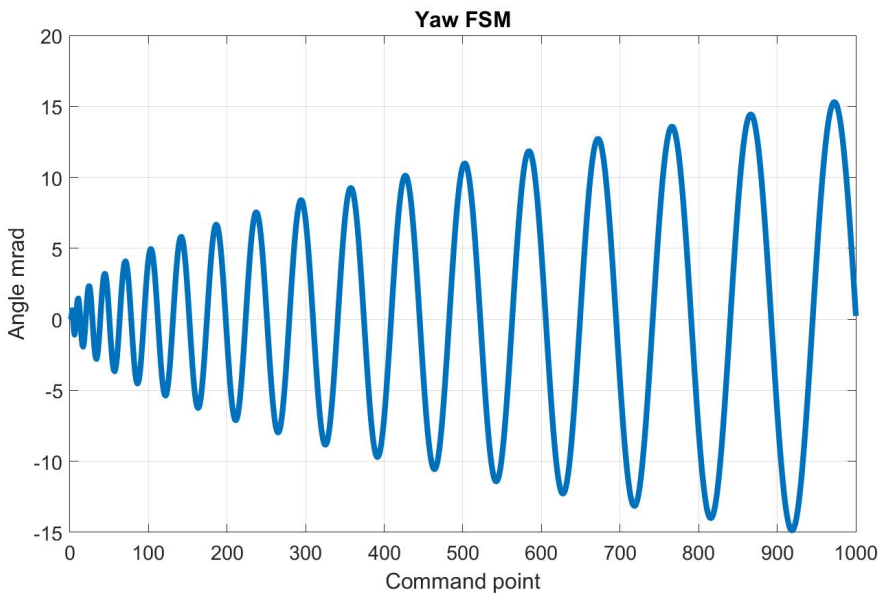**Figure 4.24:** Objective function evaluations for the spiral scan.

Figure 4.26: FSM yaw commands to generate the spiral scan.

It can be noticed from the FSM commands that the maximum angular excursion on the pitch is greater than on the yaw and the ratio between them is around $\sqrt{2}$. This is due to the initial orientation of the FSM with respect to the incident beam, being at an angle of 45°, and the law of reflection shown in Equation 4.3:

$$\vec{r} = \vec{i} + 2(\vec{n} \cdot (-\vec{i}))\vec{i} \,. \tag{4.3}$$

The resulting commands, shown in Figures 4.25 and 4.26, have then been used to generate a simulated acquisition procedure with the ray-tracing tool, without giving any offsets to the Hexapod, to better visualize the scanning procedure and the result of the commanded scan. Figure 4.27 displays the result of the ray tracing simulation with all the 1000 points of the spiral scan simulated, to gain a better understanding of the dynamics of the scan.
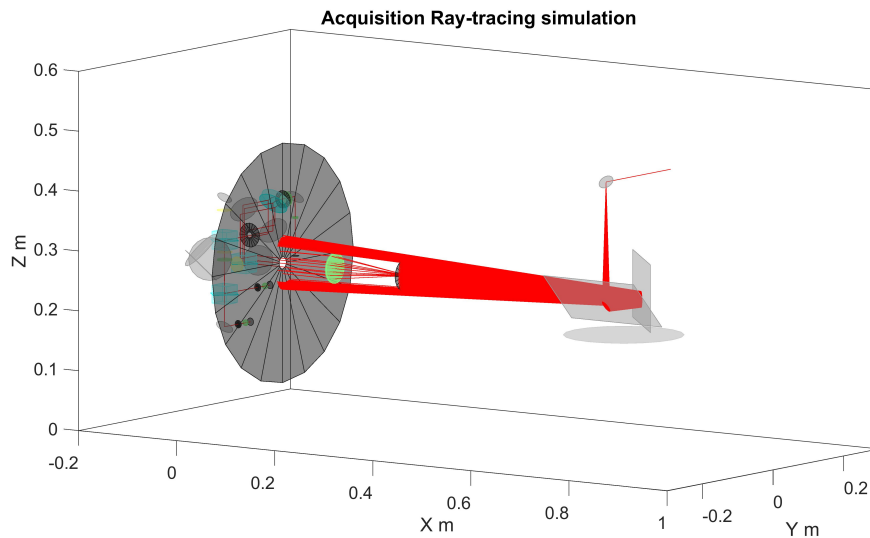
Figure 4.27: Ray tracing simulation of the spiral scan.

It is clearly visible that only a portion of the rays make it through the field stop after the first lens, and of the rays that make it past the field stop, and even smaller portion can enter the OMT with the correct angle in order for the detection on the acquisition sensor to occur.

Initial conditions

The initial conditions are defined as offsets between the Line-of-sight and the optical axes of the two terminals, which then translate into static commands to the Hexapod, as shown in Figure 4.20. The choice of initial conditions is important as it directly affects the results of the acquisition tests and the relevance of them, when comparing the experimental results with the expected outcomes.

For this test 5 different initial conditions have been used, and the values for the in-plane and out-of-plane angles of the two terminals' optical axes with respect to the line-of-sight are summarized in Table 4.5, where I-P stands for In Plane and refers to the in-plane angle between the terminal and the line-of-sight, while O-P stands for Out Plane and refers to the out-of-plane angle between the terminal and the line-of-sight. The S/C 1 is identified as the OMT, while the S/C 2 is the IFO assembly. The offsets have been chosen within the range used for the calibration of the acquisition sensor, to ensure that the beams could be correctly detected.

Initial condition	I-P S/C 1 mrad	O-P S/C 1 mrad	I-P S/C 2 mrad	O-P S/C 2 mrad
1	3	0	3	0
2	0	3	1	3
3	2	10	2	10
4	0	-15	0	-15
5	0	5	0	5

Table 4.5: Initial conditions for spiral scan test.

For each of the initial conditions sets shown in Table 4.5, the corresponding ensemble of commands for the Hexapod has been generated using an optimization routine in the ray-tracing tool.

One final element to include in the initial conditions is the offset in frequency to give to one of the two laser beams with respect to the other. As previously stated in the first paragraphs of this section, the frequency scan has not been included in the acquisition procedure, but there still needs to be a slight difference in the frequencies of the two beams in order to have heterodyne interference on the QPD and measure the beat note (and it is phase) for DWS control, exactly in the same way as it was already

done for the calibration. The offset is provided with the AOM, one of the two AOMs is set to 80 MHz, while the other is set at 80.01 MHz.

Finally, the power of the laser beams when they leave each of the terminals (in the inter-spacecraft section of the setup, where the lens system is located) is 280 μW for the laser from the OMT and 190 μW for the laser from the IFO. The power of the lasers is not representative of real world scenarios, but it has not been considered in these first steps of the project.

5

Results

In Chapter 4 the methodology of the thesis was outlined, with the various actions and procedures defined to achieve the goals set in Section 1.3 and to be able to answer the research questions in this final Results chapter.

The first research question concerns the recreation of link acquisition conditions in the lab. In order to recreate the conditions, the OFMT setup had to be assembled and aligned, as described in Section 4.1; once the setup was completed, the measurements of the relevant beam parameters (wavefront quality, polarization, diameter) became possible, and the results are shown in Section 5.1. In the second part of the section the effects of temperature changes on the acquisition sensor are evaluated, to determine whether they could represent a problem for the acquisition tests, while in the final part of the section the beam quality and characteristics measured in the OFMT setup have been compared to those achieved in the other architectures introduced in Section 3.3. In order to fully answer the first research question, the relative alignment of the OFMT elements needed to be evaluated; in Section 5.2.4, the results of the acquisition tests are compared with the expected outcomes to verify this aspect.

The second research question focuses on the ability of the OFMT to perform link acquisition strategies and procedures. The necessary steps and operations to allow the OFMT to perform link acquisition tests have been described in Sections 4.2, 4.3, 4.4 and 4.5. The results of the link acquisitions performed is shown in Section 5.2, to demonstrate the setup's ability to perform autonomous acquisition procedures and evaluate the results of the acquisition tests.

The final research question aims at determining which parameters are most relevant to the link acquisition for the OFMT and which requirements the initial link acquisition procedure poses on the OFMT architecture. The necessary information to answer the research question and achieve the goals defined were gathered throughout the whole project work, from the assembly and alignment, to the calibration, the creation of the support infrastructure with the control system, the definition of the acquisition tests, the measurements of the beam parameters and finally the execution of the link acquisition experiments. The insights obtained from all of these activities have been described in Section 5.3, divided into three different parts: the necessary hardware elements to be included in OFMT-like architecture to successfully carry out link acquisitions, followed by the improvements on the assembly and alignment steps, and the components that could improve the quality of the link acquisitions and finally requirements on the link acquisition strategies and procedures based on the results obtained in the experimental test runs.

5.1. Setup alignment results

During the assembly of the OFMT experimental setup, alignment test and procedures have been carried out to ensure the correct placement of the components and the desired quality of the beam coming from the interferometer, and to answer the first research question concerning the beam quality achieved and the ability of the setup to recreate realistic conditions for the incoming beam in the OMT. One important aspect to note regarding the OFMT setup, which sets it apart from most other optical setups

and experiments, is that the absolute alignment with respect to an absolute laboratory reference frame is of marginal importance, or at least the fine alignment of the components with respect to an external, laboratory reference frame is not crucial to achieve an optimal experimental outcome. This aspect was already introduced and discussed in Section 4.3, but it is reiterated here. What is more important for the link acquisition experiments to be performed is the relative alignment between the two terminals and the alignment of the line-of-sight. The relative alignment can be adjusted by means of static offsets from the Hexapod and the fast steering mirrors. The better the alignment, the smaller the static offset required, but as long as the static offets do not interfere with the instruments range needed to run the desired experiments, achieving a very fine alignment is not necessary.

One attribute which is also affected by the assembly of the setup and is instead of great importance for the validity of the experimental results is the beam quality, to be assessed by evaluating a number of characteristics of the beam received by the OMT from the interferometer. The beam properties evaluated are the following: the wavefront, the beam diameter and the polarization of the beam. The intensity of the beam is not evaluated as a performance parameter; it is still part of the definition of the experiments, since the appropriate beam power needs to be provided to the AOMs in order to achieve a successful beat note detection, but the power of the beam in the OFMT link acquisition is not reproduced to match the one found in space applications and the attention is instead focused on other properties. A further aspect is monitored in the setup: the effect that temperature changes have on the beam position measured on the acquisition detector, as they might introduce shifts and unwanted beam wandering. Assessing the effect of temperature differences on the acquisition is therefore essential.

5.1.1. Wavefront quality

The quality of the wavefront that reaches the OMT was evaluated using the Shack-Hartmann sensor. The sensor was used for the alignment itself, and then the wavefront was measured to assess the wavefront error (WFE) at the end of the alignment process, after the beam had been reflected by the fast steering mirror, the two mirrors on the Hexapod, and had gone through the lens system. The goal for the WFE to be achieved was set at $\lambda/30$, because it is the lowest reasonable value that can be obtained with the non-customized lenses that make up the lens system, and obtaining a greater quality while using the mirrors recycled from the projector is almost impossible. A wavefront quality of $\lambda/30$ is not a detrimental result though, and it is also the value that was achieved by the other experimental setups presented in Section 3.3 [24]. The wavefront of the beam is depicted in Figures 5.1a and 5.1b. There is a slight tilt in the wavefront but it can still reach a very decent wavefront quality, with a RMS error of 0,0256, which is below the defined threshold of $\lambda/30$. The adjustment of the lens system needed to achieve this result has been described in Section 4.1.2.
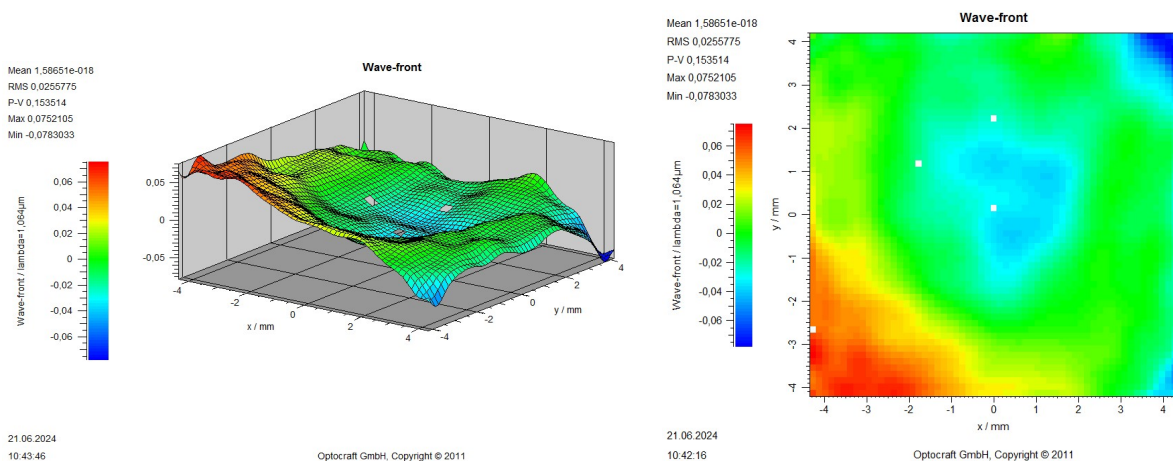
(a) 3D plot of the wavefront.

(b) Color map representing the wavefront.

Figure 5.1: Wavefront quality of the beam measured with the Shack-Hartmann sensor.

The quality of the wavefront and the aberrations and errors which contribute the most to the imperfect beam quality can be easily evaluated by looking at the Zernike polynomials that have the greatest influence on the overall wavefront error. The Zernike polynomials have been introduced in Section

2.1.4, and the values of the Zernike polynomials that describe the wavefront shown in Figures 5.1a and 5.1b are depicted in Figure 5.2. The highest coefficients are 1,2,3 and 5, which are the vertical and horizontal tilts, the defocus and then astigmatism (first order), respectively. The compensation of the single components of the wavefront error, identified through the Zernike polynomials, is performed iteratively as described in Section 4.1.2, but adjusting one component could negatively affect another one. When the overall wavefront error is below the desired target value, the alignment can be considered completed and the beam quality is then sufficient.
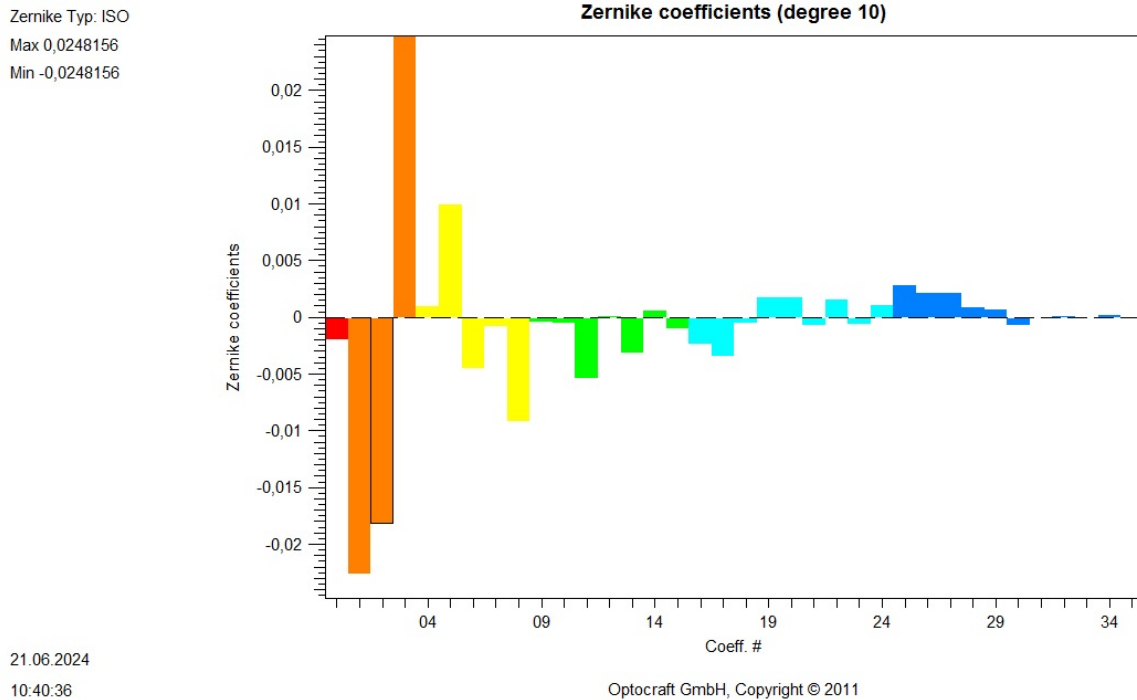

Figure 5.2: Zernike polynomials describing the incoming beam in the OMT.

5.1.2. Polarization of the beams

Another important parameter that needs to be checked in order to evaluate the quality of the assembly and alignment of the setup is the polarization of the beams, considering that the setup consists of an on-axis layout, meaning that the separation of the beams is performed by means of different polarization states. Having the wrong polarization in the beams could then render the instrument ineffective and it could hinder the ability of the OMT of keeping the beams separated when they should not be interfering.

It was explained in Section 3.4 that the polarization of the beams in between the two terminals is circular, with one beam having a right circular polarization and the other having a left circular polarization state. The beams are then converted to linear (vertical and horizontal) polarization states when entering the terminals using waveplates. When discussing the lens system assembly it was mentioned that a $\lambda/4$ waveplate was introduced between the aspheric lens and the Hexapod, to convert the beam coming from the IFO from linear to circular polarization, and the beam coming from the OMT from circular to linear.

The polarization of the beam was then measured between the aspheric lens and the Hexapod, where the beams have the smallest diameter, making it easier to correctly measure the polarization state. A perfect degree of polarization is not expected from the beams, considering the many elements with which the beams interact, and their quality in maintaining the polarization, but it should still be good enough so that when the beams are separated by the PBS in the OMT, enough beam power can still get to the detectors.

The results of the polarization measurements have been summarized in Table 5.1, where with IFO and OMT are indicated the beam coming from the IFO and from the OMT respectively, and DOP stands for

degree of polarization. The polarization angle is instead defined as the azimuth angle.

Beam	Polarization angle (°)	DOP
IFO	89.596	$\approx 82.1\%$
OMT	2.080	$\approx 85.7\%$

Table 5.1: Polarization measurement results for the IFO and OMT beams.

The graphical representation of the results through the Poincaré sphere and the ellipse diagram are shown in Figures 5.3a and 5.3b respectively, while the same results for the OMT beam are shown in Figures 5.4a and 5.4b.
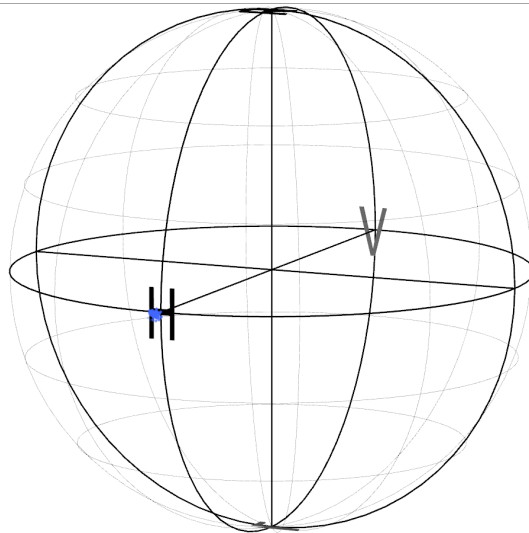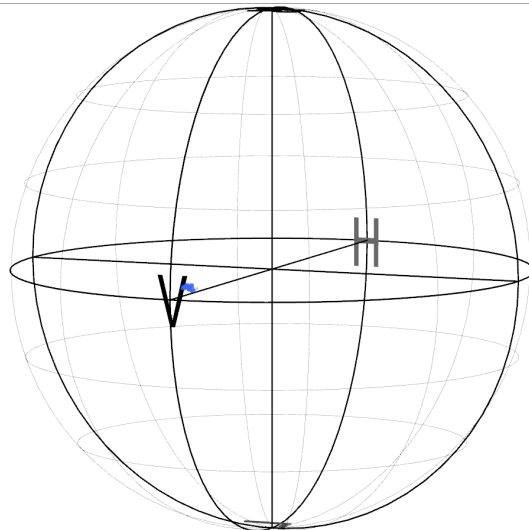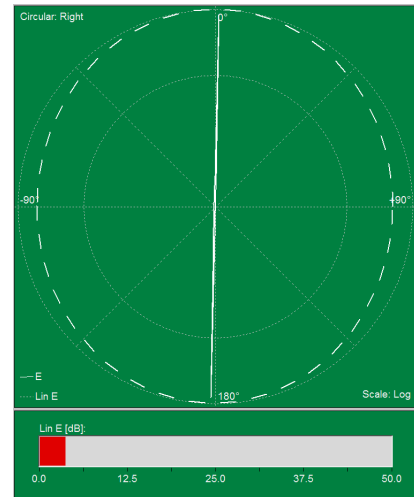

(a) Poincaré sphere for the IFO beam.
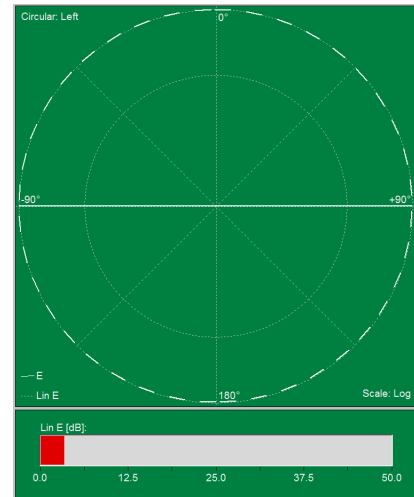
(b) Ellipse diagram representation for the IFO beam.

Figure 5.3: Polarization measurements for the IFO beam.

(a) Poincaré sphere for the OMT beam.

(b) Ellipse diagram representation for the OMT beam.

Figure 5.4: Polarization measurements for the OMT beam.

The results show that the degree of polarization is satisfactory through the setup, the polarization state is more or less correctly maintained and the polarization orientation of the two beams are orthogonal enough so that beam interference causes no significant problems for the link acquisition procedures.

5.1.3. Beam diameter

The main objective of the lens system is to simulate a distance between the two terminals significantly larger than what can be achieved in the lab, while recreating the beam characteristics a the OMT entrance aperture; this means that the enlargement of the beam, evaluated through the beam diameter, is a very important parameter when evaluating the results of the alignment procedure. The lens system has been designed to achieve a magnifying ratio of 10, with the beam going into the OMT being 10 times larger than when it leaves the IFO. The size of the beam has been evaluated using a camera, measuring the beam size before and after the lens system.

The measurements of the beam performed with the camera before and after the lens system are shown in Figures 5.5 and 5.6 respectively.
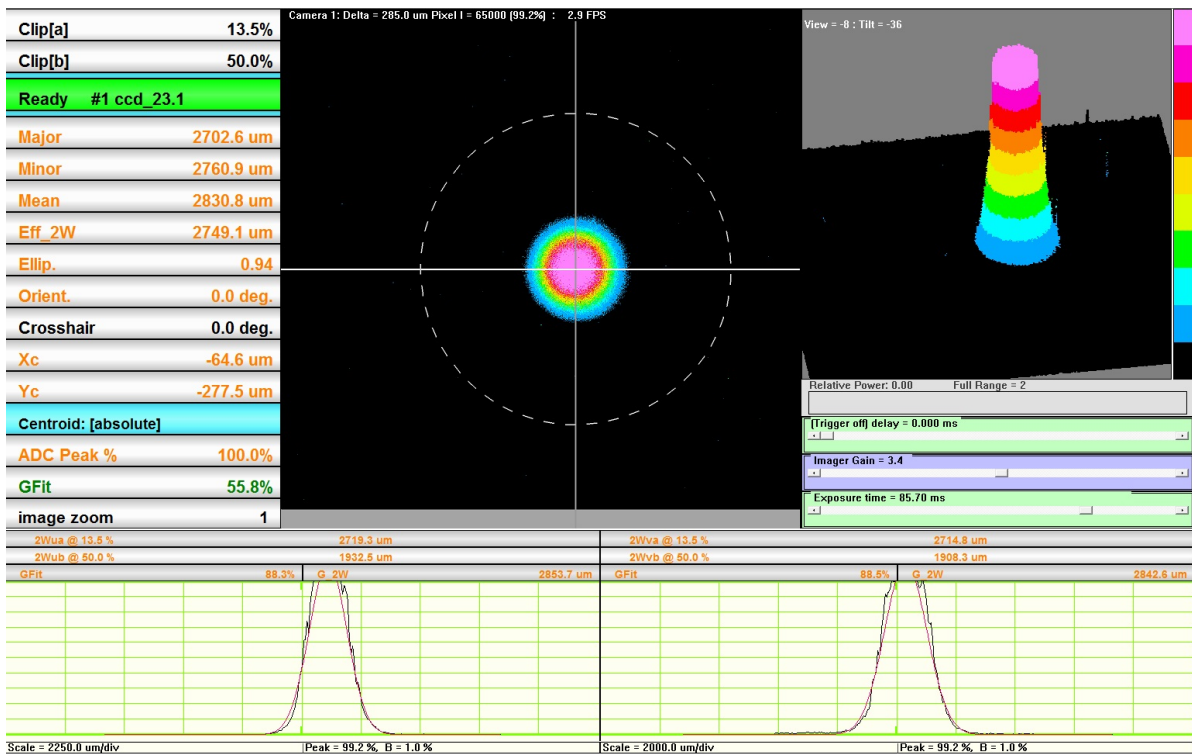

Figure 5.5: Beam dimension before the lens system.

The first detail that can be noticed when looking at the images is that before the lens system, in Figure 5.5, the beam intensity saturates the camera sensor (the ADC Peak % value is 100), the beam is clearly defined and easily recognizable, while after the lens system, in Figure 5.6, due to the magnification of the lenses, the beam is not clearly defined and it is spread out over the whole detector, with a considerably lower peak intensity (the ADC Peak % value is 16.7). It is still possible to identify the centre of the beam after the lens system, in the light blue area, not precisely centered on the detector, with the rest of the beam in a progressively darker blue tone (in Figure 5.6) that covers the whole detector space, being evidently clipped at the edges of the camera aperture. The camera is therefore too small to capture the whole beam, as can be seen from the profile diagram, but it can still receive enough light to reconstruct the beam intensity curve for the purposes of this work.

The parameters of interest for the evaluation of the lens system's performance are the beam diameter ratio between the two sides of the lens system, and the change in shape of the beam intensity profile. The shape of the beam on the Hexapod side of the lens system has a clear Gaussian intensity profile, with a strong concentration of the beam intensity in a small area. On the other side of the lens system, following the beam magnification, the beam intensity profile is considerably shallower and spread over the beam area to simulate a large distance between the terminals, where the beam can expand and change its intensity profile from a Gaussian shape, closer to a spherical front, which when clipped in a small area can be approximated by a flat intensity profile.
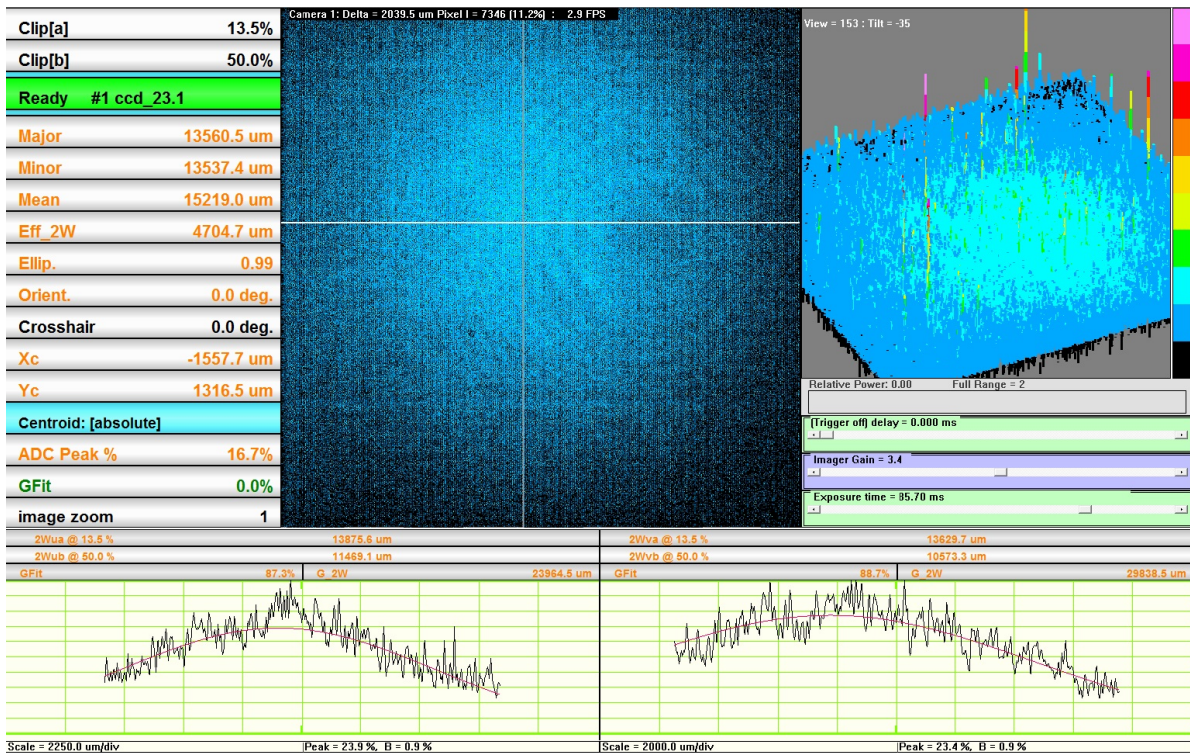
Figure 5.6: Beam dimension after the lens system.

The intensity profile of the beams before and after the lens system are shown at the bottom of Figures 5.5 and 5.6 respectively, where the less pronounced Gaussian profile after the lens system is clearly visible, even though it gets clipped by the limited aperture of the camera.

The reconstructed beam diameter for the beam measured before the lens system is 2.84 mm approximately, while after the lens system the reconstructed and fitted beam shape has a diameter of roughly 29.8 mm. These measurements have to be considered with caution, because the reconstruction of the beam due to the limited camera aperture cannot ensure an entirely accurate estimation of the beam diameter; furthermore, the intensity after the beam enlargement becomes increasingly lower towards the edges of the beam, making it fade into the background noise, rendering the calculation of the beam dimension less precise.

Even after taking into consideration all of the precautions needed when evaluating the results, it is still possible to conclude that the beam has successfully been magnified by a factor of ≈ 10, and the shape of the intensity profile is considerably flatter than the sharp Gaussian beam coming from the IFO, making it more realistic and closer to what can be found in space.

5.1.4. Temperature effects

During a round of calibration runs, a shift was noticed in the beam position on the detector while no command was provided. After an initial investigation it was decided to check whether the shift was due to temperature changes; therefore, the evolution of the temperature inside the box and on the acquisition sensor have been compared with the beam position on the detector. The tests have been conducted in different days and with different temperatures. It was immediately noticed that the temperature of the detector can change significantly (by a few degrees) when the camera is being used, as its electronics cause it to heat up, until it reaches a point of equilibrium where the temperature stops increasing and begins to stabilize around an almost constant value. The evolution of the temperature in time is shown in Figure 5.7. It can be seen that the temperature in the lab increases as well, due to the heat generated by the setup (and the people inside the lab), which can be attributed to the lack of an effective temperature regulation in the lab.

The temperature variations differ from day to day, depending on the daily conditions, time of day and
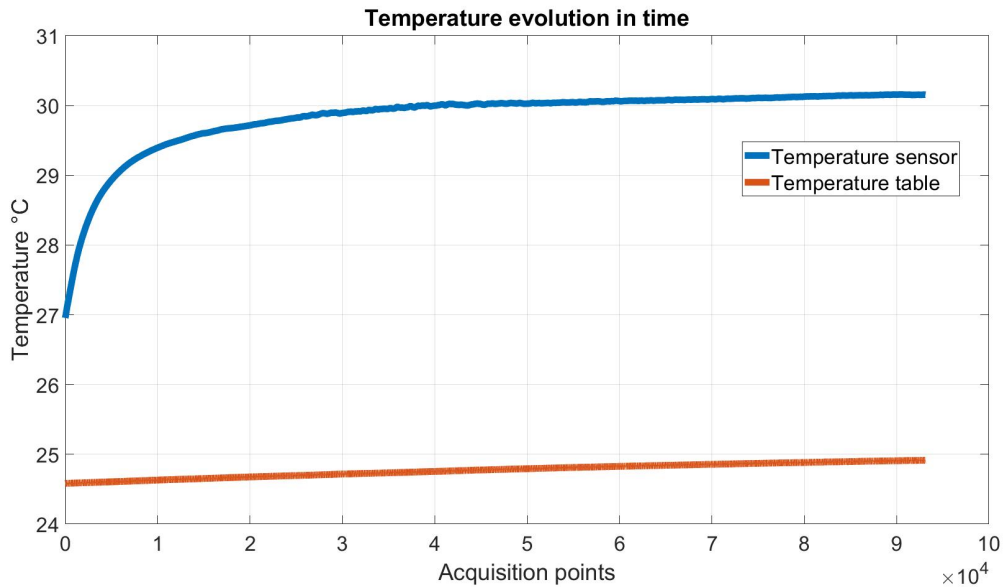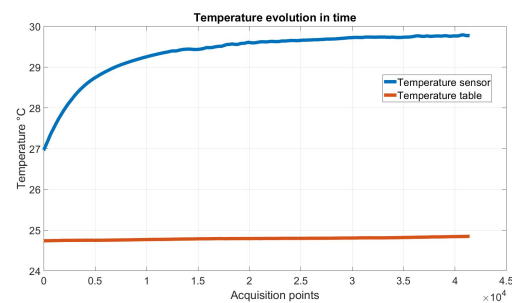
Figure 5.7: Evolution in time of the table and acquisition sensor temperatures on 29/09.

other activities being carried out in the building which drain the cool air for the temperature control of the lab. In Figures 5.8a and 5.8b are the evolutions of the temperatures for the 01/10 and the 02/10 respectively, showing how the values can differ by a few degrees. The difference in temperatures values reached is valid when compared to those measured on 29/09 in Figure 5.7 as well. The main factor that affects the temperature reached by the sensor seems to be the overall temperature of the lab, over which there is unfortunately little control.
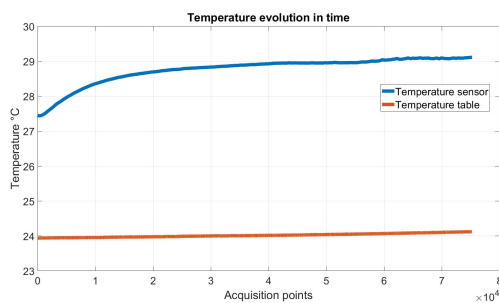
(a) Table and acquisition sensor temperatures evolution on 01/10.

(b) Table and acquisition sensor temperatures evolution on 02/10.

Figure 5.8: Comparison of table and acquisition temperatures evolution on 01/10 and 02/10.

Having assessed that the temperature in the lab and on the sensor changes in time, it is then necessary to evaluate whether there is a correlation between the temperature variations and other discrepancies that can be noticed in the setup. The position of the beam on the acquisition sensor was then monitored in time, finally comparing the change in position of the beam on the detector with the change in temperature of the detector.

Figure 5.9 displays the evolution of the position of the beam on the detector, starting from the start-up of the setup until a stable condition is reached. It is relevant to notice that the stabilization of the beam position on the detector corresponds to the stabilization of the detector temperature, shown in Figure 5.7, 5.8a and 5.8b.

To better understand if and how the temperature of the camera and the beam position measured are linked, the X and Y positions of the beam on the sensor are displayed against the temperature at which they have been recorded. In Figures 5.10a and 5.10b are the X and Y positions of the beam measured
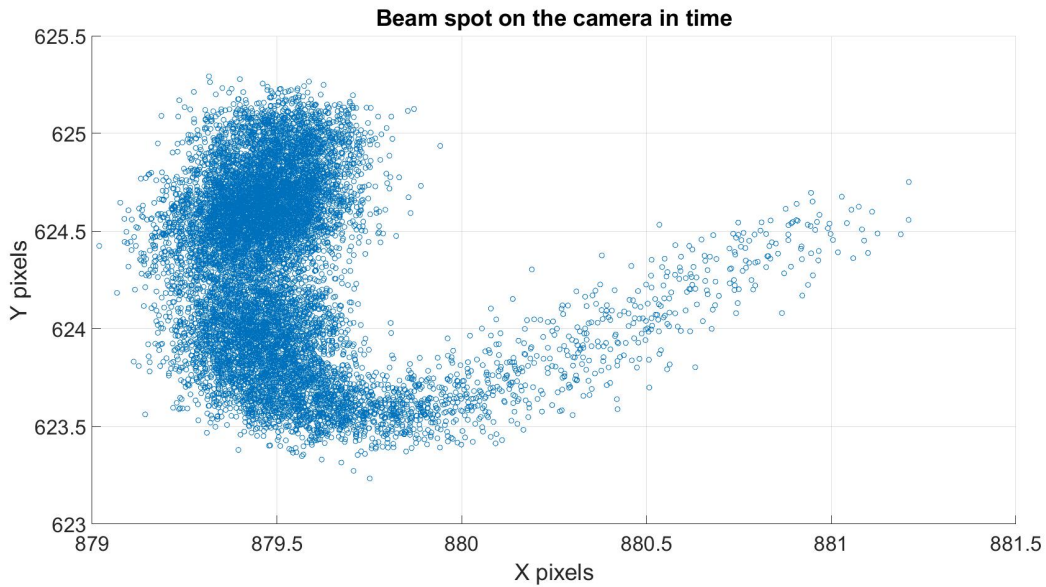
Figure 5.9: Evolution in time of beam position on the acquiistion sensor on 01/10.

on the sensor as its temperature changes. In both cases they form some sort of arch. Looking at the density of the points, it is clear that both the X and Y positions stabilize as the temperature reaches the highest values and stops increasing, showing that there probably is a link between the shift of the beam position and the temperature changes.
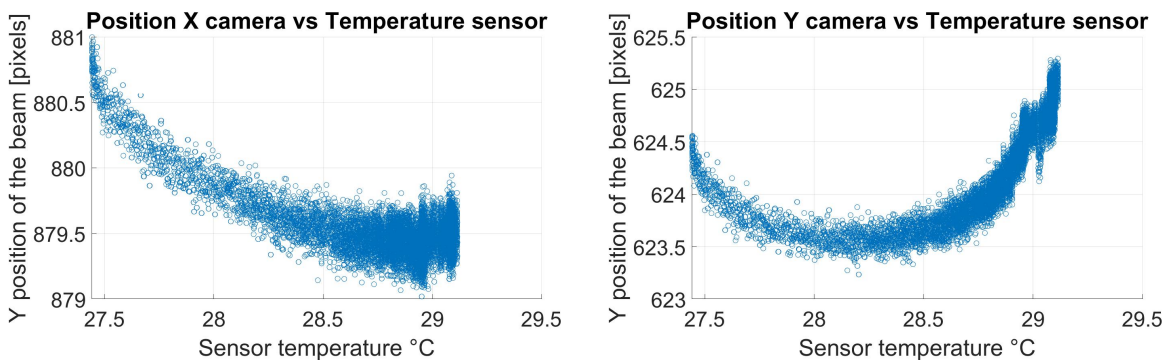
(a) X position of the beam measured for different temperatures of the camera on 01/10.

(b) Y position of the beam measured for different temperatures of the camera on 01/10.

Figure 5.10: X and Y beam positions for different acquisition sensor temperatures.

A similar behavior to the one noticed in the test on the 01/10 has been noticed on the other two tests. As an example the results of the 02/10 have been compared to the results recorded on the 01/10 in Figure 5.11. The exact movement of the beam position is different but the trend seems similar, with a sharper increase of the Y value in the test conducted on 02/10. It is important to notice that the absolute differences between the two test results are in the order of one pixel or less, which is a very small variation considering the effective displacement of the beam position on the detector during operational scenarios.

Since different temperatures have been recorded for the acquisition sensor during the two tests, the beam positions for the two tests have been evaluated accompanied by the temperatures at which they have been recorded. In Figure 5.12 the Y positions of the beam on the detector measured on 01/10 and 02/10 have been compared, considering the temperature at which they have been measured as well. The shapes of the spot evolution differ a bit but the dynamics of such a complex system like the OFMT setup are difficult to predict and the detector itself is made up of different materials, between
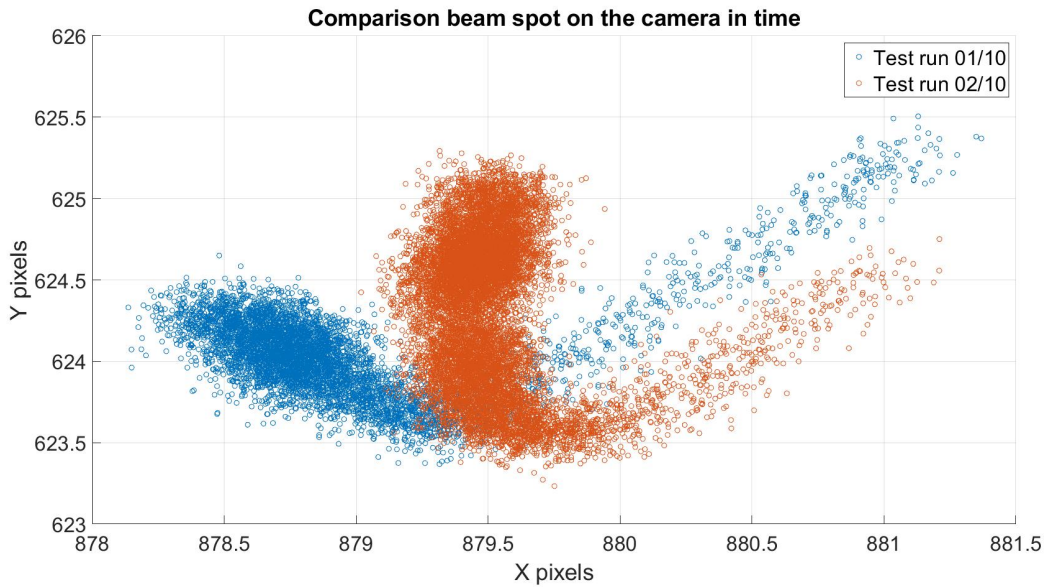
Figure 5.11: Comparison of beam position on camera on 01/10 and 02/10.

the mounting plate, the electronics and the camera itself, which possess different thermal expansion coefficients and probably respond differently to stresses caused by different thermal expansions. One additional element that can introduce uncertainties and nonlinearities in the evolution of the system is the way in which the sensor plate is mounted to its support on the OFTM Zerodur plate, which is done by using two bolts on one side of the plate, with the opposite side being unconstrained.
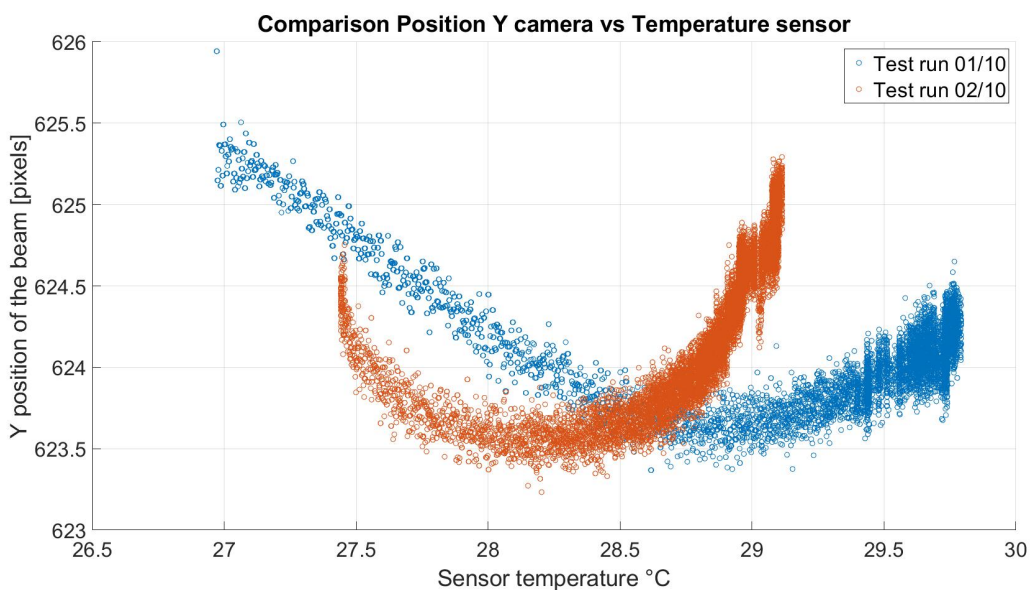

Figure 5.12: Comparison between the Y position of the beam measured on the detector and its temperature for the tests on 01/10 and 02/10.

A similar pattern is noticed in the test performed on 29/09, which is compared with the results of the 01/10 test in terms of Y position on the detector against its temperature in Figure 5.13. The trends for the two tests are more similar in this case, with the test performed on 29/09 showing a larger temperature range and a larger Y position excursion of the beam as a result.

From the results shown in this section it can be concluded that temperature changes in the lab and in the acquisition sensor affect the beam position on the detector, which stabilizes when the temper-
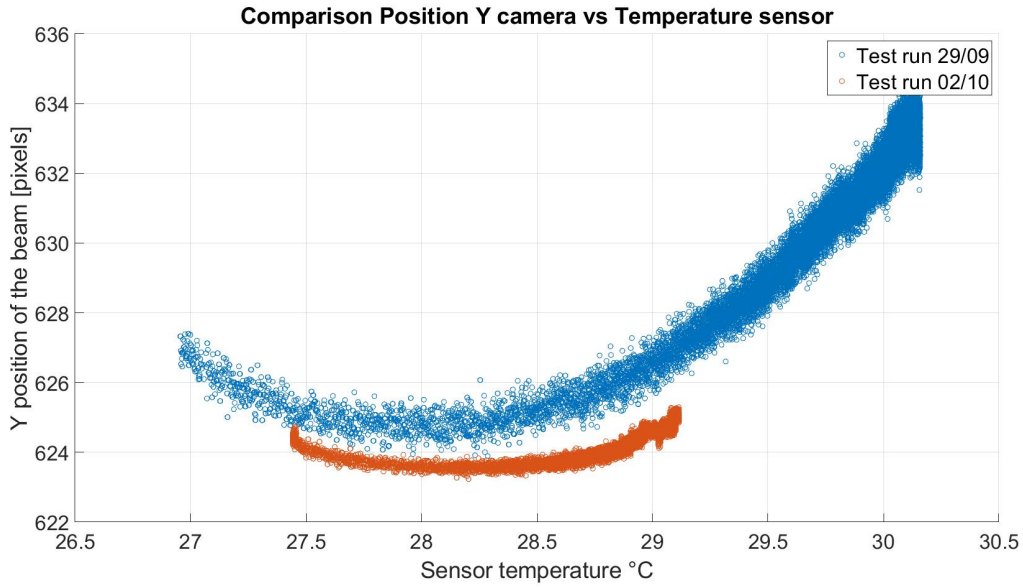
Figure 5.13: Comparison between the Y position of the beam measured on the detector and its temperature for the tests on 01/10 and 29/09.

ature does as well. The behavior of the components with temperature changes is difficult to predict and definitely nonlinear, but the correct prediction of these phenomena is not necessary to achieve a successful experimental result for the acquisition, because the changes in beam position due to temperature changes are still minute when compared to the complete detector surface. To put the shift into perspective, the same graph of the shift displayed in Figure 5.9 has been represented in Figure 5.14 again but extending the plot to the whole detector area.
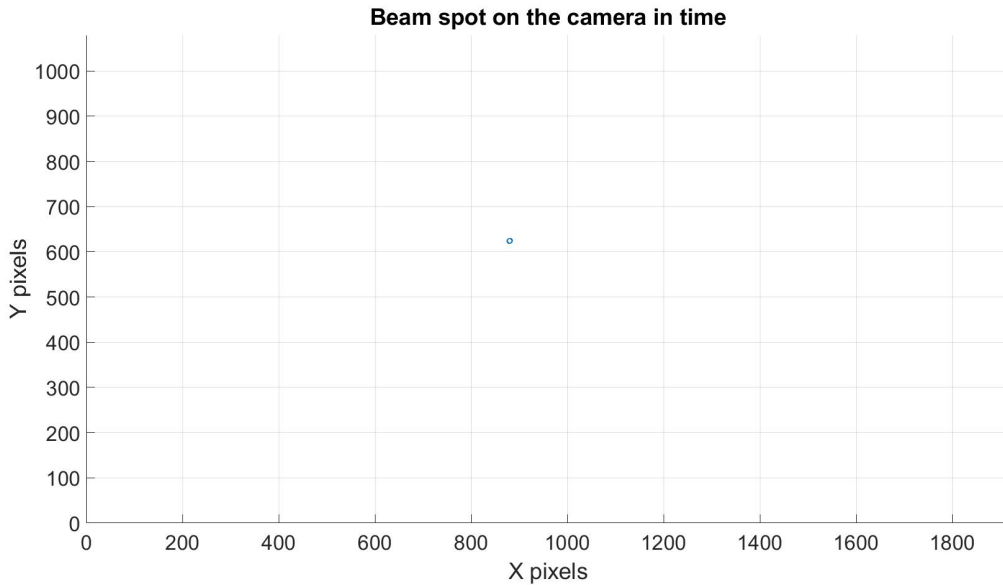
Figure 5.14: Camera position evolution on 01/10 plotting the whole detector area.

Even though the effect of the temperature on the beam position might not be hindering the effectiveness of the acquisition tests, it is still important to take note of it and consider the consequence that temperature-connected variations could have in other activities and applications that could involve the OFMT. These results also highlight the need for a better thermal management of the experimental environment, which is fundamental for performing highly precise optical metrology experiments.

5.1.5. Comparison with other link acquisition setups

The quality and characteristics of the incoming beam in the OMT have been described in the previous sections, and in order to understand how accurate the recreation of beam parameters that can emulate the situation found in space has been, the results are confronted with those obtained in the other link acquisition setups mentioned in Section 3.3. The main parameters that can be used to compare the various architectures with regards to the beam simulation are the following: the received beam diameter, the received beam shape (in the form of the m_{flat} parameter, defined in Section 3.3.3), the distance simulated and whether the beam is fiber coupled or transmitted through free-space. The beam intensity is not important for the specific type of tests being carried out with the OFMT and it is therefore not considered in the comparison, while the wavefront error in the received beam for the other link acquisition setups is between $\lambda/26$ and $\lambda/30$ [24], which is in line with the wavefront quality results achieved in this work (the wavefront error achieved in Section 5.1.1 is actually smaller).

The values for the variables considered are presented in Table 5.2 for every setup. F-S/F-C stand for Free Space or Fiber Coupled to indicate whether the setup employs a free space or a fiber coupled configuration, the second element displayed is the simulated distance between the terminals, and the diameter is meant as the diameter at the receiving aperture. The setup referred to as Taiji is the one described in Section 3.3.3, while the one called "Small Taiji" is the architecture analyzed in Section 3.3.4. The Wuchenich setup has not been included because there is fewer information available and it is redundant when the LLS and Fiber OGSE setups are included in the comparison, due to the similarities between the architectures. With regards to the beam diameter, the OFMT presents the largest beam diameter out of the free space setups, and it is not too distant from the fiber coupled architectures, while for the recreation of the flat top properties, in terms of beam shape, it is bested only by the Taiji link acquisition simulator, which achieves a higher m_{flat} factor due to a considerably smaller entrance aperture, which on the other hand puts limitations on the detectable scanning range. It is important to note that even though the beam properties presented in the table for the OFMT setup are for some areas better than those of other experimental architectures previously developed, the recreation of the beam is still far from realistic, but this result was expected, and successfully recreating all the properties of the beam in space is impossible, due to the distance needed between the terminals, which cannot be recreated on ground.

Setup	F-S/F-C	Distance (m)	Diameter (mm)	m_{flat}
Fiber OGSE	F-C	40	32	2.003
LLS	F-C	-	40	-
Taiji	F-S	10	13	13
Small Taiji	F-S	1.5	2.52	3.2
OFMT	F-S	100	29.8	3.768

Table 5.2: Comparison of relevant setup parameters for the recreation of the beam characteristics between different link acqusition architectures [24, 17, 16, 34].

The parameters for the LLS are similar to the Fiber OGSE and they can recreate the received beams in a very similar way. The first considerations that can be made are about the free space or fiber coupled configurations. A fiber coupled configuration is easier to implement and less prone to distorsions and errors due to the air medium, but it does not allow to maintain the pathlength information, meaning that the setup cannot be used to perform accurate displacement measurements between the terminals. On the other hand, a free space setup is more complex in its implementation and more delicate with regards to beam degradation due to air fluctuations and interaction with other elements, but it allows to maintain the pathlength information and perform displacement measurements. For what concerns the distance simulated between the terminals, the OFMT can simulate by far the largest distance, thanks to its lens system placed in the beam path. On the other hand, one of the main disadvantages of the OFMT setup is its inability to recreate a spherical wavefront, due to the collimated nature of the beam entering the OMT. This limitation is due to the necessity of having reasonable beam properties on the Hexapod side of the lens system for the beam being generated in the OMT and going through the lens system in the opposite direction with respect to the beam generated in the IFO.

In the end, it is possible to conclude that the OFMT setup represents a step into a previously unexplored direction, recreating a link acquisition setup in free space, which can therefore be used to

simulate complete inter-satellite laser ranging simulations, from link acquisition to accurate displacement measurement seamlessly in the same architecture, including an on-axis layout for the received and transmitted beams. While doing so it implements a new lens system architecture which allows to achieve free-space simulations with 100 meters separation between the spacecraft in a relatively small laboratory environment, ensuring an adequate simulation of the beam characteristics at the entrance aperture of the spacecraft and maintaining a low wavefront error in the received beam.

5.2. Acquisition tests results

This section represents a crucial part of the thesis as it demonstrates that all of the activities carried out up to this point led to the successful reproduction of autonomous link acquisitions, one of the main goals of the thesis and the objective of the second research question. The last part of the section tackles the critical analysis of the acquisition tests to evaluate the alignment accuracy achieved during the assembly of the setup.

The test runs were performed starting from 5 different initial offset positions, and for each position 4 scans have been performed: a scan with spiral arms separation factor of 1.3 (scan type 2 in Table 4.4) and one with factor 2 (scan type 3 in Table 4.4), with a "first detection scan" and a "full scan" for both.

Metrics for evaluation of the results

The main objective of the tests performed, as outlined in the Research Questions and thesis goals in Section 1.3 and reiterated previously, is the achievement of a stable laser link between the two terminals following a link acquisition procedure. The metrics used to analyse the results of the tests reflect this focus on the establishment of a laser link, and they have been identified in the detection on the acquisition sensor of the incoming beam, the successful engagement of DWS, and finally the voltages of the FSMs at the end of the acquisition procedure.

The detection of the beam on the acquisition sensor is a measure of the ability of the spatial scanning strategy to correctly cover the whole uncertainty space. If a detection does not occur throughout the scan, the spiral commands need to be re-evaluated. A successful detection does not imply a successful DWS engagement; the beam could be detected on the acquisition sensor with a poor beam quality that could then prevent DWS from engaging correctly. The FSMs voltages are instead analysed to evaluate the relative alignment of the two terminals, as the angles imposed by the steering mirrors on the beams should compensate the initial offsets generated with the Hexapod. The analysis of the alignment is performed in Section 5.2.4.

General overview of the results

The results for the "first detection scan" are summarized in Table 5.3, where "Detection" indicates whether the detection of the beam happened or not, and "DWS" indicates whether DWS has been successfully engaged. The other two columns diplay the voltage values of the FSMs when DWS has been engaged (if applicable).

Scan type	Initial Offset	Detection	FSM IFO (V)	FSM OMT (V)	DWS
2	1	YES	X:-0.215 Y:0.615	X:0.052 Y:0.19	YES
3	1	NO	-	-	NO
2	2	YES	X:0.548 Y:-0.06	X:0.058 Y:0.284	YES
3	2	YES	X:0.371 Y:-0.168	X:0.027 Y:0.276	YES
2	3	YES	X:1.773 Y:0.766	X:-0.18 Y:0.246	YES
3	3	YES	X:1.758 Y:0.818	X:-0.186 Y:0.245	NO
2	4	YES	X:-2.725 Y:-0.274	X:0.501 Y:0.268	YES
3	4	YES	X:-2.69 Y:-0.253	X:0.504 Y:0.268	YES
2	5	YES	X:0.838 Y:0.292	X:-0.03 Y:0.295	YES
3	5	YES	X:0.825 Y:0.303	X:-0.05 Y:0.283	YES
1	1	YES	-	-	NO

Table 5.3: Results of "first detection scan" acquisition tests.

From the table it can immediately be noticed how almost all of the acquisition tests resulted in a successful DWS engagement, with the exception of the fast scan, analysed more in detail in Section 5.2.3, and the scan type 3 from initial offset 1. An unsuccessful acquisition with the scan type 3 was something to be expected, given that the larger distance between the spiral arms means that some sections of the uncertainty space might not be covered and the correct detection point might be missed, which is what happened in these cases.

Two out of the five initial offset scenarios are analysed more in detail, to provide an example of what kind of analysis can be performed on the data and what information can be extrapolated from the test

results. The comprehensive results for all the other tests is provided in Appendix B. Of the two initial conditions examined, one represents a scenario where the initial offset is very close to the LOS, and one where the pointing error is on the limit of the calibrated range.

It is important to stress the fact that the objective of the setup was the demonstration of link acquisition capabilities, with a focus on functionality rather than performance, given the fact that the main performance drivers of real space instrumentation, like beam power and stray-light, have not been considered in this first iteration of the system; furthermore, the environmental conditions affecting the experiment, like temperature and air distortions, make it impossible to effectively compare the results of the setup with those of real world systems, in terms of acquisition performance, at this stage of development.

5.2.1. Initial offset 2 results

The initial offset 2 was defined in Table 4.5, as an offset of 3 mrad in the out-of-plane angle between the optical axes of the two terminals and the LOS, and an additional 1 mrad offset of the optical axis generated in the IFO with respect to the LOS in the in-plane angle, with the angles defined on the Hexapod side of the lens system.

Expected result

To aid in visualizing the dynamics of the acquisition, the test has been simulated in the ray tracing tool, and the results viewed in the x-y plane are shown in Figure 5.15. From the picture it can be seen that the in-plane offset of the optical axis with respect to the line-of-sight causes the outer rays of the scan to miss even the field stop and to continue towards the OMT. The same behavior is identified in the out-of-plane angle, with Figure 5.16 showing the results of the ray tracing simulation in the x-z plane. The upper-most beams go past the entrance aperture, and a very small portion of the simulated beams can make it into the OMT, as can be visualized in Figure 5.17.
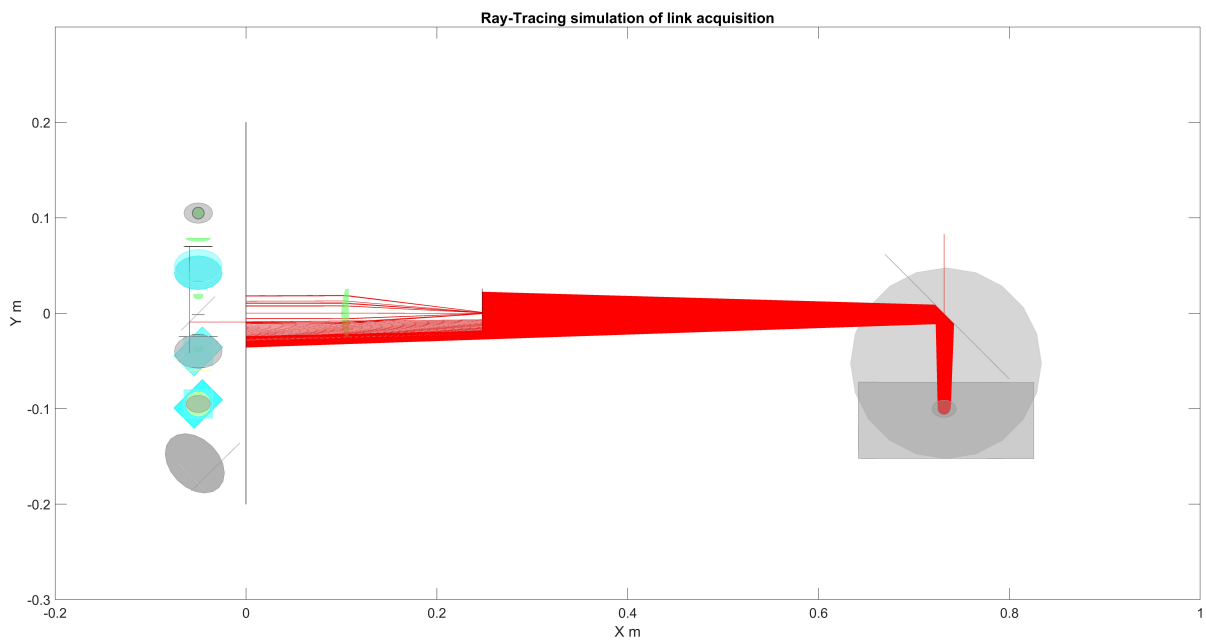

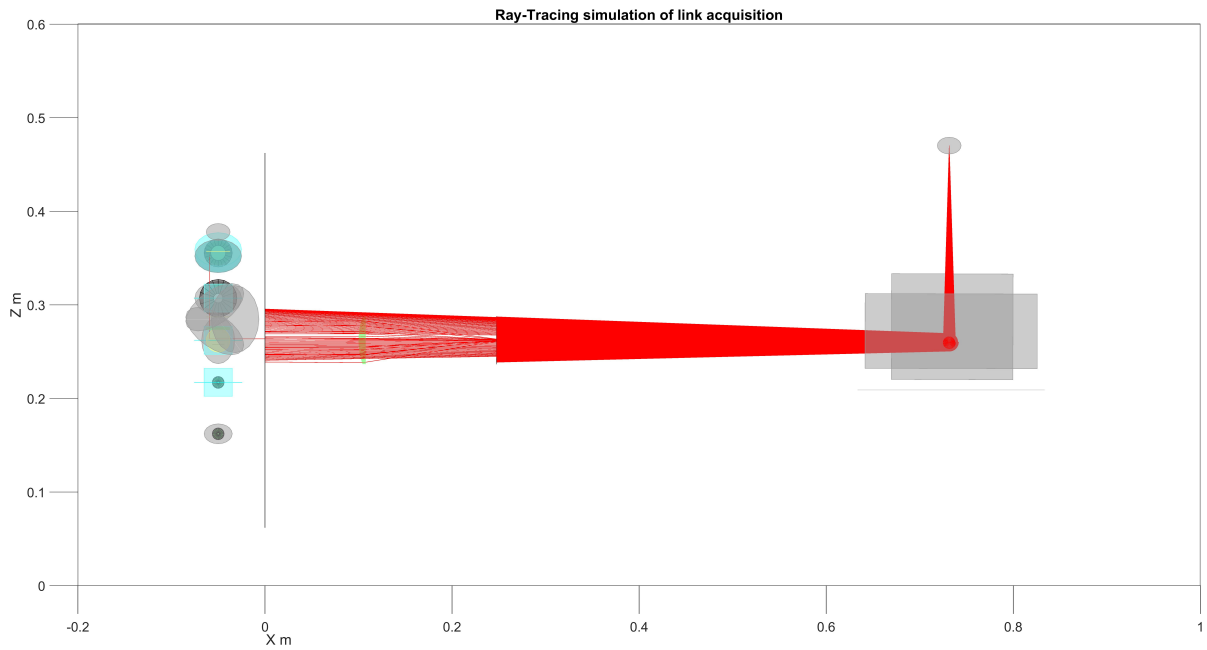**Figure 5.15:** Ray tracing simulation of the acquisition test with initial offset 1 in the x-y plane.

Figure 5.16: Ray tracing simulation of the acquisition test with initial offset 2 in the x-z plane.
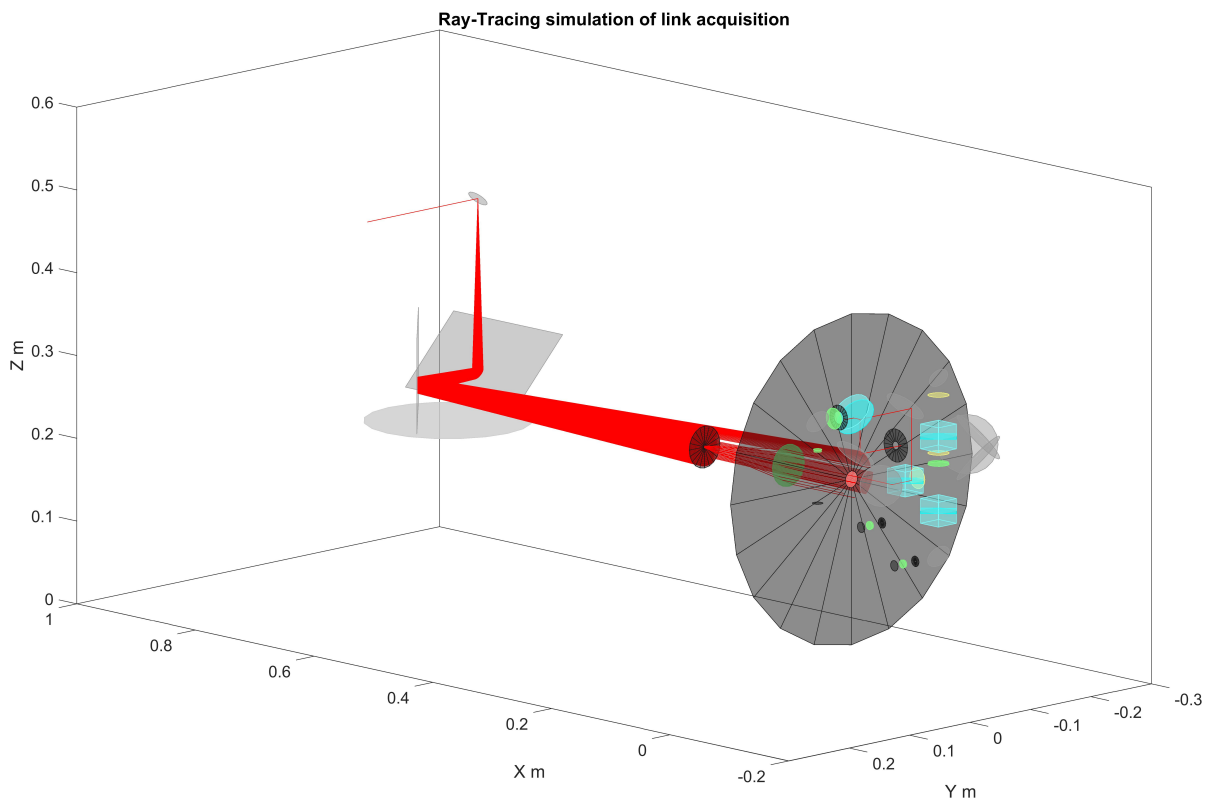

Figure 5.17: Ray tracing simulation of the acquisition test with initial offset 2 from behind the OMT.

From the simulations and the initial point of the scan, the detection of the beam is expected to happen within the first few spiral arms. The beams going past the field stop should not represent a problem as the acquisition sequence is expected to stop before the scan reaches the outer-most beams represented in the simulation. In the following paragraphs the data acquired during the experimental test are analysed in detail to evaluate whether the acquisition steps have been performed as expected.

Analysis of results

From Table 5.3 it can be seen that the beam has been detected and DWS has been engaged correctly, which means that the acquisition test was a success. When analysing the tests results in more detail, there are four different variables that can be evaluated: the position of the beam detection on the acquisition sensor, the evolution of the FSMs voltages throughout the procedure, the values of the beat note phase on the four quadrants of the QPD and the differences between them, and finally the beat note intensity on each of the QPD quadrants during the scan.

The first detection occurred at the position (X = 879; Y = 650) for the scan type 2, and at (X = 885; Y = 651) for the scan type 3. The difference in the position is due to the different distance between the spiral arms. Figures B.37 and 5.18b show the position of the beam detected on the acquisition sensor during the acquisition test. The initial "neutral" point is shown as well, this is the point where the beam is detected when no offset is applied to the Hexapod and the FSM.
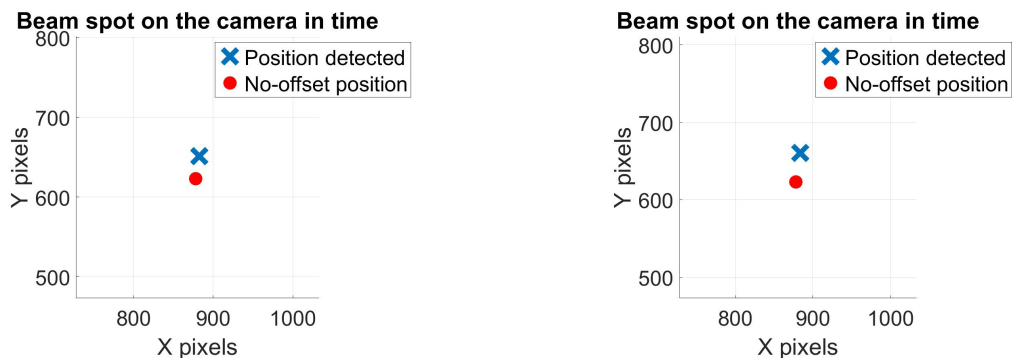
(a) Detection position on the detector for scan type 2 from the initial offset 2.

(b) Detection position on the detector for scan type 3 from the initial offset 2.

Figure 5.18: Beam position detected on the acquisition sensor for the scan types 2 and 3 starting from the initial offset 2.

The beam is detected with an offset on the Y axis of the detector, which indicates that it is entering the OMT with an out-of-plane angle with respect to the LOS, which matches the expectations. There should be no difference in the detection point between two beams coming from the same origin point at a determined initial offset, regardless of the point in the scan at which the detection occurs, due to the very large distance over which the acquisition procedure has to take place, as the beam wavefronts would be spherical, with the same centre for the curvature radius. In the OFMT experimental setup the distance is not in the order of hundreds of km, but it is "only" 100 meters, with an almost flat wavefront due to the collimated beam, meaning that beams coming from the same origin point but entering the OMT aperture in different points will still have different corresponding detection spots on the detector, as shown in Figures B.37 and 5.18b.

The next variables to be evaluated are the FSMs voltages through the acquisition tests. Figure 5.19 shows the evolution of the commands for the FSM over the Hexapod. As expected, the scanning procedure stops almost immediately, because of the small initial offsets with respect to the LOS, when compared to the spiral range of 30 mrad. When the beam is detected the scanning FSM is set to the values it had when the detection occurred, which in Figure 5.19 happens after around 2 seconds from the start of the acquisition procedure, and those values are then maintained until the end of the test. The same type of behavior is noticeable in the results for the FSM IFO with the scan type 3, with the main difference being that, due to the larger distance between the spiral arms, the acquisition point is reached faster than for the scan type 1, in around 1 second from the start of the scanning procedure.

The FSM in the OMT presents a different evolution in the acquisition scan. While the FSM over the Hexapod is performing the spiral, the FSM in the OMT is set to a neutral value, waiting for the acquisition sensor to detect the beam, at which point the FSM in the OMT is set to voltage values according to the point at which the detection occurred on the camera, based on the calibration laws obtained through the procedures outlined in Section 4.3. The FSM in the OMT therefore presents a step-like evolution, in which it stays at its initial value until the first detection, after which it has the first jump as it moves to the calibration setting, and it could have another step jump when DWS is engaged, depending on how
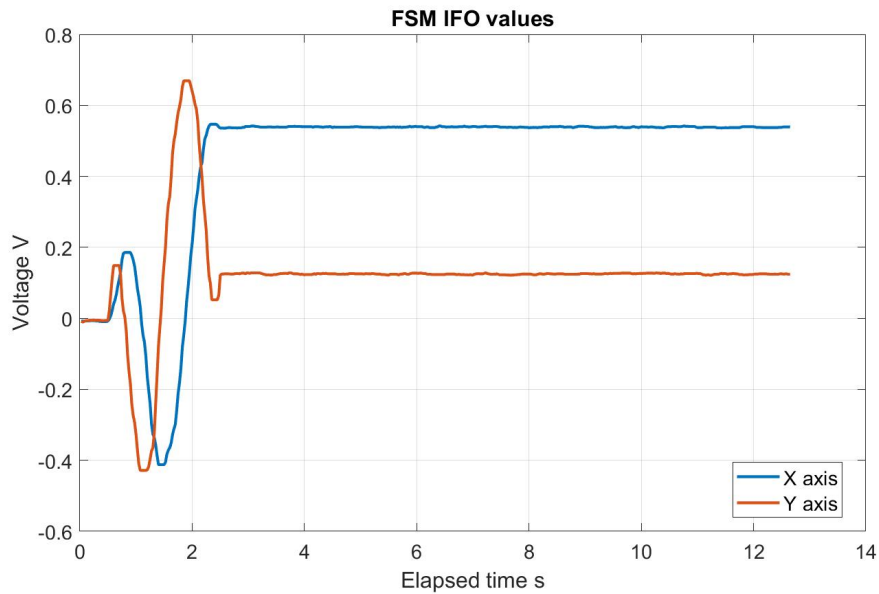
Figure 5.19: FSM over the Hexapod voltage values during the acquisition test for scan type 2 and initial offset 2.
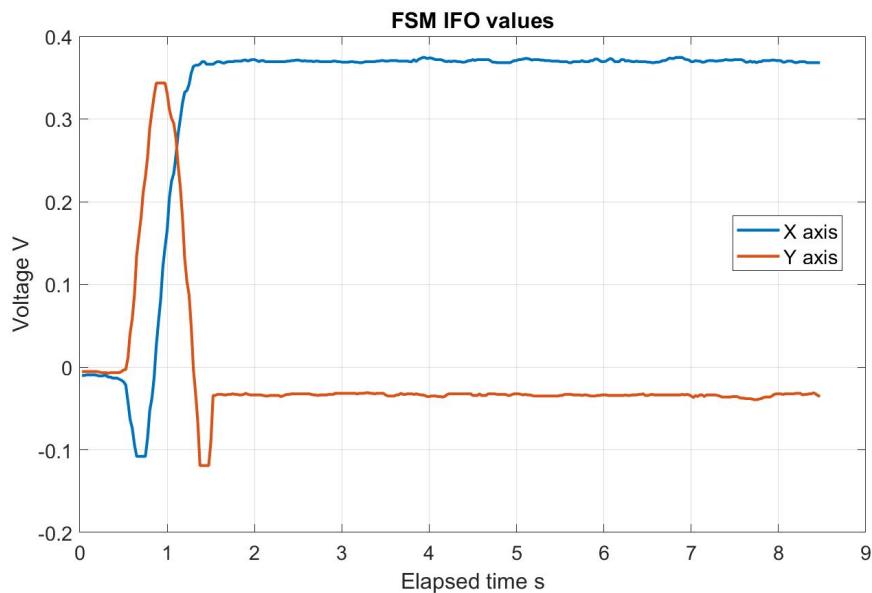

Figure 5.20: FSM over the Hexapod voltage values during the acquisition test for scan type 3 and initial offset 2.

far from the calibration value are the voltages commanded by the DWS control loop. In any case the difference rarely corresponds to jumps larger than about 130 μrad in angular deviation.

Figures 5.21 and 5.22 show the voltage values assigned to the FSM in the OMT during the acquisition procedure, the step behavior is clearly visible. In the test with the scan type 2, the FSM is first set according to calibration at the same time as the FSM over the Hexapod stops scanning, around 7.5 seconds after the start of the data collection (around 2 seconds after the start of the scan), and it then moves to the correct location according to DWS closed loop control. Once again the results for the scan type 3 follow the same evolution closely, with the only difference being that the acquisition is achieved earlier, and the voltage values differ because of the different points in which the FSMs stabilize for the detection.
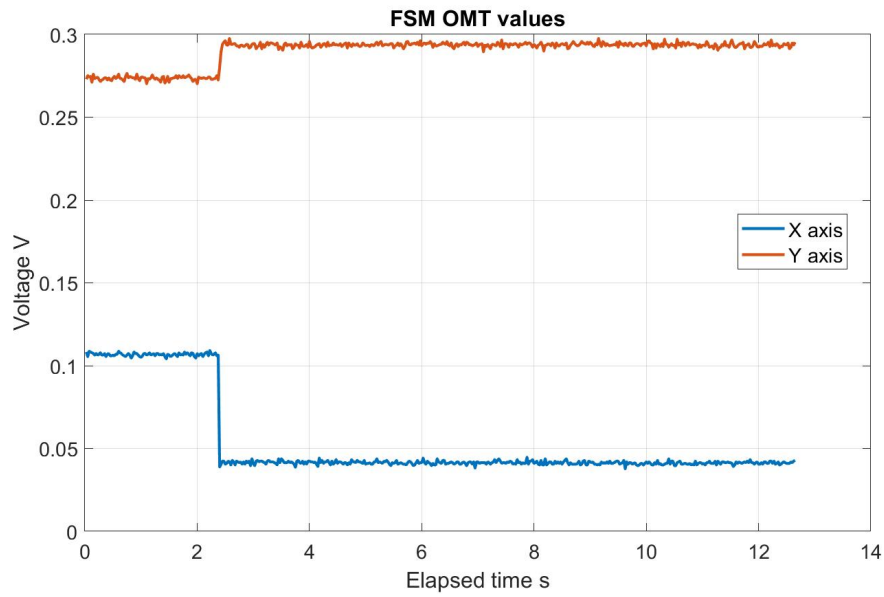
Figure 5.21: FSM in the OMT voltage values during the acquisition test for scan type 2 and initial offset 2.
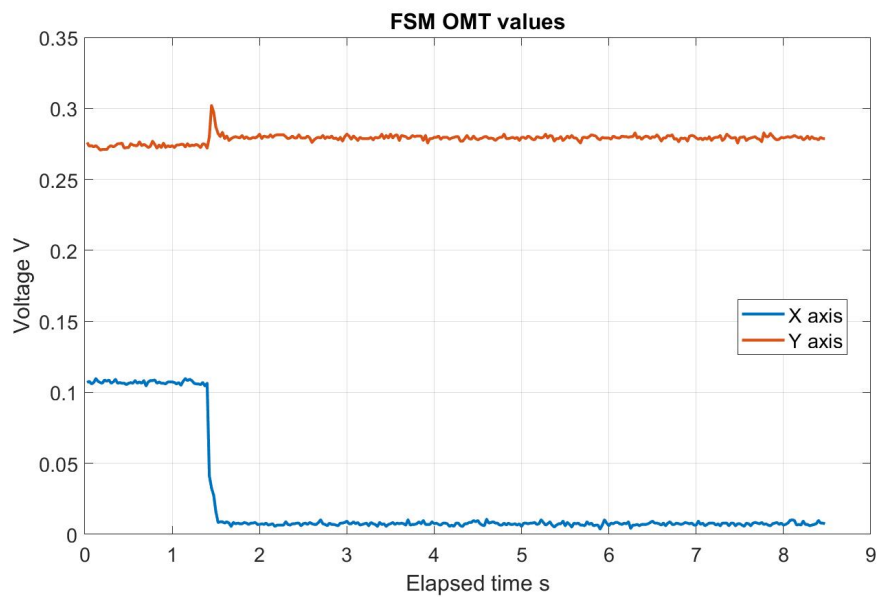

Figure 5.22: FSM in the OMT voltage values during the acquisition test for scan type 3 and initial offset 2.

The next variables to consider when examining the test results are the phases of the beat note on the quadrants of the QPD and their differences, as they need to be in the correct range for the successful engagement of the DWS control loop. Figure 5.23 shows the behavior of the phases, and what can immediately be noticed is that for the first part of the acquisition procedure the values of the phases change chaotically, until the scanning FSM is stopped and the FSM inside the OMT is set to the values determined by the calibration, at around 7.5 seconds from the start of the data acquisition. After the FSMs setting the phases maintain a constant and linear value, because the local OMT beam is being emitted from the OMT aperture close to the anti-parallel direction with respect to the incoming beam. The values of the phases are still far apart from each other, which are eliminated with the first phaseme-ter readout reset, after which they get closer, and then closer again when DWS is finally engaged. The phase values might diverge again in time toward higher values, while maintaining the same distance
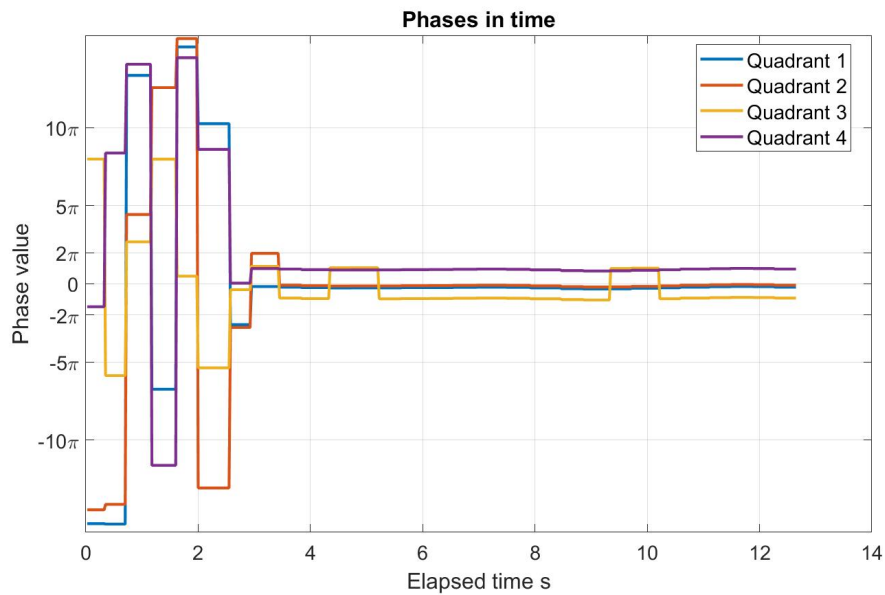
between each other.

Figure 5.23: Phases of the beat note on the four quadrants of the QPD during the acquisition test for the scan type 2 with initial offset 2.

The differences between the phase values in the quadrants of the QPD, which is what effectively runs the DWS closed loop control, are shown in Figure 5.24. Up until the detection and the setting of the FSM in the OMT according to the calibration, the differences in the phases are chaotic just like the values of the phases themselves, but as soon as the reset of the phasemeter readout happens, the difference drops and when the differences become small enough, DWS is engaged, and the differences converge towards zero. It is important for the difference between the phases to be smaller than π in order for DWS control to remain stable without diverging. While the absolute values of the phases might drift in time, as can be seen towards the end of the plot in Figure 5.23, their difference will remain close to zero for as long as DWS is engaged; there is in fact no drift at the right end of the plot in Figure 5.24. The difference between the phases should ideally be 0, a slight offset from zero is still acceptable, but the offset seen in Figure 5.24 indicates that the incoming and local beam might not be overlapping correctly on the QPD, and this fact will be explored more in detail in Section 5.2.4, but as long as DWS can be engaged successfully, the results are good enough.
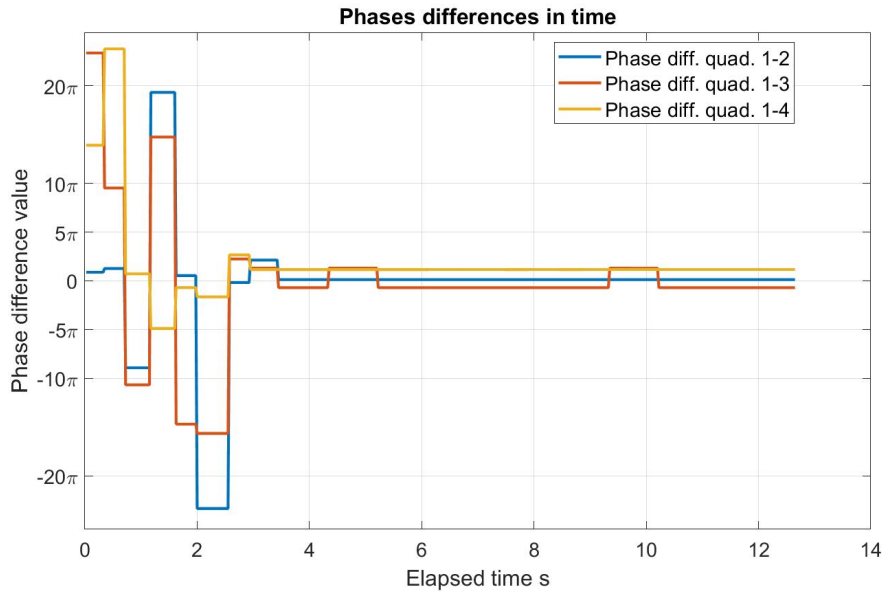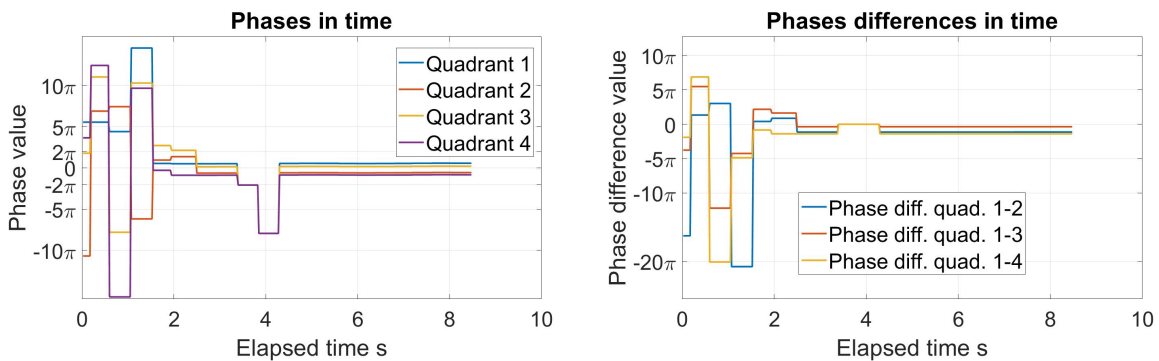
Figure 5.24: Differences between the phases of the beat note on the four quadrants of the QPD during the acquisition test for the scan type 2 with initial offset 2.

The same behavior described in the previous paragraphs for the scan type 2 can be observed when analysing the phases in the results of the scan type 3, which are shown in Figures 5.25a and 5.25b. Once again the Phases values in Figure 5.25a show a drift in time, while the differences in Figure 5.25b remain around the value of 0.

(a) Phases of the beat note on the four quadrants of the QPD during the acquisition test for the scan type 3 with initial offset 1.

(b) Phases of the beat note on the four quadrants of the QPD during the acquisition test for the scan type 3 with initial offset 1.

Figure 5.25: Phases values and phases differences for the beat note on the quadrants of the QPD during the scan type 3 with initial offset 1.

The last data acquired during the test that is evaluated in the analysis of the results is the beat note intensity on the quadrants of the QPD. When the beams are too far apart from each other on the QPD surface (when for example the incoming beam does not even reach the QPD) the intensity of the beat note is 0 (or close to zero, adjusting for background noise). When the beams are coarsely aligned they start interfering and the intensity of the beat note signal increases, but it reaches a maximum only when the two beams are correctly aligned and the local OMT beam is anti-parallel with respect to the beam being generated in the IFO over the Hexapod. The evolution of the beat note signal power for the scan type 2 is shown in Figure 5.26, where the increment of the beat note signal intensity is clearly visible when the scanning procedure stops at around 7.5 seconds from the start of the test. The intensity is normalized with respect to the maximum ADC value achievable. The beat note signal intensity is then maintained once DWS is engaged. It can be noticed, in the plot of Figure 5.26, that there is an

additional spike, at around 6 seconds from the start, which indicates that for the values of the FSM over the Hexapod and of the FSM in the OMT (at its neutral position) at that moment during the scan, the two beams were closely aligned on the QPD, but the beat note signal intensity in this spot was not as high as the one reached later at the completion of the acquisition, indicating that the beams at 6 seconds in the scan were not correctly aligned yet.
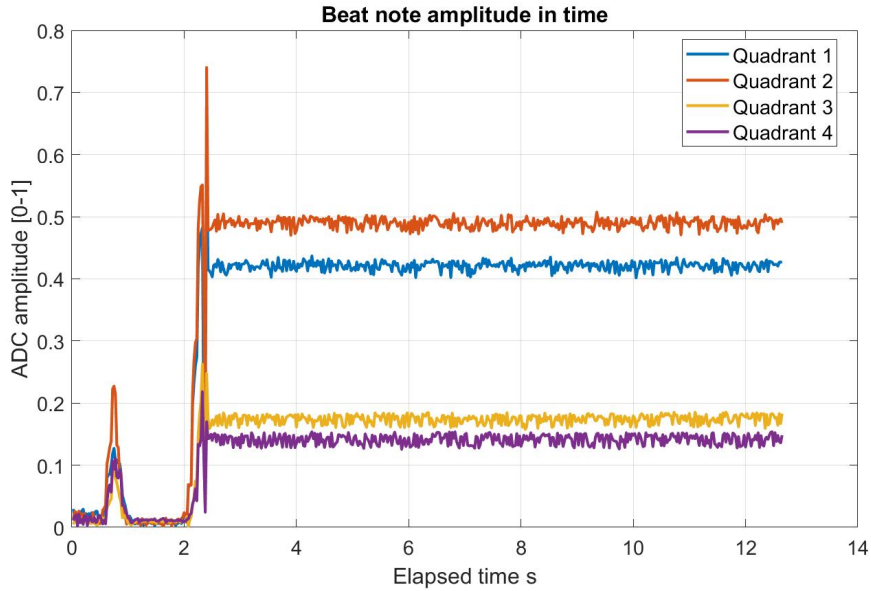

Figure 5.26: Beat note intensity on the four quadrants of the QPD during the acquisition test for the scan type 2 with initial offset 2.

The beat note intensity for the scan type 3 is shown in Figure 5.27, and it presents a different evolution, when compared to the beat note intensity during the scan type 2 in Figure 5.26, as it does not have an initial small peak, which was ignored, but demonstrates immediately a high beat note power on the QPD, skipping the smaller peak, probably beacause of the different distance between the spiral arms.
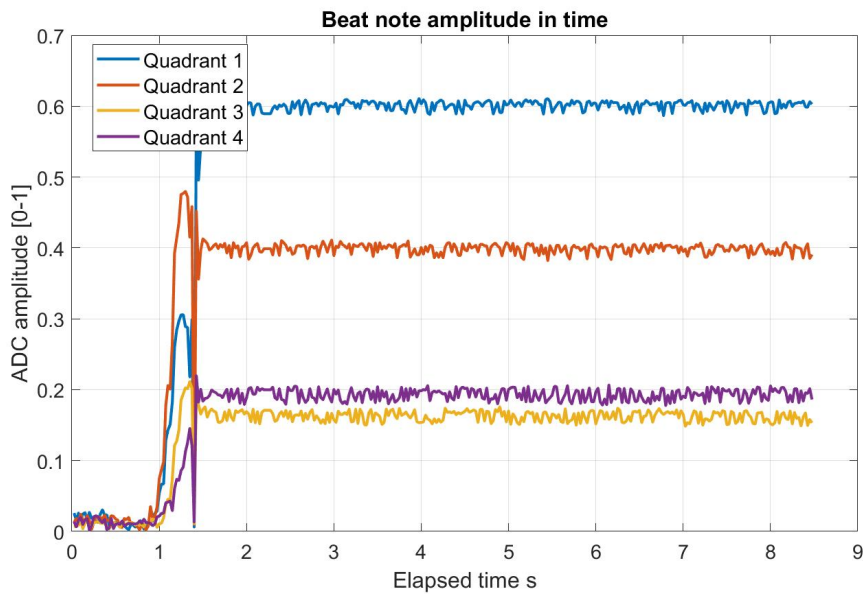

Figure 5.27: Beat note intensity on the four quadrants of the QPD during the acquisition test for the scan type 3 with initial offset 2.

The other type of scanning mode tested, the "full scan mode", does not include the engagement of DWS, but can be useful to see what points in the spiral scan lead to a detection on the acquisition sensor. For this purpose the detections that occurred during the full scan for the scan types 2 and 3 are shown in Figures 5.28a and 5.28b respectively. As mentioned earlier, ideally the points in which the detection happens should not move on the detector, due to the large distance in space between the two spacecraft, but since the experimental setup used is simulating a distance of 100 metres, it is still possible to notice some beam wandering on the detector depending on the angle of the incoming beam.
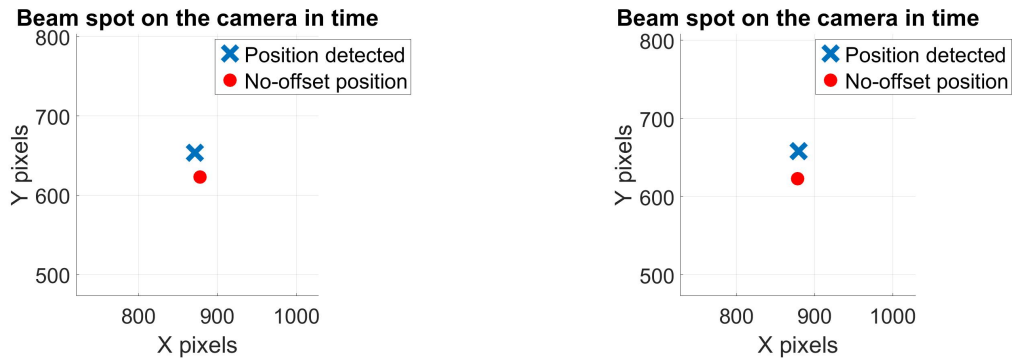
(a) Beam spots on the camera for full scan of scan type 2 and initial offset 2.

(b) Beam spots on the camera for full scan of scan type 3 and initial offset 2.

Figure 5.28: Beam spots on the acquisition sensor for scan types 2 and 3 with initial offset 2.

The FSM over the Hexapod scanning sequences are represented in Figures 5.29a and 5.29b for the scan types 2 and 3 respectively.
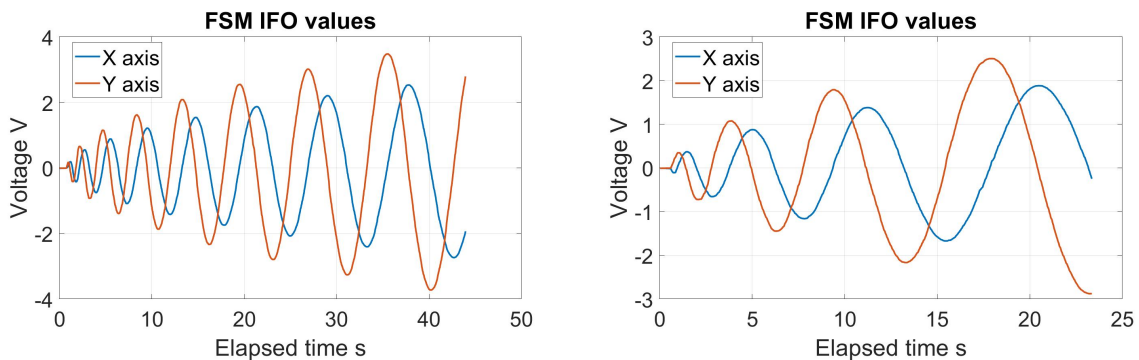
(a) Scanning FSM voltages for full scan mode of scan type 2 with initial offset 2.

(b) Scanning FSM voltages for full scan mode of scan type 3 with initial offset 2.

Figure 5.29: FSM over the Hexapod voltages for full scan mode of scan types 2 and 3 with initial offset 2.

5.2.2. Initial offset 4 results

The other scan analysed in detail is the scan with initial offset 4, described in Table 4.5, because it is closest to the edge of the calibrated range and can therefore provide an example of acquisition procedure with a bigger initial misalignment to be compensated.

The differences between the scan types 2 and 3, in terms of results, have been commented in Section 5.2.1 and the behavior is similar for the scans with other initial offsets. For this reason in this section only the "nominal" scan type 2 is evaluated, leaving the results of the scan type 3 for Appendix B.

Compared to what was expected for the test with initial offset 2, the results of this test should show a link acquisition happening after more than a couple of seconds from the start, and further along in the commanded spiral.

Analysis of results
The position at which the acquisition sensor in the "first detection mode" scan detects the beam is shown in Figure 5.30.
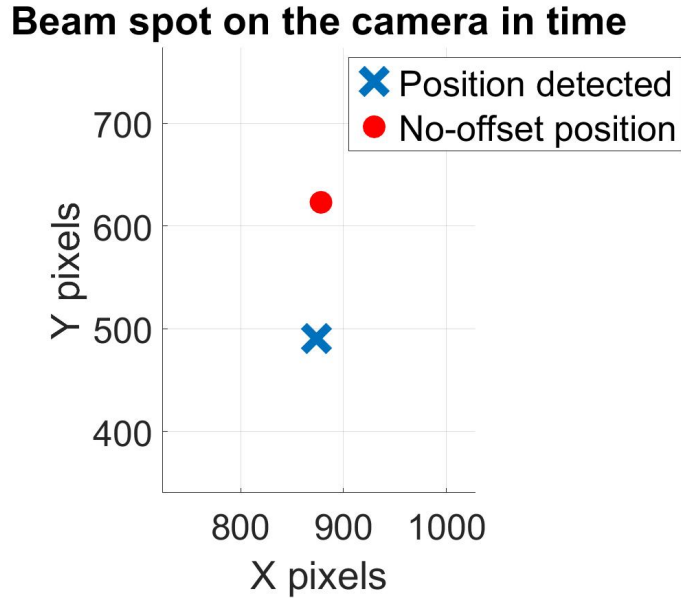
Beam spot on the camera in time

Figure 5.30: Beam position on acquisition sensor for scan type 2 with initial offset 4.

The position difference between the position of the beam detected and the no-offset position is considerably larger for the scan with initial offset 4, compared to the one that can be seen for a scan with initial offset 2 in Figure B.37, because the angular offset with which the beam enters the OMT is considerably larger.

The scanning FSM had to perform a larger portion of the spiral scan, compared to what is shown in Figures 5.19 and 5.20. Figure 5.31 shows the dynamic of the FSM over the Hexapod during the acquisition, with the sinusoidal waves of the commands which then stop at a detection and set to a constant value.
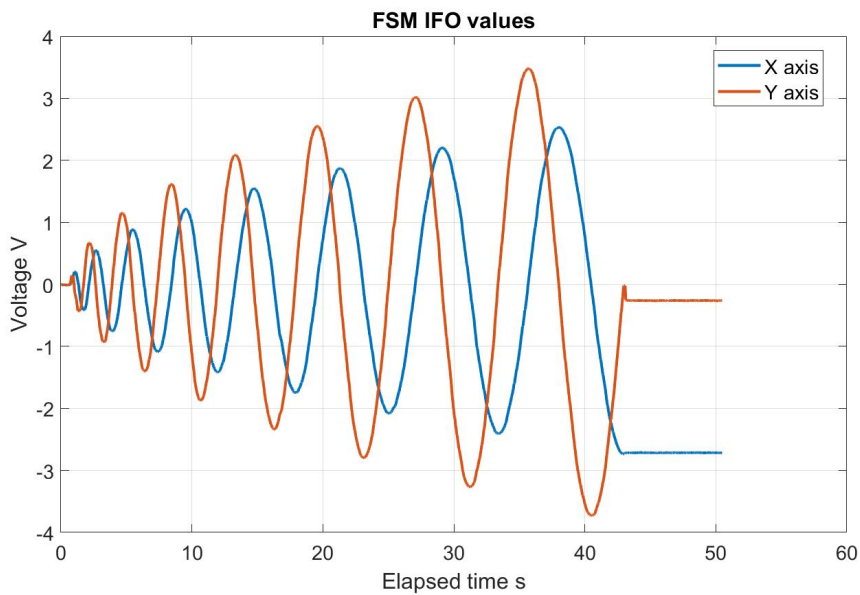

Figure 5.31: Scanning FSM voltage for scan type 2 with initial offset 4.

Along the same line as already seen for the scan with initial offset 2, the FSM in the OMT presents a step-like shape, going from a resting position to the calibration set, to the engagement of DWS. In Figure 5.32 is the evolution in time of voltages of the FSM inside the OMT. The first thing that can be noticed is the big jump on the X axis, compared to that of the Y axis, which basically remains still. This makes sense when considering that the initial FSM voltages were set to the values they have when the offset between the two optical axes and the line-of-sight is 0, and beam spot on the acquisition sensor moved considerably in the Y direction, which is compensated by movements of the X axis in the FSM in the OMT, and it did not move substantially on the X axis of the detector, which is compensated by the Y axis of the FSM in the OMT.
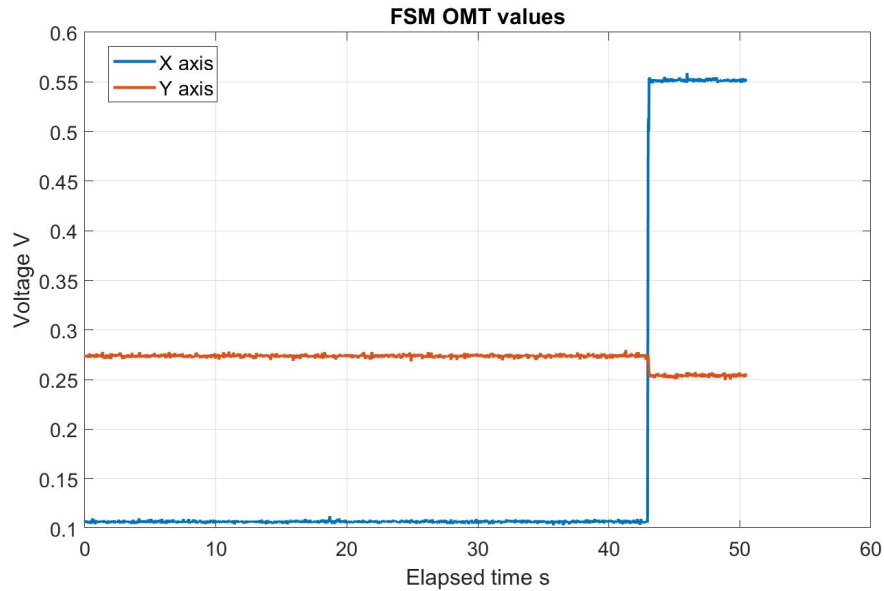

Figure 5.32: FSM in the OMT voltage for scan type 2 with initial offset 4.

The last results to analyse for the "first detection mode" are the phases of the beat note measured on the QPD, their differences and the beat note intensity. The same behaviors highlighted in Section 5.2.1 can be found again in this results shown in Figure 5.33, and again the phases do not get very close to each other, as highlighted by the difference in the phases, depicted in Figure 5.34. A further analysis on the alignment of the beams on the QPD is provided in Section 5.2.4, as mentioned previously.

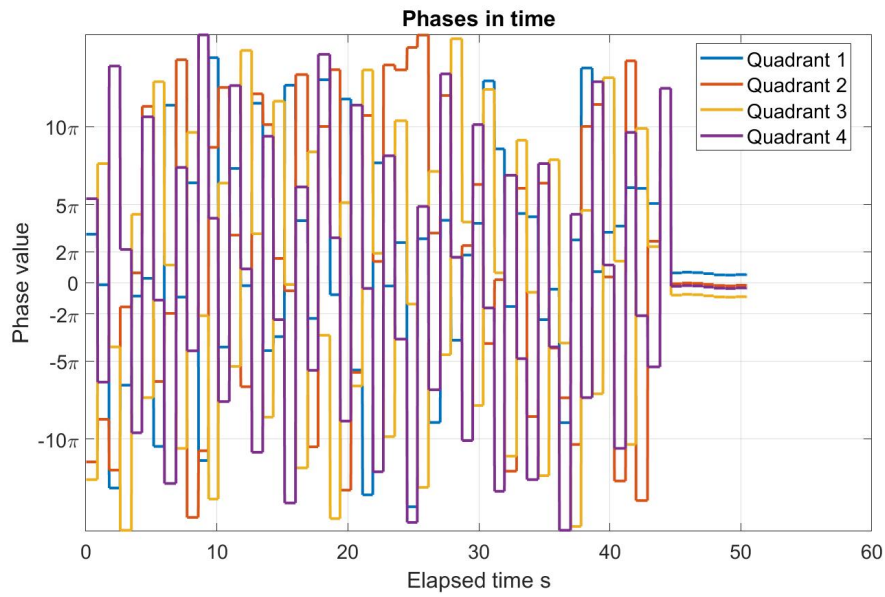**Figure 5.33:** Phases of the beat note measured on the QPD for scan type 2 with initial offset 4.
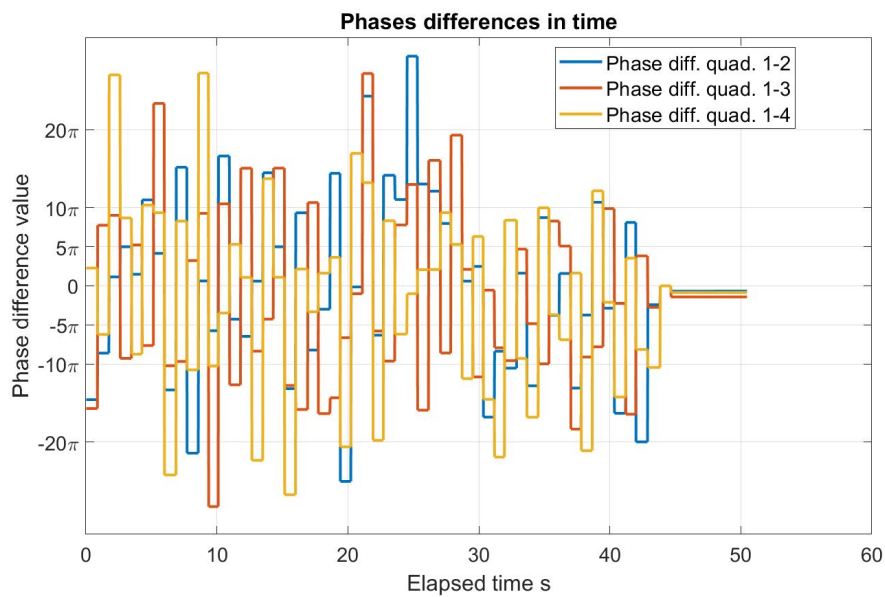

Figure 5.34: Differences between phases of the beat note measured on the QPD for scan type 2 with initial offset 4.

Finally, Figure 5.35 shows the intensity of the beat note on the four quadrants of the QPD, where the point of DWS engagement is clearly marked by a spike in the beat note intensity on the detector.
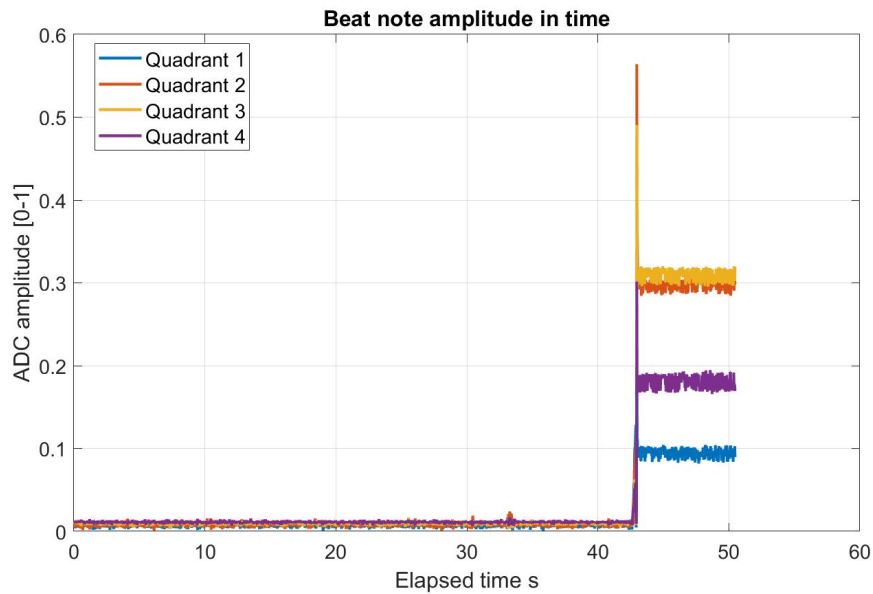
Figure 5.35: Beat note signal intensity measured on the QPD for scan type 2 with initial offset 4.

The results concerning the "full scan" acquisition mode are included in the Appendix B and will not be discussed further in this section, as they do not provide any additional insight compared to what has already been analysed in in the previous paragraphs and in Section 5.2.1.

5.2.3. Fast scan results

In Sections 5.2.1 and 5.2.2 the analyses of the results for the acquisition tests with initial offsets 2 and 4 have been conducted, concentrating on the scan types 2 and 3, but in Table 4.4 an additional scan type was introduced, scan type 1, which is the same as the scan type 2 with the exception of the scan period, which is 100 seconds instead of 500. This scan was defined to test the capability of the OFMT setup to handle fast scanning procedures. The risk with adopting quick scanning strategies is that the setup might not have enough time to react to the beam hitting the detector and it might not be able to detect any spot as a result.

This was tested, and the results show that the scan is too fast for a detection to successfully happen. Figure 5.36 shows the beam spot detected on the acquisition sensor during the fast acquisition. The point was detected but the FSM did not stop at the correct location because with the fast scan mode, the setup response to engage the acquisition was not fast enough.

Figure 5.37 depicts the voltages of the scanning FSM during the fast acquisition. Two things can immediately be noticed: the shapes of the sinusoids are not very clean, and the jump between the last scan point and the voltage to which the FSM was set to engage DWS differ significantly, compared to the other tests results seen previously. The first observation can be explained by the fact that the FSM is changing its voltage at a faster rate than the bandwidth of the FSM reading in the control software, which has implemented some filtering to eliminate the noise sources from the measurements. The second observation is explained by the fact that the operations performed in the autonomous control of the acquisition introduced a delay between the voltages at which the point was detected and when the FSM voltages have actually been set to that constant value.
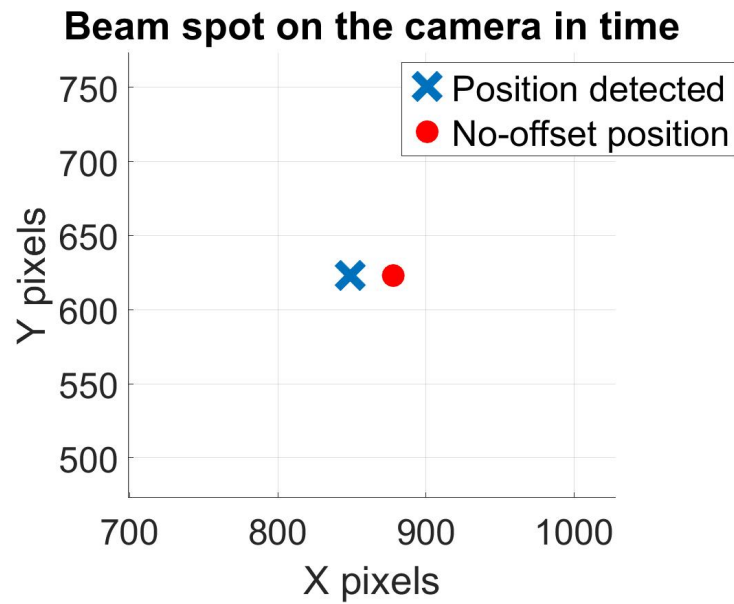
Figure 5.36: Beam position on acquisition sensor for scan type 1 and initial offset 1.
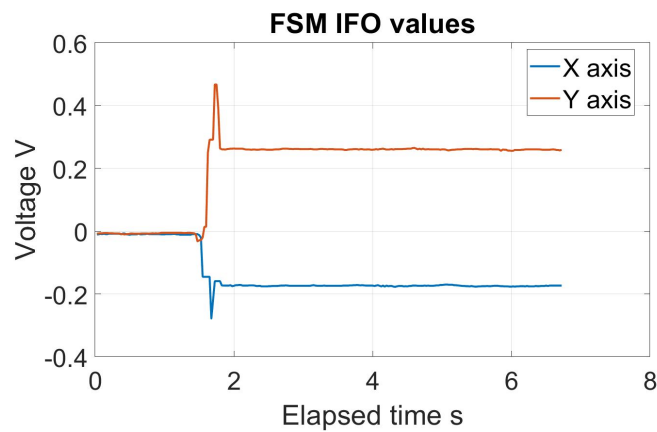
Figure 5.37: FSM over Hexapod voltages for scan type 1 and initial offset 1.

Another point to mention is that the refresh rate of the acquisition sensor was not fast enough to ensure an accurate detection of the beams, leading to missed points and detections which were not feasible. This is highlighted by the fact that for the spot which was detected in the fast scan, DWS control was not able to engage successfully. The phase and phase differences graphs are shown in Figures 5.38a and 5.38b respectively, and they demonstrate that in no point of the scan it was possible to correctly engage DWS. The phases always maintained a difference between each other which was considerably larger than π, making it impossible to have a stable DWS control.
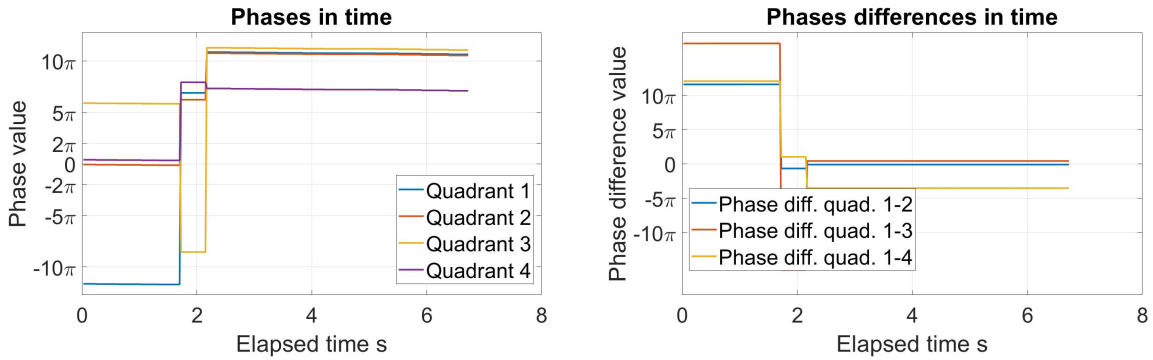
(a) Phases measurements of scan type 1 and initial offset 1.   **(b)** Phases differences of scan type 1 and initial offset 1.

Figure 5.38: Phases values and phases differences for the beat note on the quadrants of the QPD during the scan type 1 with initial offset 1.

One last aspect that can be looked at is the intensity of the beat note signal, which is shown in Figure 5.39, and has a very low value compared to the results analysed previously, indicating the in unsatisfactory alignment on the QPD between the incoming and outgoing beams.
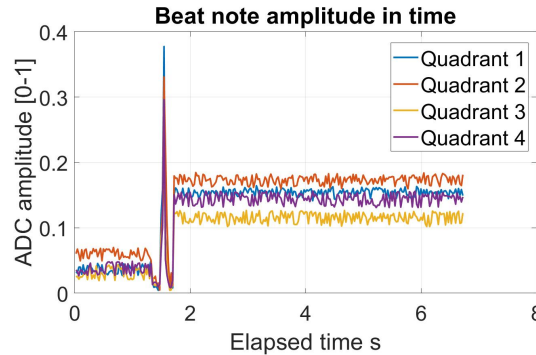

Figure 5.39: Beat note signal intensity on the quadrants of the QPD during the scan type 1 with initial offset 1.

5.2.4. Alignment accuracy from acquisition results

The results of the acquisition tests performed are important not only to show that the OFMT setup is capable of successfully performing link acquisition procedures, but also because they can provide a reference to evaluate the accuracy of the relative alignment of the different components, one of the goals set out for the first research question. If the alignment has been performed correctly, and the commands provided to the Hexapod for the set up of the initial conditions are reproducing the desired misalignments, the angles at which the FSMs engage DWS should compensate the angular offsets provided. If on the other hand the angles of the FSMs at the end of the acquisition don't match with the initial offsets with respect to the line-of-sight, it could mean that the acquisition procedure did not lock the laser link to the correct position or that the relative alignment between the two terminals is off by a certain amount.

As an example to tackle in detail, the results of the acquisition experiment with initial offset 4 are used. As a starting point, the initial offsets provided were -15 mrad in the out-of-plane angle between the two optical axes and the line-of-sight. The initial condition can therefore be showcased in Figure 5.40, where the two terminals are shown. The line-of-sight connecting them is the one in blue, the optical axis of the OMT is shown in red, which has a 15 mrad offset to the LOS, the same offset that is applied to the optical axis of the IFO-FSM-HXP terminal with respect to the LOS.

In reality the offsets are a bit different, because of the lens system and the magnification on the beam. The real situation is shown in Figure 5.41, where on the right side of the lens system in the figure the configuration is the same as the one displayed in Figure 5.40, but due to the lens system, the offset
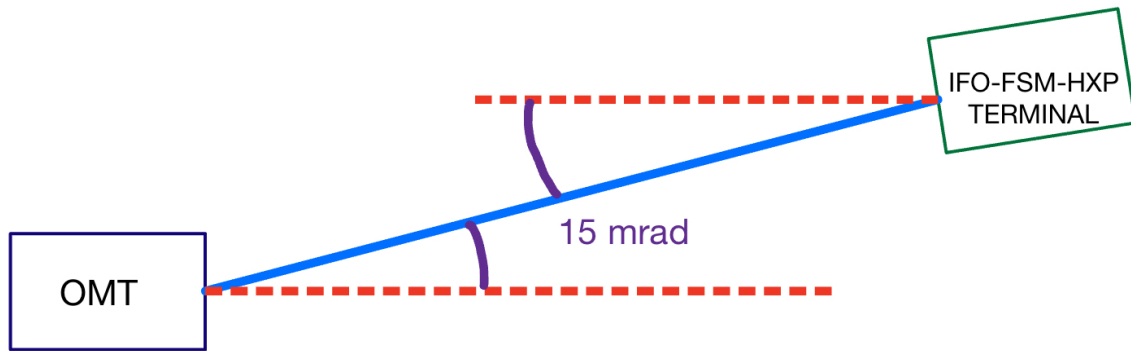
Figure 5.40: Initial conditions 4 with offset angles highlighted for the two terminals (not to scale).

angles become 10 times smaller, and on the OMT side the angle between the optical axis and the line-of-sight goes from 15 mrad to 1.5 mrad, which is in the range of the expected misalignments for this type of missions (like GRACE-FO). The angles in the figures are exaggerated and not to scale.
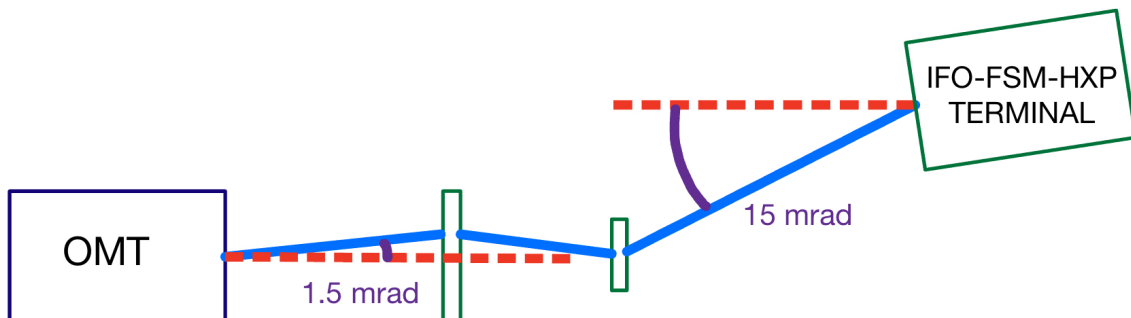

Figure 5.41: Initial conditions 4 with offset angles highlighted for the two terminals with lens system included (not to scale).

According to the initial conditions described, the FSM in the OMT should compensate the offset by providing the beam with a 1.5 mrad angle, while the FMS over the Hexapod should compensate the initial condition with a 15 mrad angle of the beam from the IFO. Before checking the values of the FSMs angles at which DWS is engaged, there are four considerations to make:

1. The angles at which the FSMs settle are mechanical angles, in order to be compared to the offset angles of the initial conditions they need to be converted in optical angles. This is usually twice the mechanical angle.

2. For the out-of-plane angles of the FSMs (which might not be the same as the optical axis angles), there is a $\sqrt{2}$ factor involved in the conversion between the mechanical and optical angles, because of the 45° orientation of the mirror with respect to the incoming beam. This feature can be found in the definition of the commands as well, in Figures 4.25 and 4.26, where for the in-plane angle, the maximum mechanical angle is half the maximum optical angle, 15 mrad and 30 mrad respectively; while for the out-of-plane FSM angle the maximum mechanical angle is half the maximum optical angle multiplied by $\sqrt{2}$.

3. When looking at the angles of the FSM in the OMT it needs to be remembered that the neutral offset position is not at 0 Volts for the pitch and yaw, but it has a slight offset of around 0.07 V on the X axis and 0.27 V on the Y axis, which have to be subtracted from the resulting voltages to obtain the net difference in angle that compensate for the initial offsets. The actual voltage values to be removed from the measured FSM voltages in the OMT are the ones that the FSM has before

the beam is detected and the mirror is set according to the calibration.

4. To convert the voltage values of the FSMs to their mechanical angles a proportion has to be applied, considering the maximum voltage range of the mirrors ($\pm$ 10 V) and their maximum angular range ($\pm$ 26.2 mrad). The optical angles are then obtained by applying the considerations made regarding the in-plane and out-of-plane angles. The conversion from FSM voltage to FSM optical angle is therefore shown for the in-plane angle of the FSM in Equation 5.1 and in Equation 5.2 for the out-of-plane angle, where FSM_{angle_O} is the optical angle of the fast steering mirror and FSM_{Volt} is the voltage value applied to the FSM, while the I-P and O-P acronym identify the in-plane and out-of-plane angles.

$$FSM_{angle_O\ (I-P)} = FSM_{Volt\ (I-P)} \times \frac{26.2\ mrad}{10\ V} \times 2 \tag{5.1}$$

$$FSM_{angle_O\ (O-P)} = FSM_{Volt\ (O-P)} \times \frac{26.2\ mrad}{10\ V} \times \frac{2}{\sqrt{2}} \tag{5.2}$$

In Table 5.4 the results for the angles are summarized, with the FSMs voltages as well as their mechanical angles, the resulting optical angles, the "objective" optical angles and the difference between the objective and the measured optical angles. The final angular $\triangle$ is given in absolute value because the sign of the FSM angle depends on the specific orientation of the steering mirror in the setup with respect to the reference frame in which the initial offsets are defined. "M angle" stands for mechanical angle, while "O angle" stands for optical angle. It is important to note that in this case, the in-plane and out-of-plane notations indicate the effect the fast steering mirror has on the beam after the mirrors on the Hexapod, and not the actual in-plane and out-of-plane angles of the FSM; in fact, due to the orientation and assembly of the elements in the setup, the in-plane angle of the FSM over the Hexapod affects the out-of-plane angle of the beam between the two terminals, and in the same fashion, the out-of-plane angle of the FSM over the Hexapod affects the in-plane angle of the beam between the Hexapod and the OMT. Due to the uncertainty on the measurement of the FSM angles, the relative misalignment between the terminals (evaluated while aligning the setup) and other smaller effects (like temperature effects), it is anticipated to have an error between the expected and the measured FSMs angles. A reasonable value for this error would be in the range of 0.35 mrad on the Hexapod side, and 0.08 mrad on the OMT side. This values are qualitative in their nature and they have to be intended as a reference point to roughly evaluate the results obtained.

	FSM OMT O-P	FSM OMT I-P	FSM IFO O-P	FSM IFO I-P
Volts (V)	0.554	0.26	-2.725	-0.274
M angle (mrad)	1.276	-0.0262	-7.14	-0.718
O angle (mrad)	1.83	-0.076	-14.279	-1.015
Initial offset (mrad)	-1.5	0	-15	0
Angular $\triangle$ (mrad)	0.33	0.076	0.721	1.015

Table 5.4: Alignment accuracy estimation from initial offset and final FSMs angles comparison for the acquisition test with initial offset 4.

By examining the results in Table 5.4 it is possible to conclude that the difference between the initial offsets and the compensated offsets is relatively large, when compared to the anticipated values, which is an indication of either a poor relative alignment of the terminals or the acquisition procedure locking to the wrong beam angles. The results for all of the offsets is shown in Table 5.5, where once again the in-plane and out-of-plane angles refer to the beam angles after the mirrors over the Hexapod, in the same way as in Table 5.4. The initial conditions for the LOS are in dark grey cells, while the initial conditions for the IFO optical axis (OA) are in light grey cells, to make them easily distinguishable from the FSM resulting optical (O) angles. The uncertainty anticipated is shown as a solid horizontal light blue line in Figures 5.42 and 5.43, where the difference between the initial angular offsets and the FSM angles after the acquisition is illustrated.

From the graphs in Figures 5.42 and 5.43 there are two things that can be deduced: the errors are large and expand over a big range, and the uncertainty on the measurements for the angles of the FSM in

Initial LOS offset	1	2	3	4	5
Initial LOS I-P (mrad)	3	0	2	0	0
Initial LOS O-P (mrad)	0	3	10	-15	5
Initial IFO OA I-P (mrad)	0	1	0	0	0
Initial IFO OA (mrad)	0	0	0	0	0
FSM IFO I-P (mrad)	1.861	0.445	2.838	-1.015	1.082
FSM IFO O-P (mrad)	1.06	2.872	9.29	-14.279	4.391
FSM OMT I-P (mrad)	-0.524	0.063	-0.185	-0.076	0.105
FSM OMT O-P (mrad)	0.074	-0.167	-0.945	1.83	-0.333

Table 5.5: Comparison between the expected and measured FSMs angles after DWS engagement.
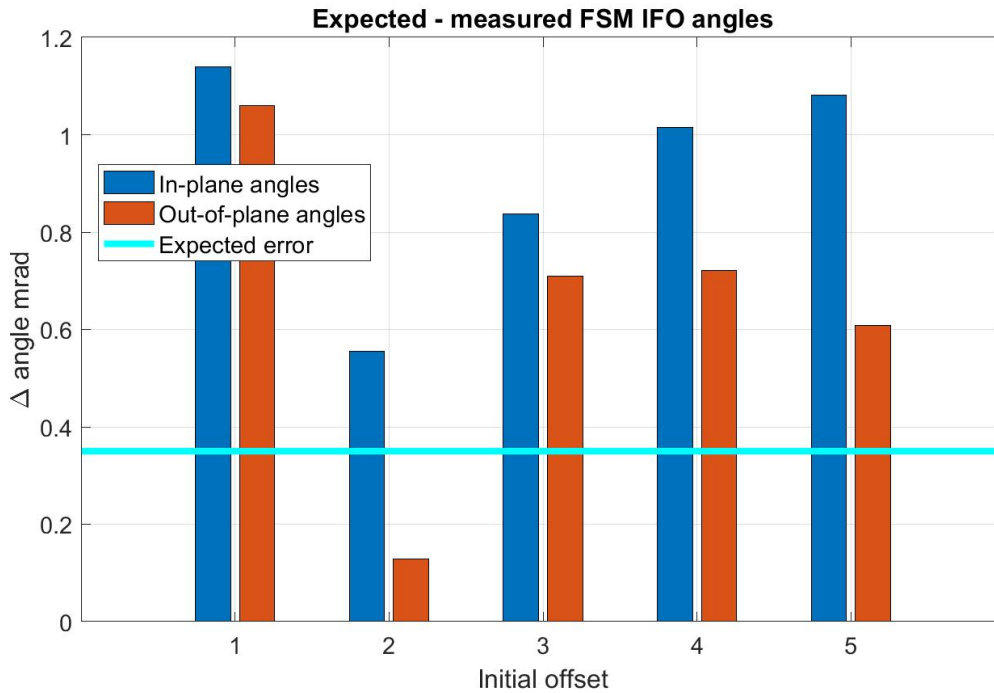

Figure 5.42: Difference between expected and measured FSM IFO angles.

the OMT can be very significant due to the small angles commanded. Considering that the results of the calibration in Section 4.3 seem to indicate a correct alignment of the components, and that the errors measured would definitely make the link acquisition procedure highly unreliable, going against what has been experienced in these initial tests, there probably is another reason for this differences between the expected and measured angles.

The reason for the offsets probably has to be traced back to the shape of the wavefront of the incoming beam. In a real world scenario, the incoming beam would have a spherical wavefront due to the extremely large distance between the spacecraft, with the centre of the curvature radius of the wavefront at the emitting satellite. In the setup the wavefront is not spherical but flat, because the beam is collimated. This was necessary in order to use the lens system with the beams coming from both sides of the lens system. The problem with using a flat wavefront beam with a "small" beam diameter compared to the entrance aperture, is that the beam could go through the lens system and into the OMT without going through the reference point of the OMT, arriving at the QPD and at the acquisition sensor with an angle that is not the one between the optical axis and the LOS. In Figure 5.44 is shown a schematic of what could happen during the acquisition procedure, when the beam coming from the scanning FSM (in purple) reaches the entrance aperture without going through the reference point of the OMT (depicted in blue). The beam in red would be the same beam when it goes through the reference point. In the real world application, as previously mentioned, this would not represent a problem. In Figure 5.45 the
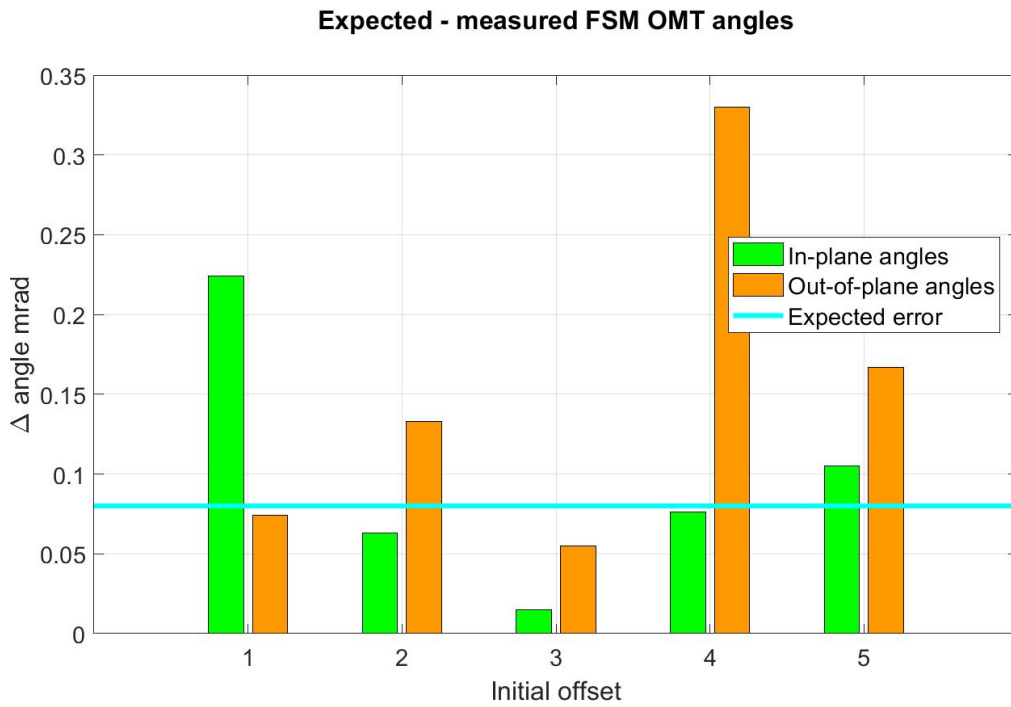
Expected - measured FSM OMT angles

Figure 5.43: Difference between expected and measured FSM OMT angles.
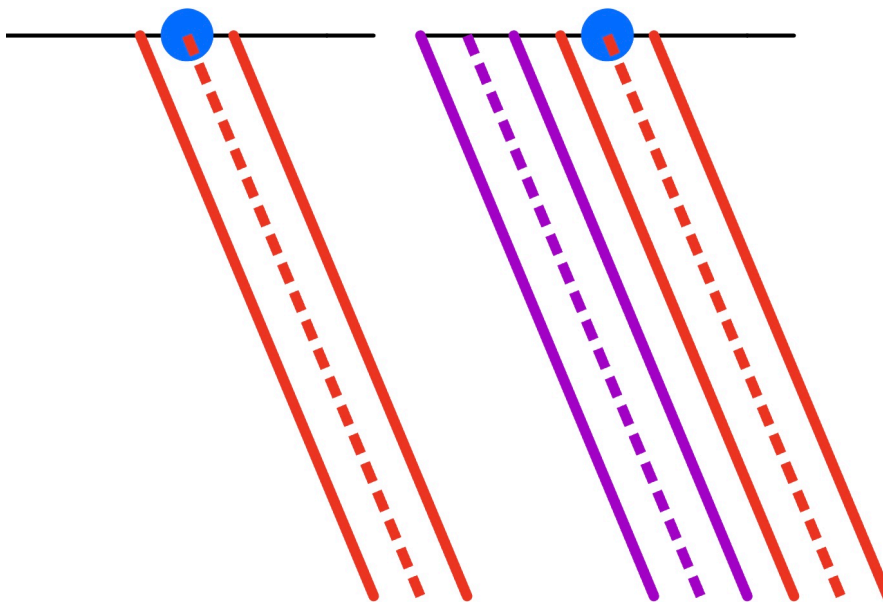

Figure 5.44: Incoming beam offset with respect to the reference point of the OMT.

spherical wavefront beam (red) is compared to the flat wavefront beam (blue), to show that even when the beam has an offset and does not reach the centre of the entrance aperture, the normal direction to the spherical wavefront is always pointing to the origin of the beam (the sending spacecraft), which means that the OMT would point its local laser exactly towards the opposite satellite. The flat wavefront beam, in blue, has the normal directions to the wavefront that are all pointing in a different direction, meaning that the local OMT laser would be pointing towards the opposite spacecraft with an offset. The only way to ensure that both the scanning FSM and the FSM in the OMT are pointing their lasers in the direction of the LOS is to make the scanning beam go through the reference point. Another clue

to this effect could be found when analysing the results in Section 5.2, when the difference between the phases on the QPD was not close enough to 0, indicating a possible misalignment between the locations at which the incoming and local beams hit the QPD.
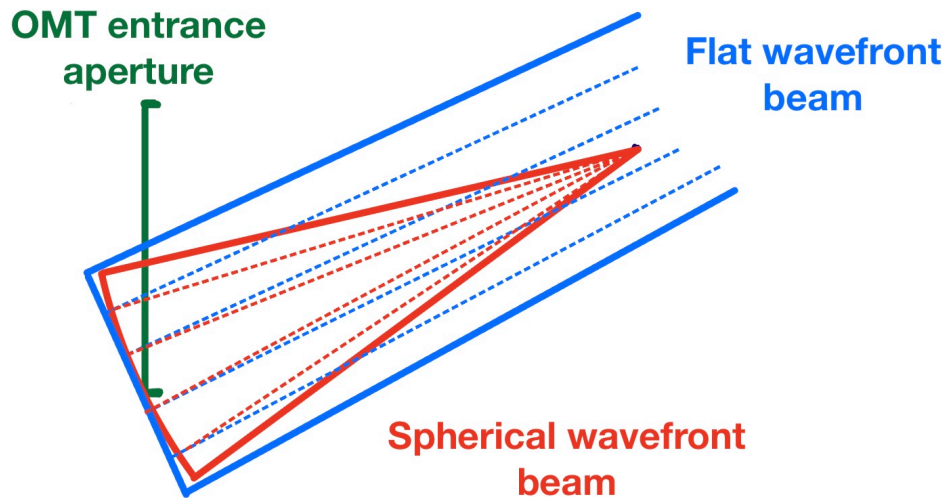

Figure 5.45: Difference between flat and spherical wavefront at the OMT entrance aperture.

Engaging DWS is still possible when the incoming beam does not intercept the OMT reference point, but it then locks to the wrong LOS offset, which would explain the big discrepancies shown in Figures 5.42 and 5.43. This hypothesis can easily be proved by monitoring the incoming beam intensity on the QPD. If the incoming beam is going through the reference point of the OMT it should also be centered on the QPD, with the power equally distributed on the four quadrants. If the beam is not centered on the QPD, it means that it is going through the system with an offset with respect to the reference point, and locking to it with DWS would then lead to a difference between the initial LOS offset and the correction commanded with the FSMs at the end of the acquisition procedure.

For every acquisition test performed with the scan type 2, detailed in Section 5.2, an additional procedure has been performed to verify the hypothesis concerning the discrepancies between the FSMs expected and measured angles. After the completion of the link acquisition procedure, the laser source for the OMT was turned off, maintaining only the laser source for the IFO. The intensity on the QPD was then monitored at the voltages set for the FSM over the Hexapod following the acquisition. In every test performed, the beam was not hitting the QPD in the centre, as shown by the power distribution on the four quadrants of the QPD for one of the initial offsets in Figure 5.46a, and the corresponding position on the QPD, depicted in Figure 5.46b (barely visible in the top left corner of the figure).

Starting from the FSM voltages derived during the acquisition, the FSM angles have been changed until the power distribution on the quadrants of the QPD became more uniform and the beam position on the sensor reached its centre. For this operation the power of the incoming beam has been increased, to limit the effect that the static noise offsets of the QPD have on the measurement (they are one of the reason for the incorrect position of the beam shown in Figure 5.46b). The power distribution on the quadrants of the QPD as well as the barycentre of the beam on the sensor are shown in Figures 5.47a and 5.47b.

Comparing the data from the QPD before and after the corrections shows how the beam was indeed not going through the reference point of the OMT. The vertical position of the beam in Figure 5.47b has maintained a slight offset, because of the static noise on the QPD, which was found to be influencing the beam vertical position when doing tests with no angular offsets between the terminals.

In order to retrieve the "corrected" angles for the FSM in the OMT, the power of the incoming beam is reduced to its nominal value and the local OMT laser is turned back on. The voltages on the FSM OMT are changed until the beat note power is maximum and DWS is engaged. The values of the FSM
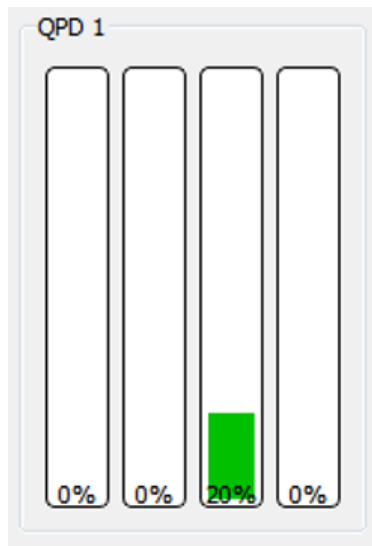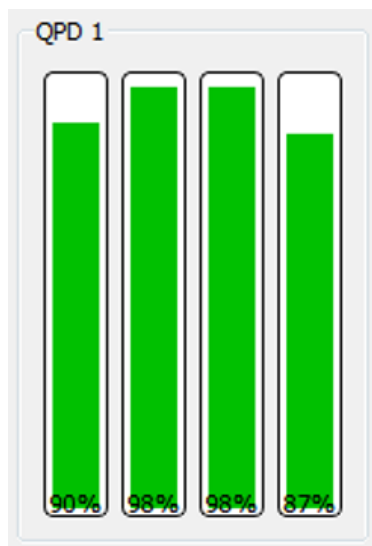
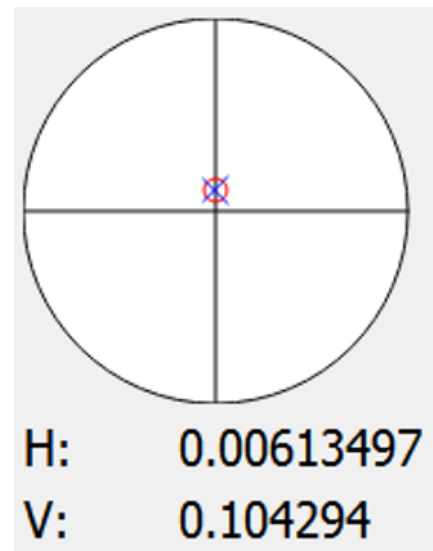**(a)** QPD intensity distribution for misaligned beam.
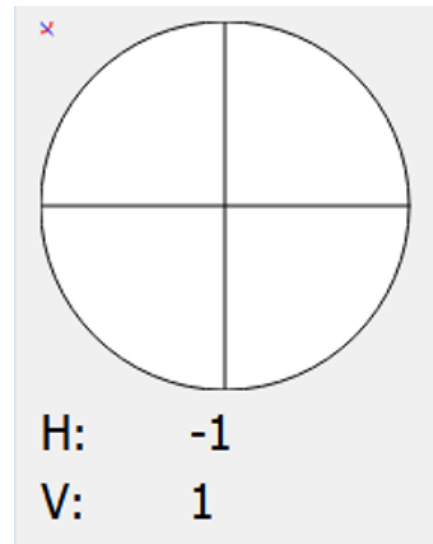
(b) Misaligned beam position on QPD.

Figure 5.46: Power distribution and position on QPD for misaligned incoming beam.

(a) QPD intensity distribution for correctly aligned beam.

(b) Correctly aligned beam position on QPD.

Figure 5.47: Power distribution and position on QPD for correctly aligned incoming beam.

voltages are then read to retrieve the correct angles to align the optical axis with the line-of-sight.

The errors between the expected FSM angles and the measured ones, following the correction procedures outlined in the previous paragraphs, are displayed in Figures 5.48 for the FSM over the Hexapod and 5.49 for the FSM in the OMT.

Comparing the results of Figures 5.48 and 5.49 with those shown in Figures 5.42 and 5.43, the effect of the correction is clearly visible and the discrepancies between the expected values and the measured ones are smaller and roughly fit with the anticipated values.

On top of the previously mentioned relative misalignment and FSM reading noise, there could be other sources of error that contribute to the results measured and the error budget defined. Additional sources of errors would be the discrepancy between the commands generated in the simulation software and the
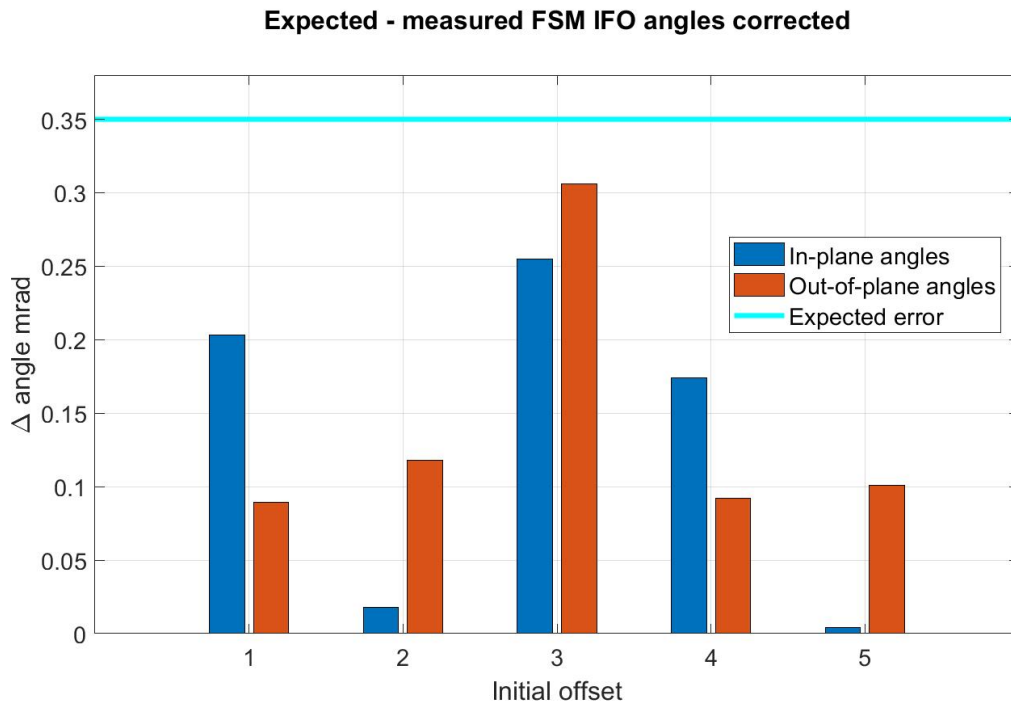
Expected - measured FSM IFO angles corrected

Figure 5.48: Difference between expected and measured FSM IFO angles following the correction procedure.

Expected - measured FSM OMT angles corrected
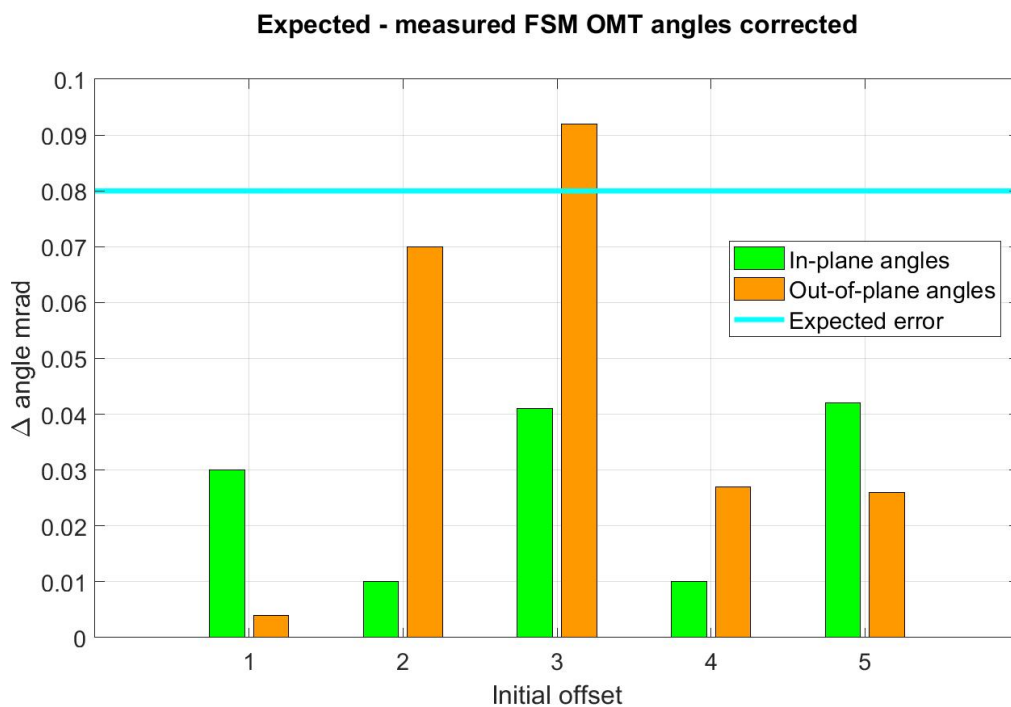
Figure 5.49: Difference between expected and measured FSM OMT angles following the correction procedure.

ones actually reproduced in the experiment, as well as the different position of the OMT reference point between the ray tracing simulation and the setup. The pathlength of the incoming beam is probably also slightly different from the expected one, leading to another LOS offset with respect to the one produced in the simulation. One element concerning the FSM that could be added to the pool of error sources is the temperature shift in the accuracy of the system, due to the temperature variations in the

lab and the temperature variations of the OMT due to the mirror heating up during operations. The temperature of the FSM has not been recorded and an estimation on this error cannot be performed, even though it can be assumed not to be the main cause of misplacements.

Autonomous correction procedure

The correction procedure outlined earlier in the section, illustrated with the QPD results in Figures 5.47 and 5.46, led to a drastic reduction in the difference between the expected and the measured QPD angles; but in order to achieve a correct and full link acquisition, the procedure would need to be performed autonomously. Thankfully, the fix for this problem is rather easy conceptually: when engaging DWS on the IFO side (as well as the OMT side) the alignment of the beams would fix itself. The initial misalignment of the beams would be detected on the IFO side as an error between the incoming and outgoing beams (on the Hexapod side) and the instrument would command the local FMS to move in closed loop control with the FSM in the OMT, while maintaining DWS signal on both sides, and the offsets between the optical axes and the LOS would be driven close to zero. This has been checked roughly with a viewing card and a camera as well, monitoring the beat note pattern on the IFO side (with a beat note frequency changed to 1 Hz, to be detectable with the naked eye): when the two beams are incorrectly aligned, the interference pattern on the camera/viewing card shows multiple lines and peaks, while when moving the FSMs to the "corrected" values, the pattern gradually becomes one pulsating point, at the frequency of the beat note, indicating the correct alignment between the beams.

The procedures to implement DWS control on the IFO side of the instrument are listed as future developments in Section 6. The current version of the setup, even with the limitation of DWS engagement on one side and without the possibility of entering a closed loop control mode for the whole architecture, can still demonstrate that the OFMT is capable of performing link acquisition procedures correctly.

5.3. Implications for instrument requirements

In the final part of the results, with the experience accumulated while building and aligning the setup, and from the insights gained by performing the acquisition tests, it is possible to identify what kind of requirements the link acquisition procedure poses on the OFMT setup. When the final research question was defined in Section 1.3, three different goals were set, which would allow to answer the question and define the requirements and the elements needed for the OFTM to perform correctly the initial link acquisition. The goals identify the three different areas in which the development of the OFMT link acquisition can be divided, and which valuable lessons were learned during the thesis project. These three areas are the essential hardware elements needed to perform the link acquisition, the methods for the assembly and alignment which can be improved to achieve a better or more accurate acquisition, and finally the requirements on the link acquisition procedure itself based on the results obtained. They are tackled in detail in the following sections.

5.3.1. Necessary elements for the acquisition procedure

The definition of the necessary elements is based on the experience accumulated while designing the link acquisition procedures and while performing the acquisition tests, as well as by elaborating future possible strategies and developments. There are a great number of elements, especially regarding the instrument hardware, that could be included in the analysis, but 4 main aspects have been identified: the acquisition sensor, the fast steering mirrors, the Hexapod or telescope pointing, and the communication between the terminals.

Acquisition sensor

A dedicated sensor for the initial link acquisition is usually associated with telescope pointing strategies, like LISA, while in-field-pointing architectures like the one employed in GRACE Follow-On have not included an acquisition sensor so far. In the work presented in this thesis it has been demonstrated that a dedicated initial acquisition sensor can work very well with an in-field-pointing setup which uses a FSM to perform the scan. The larger field of view of the acquisition sensor, with respect to the QPDs, coupled with the fast scanning abilities of the FSM, allows for fast and efficient link acquisition procedures, including the fact that it does not need to perform a full frequency scan at every point of the acquisition, but only once the beam is detected on the sensor. It was unfortunately not possible to test link acquisition strategies without making use of the acquisition sensor (a GRACE-FO type of acquisition), but it is still possible to conclude that an acquisition sensor in the OMT architecture can definitely improve its link acquisition capabilities and performance. The main downside of including an acquisition sensor is that it introduces an additional point of failure, but with one acquisition sensor per spacecraft there would be no single point of failure linked to the use of the dedicated sensor, as it has been demonstrated that it is possible to successfully perform initial link acquisitions between two terminals using only one acquisition sensor. The inclusion of an acquisition sensor on each satellite can also allow for dual scanning strategies, which can further increase the speed of acquisition (and re-acquisition) procedures.

The acquisition sensor with the associated electronics that is included in the OMT setup is shown in Figure 5.50.
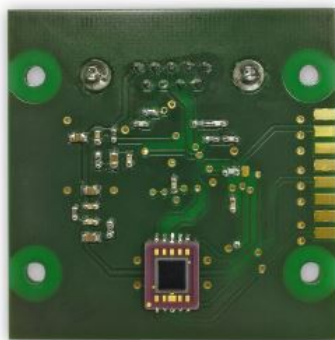

Figure 5.50: Acquisition sensor included in the OMT setup [34].

Fast steering mirrors

Fast steering mirrors have been successfully demonstrated in space as effective elements to perform acquisition scanning in the GRACE-FO mission. They allow for fast and wide scanning profiles, they are very versatile in terms of the types of geometries they can reproduce and it has been demonstrated in this work that they can definitely work very well with a dedicated acquisition sensor. As mentioned in the paragraph dedicated to the acquisition sensor, it was not possible to perform link acquisition tests without the dedicated sensor, but it is something that has been demonstrated for other setups and architectures which include FSMs, and they would therefore allow for an effective acquisition even in the case of a complete failure of both acquisition sensors (one on each spacecraft) or one if the design includes the acquisition sensor only on one end of the laser link. The downside of including a FSM in the optical path is the risk of introducing additional instabilities which might prove unacceptable for extremely precise optical metrology applications like LISA. Even considering the stability concerns, it could still be possible to find compensation mechanisms that would make the in-field-pointing architecture attractive, and its use is definitely recommended in a setup like the OFMT. The FSMs used in the OFMT setup are the same as the one depicted in Figure 5.51.

Figure 5.51: Fast steering mirror included in the OFMT setup [11].

Hexapod/Telescope pointing

The third element analysed in the list of hardware required for the link acquisition procedures related to the OFMT architecture, is the inclusion of a telescope pointing system. In the laboratory setup described in 3.4 an Hexapod should provide the telescope pointing capabilities. The Hexapod used in the experiment is shown in Figure 5.52.

Figure 5.52: Hexapod used in the OFMT setup.

Due to the problems mentioned in Section 4.2 with performing the necessary scanning commands, the Hexapod could not be used to simulate telescope pointing acquisition strategies. It was still used

to recreate the initial offsets for the link acquisition tests, but these tasks could have been performed by another precision moving stage, not necessarily by an Hexapod. Even though no telescope pointing acquisition was performed, it is safe to say that with the OFMT architecture implemented, it is not necessary to include telescope pointing capabilities, because the in-field-pointing associated with the acquisition sensor allow for robust, flexible and efficient link acquisitions. An instrument like the Hexapod can still be used in a laboratory environment to introduce offsets, simulate spacecraft jitter and evaluate tilt-to-length coupling effects. A greater control on the type of movement it can perform would be advised, to avoid the limitations faced in this thesis work.

Communication between the terminals
The term "communication" between the terminals refers to the sharing between the two spacecraft of information regarding the current state of the systems and components making up the instruments. On the OFMT experimental setup, this is done on the control software loaded onto the workstation, and it is necessary in order to make the acquisition autonomous, as the scanning terminal needs to know when the beam is detected on the acquisition sensor to stop the scan and point the beam in the direction in which the detection happened. The communication in the OFMT setup is especially important given the limitations of the waveform generator, which cannot stop the scan in any specific point, but it needs to terminate the arbitrary scan and a DC value has to be provided by the control software to both outputs. The GRACE-FO mission did not have any communication means between the two spacecraft, and all the post-processing of the acquisition data was done on-ground, but the link acquisition in GRACE-FO was not autonomous, as ground intervention was needed.

An autonomous strategy that does not involve communication capabilities between the two satellites could still be possible if the acquisition scan was slow enough to allow for the other spacecraft to detect the beam, redirect the local beam according to the calibration to have an anti-parallel direction with respect to the incoming laser, allowing the scanning spacecraft to detect the beam on its acquisition sensor (provided that both spacecraft are equipped with a dedicated acquisition sensor), to then stop the scan, perform the frequency scanning and engage DWS to conclude the acquisition. While possible, the autonomous acquisition without any means of communication between the terminals would need further investigation. It has been proven that the autonomous acquisition with the terminals having the knowledge of each other's states is possible and works efficiently. It is therefore advised, for now, to include the communication capabilities between the spacecraft if allowed by the mission scenario and the other mission requirements, but further studies are suggested to explore alternative solutions.

5.3.2. Improvements on assembly and alignment procedures
Following the analysis of the necessary hardware to perform link acquisition procedures with an OFMT-like architecture, this section concentrates on possible improvements to the assembly and alignment of the setup, which would improve the accuracy and robustness of the link acquisition procedure, as well as making the implementation easier. There are a number of solutions which could improve the setup, the most relevant are discussed in the next paragraphs.

Finding a design that can avoid the use of auxiliary mirrors on the Hexapod head would make the alignment considerably easier and more precise, given that the gluing process for such big mirrors on a critical component like the Hexapod puts inevitable limitations on the alignment accuracy that can be achieved, and in order to perform precise metrology measurements, the compensation by means of the Hexapod offsets might not be enough. The problem though does not subsist when the mirrors, IFO and FSM are replaced by another OMT, but for what concerns the link acquisition setup developed in this thesis work, the alignment of the mirrors represented the most challenging part of the assembly procedure.

Another element which proved challenging to the correct execution of the link acquisition tests was the elimination of the ghost beam from the calculation of the beam spot on the acquisition sensor. In Figure 5.53 an image from the acquisition sensor is shown, with the incoming beam clearly visible around the centre of the image, and a ghost beam on the bottom right which moves around as the FSM in the OMT angles change, and can interfere with the beam spot measurements. It would be beneficial to physically eliminate the ghost beam from the detector by finding a viable solution to block it before it reaches the detector, even though it is not as simple as it seems, given that it changes with the movements of the FSM.

Figure 5.53: Image captured by the acquisition sensor during a link acquisition test, with the main incoming beam in the centre and a ghost beam in the bottom right of the picture.

Another element of noise in the acquisition and in the setup in general which is visible in Figure 5.53, is the stray light that surround the beam spot. This comes from the internal reflections in the OMT, from the diffraction caused by the clipping of the large beam and other elements in the system. While the cancellation of the noise did make the acquisition accurate enough, a cleaner image would definitely improve the acquisition, by means of a clip or a similar physical solution, as it would also improve the quality of the beam on the QPDs.

The mounting of the acquisition sensor itself could be improved. It is currently mounted using two of the four holes visible in Figure 5.50. While it is stable enough to perform the link acquisitions, it is still susceptible to unwanted shifts, movements and changes in position or shape, for example due to temperature changes. A solution involving a sturdier fix of the sensor would improve the quality of the data acquired.

Mentioning temperature effects, an accurate control of the temperature in the laboratory environment is crucial for metrology experiments, and it is therefore advised to implement an accurate thermal control system, which could also be used to evaluate the effects that temperature changes have on the setup and on the measurements performed, including on the acquisition procedures, as the temperature environment in space can be very demanding and the sturdiness of the instrument to this variable is an important factor to be evaluated.

The two final elements which would improve the alignment capabilities of the system are the correct positioning of the FSM over the Hexapod, which currently has an offset with respect to its ideal position, and the use of customized lenses for the lens system that simulates the 100 metres distance between the terminals. For what concerns the FSM, even though its position does not significantly affect the functionality of the OFMT setup, changing its location would improve the system. The use of customized lenses for the specific purpose of the OFMT setup would allow for an improvement of the wavefront quality, but it would also represent a greater cost, which has to be weighed with the effective advantages it would bring.

5.3.3. Link acquisition requirements based on the acquisition results
The last round of considerations regarding the requirements for the OFMT link acquisition procedure concerns the acquisition strategy itself. The recommendations provided in this section are derived from

the experience accumulated through the acquisition tests performed.

The results shown in Section 5.2.3 demonstrate that the speed of the scan during the acquisition is a fundamental parameter. It depends on the maximum speed achievable by the FSM, but the limiting factor is usually the response time of the acquisition system, involving the detection on the camera, the determination of the beam position and the setting of the current FSM voltages. When the scan is too fast, the camera is not able to correctly detect the beam, and even when the beam is detected, it is not possible to correctly and exactly set the FSM voltages back to the desired location because of the filtering performed on the signals received by the FSM driver to eliminate the noise, which also introduce a delay in the reading and don't allow for the detection of high frequency changes. The correct determination of the minimum scanning speed to achieve a successful acquisition was not possible due to time limitations of the project, but the necessity to identify this parameter has been shown.

Another element of the scan design which has to be carefully addressed is the overlap between the scanning sequences. In the case of the spiral geometry, this is the distance between two arms of the spiral, which ideally needs to be close enough to allow for an overlap of the beams. This is especially important when spacecraft jitter and other external noise sources affect the acquisition. In this work the difference in the results that two different overlap factors cause has been outlined, a more conservative approach is recommended, opting for a larger overlap that ensures a complete coverage of the uncertainty space, over a smaller overlap which would make for a faster and more efficient scan, but that could result in the laser beam missing the receiving spacecraft due to external disturbances.

The last two considerations regarding the design of the link acquisition strategy concern the capabilities of the system, which should be able to stop and re-start the scan at any location, in order to evaluate the possible detection and continue with the acquisition if necessary, and it should be able to have a robust DWS engagement method. The possibility of stopping and resuming the scan is especially important in the laboratory environment when incorrect or low-quality acquisitions might be detected on the sensor. It is not unfortunately possible to implement such functionality with the waveform generator used in this thesis work, but it is a recommendations that could be implemented for similar architectures. Finally, the DWS engagement method needs to account for the possibility of the wrong DWS locking to occur, and it should be able to correct for it. The link acquisition strategy therefore has to include an iterative check on the beat note signal characteristics to correct for a wrong DWS locking, which can represent an issue, as demonstrated in Section 4.3.

6

Recommendations for future developments

The work presented in this thesis details the first part of a longer project that is devoted to the development of the OFMT setup, composed of two OMTs, one of them positioned on top of the Hexapod, and that aims to demonstrate the capabilities of optical formation metrology for a new instrument architecture like the OMT. The next step of the project therefore involves the construction and the integration of the second OMT into the existing hardware, substituting the plate with the IFO and FSM over the Hexapod, as well as the mirrors placed on the Hexapod head. The relevance of the setup built and tested in this thesis for the OFMT project is its ability to demonstrate the link acquisition capabilities of the OFMT architecture, developing and testing strategies that will be employed in the later stages of the OFMT development and that allowed to gain insights into the strong and weak points of the design with regards to the acquisition procedures. In this chapter the recommendations for future developments of the OFMT link acquisition setup and testing are provided, based on the work performed and the results achieved. The future recommendations can be divided into two categories: the recommendations regarding the hardware developments, and those regarding the link acquisition procedures.

Concerning the recommendations about the hardware developments, there are many points that could be improved, but the attention will be put on three crucial elements, other than those already mentioned in Section 5.3. The three elements are: replacing the scanning FSM control, implementing a better reading of the FSMs voltages, and fixing the Hexapod limitations.

The waveform generator currently used has been a limiting factor to achieving effective and smooth acquisition operations, mostly for its inability to interrupt an arbitrary scan in any of the scan points and resume a scan from any point of the arbitrary waveform, and the impossibility of receiving a signal with information on the current voltages provided at the outputs while the waveform is being generated. Replacing the DG4062 with a high-performance waveform generator or another piece of equipment capable of the functions mentioned previously would allow for the implementation of more complex procedures and strategies, as well as more accurate and fast responses to the commands.

The reading of the FSMs voltages is in part a consequence of the waveform generator limitations. Because of the inability of the waveform generator to provide information on the voltages at the outputs, the FSM driver outputs have to be used. However, the outputs have turned out to be very noisy, which required both physical filtering by means of a capacitor, and digital filtering in the control software. This additional elements reduce the response time of the system and make it more prone to errors and wrong readings. A better FSM voltage reading method would improve the link acquisition performance and is therefore recommended.

The final hardware element that would need improvement is the Hexapod, and specifically the ability of the Hexapod to perform certain movements and trajectories in a controlled way. This aspect in particular caused quite a few problems during the development of the thesis project, and it made it

impossible to perform telescope pointing strategies with the setup. Finding a solution to the Hexapod movement limitations would allow for the implementation of telescope pointing in the link acquisition, as well as the introduction of more complicated disturbances like spacecraft jitter.

For the link acquisition procedures recommendations, other than the details already discussed in Section 5.3, there are a number of new developments and improvements that could be adopted and implemented in the future:

- Telescope pointing link acquisitions would be an important addendum to the current pool of link acquisition strategies currently available for the OFMT setup.

- Dual scanning strategies implementation, by having one acquisition detector on each spacecraft, could open up the options of acquisition strategies even more, and simulations on the loss of one acquisition sensor could be performed, to demonstrate the fault tolerance of the setup.

- The implementation of GRACE-FO scenarios in which the acquisition sensor is not used would showcase the flexibility of the system and are therefore recommended.

- The OFMT architecture could be used for the experimentation of new and innovative scanning geometries.

- All of the previously mentioned scanning strategies and procedures, as well as those mentioned and implemented in the thesis work, would need to be tested in the future for their reliability, total acquisition time required, probability of acquisition and robustness against spacecraft jitter, all of which require numerous and long tests, that did not fit well in the limited time constraints of the thesis, but that definitely provide valuable insights and prove to be necessary for serious space-graded developments.

- The final recommendations regarding future link acquisition tests to be performed concerns the implementation of link acquisition tests under realistic space environment conditions. This requires the possibility of performing the tests in different thermal environments, at vacuum pressures and possibly completing full acquisitions from the initial offsets all the way to the engagement of science mode with the first displacement measurements between the terminals.

One final activity that could be carried out in the future to complement the results of the system would be a precise calibration of all the components, which is a lengthy process, but that would allow for the exact definition of the offsets and the errors which affect the setup.

7

Conclusion

The extensive research into the literature and the previously developed works in the fields of inter-satellite optical metrology and laser link acquisition experimental demonstrations highlighted the need for a new instrument architecture and an innovative testbed to experiment with link acquisition strategies and procedures. This led to the creation of the OMT and subsequently of the OFMT project, of which this thesis work is a part of, concentrating on the link acquisition procedure for the system. The research question identified is here reiterated and the answers to the respective subquestions are provided.

R.Q. : How can link acquisition strategies be recreated in the OFMT setup under realistic laboratory conditions?

- ***R.Q. 1: How can conditions in the lab be re-created realistically (especially with regards to the received beam), and how does the setup compare with previous link acquisition setups in this aspect?***

  The conditions in the lab can be re-created realistically by developing a free-space setup that allows for the preservation of the path length information, while using a lens system to enlarge the laser beam between the terminals and simulate a larger distance between the spacecraft. With special attention to assembly and alignment procedures, as detailed in Sections 4.1 and 5.1, it is possible to obtain satisfactory beam and wavefront quality, in terms of what can be achieved on ground, that lead to the creation of a system that covers a new path previously unexplored by other experimental architectures, as demonstrated in Section 5.1.5. The system still presents some limitations with respect to the beam representation, especially with regards to the wavefront shape and the beam diameter with respect to the aperture size, as demonstrated in Section 5.2.4, but it will not represent an issue once the full DWS engagement will be completed.

- ***R.Q. 2: How well can the OFMT setup perform autonomous link acquisition strategies and procedures?*** The OFMT setup can successfully perform link acquisition procedures, as demonstrated in Section 5.2, a result achieved by developing the necessary infrastructure to conduct such tests, detailed in Sections 4.2, 4.4 and 4.5. Further testing activities and hardware developments are envisioned and have been explored as future recommendations in Chapter 6.

- ***R.Q. 3: What requirements does the OFMT link acquisition procedure put on the instrument's hardware?*** The OFMT link acquisition setup has demonstrated to benefit greatly from the combination of an in-field-pointing architecture using FSMs and dedicated acquisition sensors, which have naturally become recommended components of the instrument's hardware, as detailed in Section 5.3, along with additional considerations concerning the requirements on the acquisition strategy to ensure a successful laser link establishment between the terminals. The lessons learned proved to be relevant for all future projects involving link acquisition, and it represent the first step in the development of laser ranging instruments with a similar architecture.

The work described in the thesis allowed for the Research Questions set out at the start to be answered effectively, leading to the development of a new link acquisition testbed that allowed to gain valuable

insights into the design of inter-satellite optical metrology instruments and their related link acquisition procedures, and that shows great potential for future improvements, in a field that is seeing growing scientific interest in recent years and that is in need of new and rapidly developing technological solutions.

References

[1] Filippo Ales et al. "Line of Sight Alignment Algorithms for Future Gravity Missions". In: *AIAA Guidance, Navigation, and Control Conference* (Jan. 2015). DOI: `10.2514/6.2015-0094`.

[2] M Armano et al. "LISA Pathfinder: the experiment and the route to LISA". In: *Classical and Quantum Gravity* 26 (Apr. 2009), p. 094001. DOI: `10.1088/0264-9381/26/9/094001`. (Visited on 03/26/2024).

[3] Peter Bårmann. "Development of a Heterodyne Laser Interferometer for Very Small High Frequency Displacements Detection". PhD thesis. Oct. 1992. URL: `https://inis.iaea.org/collection/NCLCollectionStore/_Public/24/075/24075615.pdf` (visited on 04/02/2024).

[4] Charlotte Bond et al. "Interferometer techniques for gravitational-wave detection". In: *Living Reviews in Relativity* 19 (Dec. 2016). DOI: `10.1007/s41114-016-0002-8`.

[5] Christopher Boucher. *Curve Fitting of Solution Data in COMSOL Multiphysics®*. COMSOL, 2021. URL: `https://www.comsol.com/blogs/curve-fitting-of-solution-data-in-comsol-multiphysics` (visited on 09/24/2024).

[6] Kristian Breili and Cecilie Rolstad. "Ground-based gravimetry for measuring small spatial-scale mass changes on glaciers". In: *Annals of Glaciology* 50 (2009), pp. 141–147. DOI: `10.3189/172756409787769717`. (Visited on 07/07/2021).

[7] LIGO Caltech. *What are Gravitational Waves?* LIGO Lab | Caltech, 2019. URL: `https://www.ligo.caltech.edu/page/what-are-gw`.

[8] Marco Ciccu. "Development, Implementation and Test of Different Acquisition Strategies for LISA". PhD thesis. Apr. 2007. URL: `https://core.ac.uk/display/14693367` (visited on 03/26/2024).

[9] Francesca Cirillo. "Controller Design for the Acquisition Phase of the LISA Mission using a Kalman Filter". PhD thesis. July 2007. URL: `https://etd.adm.unipi.it/t/etd-06202007-101808/` (visited on 03/26/2024).

[10] Francesca Cirillo and Peter F Gath. "Control system design for the constellation acquisition phase of the LISA mission". In: *Journal of Physics: Conference Series* 154 (Mar. 2009), p. 012014. DOI: `10.1088/1742-6596/154/1/012014`. (Visited on 03/26/2024).

[11] Newport Corporation. *FSM-300-01 Fast Steering Mirror System*. Newport.com, 2024. URL: `https://www.newport.com/p/FSM-300-01` (visited on 10/05/2024).

[12] K. Danzmann. "LISA mission overview". In: *Advances in Space Research* 25 (Jan. 2000), pp. 1129–1136. DOI: `10.1016/s0273-1177(99)00973-4`. (Visited on 08/19/2021).

[13] Karsten Danzmann et al. "Laser ranging interferometer for GRACE follow-on". In: *International Conference on Space Optics — ICSO 2012* (Nov. 2017). Ed. by Errico Armandillo, Nikos Karafolas, and Bruno Cugny. DOI: `10.1117/12.2309099`. (Visited on 03/26/2024).

[14] The Editors of Encyclopaedia Britannica. *Michelson interferometer*. Encyclopedia Britannica. URL: `https://www.britannica.com/technology/Michelson-interferometer` (visited on 04/02/2024).

[15] William M Folkner and David J Seidel. "Gravitational Wave Missions from LISA to Big Bang Observer". In: *Collection of Technical Papers - AIAA Space 2005 Conference and Exposition* 1 (June 2005). DOI: `10.2514/6.2005-6711`. (Visited on 03/27/2024).

[16] Ruihong Gao et al. "Laser acquisition experimental demonstration for space gravitational wave detection missions". In: *Optics Express* 29 (Feb. 2021), p. 6368. DOI: `10.1364/oe.414741`. (Visited on 03/26/2024).

[17] Ruihong Gao et al. "On-ground demonstration of laser-link construction for space-based detection of gravitational waves". In: *Optics and lasers in engineering* 160 (Jan. 2023), pp. 107287–107287. DOI: `10.1016/j.optlaseng.2022.107287`. (Visited on 04/18/2024).

[18]   Guillaume Gey, Guillaume Dovillaire, and Mathias Bach. *Simple alignment of complex laboratory optics using a HASO3 wavefront sensor*. Imagine Optic. URL: `https://photonlines.co.uk/wp-content/uploads/2020/08/imagine-optic_application-note_simple-alignment-of-optical-setup-using-haso3.pdf` (visited on 08/14/2024).

[19]   A Görth et al. "Test environments for the GRACE follow-on laser ranging interferometer". In: *Journal of Physics: Conference Series* 716 (May 2016). DOI: `10.1088/1742-6596/716/1/012011`. (Visited on 04/17/2024).

[20]   Max Planck Institute for Gravitational Physics. *LISA reaches a crucial milestone*. www.aei.mpg.de. URL: `https://www.aei.mpg.de/919602/lisa-erreicht-entscheidenden-meilenstein` (visited on 03/27/2024).

[21]   Gerald Hechenblaikner. "Analysis of performance and robustness against jitter of various search methods for acquiring optical links in space". In: *Applied optics* 60 (Apr. 2021), pp. 3936–3936. DOI: `10.1364/ao.419594`. (Visited on 04/09/2024).

[22]   NASA JPL. Nasa.gov, 2018. URL: `https://gracefo.jpl.nasa.gov/system/resources/detail_files/36_GRACE_FO_final_1600.jpg` (visited on 08/14/2024).

[23]   NASA JPL. *GRACE-FO | Mission*. GRACE Tellus. URL: `https://grace.jpl.nasa.gov/mission/grace-fo/#:~:text=GRACE%2DFO%20was%20injected%20into` (visited on 04/08/2024).

[24]   Alexander Koch. "Link Acquisition and Optimization for Intersatellite Laser Interferometry". PhD thesis. Feb. 2020. URL: `https://www.repo.uni-hannover.de/handle/123456789/9856` (visited on 03/26/2024).

[25]   Alexander Koch et al. "Line of sight calibration for the laser ranging interferometer on-board the GRACE Follow-On mission: on-ground experimental validation". In: *Optics Express* 26 (Sept. 2018), p. 25892. DOI: `10.1364/oe.26.025892`. (Visited on 03/26/2023).

[26]   Richard P. Kornfeld et al. "GRACE-FO: The Gravity Recovery and Climate Experiment Follow-On Mission". In: *Journal of Spacecraft and Rockets* 56 (May 2019), pp. 931–951. DOI: `10.2514/1.a34326`. (Visited on 09/09/2021).

[27]   Ariane Kujau. *Geoid: Die Potsdamer Schwerekartoffel*. www.gfz-potsdam.de. URL: `https://www.gfz-potsdam.de/presse/infothek/mediathek/bilder/geoid-die-potsdamer-schwerekartoffel` (visited on 03/26/2024).

[28]   Felix W. Landerer et al. "Extending the Global Mass Change Data Record: GRACE Follow␣On Instrument and Science Data Performance". In: *Geophysical Research Letters* 47 (June 2020). DOI: `10.1029/2020gl088306`.

[29]   Lauri Lipiäinen, Kimmo Kokkonen, and Matti Kaivola. "Homodyne full-field interferometer for measuring dynamic surface phenomena in microstructures". In: *Optics and Lasers in Engineering* 88 (Aug. 2016), pp. 178–183. DOI: `10.1016/j.optlaseng.2016.08.004`. URL: `https://www.sciencedirect.com/science/article/abs/pii/S0143816616301646` (visited on 10/25/2024).

[30]   Andrea N. Lommen. "Pulsar timing for gravitational wave detection". In: *Nature Astronomy* 1 (Dec. 2017), pp. 809–811. DOI: `10.1038/s41550-017-0324-9`. (Visited on 04/10/2022).

[31]   DLR (Deutsche Zentrum für Luft- und Raumfahrt). *GRACE-C – German-US-American environmental mission has been extended*. www.dlr.de. URL: `https://www.dlr.de/en/latest/news/2024/grace-c-german-us-american-environmental-mission-has-been-extended` (visited on 03/27/2024).

[32]   Ziren Luo et al. "The Taiji program: A concise overview". In: *Progress of Theoretical and Experimental Physics* 2021 (July 2020). DOI: `10.1093/ptep/ptaa083`. (Visited on 03/26/2024).

[33]   Christoph Mahrdt. "Laser link acquisition for the GRACE follow-on laser ranking interferometer". PhD thesis. Jan. 2014. URL: `https://d-nb.info/1053573553/04` (visited on 03/2024).

[34]   Oliver Mandel. "Optical Metrology Terminal for Satellite-to-Satellite Laser Ranging". PhD thesis. Jan. 2022. URL: `https://media.suub.uni-bremen.de/bitstream/elib/5791/1/OMT_Mandel_diss.pdf` (visited on 03/26/2024).

[35] Jianwei Mei et al. "The TianQin project: Current progress on science and technology". In: *Progress of Theoretical and Experimental Physics* 2021 (Aug. 2020). DOI: `10.1093/ptep/ptaa114`. (Visited on 03/26/2024).

[36] Asloob Mudassar. *Laser Physics*. Aug. 2015. URL: `https://www.researchgate.net/publication/281235580_Laser_Physics` (visited on 09/23/2024).

[37] K. Nicklaus et al. "Optical bench of the laser ranging interferometer on grace follow-on". In: *International Conference on Space Optics — ICSO 2014* (Nov. 2017). Ed. by Bruno Cugny, Zoran Sodnik, and Nikos Karafolas. DOI: `10.1117/12.2304195`. (Visited on 03/26/2024).

[38] Kolja Nicklaus et al. "Towards NGGM: Laser Tracking Instrument for the Next Generation of Gravity Missions". In: *Remote Sensing* 14 (Aug. 2022), p. 4089. DOI: `10.3390/rs14164089`. (Visited on 03/26/2024).

[39] Dr Rüdiger Paschotta. *Optical Aberrations*. www.rp-photonics.com. URL: `https://www.rp-photonics.com/optical_aberrations.html` (visited on 05/02/2022).

[40] Dr Rüdiger Paschotta. *Polarization of Light*. www.rp-photonics.com. URL: `https://www.rp-photonics.com/polarization_of_light.html` (visited on 04/24/2022).

[41] R Paschotta. *Beat Note*. RP Photonics AG, Jan. 2005. URL: `https://www.rp-photonics.com/beat_note.html` (visited on 04/03/2024).

[42] R Paschotta. *Interference*. RP Photonics AG, Feb. 2005. URL: `https://www.rp-photonics.com/interference.html` (visited on 04/04/2024).

[43] R Paschotta. *Optical Heterodyne Detection*. RP Photonics AG, Oct. 2009. URL: `https://www.rp-photonics.com/optical_heterodyne_detection.html` (visited on 04/03/2024).

[44] Rüdiger Paschotta. *Beam Quality*. www.rp-photonics.com. URL: `https://www.rp-photonics.com/beam_quality.html` (visited on 04/21/2021).

[45] Rüdiger Paschotta. *Coherence*. URL: `https://www.rp-photonics.com/coherence.html`.

[46] Rüdiger Paschotta. *Laser Beams*. www.rp-photonics.com. URL: `https://www.rp-photonics.com/laser_beams.html` (visited on 02/02/2022).

[47] Rüdiger Paschotta. *RP Photonics Encyclopedia - Gaussian beams, laser beam, fundamental transverse modes*. Rp-photonics.com, June 2019. URL: `https://www.rp-photonics.com/gaussian_beams.html` (visited on 07/02/2019).

[48] Rüdiger Paschotta. *Wavefronts*. www.rp-photonics.com. URL: `https://www.rp-photonics.com/wavefronts.html` (visited on 05/02/2022).

[49] Karl F Renk. *BASICS OF LASER PHYSICS : for students of science and engineering.* Springer International Publishing AG, 2019.

[50] Co. Ltd. RIGOL Technologies. *DG4000-RIGOL Technologies, Co. Ltd.* Rigol.com, 2019. URL: `https://eu.rigol.com/eu/products/DG_detail/DG` (visited on 09/17/2024).

[51] S. Rosat and J. Hinderer. "Limits of Detection of Gravimetric Signals on Earth". In: *Scientific Reports* 8 (Oct. 2018), p. 15324. DOI: `10.1038/s41598-018-33717-z`. URL: `https://www.nature.com/articles/s41598-018-33717-z`.

[52] A Saleh and Malvin Carl Teich. *Fundamentals of Photonics*. 2nd ed. Wiley-Interscience, Mar. 2007.

[53] Josep Sanjuan et al. "Interspacecraft link simulator for the laser ranging interferometer onboard GRACE Follow-On". In: *Applied Optics* 54 (July 2015), p. 6682. DOI: `10.1364/ao.54.006682`. (Visited on 04/17/2024).

[54] V. Saptari. *Fourier-Transform Spectroscopy Instrumentation Engineering*. SPIE Press, Nov. 2003.

[55] Michael Scheinfeild and N Kopeika. *Acquisition System for Microsatellites Laser Communication in Space.* 2000. (Visited on 03/26/2024).

[56] Michael Scheinfeild, Norman S Kopeika, and Arnon Shlomi. "Acquisition time calculation and influence of vibrations for microsatellite laser communication in space</title>". In: *Proceedings of SPIE* 4365 (Aug. 2001). DOI: `10.1117/12.438047`. (Visited on 03/26/2024).

[57] B. S. Sheard et al. "Intersatellite laser ranging instrument for the GRACE follow-on mission". In: *Journal of Geodesy* 86 (May 2012), pp. 1083–1095. DOI: `10.1007/s00190-012-0566-3`. (Visited on 03/26/2024).

[58] B. D. Tapley. "GRACE Measurements of Mass Variability in the Earth System". In: *Science* 305 (July 2004), pp. 503–505. DOI: `10.1126/science.1099192`.

[59] B. D. Tapley et al. "The gravity recovery and climate experiment: Mission overview and early results". In: *Geophysical Research Letters* 31 (May 2004), n/a–n/a. DOI: `10.1029/2004gl019920`.

[60] Ernie Tretkoff. *This Month in Physics History*. @apsphysics, 2019. URL: `https://www.aps.org/publications/apsnews/200606/history.cfm` (visited on 03/26/2024).

[61] Junya Wang, Gaofei Zhang, and Zheng You. "Design rules for dense and rapid Lissajous scanning". In: *Microsystems Nanoengineering* 6 (Nov. 2020). DOI: `10.1038/s41378-020-00211-4`.

[62] Xuan Wang et al. "Beam Scanning and Capture of Micro Laser Communication Terminal Based on MEMS Micromirrors". In: *Micromachines* 14 (June 2023), p. 1317. DOI: `10.3390/mi14071317`. (Visited on 03/26/2024).

[63] L. Wörner et al. "MaQuIs—Concept for a Mars Quantum Gravity Mission". In: *Planetary and Space Science* 239 (Dec. 2023), pp. 105800–105800. DOI: `10.1016/j.pss.2023.105800`. (Visited on 03/26/2024).

[64] Danielle Wuchenich. "Inter-Satellite Laser Interferometry". PhD thesis. Feb. 2014.

[65] Danielle Wuchenich et al. "Laser link acquisition demonstration for the GRACE Follow-On mission". In: *Optics express* 22 (May 2014), pp. 11351–11351. DOI: `10.1364/oe.22.011351`. (Visited on 04/09/2024).

[66] Jing-Yi Zhang et al. "Inter-satellite laser link acquisition with dual-way scanning for Space Advanced Gravity Measurements mission". In: *Review of Scientific Instruments* 89 (June 2018). DOI: `10.1063/1.5019433`. (Visited on 04/09/2024).

[67] Maria T. Zuber et al. "Gravity field of the Moon from the Gravity Recovery and Interior Laboratory (GRAIL) mission". In: *Science (New York, N.Y.)* 339 (Feb. 2013), pp. 668–671. DOI: `10.1126/science.1231507`. URL: `https://pubmed.ncbi.nlm.nih.gov/23223395/` (visited on 11/09/2022).

A
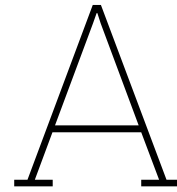
Waveform generator code

In this Appendix a few pieces of the code written to control the waveform generator are provided, concentrating especially on the parts where SCPI commands are sent and received.

Querying the instrument to get the status of the outputs.

```
1   ViChar *output_1_query;
2   output_1_query = ":OUTPut1?\n"; // Query for the status of OUTPUT 1 (ON/OFF)
3
4   ViChar *output_2_query;
5   output_2_query = ":OUTPut2?\n"; // Query for the status of OUTPUT 1 (ON/OFF)
6
7   status = viWrite(instr,(ViBuf)output_1_query, strlen(output_1_query),&retCount); //
        Writing query signal to the instrument
8   if (status<VI_SUCCESS){
9       emit Channel1Status("Query␣of␣outputs␣status␣failed");
10  }
11
12  ViChar Output_1_status[1024];
13  QString output_1_status;
14  status = viRead(instr,(ViBuf)Output_1_status,strlen(Output_1_status),&retCount); //
        Reading the instrument response, then saved in Output_1_status
15  if (status < VI_SUCCESS){
16      emit Channel1Status("Error␣reading␣the␣status␣of␣the␣Output");
17  } else {
18      output_1_status = QString::fromUtf8(Output_1_status);
19  }
20
21  // Same query and reading procedure performed for the second output
22  status = viWrite(instr,(ViBuf)output_2_query, strlen(output_2_query),&retCount);
23  if (status<VI_SUCCESS){
24      emit Channel2Status("Query␣of␣outputs␣status␣failed");
25  }
26
27  ViChar Output_2_status[1024];
28  QString output_2_status;
29  status = viRead(instr,(ViBuf)Output_2_status,strlen(Output_1_status),&retCount);
30  if (status < VI_SUCCESS){
31      emit Channel2Status("Error␣reading␣the␣status␣of␣the␣Output");
32  } else {
33      output_2_status = QString::fromUtf8(Output_2_status);
34  }
35
36  // Check the status of the outputs comparing with the keyword "ON". Sends signal to
        update UI
37  if (output_1_status.startsWith("ON\n")) {
38      emit Channel1ON(true);
39  } else {
40      emit Channel1ON(false);
41  }
```

```
42
43     if (output_2_status.startsWith("ON\n")) {
44         emit Channel2ON(true);
45     } else {
46         emit Channel2ON(false);
47     }
48
49     if (output_1_status.startsWith("ON\n") && output_2_status.startsWith("ON\n")) {
50         emit ChannelsON(true);
51     } else {
52         emit ChannelsON(false);
53     }
54 }
```

Loading file with arbitrary points to the waveform generator.

```
1  void WaveformGeneratorWorker::LoadFile(QString filename) {
2      ViStatus status;
3      ViUInt32 retCount;
4
5      // Definition of variables for the waveform. The file will be read and the lines saved in
            these variables
6      char points_1[32768];
7      char points_2[32768];
8      char period_1[1024];
9      char period_2[1024];
10     char amplitude_1[1024];
11     char amplitude_2[1024];
12
13     pointsChannel1.clear();
14     pointsChannel2.clear();
15
16     QFile file(filename);
17
18     // Check if file with this name exists in the directory
19     if(!file.exists()){
20         emit LoadFileStatus("Error - the file doesn't exist");
21     }
22
23     // Read file and assign strings to the appropriate variables
24     if (file.open(QFile::ReadOnly)) {
25         // Read fist line, with points for the first channel
26         qint64 lineLength1 = file.readLine(points_1, sizeof(points_1));
27
28         // Check if reading operation failed
29         if (lineLength1 == -1){
30             emit LoadFileStatus("Error in reading file line 1");
31         }
32
33         QString points1 = QString::fromUtf8(points_1);
34         QStringList parts = points1.split(',');
35         for (int i=1; i < parts.size(); i++) {
36             bool ok;
37             QString str = parts[i];
38             double num = str.toDouble(&ok);
39             if (ok) {
40                 pointsChannel1.append(num);
41             }
42         }
43
44         // Read second line, with points for the second channel
45         qint64 lineLength2 = file.readLine(points_2, sizeof(points_2));
46
47         // Check if reading operation failed
48         if (lineLength2 == -1){
49             emit LoadFileStatus("Error in reading file line 2");
50         }
51
52         parts.clear();
53         QString points2 = QString::fromUtf8(points_2);
54         parts = points2.split(',');
```

```
55          for (int i=1; i < parts.size(); i++) {
56              bool ok;
57              QString str = parts[i];
58              double num = str.toDouble(&ok);
59              if (ok) {
60                  pointsChannel2.append(num);
61              }
62          }
63          // Read third line, with period for the first channel
64          qint64 lineLength3 = file.readLine(period_1, sizeof(period_1));
65
66          // Check if reading operation failed
67          if (lineLength3 == -1){
68              emit LoadFileStatus("Error␣in␣reading␣file␣line␣3");
69          }
70
71          parts.clear();
72          QString period1 = QString::fromUtf8(period_1);
73          parts = period1.split("␣");
74          for (int i=1; i < parts.size(); i++) {
75              bool ok;
76              QString str = parts[i];
77              double num = str.toDouble(&ok);
78              if (ok) {
79                  periodChannels = num;
80                  qDebug() << "Period:␣" << periodChannels << "\n";
81              }
82          }
83
84          // Read fourth line, with period for the second channel
85
86          qint64 lineLength4 = file.readLine(period_2, sizeof(period_2));
87
88          // Check if reading operation failed
89          if (lineLength4 == -1){
90              emit LoadFileStatus("Error␣in␣reading␣file␣line␣4");
91          }
92
93          // Read fifth line, with amplitude for the first channel
94
95          qint64 lineLength5 = file.readLine(amplitude_1, sizeof(amplitude_1));
96
97          // Check if reading operation failed
98          if (lineLength5 == -1){
99              emit LoadFileStatus("Error␣in␣reading␣file␣line␣5");
100         }
101
102         parts.clear();
103         QString amplitude1 = QString::fromUtf8(amplitude_1);
104         parts = amplitude1.split("␣");
105         for (int i=1; i < parts.size(); i++) {
106             bool ok;
107             QString str = parts[i];
108             double num = str.toDouble(&ok);
109             if (ok) {
110                 amplitudeChannel1 = num;
111                 qDebug() << "Amplitude␣1:␣" << amplitudeChannel1 << "\n";
112             }
113         }
114         // Read sixth line, with amplitude for the second channel
115
116         qint64 lineLength6 = file.readLine(amplitude_2, sizeof(amplitude_2));
117
118         // Check if reading operation failed
119         if (lineLength6 == -1){
120             emit LoadFileStatus("Error␣in␣reading␣file␣line␣6");
121         }
122
123         parts.clear();
124         QString amplitude2 = QString::fromUtf8(amplitude_2);
125         parts = amplitude2.split("␣");
```

```
126        for (int i=1; i < parts.size(); i++) {
127            bool ok;
128            QString str = parts[i];
129            double num = str.toDouble(&ok);
130            if (ok) {
131                amplitudeChannel2 = num;
132                qDebug() << "Amplitude 2: " << amplitudeChannel2 << "\n";
133            }
134        }
135
136    } else {
137        emit LoadFileStatus("Error opening the file");
138    }
139
140    // The lines written in the file are already full SCPI commands
141    //that do not need anything additional and just need to be sent to the instrument
142    // Set the periods, points and the amplitudes to the channels
143
144    // Period 1 setting
145    status = viWrite(instr, (ViBuf)period_1, strlen(period_1), &retCount);
146    //status = viWrite(instr, (ViBuf)"SOURce1:PERiod 327.000000\n", 27, &retCount);
147    if (status < VI_SUCCESS){
148        emit LoadFileStatus("Error setting period on channel 1 on ... Exiting");
149    }
150    // Points 1 setting
151    status = viWrite(instr, (ViBuf)points_1, strlen(points_1), &retCount);
152    if (status < VI_SUCCESS){
153        emit LoadFileStatus("Error setting points on output 1 on ... Exiting");
154    }
155    // Amplitude 1 setting
156    status = viWrite(instr, (ViBuf)amplitude_1, strlen(amplitude_1), &retCount);
157    if (status < VI_SUCCESS){
158        emit LoadFileStatus("Error setting amplitude on channel 1 on ... Exiting");
159    }
160    // Period 2 setting
161    status = viWrite(instr, (ViBuf)period_2, strlen(period_2), &retCount);
162    //status = viWrite(instr, (ViBuf)"SOURce2:PERiod 327.000000\n", 27, &retCount);
163    if (status < VI_SUCCESS){
164        emit LoadFileStatus("Error setting period on channel 2 on ... Exiting");
165    }
166    // Points 2 setting
167    status = viWrite(instr, (ViBuf)points_2, strlen(points_2), &retCount);
168    if (status < VI_SUCCESS){
169        emit LoadFileStatus("Error setting points on output 2 on ... Exiting");
170    }
171    // Amplitude 2 setting
172    status = viWrite(instr, (ViBuf)amplitude_2, strlen(amplitude_2), &retCount);
173    if (status < VI_SUCCESS){
174        emit LoadFileStatus("Error setting amplitude on channel 2 on ... Exiting");
175    }
176 }
```

Setting DC value on waveform generator

```
1  void WaveformGeneratorWorker::SetDCValue(double DC_x, double DC_y) {
2      ViStatus status;
3      ViUInt32 retCount;
4
5
6      // The double values are transformed into strings
7      std::string DC_X = std::to_string(DC_x);
8      std::string DC_Y = std::to_string(DC_y);
9
10     // Variables selecting the DC function type on the waveform generator are created ( in
           SCPI language )
11     ViChar *Wave_type_1;
12     Wave_type_1 = ":SOURce1:FUNCtion:SHAPe DC\n";
13     ViChar *Wave_type_2;
14     Wave_type_2 = ":SOURce2:FUNCtion:SHAPe DC\n";
15
16     // Full SCPI string to set the DC value is created
```

```
17
18     std::string DC_value_x = ":SOURce1:APPLy:USER␣0,0," + DC_X + ",0\n";
19     std::string DC_value_y = ":SOURce2:APPLy:USER␣0,0," + DC_Y + ",0\n";
20
21     // Strings of commands are transformed into ViChar types to be written on the instrument
22     ViChar DCX[DC_value_x.size()];
23     strcpy(DCX,DC_value_x.c_str());
24     ViChar DCY[DC_value_y.size()];
25     strcpy(DCY,DC_value_y.c_str());
26
27     // Wave type DC is set on output 1
28     status = viWrite(instr, (ViBuf)Wave_type_1, strlen(Wave_type_1), &retCount);
29     if (status < VI_SUCCESS){
30         emit Channel1Status("Error␣setting␣DC␣wave␣on␣Channel␣1");
31     }
32     // DC value for Channel 1 is set
33     status = viWrite(instr, (ViBuf)DCX, strlen(DCX), &retCount);
34     if (status < VI_SUCCESS){
35         emit Channel1Status("Error␣setting␣DC␣value␣on␣Channel␣1");
36     }
37
38     // Wave type DC is set on output 2
39     status = viWrite(instr, (ViBuf)Wave_type_2, strlen(Wave_type_2), &retCount);
40     if (status < VI_SUCCESS){
41         emit Channel2Status("Error␣setting␣DC␣wave␣on␣Channel␣2");
42     }
43   // DC value for Channel 2 is set
44     status = viWrite(instr, (ViBuf)DC_value_y.c_str(), strlen(DC_value_y.c_str()), &retCount)
           ;
45     if (status < VI_SUCCESS){
46         emit Channel2Status("Error␣setting␣DC␣value␣on␣Channel␣2");
47     }
```

Acquisition tests results

In this Appendix the test results that have not been included in the thesis are shown.

B.1. Offset 1
B.1.1. Scan type 2

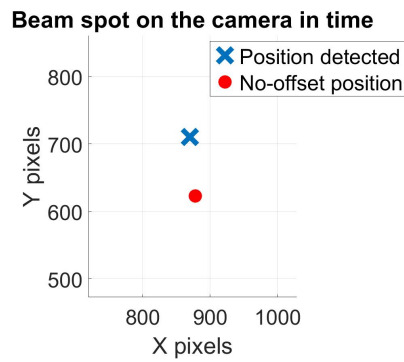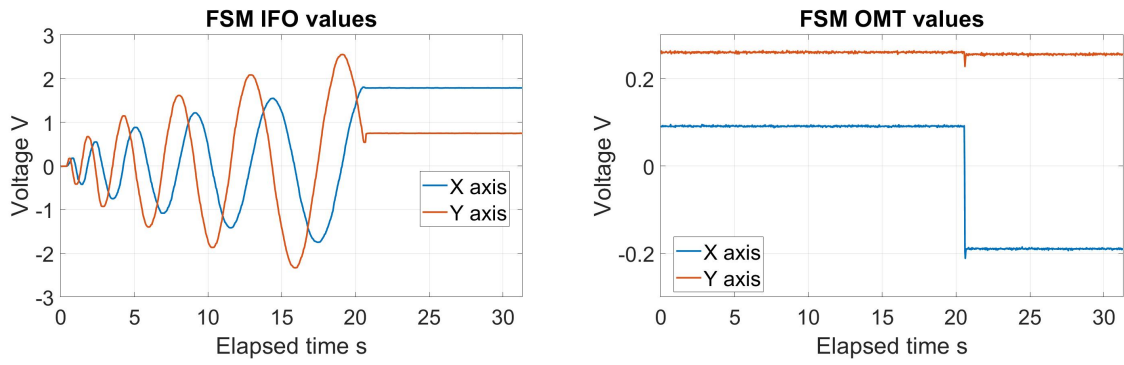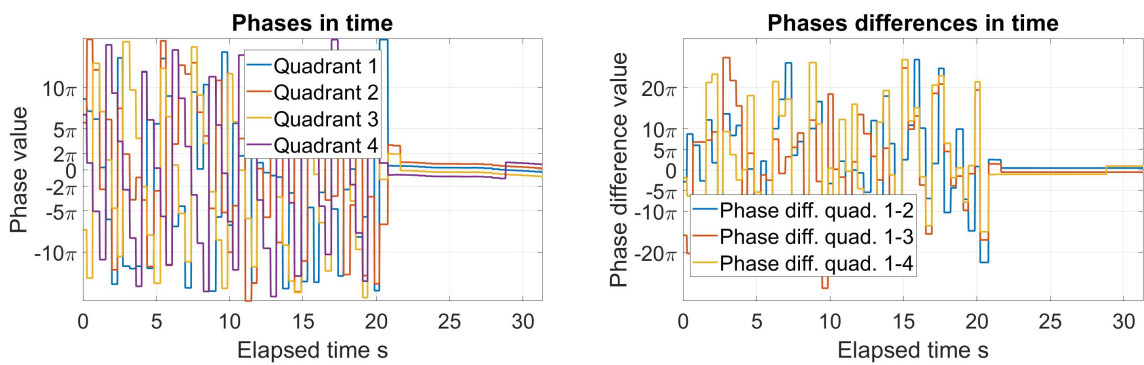**Beam spot on the camera in time**
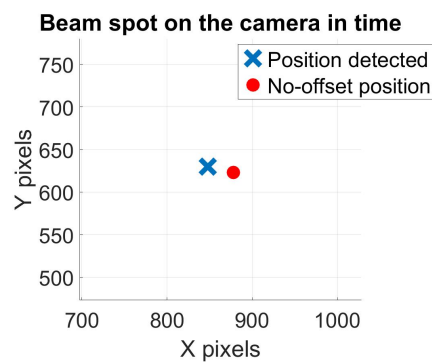
Figure B.1: Detection position on the detector for scan type 2 from the initial offset 1.
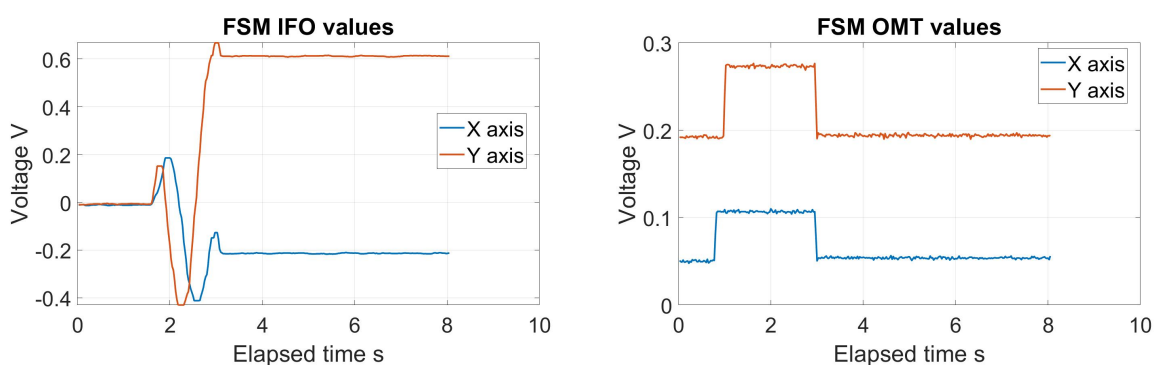
(a) FSM over the Hexapod voltage values during the acquisition test for scan type 2 and initial offset 1.

(b) FSM in the OMT voltage values during the acquisition test for scan type 2 and initial offset 1.

Figure B.2: FSM voltages for scan type 2 and initial offset 1.

Phases in time

(a) Phases values for scan type 2 and initial offset 1.

Phases differences in time

(b) Phase differences values for scan type 2 and initial offset 1.

Figure B.3: Phases and phase differences for scan type 2 and initial offset 1.
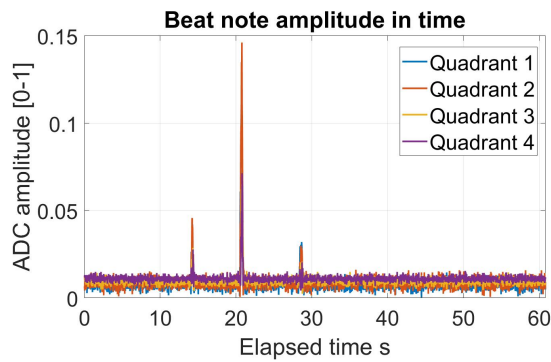
Beat note amplitude in time
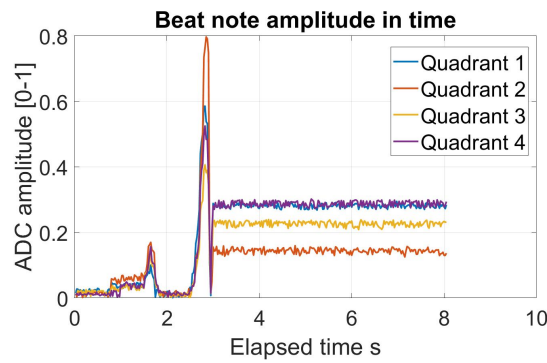
Figure B.4: Beat note intensity on the QPD for scan type 2 from the initial offset 1.
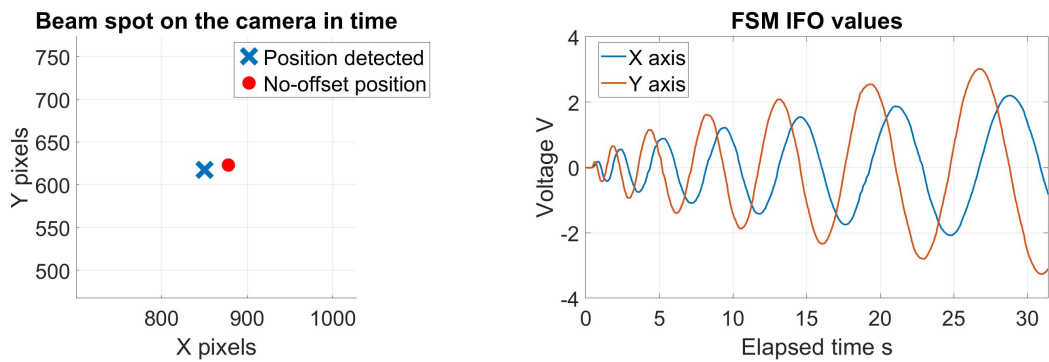
Beam spot on the camera in time

(a) Detection position on the detector for full scan type 2 from the initial offset 1.

FSM IFO values

(b) FSM over the Hexapod voltage values during the acquisition test for full scan type 2 and initial offset 1.

Figure B.5: Detector and FSM results for full scan type 2 and initial offset 1.
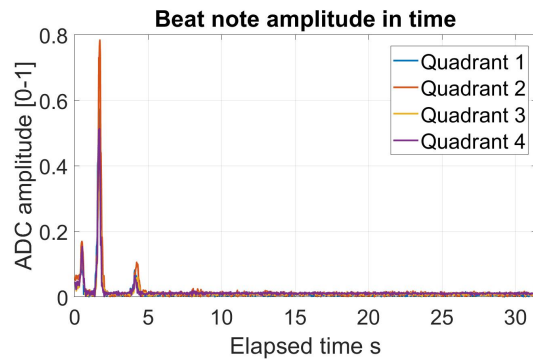
Figure B.6: Beat note intensity on the QPD for full scan type 2 from the initial offset 1.
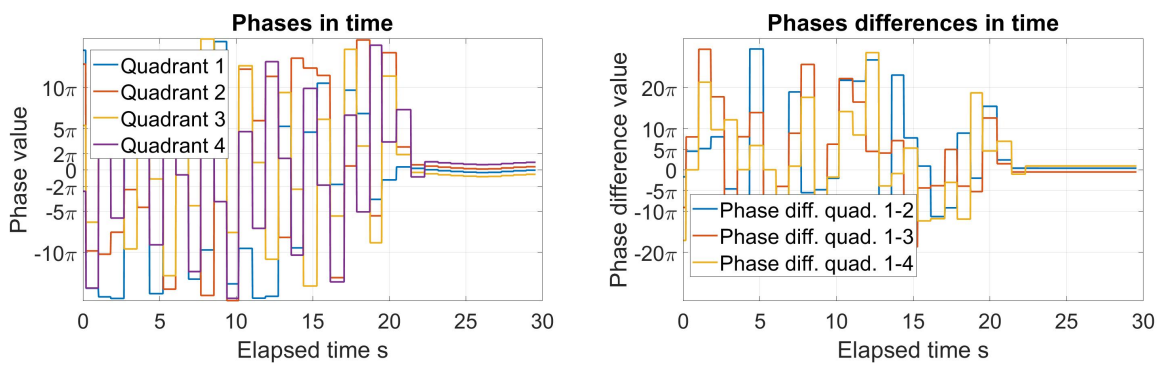
B.1.2. Scan type 3
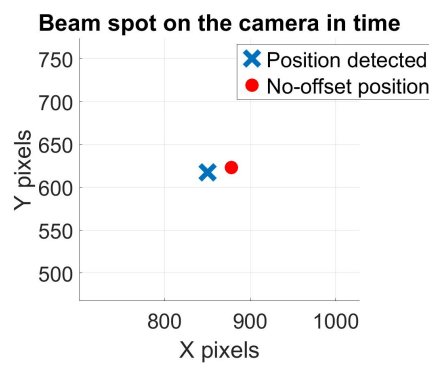
Figure B.7: Detection position on the detector for scan type 3 from the initial offset 1.
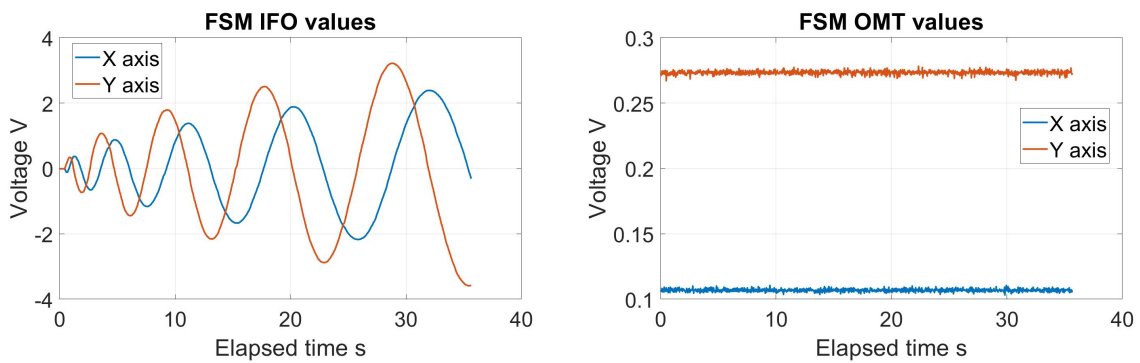
(a) FSM over the Hexapod voltage values during the acquisition test for scan type 3 and initial offset 1.

(b) FSM in the OMT voltage values during the acquisition test for scan type 3 and initial offset 1.

Figure B.8: FSM voltages for scan type 3 and initial offset 1.
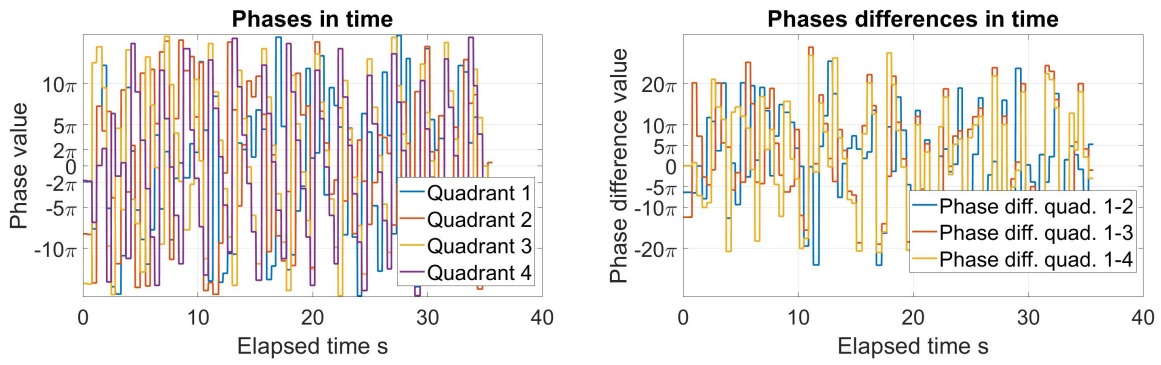
(a) Phases values for scan type 3 and initial offset 1.

(b) Phase differences values for scan type 3 and initial offset 1.

Figure B.9: Phases and phase differences for scan type 3 and initial offset 1.
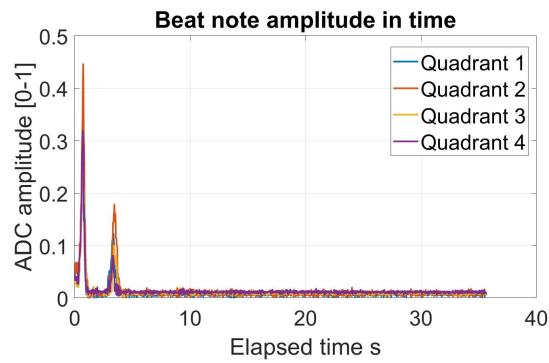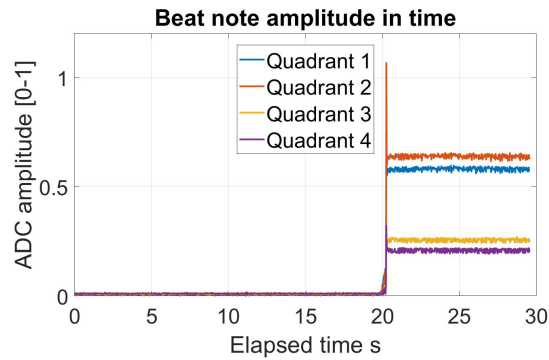

Figure B.10: Beat note intensity on the QPD for scan type 3 from the initial offset 1.
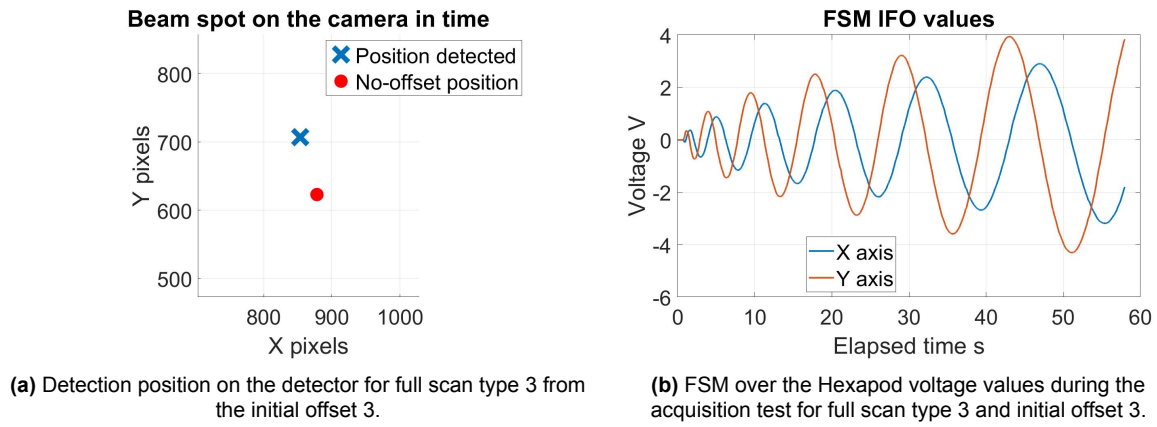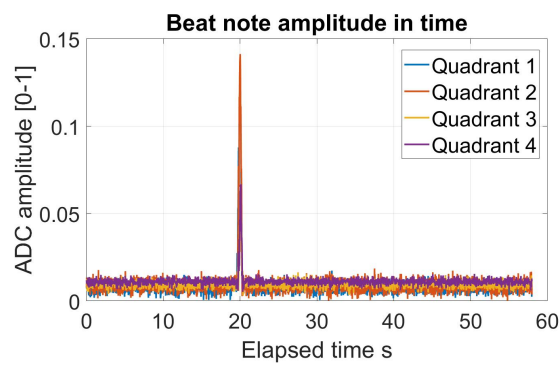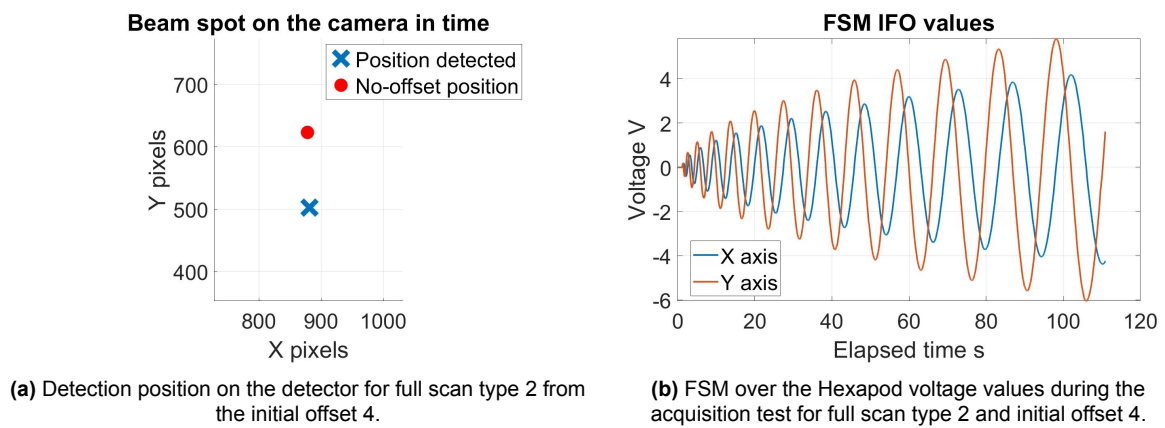
B.2. Offset 3

B.2.1. Scan type 2

Figure B.11: Detection position on the detector for scan type 2 from the initial offset 3.

(a) FSM over the Hexapod voltage values during the acquisition test for scan type 2 and initial offset 3.

(b) FSM in the OMT voltage values during the acquisition test for scan type 2 and initial offset 3.

Figure B.12: FSM voltages for scan type 2 and initial offset 3.

(a) Phases values for scan type 2 and initial offset 3.

(b) Phase differences values for scan type 2 and initial offset 3.

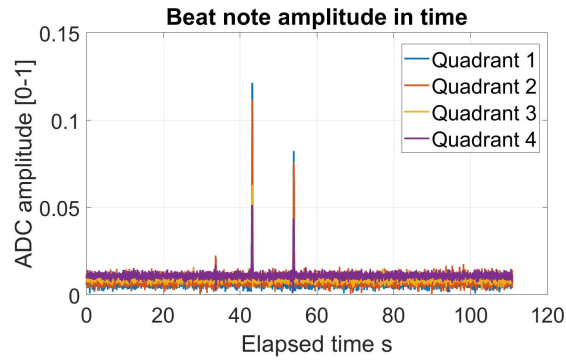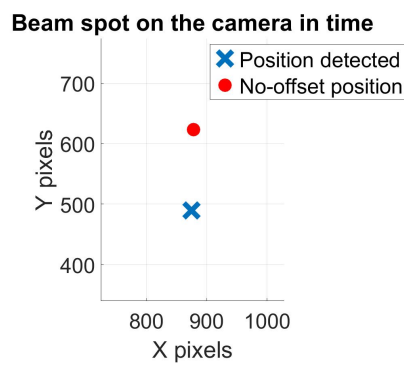**Figure B.13:** Phases and phase differences for scan type 2 and initial offset 3.
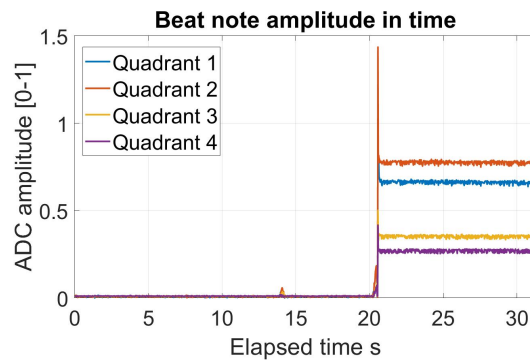
Figure B.14: Beat note intensity on the QPD for scan type 2 from the initial offset 3.
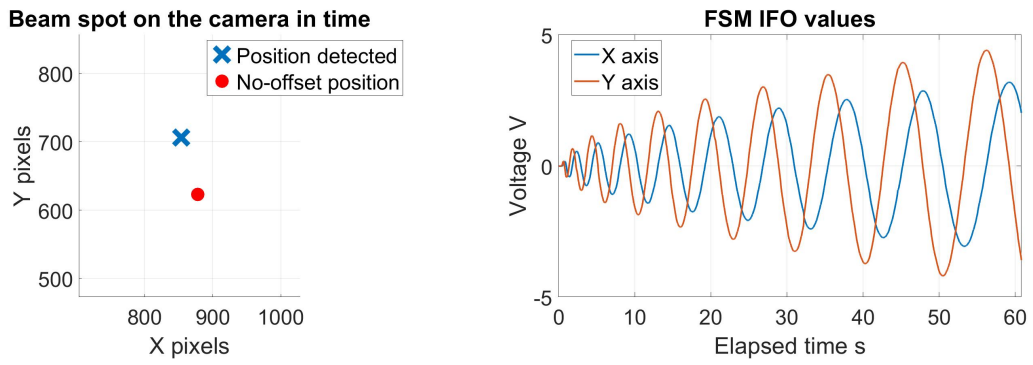
Beam spot on the camera in time

(a) Detection position on the detector for full scan type 2 from the initial offset 3.

FSM IFO values

(b) FSM over the Hexapod voltage values during the acquisition test for full scan type 2 and initial offset 3.

Figure B.15: Detector and FSM results for full scan type 2 and initial offset 3.

Beat note amplitude in time

Figure B.16: Beat note intensity on the QPD for full scan type 2 from the initial offset 3.

B.2.2. Scan type 3
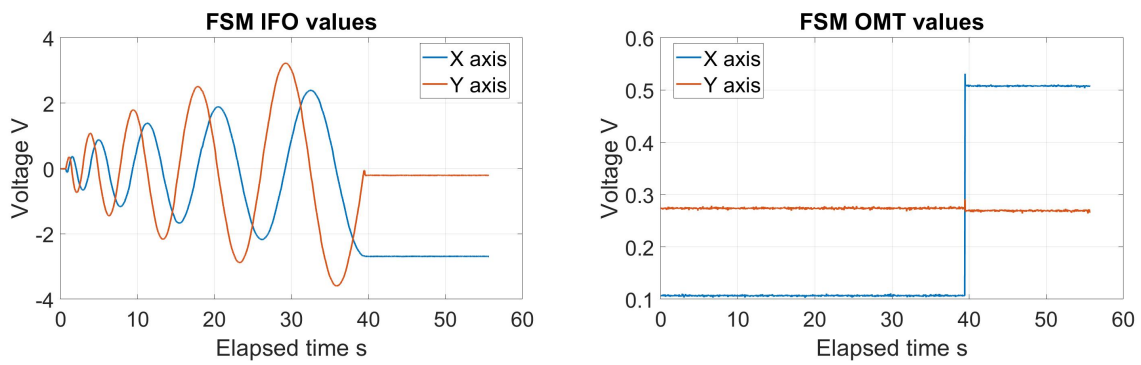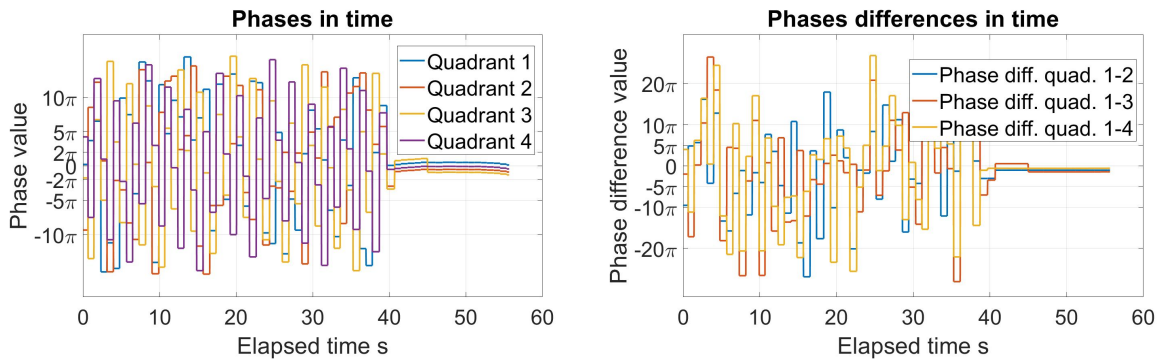
Beam spot on the camera in time
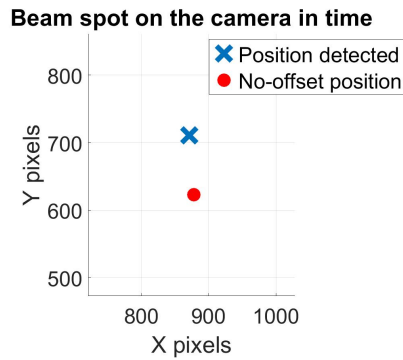
Figure B.17: Detection position on the detector for scan type 3 from the initial offset 3.
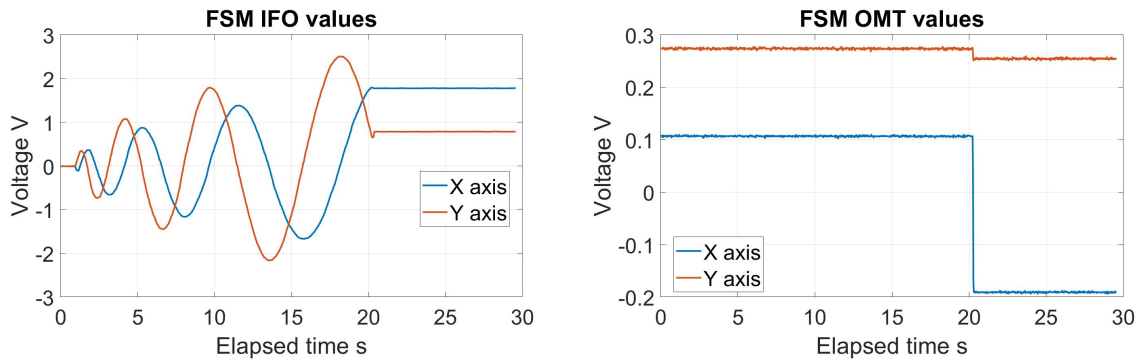
(a) FSM over the Hexapod voltage values during the acquisition test for scan type 3 and initial offset 3.

(b) FSM in the OMT voltage values during the acquisition test for scan type 3 and initial offset 3.

Figure B.18: FSM voltages for scan type 3 and initial offset 3.

(a) Phases values for scan type 3 and initial offset 3.

(b) Phase differences values for scan type 3 and initial offset 3.

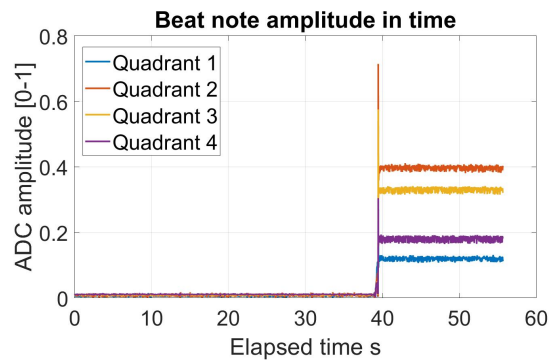**Figure B.19:** Phases and phase differences for scan type 3 and initial offset 3.

Figure B.20: Beat note intensity on the QPD for scan type 3 from the initial offset 3.

Beam spot on the camera in time

(a) Detection position on the detector for full scan type 3 from the initial offset 3.

FSM IFO values

(b) FSM over the Hexapod voltage values during the acquisition test for full scan type 3 and initial offset 3.

**Figure B.21:** Detector and FSM results for full scan type 3 and initial offset 3.

Beat note amplitude in time

Figure B.22: Beat note intensity on the QPD for full scan type 3 from the initial offset 3.

B.3. Offset 4

B.3.1. Scan type 2

Beam spot on the camera in time

(a) Detection position on the detector for full scan type 2 from the initial offset 4.

FSM IFO values

(b) FSM over the Hexapod voltage values during the acquisition test for full scan type 2 and initial offset 4.

Figure B.23: Detector and FSM results for full scan type 2 and initial offset 4.

Figure B.24: Beat note intensity on the QPD for full scan type 2 from the initial offset 4.

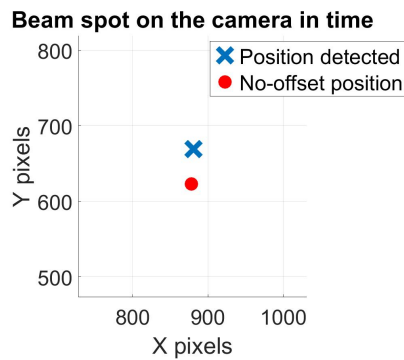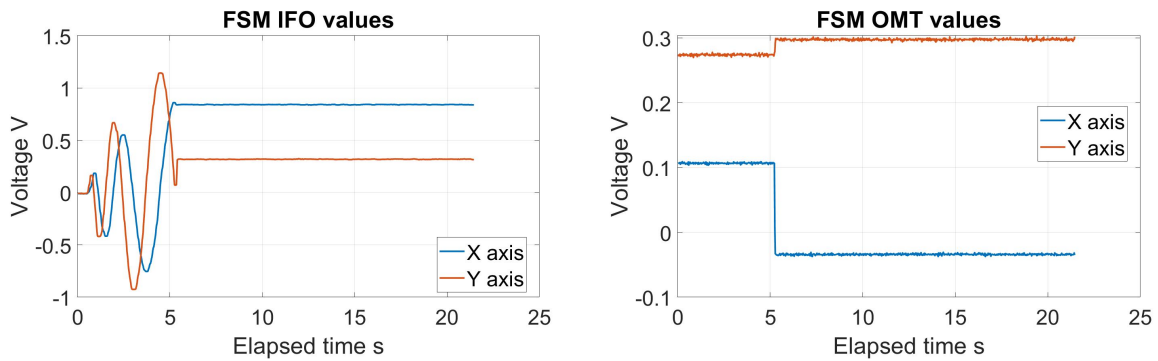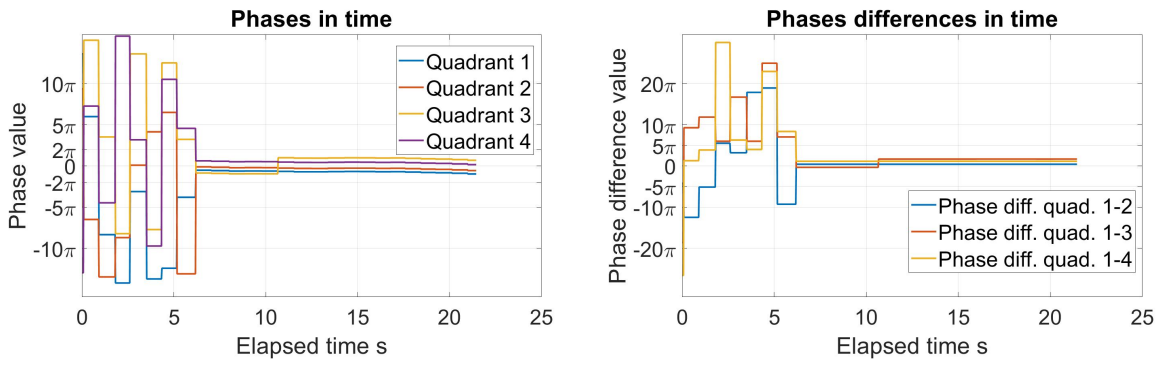## B.3.2. Scan type 3

Figure B.25: Detection position on the detector for scan type 3 from the initial offset 4.

(a) FSM over the Hexapod voltage values during the acquisition test for scan type 3 and initial offset 4.

(b) FSM in the OMT voltage values during the acquisition test for scan type 3 and initial offset 4.

Figure B.26: FSM voltages for scan type 3 and initial offset 4.

(a) Phases values for scan type 3 and initial offset 4.

(b) Phase differences values for scan type 3 and initial offset 4.

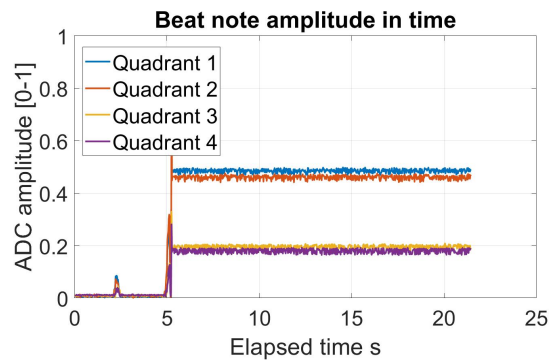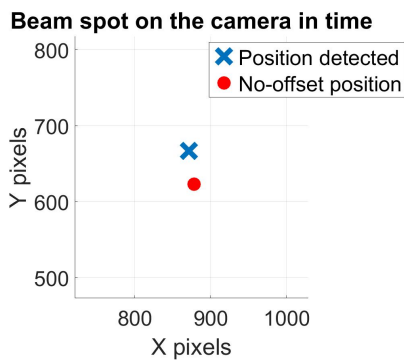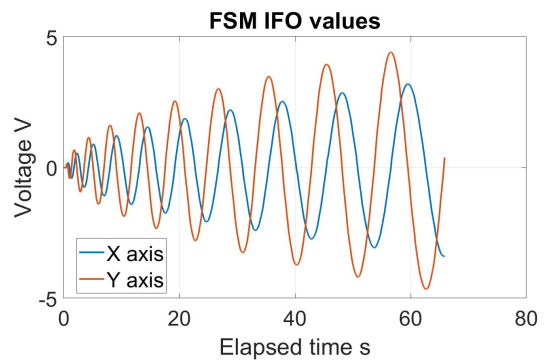**Figure B.27:** Phases and phase differences for scan type 3 and initial offset 4.

Figure B.28: Beat note intensity on the QPD for scan type 3 from the initial offset 4.
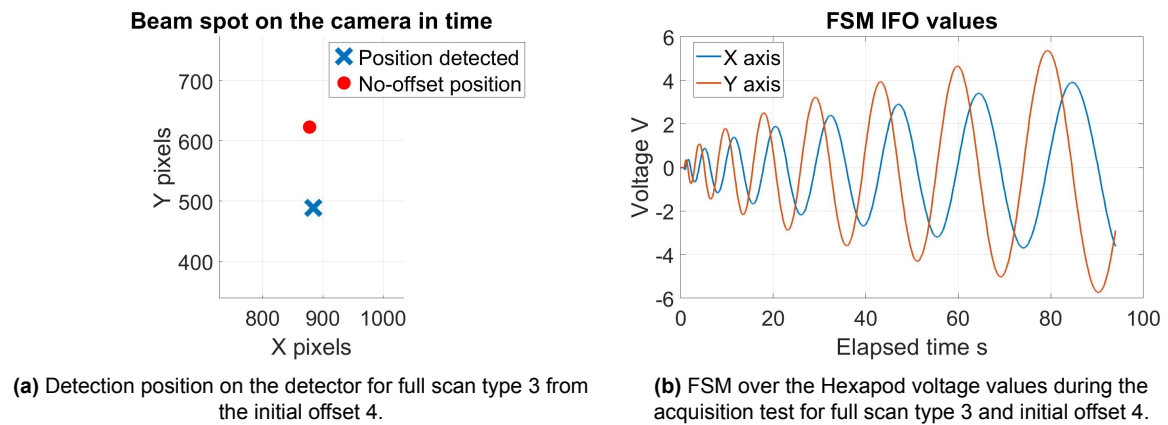
(a) Detection position on the detector for full scan type 3 from the initial offset 4.

(b) FSM over the Hexapod voltage values during the acquisition test for full scan type 3 and initial offset 4.

Figure B.29: Detector and FSM results for full scan type 3 and initial offset 4.
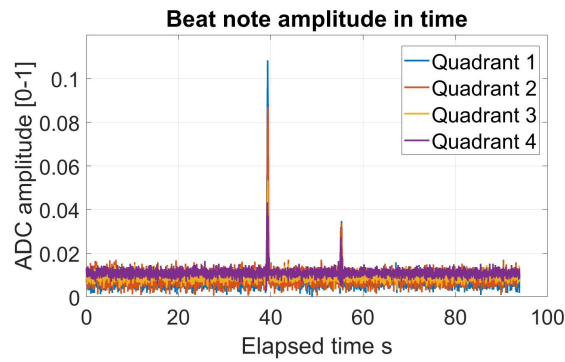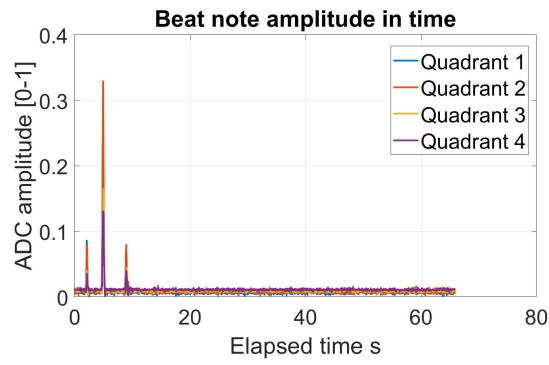
Figure B.30: Beat note intensity on the QPD for full scan type 3 from the initial offset 4.

B.4. Offset 5
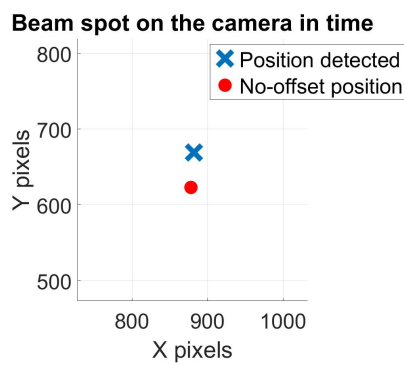## B.4.1. Scan type 2

Figure B.31: Detection position on the detector for scan type 2 from the initial offset 5.

(a) FSM over the Hexapod voltage values during the acquisition test for scan type 2 and initial offset 5.

(b) FSM in the OMT voltage values during the acquisition test for scan type 2 and initial offset 5.

Figure B.32: FSM voltages for scan type 2 and initial offset 5.

(a) Phases values for scan type 2 and initial offset 5.

(b) Phase differences values for scan type 2 and initial offset 5.

Figure B.33: Phases and phase differences for scan type 2 and initial offset 5.

Figure B.34: Beat note intensity on the QPD for scan type 2 from the initial offset 5.

(a) Detection position on the detector for full scan type 2 from the initial offset 5.

(b) FSM over the Hexapod voltage values during the acquisition test for full scan type 2 and initial offset 5.

Figure B.35: Detector and FSM results for full scan type 2 and initial offset 5.

Figure B.36: Beat note intensity on the QPD for full scan type 2 from the initial offset 5.
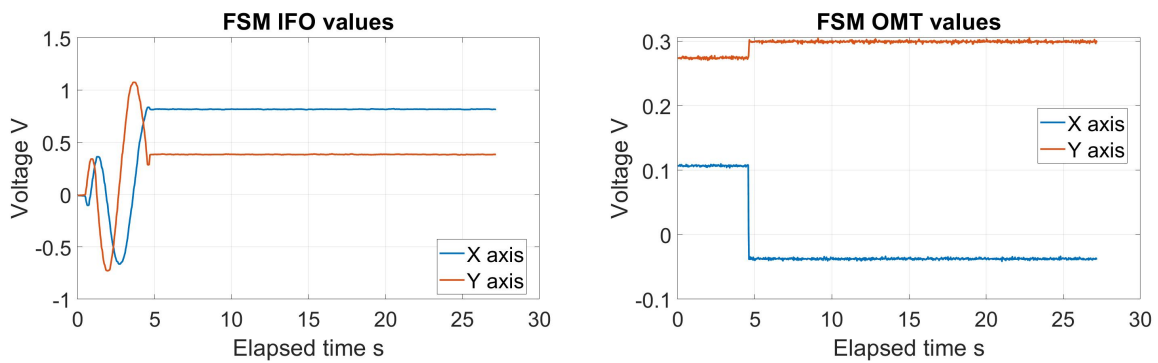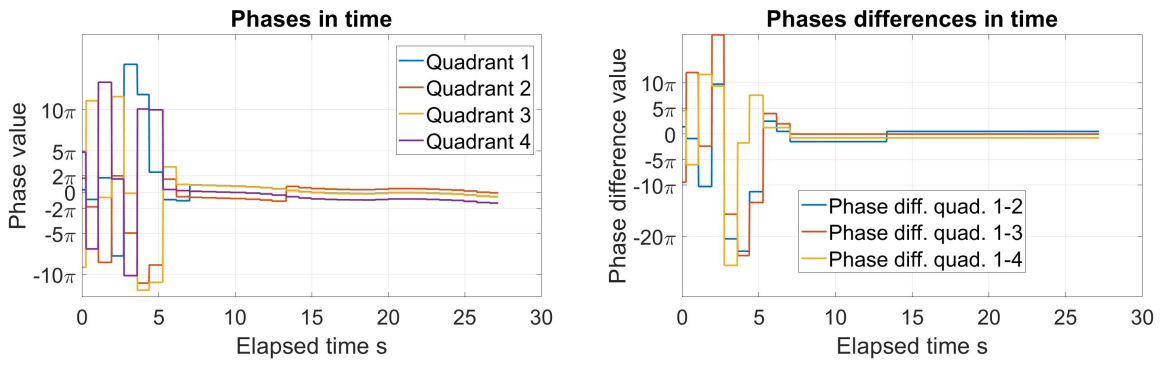
B.4.2. Scan type 3

Figure B.37: Detection position on the detector for scan type 3 from the initial offset 5.

(a) FSM over the Hexapod voltage values during the acquisition test for scan type 3 and initial offset 5.

(b) FSM in the OMT voltage values during the acquisition test for scan type 3 and initial offset 5.

Figure B.38: FSM voltages for scan type 3 and initial offset 5.

(a) Phases values for scan type 3 and initial offset 5.

(b) Phase differences values for scan type 3 and initial offset 5.

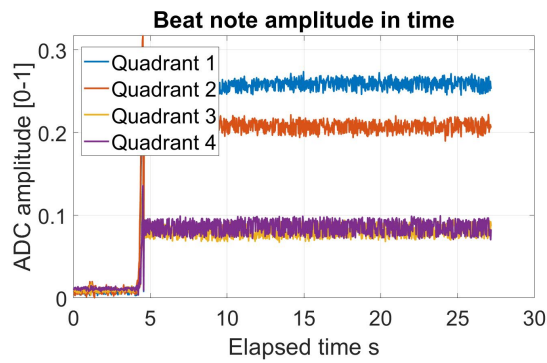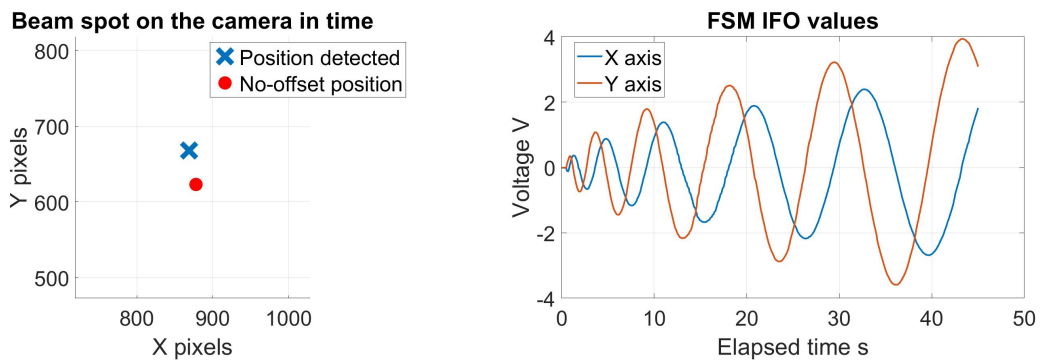**Figure B.39:** Phases and phase differences for scan type 3 and initial offset 5.

Figure B.40: Beat note intensity on the QPD for scan type 3 from the initial offset 5.

(a) Detection position on the detector for full scan type 3 from the initial offset 5.

(b) FSM over the Hexapod voltage values during the acquisition test for full scan type 3 and initial offset 5.

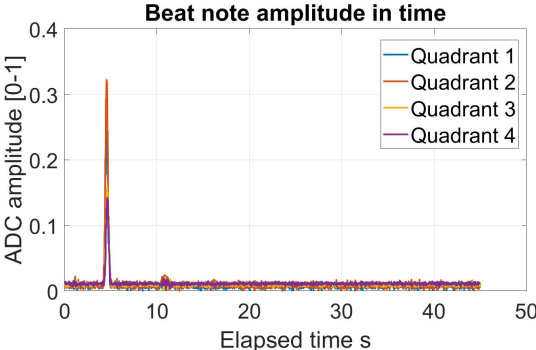**Figure B.41:** Detector and FSM results for full scan type 3 and initial offset 5.

Figure B.42: Beat note intensity on the QPD for full scan type 3 from the initial offset 5.